

University of New Mexico

UNM Digital Repository

Earth and Planetary Sciences ETDs

Electronic Theses and Dissertations

Fall 12-13-2020

**MICROSTRUCTURAL CONSTRAINTS ON THE NEBULAR AND
ASTEROIDAL HISTORIES OF CALCIUM-ALUMINUM-RICH
INCLUSIONS FROM CV3 CHONDRITES**

Shaofan Che
University of New Mexico

Follow this and additional works at: https://digitalrepository.unm.edu/eps_etds



Part of the [Cosmochemistry Commons](#), and the [Geology Commons](#)

Recommended Citation

Che, Shaofan. "MICROSTRUCTURAL CONSTRAINTS ON THE NEBULAR AND ASTEROIDAL HISTORIES OF CALCIUM-ALUMINUM-RICH INCLUSIONS FROM CV3 CHONDRITES." (2020).

https://digitalrepository.unm.edu/eps_etds/286

This Dissertation is brought to you for free and open access by the Electronic Theses and Dissertations at UNM Digital Repository. It has been accepted for inclusion in Earth and Planetary Sciences ETDs by an authorized administrator of UNM Digital Repository. For more information, please contact disc@unm.edu.

Shaofan Che

Candidate

Earth and Planetary Sciences

Department

This dissertation is approved, and it is acceptable in quality and form for publication:

Approved by the Dissertation Committee:

Dr. Adrian J. Brearley, Chairperson

Dr. Charles K. Shearer

Dr. Zachary D. Sharp

Dr. Steven B. Simon

Dr. Karen Ziegler

Dr. Lindsay P. Keller

**MICROSTRUCTURAL CONSTRAINTS ON THE NEBULAR
AND ASTEROIDAL HISTORIES OF CALCIUM-ALUMINUM-
RICH INCLUSIONS FROM CV3 CHONDRITES**

by

SHAOFAN CHE

B.S., Geology, China University of Geosciences (Wuhan), 2013

M.S., Geology, China University of Geosciences (Wuhan), 2016

DISSERTATION

Submitted in Partial Fulfillment of the
Requirements for the Degree of

**Doctor of Philosophy
Earth and Planetary Sciences**

The University of New Mexico
Albuquerque, New Mexico

May, 2021

ACKNOWLEDGMENTS

Throughout my Ph.D. study I have received a great deal of help and support from many people at the University of New Mexico. I first wish to express my sincere appreciation to my advisor, Adrian Brearley, for providing me the great opportunity to pursue a PhD in U.S. and for offering inspiration, guidance, and encouragement that helped me become a real scientist. It has always been a pleasant experience for me to read the insightful comments and suggestions he made in my dissertation, which pushed me to sharpen my thinking and significantly improved the organization and quality of my work. I also would like to thank my dissertation committee: Chip Shearer, Steve Simon, Zach Sharp, Karen Ziegler, and Lindsay Keller for their constant support. Special thanks to Chip for being my second project advisor and to Steve for many discussions and suggestions on my dissertation.

I am grateful to the Department of Earth and Planetary Sciences for providing a nurturing and motivating environment for me to grow as a researcher. Many thanks to those knowledgeable and passionate professors in my graduate courses. I also want to thank Elena Dobrică, Ying-Bing Jiang, and Mike Spilde for their tremendous help with electron microscopy. I am deeply indebted to Cecilia Arias, Cindy Jaramillo, Faith Mutchnik, and Paula Pascetti for their assistance during my stay in the department.

I very much appreciate the valuable suggestions from my colleagues. Their constructive input turned my online dissertation defense into a small Meteoritical Society meeting, which was definitely one of the best experiences I have ever had in my research career.

To all of my friends – thank you for your support and friendship. Especially our small and lovely chondrite group (Fig. 1). I am exceptionally grateful to Jess Johnson, Elena Dobrică, and Han Zhang, who have always been endlessly patient, thoughtful, and loving. I also benefited a lot from the helpful career advice from Elena Dobrică, Jangmi Han, Jon Lewis, and Jin Zhang. Thanks also to my indoor soccer team “Game of Throw-ins” and outdoor soccer team for the wonderful times on every weekend.

Finally, I want to thank my wife Hui Sun and my parents for their emotional support and belief that I was capable of taking on the Ph.D.

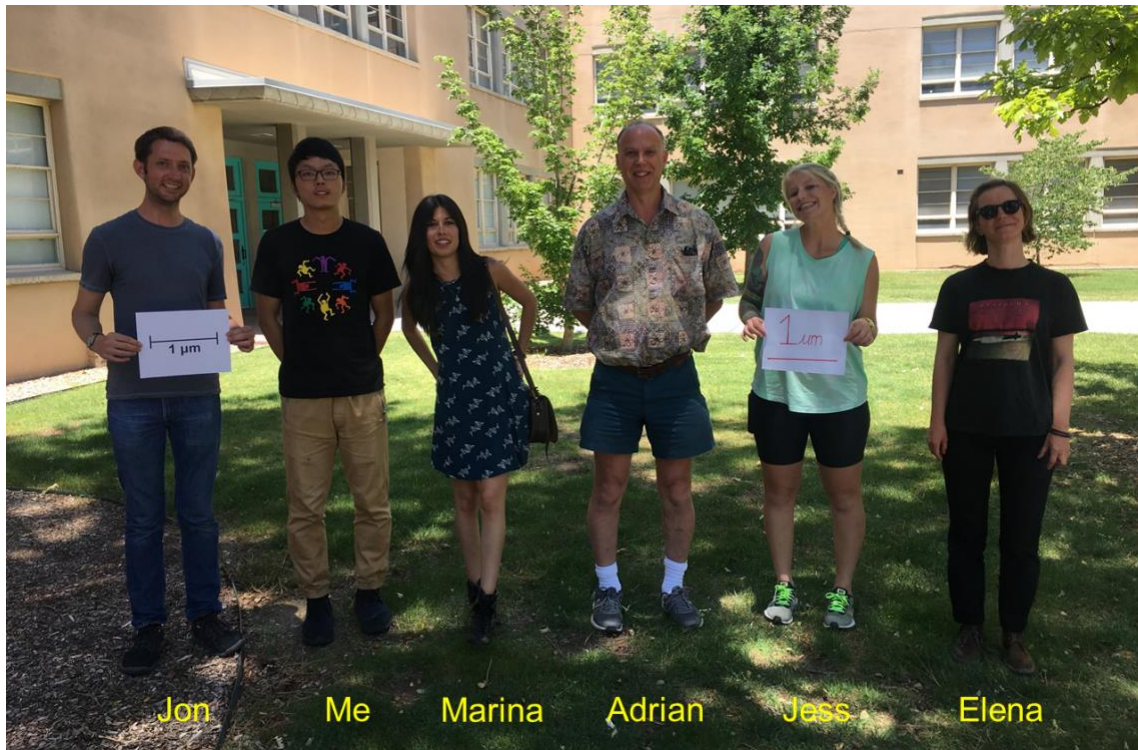


Fig. 1. UNM Chondrite Group (2018). This “Borax Day” photo was taken after we cleaned the electron microscope labs on June 8th, 2018. We added a new member, Houda El Kerni, in 2019.

This work was funded by NASA Cosmochemistry grants NNX15AD28G to A. J. Brearley (PI). The analyses in this work were carried out in the Electron Microbeam Analysis Facility, Department of Earth and Planetary Sciences and Institute of Meteoritics, University of New Mexico. The facility is supported by funds from the State of New Mexico, NSF, and NASA.

MICROSTRUCTURAL CONSTRAINTS ON THE NEBULAR AND ASTEROIDAL HISTORIES OF CALCIUM-ALUMINUM- RICH INCLUSIONS FROM CV3 CHONDRITES

by

Shaofan Che

B.S., Geology, China University of Geosciences (Wuhan), 2013

M.S., Geology, China University of Geosciences (Wuhan), 2016

Ph.D., Earth and Planetary Sciences, University of New Mexico, 2021

ABSTRACT

The petrology and mineralogy of calcium-aluminum-rich inclusions (CAIs) from CV3 carbonaceous chondrites have been investigated using transmission electron microscopy (TEM). The goal of this dissertation is twofold: (1) to gain new insights into the nebular processes, such as vapor-solid reactions, accretion, transport, that are responsible for the formation of non-igneous CAIs, and (2) to better understand the role of fluid in the secondary alteration of CAIs on the CV3 chondrite parent body. This work represents the first systematic microstructural study of CAIs from CV3 chondrites.

Chapter 2 presents the microstructural observations of primary mineralogies of fine-grained, spinel-rich inclusions (FGIs) from the Leoville and Efremovka meteorites. We observe microscale heterogeneities that have not been reported in previous studies and suggest that these FGIs have recorded an evolutionary condensation sequence in the solar nebula. In Chapter 3, we report microstructures of an enstatite-bearing FGI from Leoville. Investigations

of this FGI and several other fine-grained CAIs from Leoville and Efremovka suggest that enstatite is a common, fine-grained condensation phase in CAIs, and it could have recorded a rapid cooling rate in the CAI-forming region. Chapter 4 presents three forsterite-bearing FGIs with a zoning structure from Leoville. The different occurrences of forsterite in the zones may have formed at successively lower pressure conditions and thus their formation may be caused by transport along a negative nebular pressure gradient. In Chapter 5, we study the secondary alteration features of melilite-rich CAIs from Allende. We show that the secondary mineral sequence of melilite can be explained by formation of different phases on a μCaO - μSiO_2 gradient in the fluid. The Wark-Lovering rims surrounding these CAIs also show complex alteration microstructures, which are likely to be products of microchemical environments. Finally, in Chapter 6, we study a unique, forsterite-bearing Type C CAI from Allende. Based on the SEM and TEM observations, the observed iron-alkali-halogen zonal sequence can be best explained by a two-stage fluid alteration process on the Allende parent body.

TABLE OF CONTENTS

| | |
|---|------------|
| ACKNOWLEDGMENTS | iii |
| ABSTRACT..... | vi |
| LIST OF FIGURES | xii |
| LIST OF TABLES..... | xv |
| CHAPTER 1. Introduction | 1 |
| 1. OBJECTIVES OF THE DISSERTATION..... | 3 |
| 2. OVERVIEW OF THE CHAPTERS..... | 5 |
| 3. KEY ADVANCES TO THE STUDY OF CAIS | 9 |
| REFERENCES..... | 10 |
| CHAPTER 2. An evolutionary condensation sequence revealed by mineralogically- distinct nodules in fine-grained, spinel-rich inclusions from CV3 chondrites: Implications for the genetic links between different types of non-igneous refractory inclusions..... | 13 |
| ABSTRACT..... | 13 |
| 1. INTRODUCTION | 15 |
| 2. ANALYTICAL METHODS | 17 |
| 3. RESULTS..... | 19 |
| 3.1. SEM observations | 19 |
| 3.1.1. Mineralogically homogeneous FGIs | 20 |
| 3.1.2. Mineralogically zoned FGIs..... | 22 |
| 3.1.3. Mineralogically heterogeneous FGIs..... | 29 |
| 3.2. Mineral compositions..... | 37 |
| 3.3. Microstructures | 37 |
| 4. DISCUSSION | 46 |
| 4.1. Formational and evolutionary histories of nodules in the Leoville and Efremovka FGIs..... | 50 |
| 4.1.1. Spinel-melilite-diopside nodules | 51 |
| 4.1.2. Melilite-diopside nodules | 55 |
| 4.1.3. Anorthite-rich nodules..... | 57 |
| 4.1.4. Enstatite-bearing nodules | 60 |
| 4.2. An evolutionary condensation sequence revealed by various nodules in FGIs..... | 61 |
| 4.3. Agglomeration of nodules to form mineralogically zoned and heterogeneous FGIs | 65 |
| 4.4. New insights into the origin of zoned FGIs in CV3 chondrites | 70 |
| 5. CONCLUSIONS..... | 73 |
| ACKNOWLEDGEMENTS | 75 |
| REFERENCES..... | 75 |

CHAPTER 3. Microstructures of enstatite in fine-grained CAIs from CV3 chondrites: Implications for mechanisms and conditions of formation..... 83

| | |
|---|-----|
| ABSTRACT..... | 83 |
| 1. INTRODUCTION | 85 |
| 2. ANALYTICAL METHODS | 87 |
| 3. RESULTS..... | 88 |
| 3.1. SEM observations | 88 |
| 3.2. Mineral compositions..... | 94 |
| 3.3. Microstructures | 94 |
| 3.4. Enstatite in fine-grained CAIs from other CV3 chondrites..... | 108 |
| 4. DISCUSSION | 110 |
| 4.1. Formation mechanisms of enstatite in Ef1014-01..... | 111 |
| 4.1.1. Microstructural constraints on the precursor polymorph of enstatite in Ef1014-01 | 111 |
| 4.1.2. Crystallization from a pyroxene-normative melt | 115 |
| 4.1.3. Formation by equilibrium condensation | 116 |
| 4.1.4. Formation by direct condensation..... | 117 |
| 4.1.5. Formation by reheating..... | 120 |
| 4.1.6. Crystallization from amorphous silicate dust material | 121 |
| 4.2. Implications of the cooling rate of enstatite in Ef1014-01 | 123 |
| 4.3. The nebular reservoirs of enstatite-bearing, fine-grained CAIs | 126 |
| 5. CONCLUSIONS..... | 127 |
| ACKNOWLEDGEMENTS | 128 |
| REFERENCES..... | 128 |

CHAPTER 4. A microstructural study of forsterite-bearing, fine-grained, spinel-rich inclusions from the Leoville CV3 chondrite: Implications for the transportation process in the formation regions of refractory inclusions..... 139

| | |
|---|-----|
| ABSTRACT..... | 139 |
| 1. INTRODUCTION | 140 |
| 2. ANALYTICAL METHODS | 142 |
| 3. RESULTS..... | 143 |
| 3.1. SEM observations | 143 |
| 3.2. Mineral compositions..... | 147 |
| 3.3. Microstructures | 150 |
| 4. DISCUSSION | 154 |
| 4.1. The origins of forsterite in the forsterite-bearing FGIs | 154 |
| 4.1.1. Forsterite in the intergrowth zones | 158 |
| 4.1.2. Forsterite in the sinuous zones..... | 165 |
| 4.1.3. Forsterite in the AOA-like zones | 168 |
| 4.2. The transportation process recorded in the forsterite-bearing FGIs | 169 |
| 5. CONCLUSIONS..... | 175 |

| | |
|------------------------|-----|
| ACKNOWLEDGEMENTS | 175 |
| REFERENCES..... | 176 |

CHAPTER 5. The role of fluid chemistry in the alteration of melilite-rich CAIs and their Wark-Lovering rims from the Allende CV3 chondrite 182

| | |
|--|-----|
| ABSTRACT..... | 182 |
| 1. INTRODUCTION | 183 |
| 2. ANALYTICAL METHODS | 185 |
| 3. RESULTS..... | 187 |
| 3.1. SEM observations | 187 |
| 3.1.1. <i>Slightly altered melilite-rich CAIs</i> | 187 |
| 3.1.2. <i>Moderately altered melilite-rich CAIs</i> | 190 |
| 3.1.3. <i>Extensively altered melilite-rich CAIs</i> | 192 |
| 3.1.4. <i>The alteration features of WL rims on melilite-rich CAIs</i> | 196 |
| 3.2. Microstructures | 199 |
| 4. DISCUSSION | 203 |
| 4.1. The alteration sequence of melilite | 204 |
| 4.1.1. <i>The effect of chemical potential gradient</i> | 205 |
| 4.1.2. <i>Complexities of the alteration sequence</i> | 208 |
| 4.2. The effects of secondary alteration on WL rims..... | 212 |
| 5. CONCLUSIONS..... | 217 |
| ACKNOWLEDGEMENTS | 218 |
| REFERENCES..... | 219 |

CHAPTER 6. The formation and alteration history of a forsterite-bearing Type C CAI from Allende: Evidence for a Type B CAI precursor, and implications for fluid-assisted metasomatism on the CV chondrite parent body 228

| | |
|--|-----|
| ABSTRACT..... | 228 |
| 1. INTRODUCTION | 230 |
| 2. ANALYTICAL METHODS | 234 |
| 3. RESULTS..... | 237 |
| 3.1. SEM observations | 237 |
| 3.2. Bulk composition and mineral compositions | 242 |
| 3.3. Microstructures | 246 |
| 4. DISCUSSION | 257 |
| 4.1. The primary features of ALNH-04..... | 259 |
| 4.1.1. <i>Comparison with other Type C CAIs from CV3 chondrites</i> | 259 |
| 4.1.2. <i>Origin of the primary features of ALNH-04</i> | 262 |
| 4.2. Origin of the secondary features of ALNH-04..... | 267 |
| 4.2.1. <i>Nebular vs. parent body alteration</i> | 267 |
| 4.2.2. <i>Origin of the alkali-halogen zonal sequence</i> | 272 |
| 4.2.3. <i>Relationship of the Fe-rich secondary phases with the alkali-halogen zoning sequence</i> | |

| | |
|--|-----|
| | 281 |
| 4.3. The role of fluid in altering ALNH-04 | 284 |
| 4.4. Implications on the alteration processes on the CV3 parent body | 286 |
| 5. CONCLUSIONS..... | 293 |
| ACKNOWLEDGEMENTS | 295 |
| REFERENCES..... | 295 |
| Supplementary data..... | 314 |

LIST OF FIGURES

CHAPTER 2

| | |
|---|----|
| Fig. 1. BSE images of two mineralogically homogeneous FGIs: Leo-H05 from Leoville and Ef1014-13 from Efremovka..... | 21 |
| Fig. 2. Combined EDS X-ray elemental map in Mg (red), Ca (green), and Al (blue) (a), and BSE images (b-g) of a mineralogically zoned FGI Ef1014-04 from the Efremovka chondrite | 23 |
| Fig. 3. BSE image (a, c-f) and combined EDS X-ray elemental map in Mg (red), Ca (green), and Al (blue) (b) of a zoned FGI Leo-H07 from Leoville | 26 |
| Fig. 4. BSE images of another zoned FGI Leo-H09 from Leoville..... | 28 |
| Fig. 5. BSE image (a) and combined EDS X-ray elemental map in Mg (red), Ca (green), and Al (blue) (b) of a mineralogically heterogeneous FGI Leo-H01 from Leoville | 30 |
| Fig. 6. BSE images of nodules from different regions of Leo-H01 showing variations in texture and mineralogy..... | 31 |
| Fig. 7. BSE images (a, c-f) and combined EDS X-ray elemental map in Mg (red), Ca (green), and Al (blue) (b) of a mineralogically heterogeneous FGI Leo-H03 from Leoville | 33 |
| Fig. 8. BSE images of a mineralogically heterogeneous FGI Ef1014-05 from Efremovka ... | 35 |
| Fig. 9. The locations of the FIB sections extracted for TEM studies | 43 |
| Fig. 10. TEM images of spinel-cored nodules from Leo-H07 and Leo-H05..... | 45 |
| Fig. 11. TEM images of melilite-rich nodules from Leo-H09..... | 47 |
| Fig. 12. TEM images of spinel-anorthite-diopside nodules in FIB-05 and -06 from Leo-H07 | 49 |
| Fig. 13. Schematic cartoon illustrating the evolutionary condensation sequence that has been recorded by nodules with different mineralogies..... | 63 |

CHAPTER 3

| | |
|--|-----|
| Fig. 1. SEM and EDS X-ray maps of the enstatite-bearing CAI Ef1014-01 from Efremovka | 89 |
| Fig. 2. Backscattered electron SEM images showing the mineralogy of spinel-rich nodules | 90 |
| Fig. 3. Backscattered electron SEM images of the AOA-like material surrounding Ef1014-01 | 92 |
| Fig. 4. The positions of FIB sections subtracted from Ef1014-01 | 100 |
| Fig. 5. Dark-field STEM mosaics of the four FIB sections extracted from Ef1014-01 | 102 |
| Fig. 6. Dark-field STEM (a-c) and BF-TEM images (d-e) showing the interfaces between enstatite and diopside in FIB-01 | 103 |
| Fig. 7. Dark-field STEM images of the mineralogy and textural characteristics of FIB-02 | 104 |
| Fig. 8. Dark-field STEM images (a-c) of the enstatite layer in FIB-03, and its relationship with other adjacent phases | 105 |

| | |
|---|-----|
| Fig. 9. Bright-field TEM image (a) and HRTEM images (b-e) of adjacent enstatite and diopside grains from the upper right region of FIB-04 | 106 |
| Fig. 10. SEM and TEM images showing occurrences of enstatite in other CAIs from Efremovka and Leoville..... | 109 |
| Fig. 11. Phase diagram for MgSiO ₃ polymorphs..... | 112 |
| Fig. 12. A schematic cartoon illustrating the direct condensation process of enstatite on diopside..... | 119 |
| Fig. 13. A cartoon figure illustrating possible transportation processes in the protoplanetary disk that could have caused reheating of Ef1014-01 | 122 |

CHAPTER 4

| | |
|---|-----|
| Fig. 1. BSE images (a, c, e) and combined EDS elemental X-ray maps in Mg (red), Ca (green), and Al (blue) (b, d, f) of three mineralogically-zoned, forsterite-bearing FGIs from the Leoville chondrite | 144 |
| Fig. 2. BSE images of the intergrowth zones in the forsterite-bearing FGIs..... | 146 |
| Fig. 3. BSE images of the sinuous zones in the forsterite-bearing FGIs | 148 |
| Fig. 4. BSE images of the AOA-like zones in the forsterite-bearing FGIs..... | 149 |
| Fig. 5. Compositional plots (a) MnO vs. Fa and (b) CaO vs. Fa of forsterite in the forsterite-bearing FGIs in this study..... | 154 |
| Fig. 6. BSE images showing the positions where the three FIB sections were extracted | 155 |
| Fig. 7. DF-STEM images of FIB-01 and FIB-03 from the intergrowth zones showing the textural relationships between forsterite, diopside and anorthite..... | 157 |
| Fig. 8. DF-STEM images of FIB-02 from the sinuous zone in Leo-H08..... | 158 |
| Fig. 9. Equilibrium condensation curves for the formation of diopside and forsterite illustrating the effect of pressure on the relative sequence of different reactions | 164 |

CHAPTER 5

| | |
|---|-----|
| Fig. 1. Combined X-ray elemental map in Mg (red), Ca (green), and Al (blue) (a) and BSE images (b-e) of a slightly altered Type B1 CAI ALNA3-01 from Allende..... | 188 |
| Fig. 2. Combined X-ray elemental map in Mg (red), Ca (green), and Al (blue) (a) and BSE images (b-d) of a moderately altered compact Type A CAI ALNH-06 from Allende showing the textural relationships between melilite and secondary phases | 190 |
| Fig. 3. Combined X-ray elemental map in Mg (red), Ca (green), and Al (blue) (a) and BSE images (b-d) of a moderately altered compact Type A CAI ALNG-01 from Allende .. | 192 |
| Fig. 4. Combined X-ray elemental maps (a-b) and BSE images (c-h) of an extensively altered compact Type A CAI “The Bear” from Allende | 194 |
| Fig. 5. BSE images (a, c-f) and combined X-ray elemental map in Mg (red), Si (green), and Fe (blue) (b) of WL rims from several Allende melilite-rich CAIs | 197 |

| | |
|--|-----|
| Fig. 6. The positions of the FIB sections for this study | 200 |
| Fig. 7. TEM images of fine-grained, massive Ca-feldspar in FIB-04 | 201 |
| Fig. 8. Dark-field STEM images of FIB-02 that was extracted from the altered WL rim on ALNA3-01 from Allende..... | 202 |
| Fig. 9. A chemical potential diagram constructed using the thermodynamic database of Holland and Powell (2011) | 207 |
| Fig. 10. A schematic diagram illustrating the alteration process of WL rims on Allende melilite-rich CAIs..... | 216 |

CHAPTER 6

| | |
|--|-----|
| Fig. 1. SEM and X-ray maps of the Type C inclusion ALNH-04 from Allende..... | 235 |
| Fig. 2. BSE images showing the alteration features in ALNH-04 | 239 |
| Fig. 3. BSE images showing additional alteration features in ALNH-04..... | 241 |
| Fig. 4. Plots of diopside compositions in ALNH-04: (a) TiO_2 vs. Al_2O_3 (wt%) and (b) Cr_2O_3 vs. Al_2O_3 (wt%)..... | 245 |
| Fig. 5. The locations for the six FIB sections extracted from ALNH-04..... | 247 |
| Fig. 6. TEM images of FIB-01 that was extracted from an alteration zone between anorthite and diopside in the inner mantle region of the CAI..... | 249 |
| Fig. 7. DF-STEM images of FIB-04 from the altered interface between anorthite and diopside in the inner mantle region of the CAI | 251 |
| Fig. 8. BF-TEM images of FIB-02 from a fine-grained, extensively altered anorthite grain in the outer mantle region of the CAI | 252 |
| Fig. 9. Mosaic DF-STEM image of FIB-03 that was lifted out from the interface between an anorthite grain and its alteration products (feldspathoids and Fe-bearing olivine) in the outer mantle region of the CAI | 253 |
| Fig. 10. DF-STEM images (a and b) of FIB-06 that is from an outer mantle region where secondary iron sulfides are abundant..... | 254 |
| Fig. 11. DF-STEM mosaic image of FIB-05 from an altered anorthite grain in the core region of the CAI | 256 |
| Fig. 12. (a) A CMAS diagram showing the position of the bulk composition of ALNH-04. Other types of refractory inclusions and chondrules are also plotted for comparison.. | 258 |
| Fig. 13. Minor element plots of (a) Cr_2O_3 (wt%) vs. Fa (mol%), (b) MnO (wt%) vs. Fa (mol%), and (c) CaO (wt%) vs. Fa (mol%) of forsterite in ALNH-04, in comparison with olivine in other Type C CAIs and AOAs from CV3 chondrites | 265 |
| Fig. 14. BSE images (a, c, e, g) and combined elemental maps (Ca (red), Na (green), and Cl (blue)) (b, d, f, h) of CAIs and chondrules in the ALNH thin section from Allende, which also show iron-alkali-halogen zonal sequences | 287 |
| Fig. 15. BSE images of the alteration features in ALNH-08 | 290 |
| Fig. S1. The phase image of ALNH-04 produced using the modal recombination analysis method by Berlin (2012)..... | 314 |

LIST OF TABLES

CHAPTER 2

| | |
|---|----|
| Table 1. Representative electron microprobe analyses (wt%) of spinel in FGIs from Leoville | 38 |
| Table 2. Representative electron microprobe analyses (wt%) of melilite in FGIs from Leoville | 39 |
| Table 3. Representative electron microprobe analyses (wt%) of anorthite in FGIs from Leoville | 40 |
| Table 4. Representative electron microprobe analyses (wt%) of diopside in FGIs from Leoville | 41 |

CHAPTER 3

| | |
|--|----|
| Table 1. Representative electron microprobe analyses (wt%) of spinel in Ef1014-01 | 95 |
| Table 2. Representative electron microprobe analyses (wt%) of anorthite in Ef1014-01 | 96 |
| Table 3. Representative electron microprobe analyses (wt%) of diopside in Ef1014-01 | 97 |
| Table 4. Representative electron microprobe analyses (wt%) of enstatite in Ef1014-01 | 98 |
| Table 5. Representative electron microprobe analyses (wt%) of olivine in Ef1014-01 | 99 |

CHAPTER 4

| | |
|--|-----|
| Table 1. Representative electron microprobe analyses (wt%) of forsterite in forsterite-bearing FGIs..... | 151 |
| Table 2. Representative electron microprobe analyses (wt%) of anorthite in forsterite-bearing FGIs..... | 152 |
| Table 3. Representative electron microprobe analyses (wt%) of diopside in forsterite-bearing FGIs..... | 153 |

CHAPTER 6

| | |
|---|-----|
| Table 1. Data for calculating the bulk composition of ALNH-04..... | 244 |
| Table 2. Average compositions of individual minerals and the calculated bulk compositions | 244 |
| Table S1. Representative electron microprobe analyses of anorthite in ALNH-04 | 315 |
| Table S2. Representative electron microprobe analyses of pyroxene in ALNH-04 | 316 |
| Table S3. Representative electron microprobe analyses of spinel in ALNH-04..... | 317 |
| Table S4. Representative electron microprobe analyses of forsterite in ALNH-04..... | 318 |
| Table S5. Representative electron microprobe analyses of Al-Fe silicate in ALNH-04..... | 319 |

CHAPTER 1

Introduction

Chondrites are the most primitive rock samples in the solar system: chondritic components formed during the earliest stages of the solar nebula; chondrites did not experience melting and igneous differentiation; and the elemental abundances of bulk chondrites are close to those in the solar photosphere, except some highly volatile and moderately volatile elements (see Krot et al., 2014; Scott and Krot, 2014). Among the different chondritic components, calcium-aluminum-rich inclusions (CAIs) are particularly important in several aspects. First, CAIs are the oldest objects that formed in the solar system, with an absolute Pb-Pb age of 4567.30 ± 0.16 Ma (Connelly et al., 2017) and they have experienced various high-temperature thermal processes, including condensation, evaporation, annealing, and melting, in the innermost region of the solar nebula (see MacPherson, 2014). Second, carbonaceous chondrites contain high abundances of CAIs which often show more diverse textures, mineralogies, and compositions, compared with other chondritic components. This diversity is mainly the product of a combination of primary thermal processes mentioned above and secondary processes that occurred on chondrite parent bodies (see Brearley and Krot, 2013; MacPherson, 2014). Third, CAIs and related objects, such as amoeboid olivine aggregates (AOAs), Wark-Lovering rims (WL rims), and accretionary rims, may have recorded complex

transport processes in the protoplanetary disk, before they accreted onto the parental asteroids (e.g., see Scott et al., 2018). Therefore, studying CAIs provide us an opportunity to better understand the thermal history of the early solar nebula.

Despite the extensive literature on the characteristics of CAIs, there still remain many open questions, including, but not limited to (1) what is the origin of the systematic deviation between the CAI bulk composition trend and predicted equilibrium condensation trend? (2) are there any age differences between different types of CAIs? (3) what is the origin of the internal oxygen isotopic heterogeneity in CAIs? (4) can we better constrain the timing and environment of secondary alteration of CAIs? and (5) what can we tell about the origin and early distribution patterns of some nuclides (e.g., ^{26}Al , ^{16}O and ^{10}Be) based on the studies of CAIs? In addition, most previous research work on CAIs focused on SEM (scanning electron microscopy)-scale features, and only a few (e.g., Greshake et al., 1998; Ford and Brearley, 2010; Ishii et al., 2010; Han et al., 2015, 2019a,b; Bolser et al., 2016) have investigated the submicron-to-nano scale phase relationships using the FIB/TEM (focused ion beam/transmission electron microscopy) techniques. Each of these microstructural studies has revealed important new details that further constrain the complex evolution of CAIs. However, there are many more complex microstructures in CAIs that have not been investigated systematically. Consequently, additional detailed TEM studies have the potential to further expand our knowledge of the mechanisms and processes that have contributed to the formation and modification of CAIs.

1. OBJECTIVES OF THE DISSERTATION

In this study, we conduct a systematic investigation of the mineralogy and petrology of CAIs from CV3 carbonaceous chondrites (Leoville, Efremovka, and Allende), using mainly SEM and FIB/TEM techniques. There are abundant studies on CV3 CAIs (e.g., Ulyanov, 1984; Boynton et al., 1986; Simon et al., 1999; MacPherson et al., 2002; Krot et al., 2004; Aléon et al., 2005) and they have provided fundamental information of how these refractory inclusions formed and evolved in the solar nebula. However, many of the primary, micro-scale heterogeneities commonly observed in these CAIs can only be studied in detail with the help of high-resolution and high-precision instruments. On the other hand, CV3 CAIs have been significantly affected by secondary alteration on the parent body(ies) that has modified or even completely destroyed the records of primary nebular processes (see Brealey and Krot, 2013). A variety of secondary mineralization features have been observed, especially in CAIs from Allende, which belongs to the oxidized subgroup of CV3 chondrites.

The aim of this dissertation is twofold. First, we study the formational and evolutionary histories of fine-grained CAIs (from less altered samples Leoville and Efremovka) that have not been significantly affected by melting. The typical layered mineral sequences in these CAIs can be generally explained by equilibrium and disequilibrium condensation models (e.g., Yoneda and Grossman, 1995; Petaev and Wood, 1998; Ebel, 2006). There are, however, textural relationships that apparently deviate from these theoretical models. While different mechanisms have been proposed to explain such a deviation, many of the interpretations are

primarily based on SEM observations and are thus likely to be ambiguous due to the fine-grained nature of these CAIs. Additionally, there are several questions about the origin of micro-scale variability in mineralogy and texture of fine-grained CAIs: (1) is the variability caused by different thermal histories? (2) what can microstructures tell about the relative roles of different primary processes, such as condensation and annealing? (3) did these primary processes occur in equilibrium or disequilibrium conditions? (4) can microstructures help us better constrain the potential precursors or nucleation sites of CAI phases? Finally, although it is well-known that the bulk compositions of different types of refractory inclusions is controlled by vapor-solid reactions in the solar nebula (MacPherson and Huss, 2005), the precursors of these refractory inclusions as well as the exact genetic relationships between them are not fully constrained. Our detailed study of fine-grained CAIs can potentially gain further insights into these problems.

The second aspect of this dissertation is to study the secondary alteration histories of Allende CAIs. The secondary alteration of Allende is generally well-studied and there is a consensus that the alteration happened in a parent body environment (e.g., Krot et al., 1998; Brearley, 2006, 2014). When it comes to CAIs, however, the alteration mechanisms are more poorly constrained, which is mainly due to the diversity in the primary mineralogy of CAIs and the fine-grained nature of the alteration products. Fortunately, the secondary alteration in Allende CAIs often did not go to completion, which allows for detailed studies of the mechanisms of the alteration reactions. By taking advantage of FIB/TEM techniques, we are able to test the following two hypotheses. (1) Fluids played an important role in producing

various alteration features observed in Allende CAIs. Different alteration phases have been reported in these CAIs; however, it is not clear what stage of alteration each phase represents, especially when different phases form complex assemblages. Minerals formed at different stages may have recorded changes in the fluid composition. (2) Microchemical environments contributed significantly to the establishment of heterogeneities in alteration effects of Allende CAIs. Localized variations in fluid chemistry, such as pH and cation activity, or variations in water/rock ratio could cause highly localized variations in reaction pathways that involved the dissolution and precipitation of primary and secondary mineral phases. Therefore, a convincing interpretation of the heterogeneous alteration effects strongly depends on the careful investigation of secondary microstructures using high resolution techniques like TEM.

2. OVERVIEW OF THE CHAPTERS

This dissertation is composed of five chapters, excluding this introduction chapter. Each chapter is prepared as a separate manuscript that has been or will be submitted to peer-reviewed journals. The chapters can be divided into two parts: (1) Chapter 2-4 describe the primary mineralogy and petrology of fine-grained CAIs from the Leoville and Efremovka chondrites; (2) Chapter 5 and 6 investigate the secondary mineralization of CAIs from the Allende chondrite. The major observations and implications of each chapter are summarized below.

In Chapter 2, we conduct a systematic study on fine-grained, spinel-rich inclusions (FGIs) from Leoville and Efremovka. Based on the mineralogy and texture, these FGIs can be divided into three categories: homogeneous, zoned, and heterogeneous. We focus on the latter two

categories, whose nodules typically show significant variations in mineralogy and size. The size of the nodules is intimately related to their mineralogy: large nodules usually contain more compact and polycrystalline cores than small nodules. In individual FGIs, clusters of small nodules are commonly observed, which either enclose large nodules or are encompassed by shells of large nodules. We propose that such a relationship can be explained well if physical isolation controlled the size difference of nodules, which in turn controlled the accretion rates of nodules. A closer look at the microstructures of the nodules reveals many interesting features. The most important one is that several phases, such as spinel, diopside, and perovskite, have different occurrences, which may correspond to different generations of phases in a disequilibrium condensation process. We also find that many nodules share similarities with other types of non-igneous CAIs, e.g., hibonite-spinel inclusions and fluffy Type A CAIs. This likely points to an evolutionary condensation sequence, in which mineralogically-distinct nodules represent micrometer-sized counterparts of different types of non-igneous CAIs. Finally, our new observations of some mineralogically zoned FGIs suggest that the zonation may be produced by condensation in different reservoirs.

Chapter 3 presents the microstructures of some enstatite-bearing, fine-grained CAIs from Leoville and Efremovka. We focus the study on a unique FGI (Ef1014-01), in which enstatite occurs as outer layers on spinel-anorthite-diopside nodules. The crystal structure of enstatite and its textural relationship with other phases are examined using FIB/TEM: (1) it is dominantly twinned, low-temperature clinoenstatite (CLEN), with minor thin orthoenstatite (OREN) lamellae, and (2) a crystallographic orientation relationship is observed between

enstatite and diopside. The microstructural and compositional results suggest a protoenstatite precursor for the CLEN-OREN intergrowths, which may be produced by direct condensation or reheating in the solar nebula. During the condensation, the nucleation of enstatite was facilitated by the crystallographic orientation relationship between enstatite and diopside. An extremely rapid cooling rate ($\sim 10^4$ K/h) is inferred, and it could reflect the cooling rate either during the primary condensation or during the secondary reheating event.

In Chapter 4, we investigate three forsterite-bearing FGIs from Leoville. These FGIs are mineralogically zoned, and forsterite has different occurrences in these zones. The innermost zone is composed of a complex intergrowth of forsterite, anorthite, and diopside. In the sinuous zone, forsterite occurs as an interstitial phase between spinel grains, and TEM observations show that forsterite is closely associated with fine-grained Al-diopside. Forsterite in the outermost zone forms an AOA-like shells surrounding spinel-anorthite-diopside nodules. We suggest that forsterite grains in different zones formed by different gas-solid reactions, whose phase boundaries on the P-T diagram vary with pressure. Therefore, the formation of these forsterite-bearing FGIs may have recorded a transport process along a negative nebular pressure gradient.

In Chapter 5, melilite-rich CAIs from Allende are investigated to understand the role of fluid in the secondary alteration. What is common to all the CAIs studied is an alteration sequence of grossular, Ca-rich feldspar, and feldspathoids in melilite. The alteration sequence in melilite is likely to be the product of changing fluid chemistry, which resulted from the interactions between melilite and the fluid. The dissolution of melilite created a $\mu\text{CaO}-\mu\text{SiO}_2$

gradient in the altering fluid, and different secondary phases formed at different locations from the alteration front, based on the local activities of CaO and SiO₂. The important role of fluid chemistry is further strengthened by the alteration behavior of WL rims on melilite-rich CAIs. Two very interesting observations of WL rims are (1) ubiquitous presence of ilmenite closely associated with feldspathoids, and (2) the inner edge of diopside layers has been replaced by Fe-rich olivine. We suggest that microchemical environments played an important role in the alteration of WL rims. Specifically, the precursor matrix materials, due to their finer grain sizes, adjacent to the WL rims could have been altered preferentially compared with the WL rims. This resulted in a higher pH condition in the matrix, and therefore the inner edge of the diopside layers experienced more extensive alteration. The pH in the WL rims progressively increased and ilmenite, which likely formed by alteration of Ti-rich or Ti-bearing diopside, eventually became stabilized at a late stage.

In Chapter 6, we study the formation and alteration history of a Type C CAI ALNH-04 from Allende. This CAI is unique in that it contains forsterite in the core region, and it shows a secondary iron-alkali-halogen zoning sequence. A comparison between this CAI and other Type C CAIs in the literature suggests that the forsterite grains were inherited from a forsterite-bearing Type B CAI precursor. This CAI was likely to have experienced at least two melting events. The zonal distribution of nepheline and sodalite can be attributed to a two-stage alteration process, in which two fluids with different activities of NaCl ($a_{NaCl(aq)}$) were introduced into the CAI. The precipitation of Fe-rich secondary phases was induced by the rise in pH and $a_{SiO_2(aq)}$ of the fluid due to the extensive alteration of the outer part of ALNH-04.

We also investigate several other CAIs and chondrules from Allende, and find that they have been affected by the same two-stage alteration process. The distribution pattern of nepheline and sodalite differs between different objects, which can be caused by the different SiO_2 chemical potential gradients in the fluid.

3. KEY ADVANCES TO THE STUDY OF CAIS

This study presents many micron-to-submicron observations of CAIs that have not been reported in previous studies and provides some new insights into the formation and alteration histories of CAIs from CV3 chondrites.

Disequilibrium condensation should have played an important role throughout the thermal and accretionary histories of non-igneous CAIs in the solar nebula. This process has been recorded in FGIs, in which nodules often vary in mineralogy and size, and show microscale complexities. It is very likely that these nodules represent micrometer-sized counterparts of different types of non-igneous CAIs on an evolutionary condensation sequence, which provides a solution to how different CAIs can be genetically linked. The important role of disequilibrium condensation is further strengthened by the microstructures of enstatite and forsterite in FGIs: the epitaxial growth relationship between enstatite and diopside is likely to be kinetically controlled; the formation of different occurrences of forsterite can be explained by physical transport along a negative pressure gradient.

Our study of Allende CAIs clearly suggests that fluid(s) played an important role in the secondary alteration of these CAIs. The formation of complex secondary alteration features,

such as mineralogical zonation, in Allende CAIs is controlled by the fluid chemistry. The interactions between fluid and primary phases in CAIs produced localized variations in the activities of aqueous species, stabilizing different secondary mineral assemblages at different regions. For example, the secondary alteration sequences in melilite can be attributed to the establishment of CaO and SiO₂ chemical potential gradients. The grain size differences in primary phases of CAIs, and between CAIs, WL rims, and surrounding matrices also have contributed significantly to the generation of heterogeneities in fluid chemistry.

REFERENCES

- Aléon J., Krot A. N., McKeegan K. D., MacPherson G. J. and Ulyanov A. A. (2005) Fine-grained, spinel-rich inclusions from the reduced CV chondrite Efremovka: II. Oxygen isotopic compositions. *Meteorit. Planet. Sci.* **40**, 1043–1058.
- Bolser D., Zega T. J., Asaduzzaman A., Bringuier S., Simon S. B., Grossman L., Thompson M. S. and Domanik K. J. (2016) Microstructural analysis of Wark-Lovering rims in the Allende and Axtell CV3 chondrites: Implications for high-temperature nebular processes. *Meteorit. Planet. Sci.* **51**, 743–756.
- Boynnton W. V., Wark D. A. and Ulyanov A. A. (1986) Trace elements in Efremovka fine-grained inclusion E14: Evidence for high temperature, oxidizing fractionations in the solar nebula. *Lunar Planet. Sci.* **17**, 78–79.
- Brearley A. J. (2014) Nebular versus parent body processing. In *Treatise on Geochemistry: Second Edition* (eds. H. D. Holland and K. K. Turekian). Elsevier, Oxford. pp. 309–334.
- Brearley A. J. (2006) The action of water. In *Meteorites and the Early Solar System II* (eds. D. S. Lauretta and H. Y. McSween). University of Arizona Press, Tucson. pp. 587–624.
- Brearley A. J. and Krot A. N. (2013) Metasomatism in the early solar system: The record from chondritic meteorites. In *Metasomatism and the chemical transformation of rock* (eds. D. E. Harlov and A. Austrheim). Springer, Berlin Heidelberg. pp. 659–789.

- Connelly J. N., Bollard J. and Bizzarro M. (2017) Pb–Pb chronometry and the early Solar System. *Geochim. Cosmochim. Acta* **201**, 345–363.
- Ebel D. S. (2006) Condensation of rocky material in astrophysical environments. In *Meteorites and the Early Solar System II* (eds. D. S. Lauretta and H. Y. McSween). University of Arizona Press, Tucson. pp. 253–277.
- Ford R. L. and Brearley A. J. (2010) Discovery of vesuvianite and kaolinite formed during the alteration of melilite in an Allende type A CAI: Characterization by FIB-TEM. *Lunar Planet. Sci.*, 1402.
- Greshake A., Bischoff A. and Putnis A. (1998) Transmission electron microscope study of compact Type A calcium-aluminum-rich inclusions from CV3 chondrites: Clues to their origin. *Meteorit. Planet. Sci.* **33**, 75–87.
- Han J., Brearley A. J. and Keller L. P. (2015) Microstructural evidence for a disequilibrium condensation origin for hibonite-spinel inclusions in the ALHA77307 CO3.0 chondrite. *Meteorit. Planet. Sci.* **50**, 2121–2136.
- Han J., Jacobsen B., Liu M.-C., Brearley A. J., Matzel J. E. and Keller L. P. (2019) Origin of ¹⁶O-rich fine-grained Ca-Al-rich inclusions of different mineralogy and texture. *Geochemistry* **79**, 125543.
- Han J., Keller L. P., Liu M. C., Needham A. W., Hertwig A. T., Messenger S. and Simon J. I. (2020) A coordinated microstructural and isotopic study of a Wark-Lovering rim on a Vigarano CAI. *Geochim. Cosmochim. Acta* **269**, 639–660.
- Ishii H. A., Krot A. N., Bradley J. P., Keil K., Nagashima K., Teslich N., Jacobsen B. and Yin Q.-Z. (2010) Discovery, mineral paragenesis, and origin of wadalite in a meteorite. *Am. Mineral.* **95**, 440–448.
- Krot A. N., Keil K., Scott E. R. D., Goodrich C. A. and Weisberg M. K. (2014) Classification of meteorites and their genetic relationships. In *Treatise on Geochemistry: Second Edition* (eds. H. D. Holland and K. K. Turekian). Elsevier, Oxford. pp. 1–63.
- Krot A. N., MacPherson G. J., Ulyanov A. A. and Petaev M. I. (2004) Fine-grained, spinel-rich inclusions from the reduced CV chondrites Efremovka and Leoville: I. Mineralogy, petrology, and bulk chemistry. *Meteorit. Planet. Sci.* **39**, 1517–1553.
- Krot A. N., Petaev M. I., Scott E. R. D., Choi B. G., Zolensky M. E. and Keil K. (1998) Progressive alteration in CV3 chondrites: More evidence for asteroidal alteration.

Meteorit. Planet. Sci. **33**, 1065–1085.

MacPherson G. J. (2014) Calcium-aluminum-rich inclusions in chondritic meteorites. In *Treatise on Geochemistry: Second Edition* (eds. H. D. Holland and K. K. Turekian). Elsevier, Oxford. pp. 139–179.

MacPherson G. J. and Huss G. R. (2005) Petrogenesis of Al-rich chondrules: Evidence from bulk compositions and phase equilibria. *Geochim. Cosmochim. Acta* **69**, 3099–3127.

MacPherson G. J., Krot A. N., Ulyanov A. a. and Hicks T. (2002) A comprehensive study of pristine, fine-grained, spinel-rich inclusions from the Leoville and Efremovka CV3 chondrites, I: petrology. *Lunar Planet. Sci.* **33**, 1526.

Petaev M. I. and Wood J. A. (1998) The condensation with partial isolation (CWPI) model of condensation in the solar nebula. *Meteorit. Planet. Sci.* **33**, 1123–1137.

Scott E. R. D. and Krot A. N. (2014) Chondrites and their components. In *Treatise on Geochemistry: Second Edition* (eds. H. D. Holland and K. K. Turekian). Elsevier, Oxford. pp. 65–137.

Scott E. R. D., Krot A. N. and Sanders I. S. (2018) Isotopic dichotomy among meteorites and its bearing on the protoplanetary disk. *Astrophys. J.* **854**, 164.

Simon S. B., Davis A. M. and Grossman L. (1999) Origin of compact type A refractory inclusions from CV3 carbonaceous chondrites. *Geochim. Cosmochim. Acta* **63**, 1233–1248.

Ulyanov A. A. (1984) On the origin of fine-grained Ca, Al-rich inclusions in the Efremovka carbonaceous chondrite. *Lunar Planet. Sci.*, 872–873.

Yoneda S. and Grossman L. (1995) Condensation of CaO–MgO–Al₂O₃–SiO₂ liquids from cosmic gases. *Geochim. Cosmochim. Acta* **59**, 3413–3444.

CHAPTER 2

An evolutionary condensation sequence revealed by mineralogically-distinct nodules in fine-grained, spinel-rich inclusions from CV3 chondrites: Implications for the genetic links between different types of non-igneous refractory inclusions

Abstract

Fine-grained, spinel-rich inclusions (FGIs) are abundant in CV3 chondrites and exhibit textures and compositions that are consistent with a condensation origin. Previous petrologic studies on the primary phases in FGIs and related refractory inclusions reported many complex textural relationships, based on which different condensation reactions have been proposed. However, there are critical microscale variations in the primary mineralogies and textures of nodules in these fine-grained CAIs, which imply more complex formational and evolutionary histories. The systematic investigation of FGIs from the Leoville and Efremovka CV3 chondrites in this study has revealed a number of petrologic characteristics, which provide further insights into the origins of FGIs. Nodules in individual FGIs vary in size and exhibit variations in their mineralogical zonation, resulting in significant heterogeneity within each FGI. In individual FGIs, nodules with a small size commonly form clusters, whereas larger nodules are either embedded in the mass of small nodules or occur as shells surrounding clusters of small nodules. The size difference is associated with a difference in mineralogy: small nodules typically contain single or a few spinel/melilite grains as cores, while the cores

of large nodules are polycrystalline and more compact. Transmission Electron Microscope observations show that the nodules have complex microstructures, including the presence of fine-grained spinel, the close association of fine-grained Al-Ti-diopside with spinel, and a crystallographic orientation relationship between adjacent clinoenstatite and diopside grains.

Our microstructural observations indicate that disequilibrium condensation played an important role in the formation of FGIs, consistent with some previous studies. Specifically, the presence of spinel-cored and melilite-dominant nodules, as well as the different occurrences of spinel (in the cores and on the periphery), suggest that formation of these nodules occurred under disequilibrium conditions, which may be caused by physical isolation of condensates. The textural relationship between melilite and anorthite is indicative of a direct, pseudomorphic replacement reaction, but the exact nature of the reaction is unclear.

Nodules in FGIs show textural and compositional similarities with other types of non-igneous CAIs: hibonite-spinel inclusions and fluffy Type A CAIs. We suggest that mineralogically-distinct nodules are micrometer-sized counterparts of different types of non-igneous CAIs and record an evolutionary condensation sequence in the solar nebula. It is likely that different nodules in individual FGIs formed in the same gaseous reservoir, but at different times. The mechanism of physical isolation of condensates probably controlled the accretion behaviors of nodules with different mineralogies and sizes, resulting in the observed distribution patterns of nodules. On the other hand, some mineralogically-zoned FGIs, with a Mg-rich core and a Ca-rich mantle, can be better explained by condensation followed by transport of the inclusions to a different region of the protoplanetary disk.

1. INTRODUCTION

Calcium-aluminum-rich inclusions (CAIs) are submillimeter-to-centimeter sized refractory objects that represent the oldest materials formed in the solar nebula (e.g., Pb-Pb ages of 4567.30 ± 0.16 Ma, Connelly et al., 2012), and have experienced subsequent heating and melting events for at least 0.3 Ma, calculated from the inferred initial $^{26}\text{Al}/^{27}\text{Al}$ ratios (e.g., MacPherson et al., 2010, 2012; Kita et al., 2012). Therefore, these inclusions provide important constraints on the early evolutionary history of the solar nebula. Despite the great advances in recent decades that have been achieved in understanding the chronological and chemical evolution histories, as well as the isotopic reservoirs of CAIs, most research has been focused on “coarse-grained” inclusions, which commonly have experienced melting events in the solar nebula. On the other hand, although there are a number of studies of fine-grained, spinel-rich inclusions (FGIs) (e.g., Davis and Grossman, 1979; MacPherson et al., 2002; Lin and Kimura, 1998; Krot et al., 2004a; Wang and Hsu, 2009; Aléon et al., 2005; Russell and Howard, 2013; Han and Brearley, 2016; Han et al., 2019; Kawasaki et al., 2020), which were first identified in Allende CV3 chondrite, the origin of these inclusions is not fully understood. For example, the observed textural relationships in these CAIs are often inconsistent with the predicted equilibrium condensation sequence (e.g., Krot et al., 2004a, Han and Brearley, 2016; Han et al., 2019). Further complications come from ^{26}Al - ^{26}Mg isotopic studies of FGIs, which have revealed significant variations in the initial $^{26}\text{Al}/^{27}\text{Al}$ ratios that may correspond to a time span of ~ 0.4 Ma (e.g., Han et al., 2020; Kawasaki et al., 2020). Such variations may indicate that condensation and melting that are responsible for CAI formation occurred repeatedly and

contemporaneously over a short time interval in the early solar nebula.

Fine-grained, spinel-rich inclusions are characterized by aggregations of micrometer-sized, commonly rounded nodules separated from each other by sinuous diopside layers; the detailed mineralogy of individual nodules varies, but a layered sequence of spinel-anorthite-Al-rich diopside is commonly observed. Melilite, perovskite, and Fe,Ni metal are also present in some FGIs. Another unique feature of FGIs is that they are often found to be associated with amoeboid olivine aggregates (AOAs), and therefore, may be genetically related (e.g., Krot et al., 2004b,c; Han and Brearley, 2016). Other types of CAIs and refractory inclusions also have potential genetic relationships with FGIs, based on their bulk compositions (e.g., Lin and Kimura, 1998; Lin et al., 2006; MacPherson, 2014). An obstacle to studying the primary mineralogy of FGIs is the susceptibility of their components to secondary alteration processes. For example, in the CV3 chondrite Allende, the primary phases in FGIs have been extensively altered to hercynitic spinel, feldspathoids, Fe-bearing diopside, ferroan olivine, and metal oxides (e.g., Ulyanov, 1984; Boynton et al., 1986; MacPherson et al., 2002; Brearley and Krot, 2013). One way to overcome this obstacle is to study the relatively less-altered chondrites (e.g., Lin and Kimura, 1998; Krot et al., 2004a; Wang and Hsu, 2009; Han et al., 2019). Careful petrographic observations in these studies have provided fundamental information of the formational and evolutionary histories of FGIs in the solar nebula. However, the primary mineralogy of FGIs often shows significant variability, and a range of different textural relationships is commonly observed. Due to these complexities, the proposed formation reactions in the previous studies are sometimes not consistent with the petrographic

observations. In addition, interpretations of the textural relationships of FGIs observed by scanning electron microscopy (SEM) are not always unambiguous due to the fine-grained nature of these CAIs, and thus may require further investigations using higher resolution techniques, such as transmission electron microscopy (TEM).

In this study, we focus on several FGIs from Leoville and Efremovka, two relatively pristine chondrites (CV3.1-3.4; Bonal et al., 2006) from the CV3 reduced subgroup. These meteorites show a lower degree of secondary alteration compared to the CV3 oxidized subgroup, e.g., Allende (e.g., Ulyanov, 1984; Boynton et al., 1986; Komatsu et al., 2001; Fagan et al., 2004; Ruzicka et al., 2012; Brearley, 2014; Gattacceca et al., 2020), and thus are attractive for studying the primary features inherited from the early solar nebular high-temperature events. In this study, we report detailed petrological and mineralogical observations of FGIs in Leoville and Efremovka using SEM, electron probe microanalysis (EPMA), and TEM. Possible formational and evolutionary histories are proposed for different nodules in FGIs, based on the detailed textural and microstructural observations. We also examine the possible relationships of nodules in FGIs with other types of refractory inclusions.

2. ANALYTICAL METHODS

Backscattered electron (BSE) images and full spectral X-ray maps of 1 inch-round polished thin sections Leoville 577 and Efremovka 1014 (both sections are from the Meteorite Collection of the Institute of Meteoritics, University of New Mexico (UNM)) were obtained on a FEI Quanta 3D DualBeam[®] field emission gun scanning electron microscope/focused ion

beam (FEG-SEM/FIB) instrument fitted with an EDAX Apollo 40 mm² SDD Energy Dispersive Spectroscopy (EDS) system with Genesis software UNM. Full thin section BSE and X-ray map mosaics were produced using ImageJ software, by combination of multiple image fields. These mosaics were then used to locate refractory inclusions and chondrules on the thin section. The petrology and mineralogy of individual objects were characterized in detail by high-resolution BSE imaging and X-ray mapping. The instrument operating conditions for BSE imaging were: accelerating voltage of 15 kV, and beam current of 11 nA. The X-ray mapping was conducted at 15 kV and 11 nA.

The major and minor element compositions of phases in FGIs were obtained using wavelength dispersive spectrometry (WDS) on a JEOL JXA-8200 electron probe microanalyzer (EPMA) at UNM. All analyses were obtained at an accelerating voltage of 15 kV, a beam current of 20 nA, and a spot size of 1 μm . Taylor Company Microprobe Standards were used for calibration: Na on albite, Mg, Si, and Fe on olivine, Al and K on orthoclase, S on pyrite, Ca on diopside, Ti on titanite, V on V-metal, Cr on chromite, Mn on spessartine, and Ni on Ni-metal. In addition, an almandine oxygen standard and an apatite-F (Wilberforce) standard were also used for Al and P, respectively. The detection limits for Fe and Ni are ~ 0.02 wt%, while those for all the other elements are ~ 0.01 wt%. Data were reduced using the modified ZAF correction procedure in Probe for EPMA.

A total of six FIB sections were extracted from Leoville 577 using the FEI Quanta 3D FEG-SEM/FIB instrument using the method described by Han and Brearley (2015). The microstructures of the FIB sections were then characterized on a JEOL 2010F FASTEM field

emission gun scanning TEM (STEM/TEM) instrument at UNM. A variety of different techniques were used, including bright-field TEM (BF-TEM), Dark-Field scanning TEM (DF-STEM), selected area electron diffraction (SAED), and high-resolution TEM (HRTEM). We also performed quantitative microanalysis using an Oxford Instruments AZtec Energy Dispersive X-ray Spectroscopy system with Oxford Instruments XMax 80N 80mm² SDD detector on the JEOL 2010F FASTEM. The Cliff–Lorimer thin film approximation was used for quantification using theoretical k-factors.

3. RESULTS

3.1. SEM observations

Thin section UNM 577 was sectioned from the location near the contact between the Leoville host and a dark inclusion LV-2 (Kracher et al., 1985). In this thin section, the areas of the host and dark inclusion are similar (~42% and ~47%, respectively). The host is composed of relatively large chondrules and refractory inclusions, which are embedded in a fine-grained matrix. Fine-grained, spinel-rich inclusions are the only type of CAIs found in the host, except for one spinel-melilite inclusion, and they are commonly associated with AOA-like materials. Chondrules and refractory inclusions in dark inclusion LV-2 have much smaller sizes than those in the host, and most of them have irregular or fragmented shapes and appear to be debris of larger objects. Most of the CAIs in LV-2 are FGIs, though rare fine-grained, spinel-hibonite inclusions are also present. A total of 50 CAIs were found in LV-2, compared to 14 CAIs in the host. The Leoville host and dark inclusion LV-2 are separated by a fine-grained, matrix-like

layer, which was named LV-2R in Kracher et al. (1985). This layer is composed of olivine and pyroxene grains embedded in a fine-grained matrix. The contact between this layer and LV-2 is sharp, but grades continuously into the host matrix. In this work, we only studied FGIs from the Leoville host, since the dark inclusion LV-2 is texturally similar to CM chondrites (Kracher et al., 1985). In addition, FGIs in LV-2 have been significantly affected by parent body alteration, which has produced a variety of secondary phases, such as Fe-rich olivine, phosphates, and feldspathoids.

In the Efremovka 1014 thin section, we discovered 25 CAIs. Most of the CAIs are FGIs, and 4 of them are Type A CAIs. Many of the FGIs are associated with AOAs or AOA-like materials.

3.1.1. Mineralogically homogeneous FGIs

Some of the FGIs in Leoville and Efremovka are mineralogically homogeneous: nodules in individual FGIs do not show significant variations in mineralogy. Two such FGIs are Leo-H05 (~150 μm in size) and Ef1014-13 (~400 μm in size) (Fig. 1). Nodules in both FGIs have cores that are composed of dense aggregates of spinel grains, with randomly distributed, minor perovskite. Nodules in Leo-H05 often have oval shapes, and sizes typically in the range of 15-20 μm (Fig. 1a). The spinel cores account for more than 70 vol% and are surrounded by layers of melilite 2-4 μm in thickness (Fig. 1b). The outermost diopside layers are very thin (<1 μm). Nodules in this FGI are separated by interstitial, matrix-like materials. Compared with Leo-H05, Ef1014-13 is more compacted (Fig. 1c), exhibiting elongate nodules, with their longer

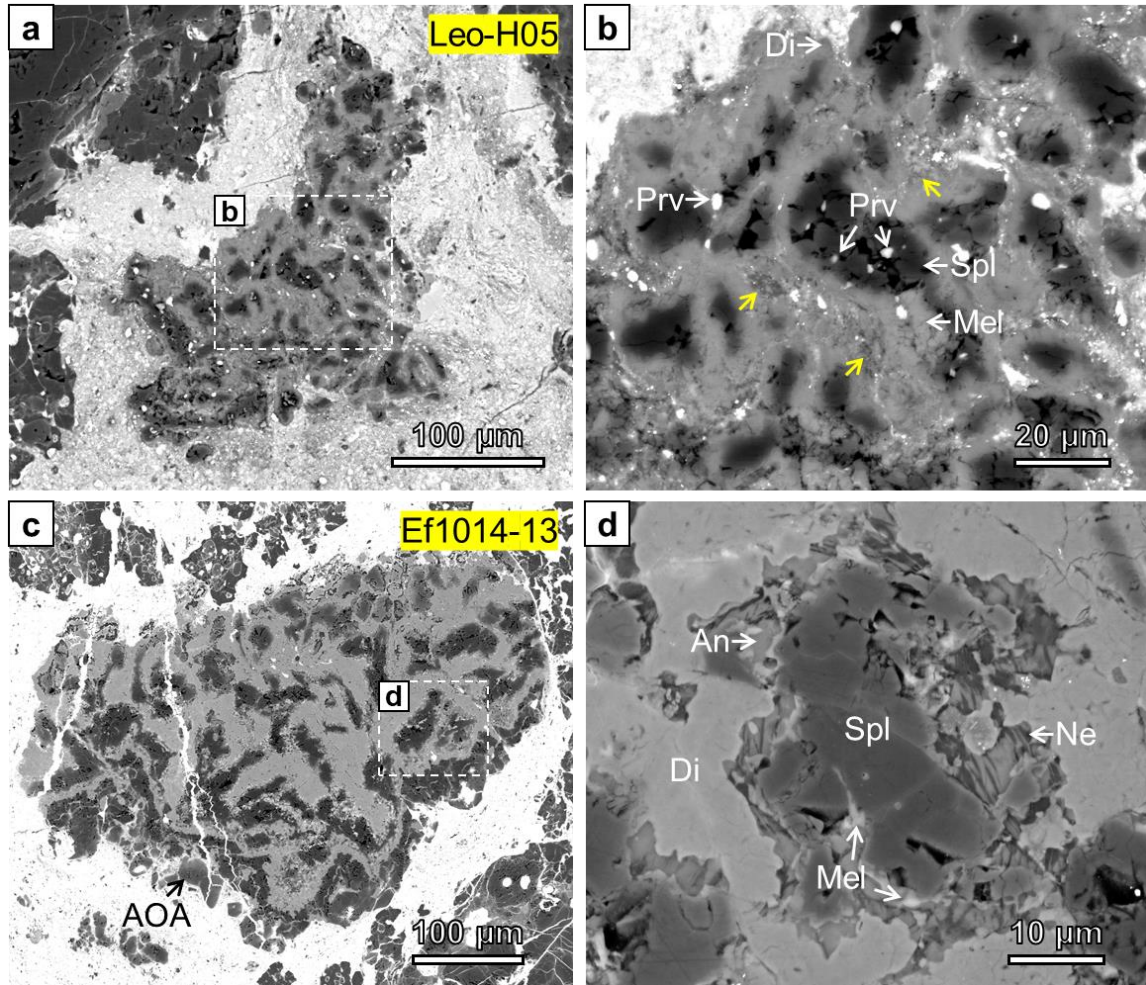


Fig. 1. BSE images of two mineralogically homogeneous FGIs: Leo-H05 from Leoville and Ef1014-13 from Efremovka. (a) Leo-H05 is composed of spinel-melilite-diopside nodules. Matrix-like materials are present interstitially to nodules. (b) The spinel cores are polycrystalline, and perovskite grains often occur in the core region of the nodules. Fine-grained, matrix-like materials are indicated by yellow arrows. (c) Ef1014-13 is a more compacted FGI, compared to Leo-H05. On the bottom side of this FGI in the BSE image is an AOA-like material that is composed of forsterite and Fe,Ni metal. (d) Nodules in Ef1014-13 have a spinel-anorthite-diopside layered sequence. Relict melilite that shows a replacement relationship with anorthite is sometimes present between spinel and anorthite. Anorthite in some nodules has been partially replaced by nepheline. Abbreviations: An = anorthite, Di = diopside, Fe,Ni = Fe,Ni metal, Fo = forsterite, Mel = melilite, Ne = nepheline, Prv = perovskite, Spl = spinel.

axes varying from 35-50 μm . The general layered sequence from interior to exterior in the nodules from this FGI is spinel-anorthite-diopside, with a thick outer diopside layer (5-20 μm).

Minor melilite occurs at the spinel-anorthite interfaces (Fig. 1d). Anorthite sometimes shows evidence of secondary parent body alteration by nepheline. Ef1014-13 is partly surrounded by an AOA-like, forsterite-rich rim that also contains Fe,Ni metal.

3.1.2. Mineralogically zoned FGIs

Some FGIs contain nodules with different mineralogies that form a distinct zoned structure. These FGIs usually have core and mantle regions whose bulk compositions are different. For example, Ef1014-04 has a Mg-rich core and a Ca-rich mantle (Fig. 2). Other FGIs, such as Leo-H07 (Fig. 3) and Leo-H09 (Fig. 4), do not have a concentric zoning structure, but instead show a gradual compositional change from one side to the other. The size of nodules in individual zoned FGIs has a limited range of variation, though some nodules are significantly larger. Below we described three zoned FGIs in detail: Ef1014-04, Leo-H07, and Leo-H09.

Ef1014-04 is 2 mm in size with an irregular shape and has a zoned structure, with a Mg-rich core and Ca-rich mantle (Fig. 2a). The boundary between the core and mantle regions is diffuse and parallel to the shape of the FGI. The core region is exclusively composed of nodules (5-15 μm in size), consisting of polycrystalline aggregates of spinel (Fig. 2b-c). In most of these nodules, spinel cores comprise more than 80 vol%, and are surrounded successively by a thin anorthite layer (mostly $<1 \mu\text{m}$) and an outermost diopside layer (1-3 μm in thickness). Melilite is a rare phase in the nodules from the core region, and where present has a clear replacement relationship by anorthite. The mantle region is melilite-rich and contains nodules

with and without a spinel core (Fig. 2d-e). The spatial distribution of these two types of nodules is random within the FGI. Many of these nodules also contain fine-grained spinel, which occurs as chains close to the inner edge of diopside layers. Melilite in some nodules from the mantle region has been partly replaced by anorthite. Most of the nodules are 10-15 μm in size but some rarer large nodules (25-30 μm) occur in the mantle region. This FGI also contains some hibonite-bearing nodules, typically 20-30 μm in size, but sometimes as large as (~50 μm), which often form clusters, and are present in the outer part of the core region and in the mantle region (Fig. 2f-g). Hibonite in these nodules is coarse-grained (10-15 μm) and has a euhedral-

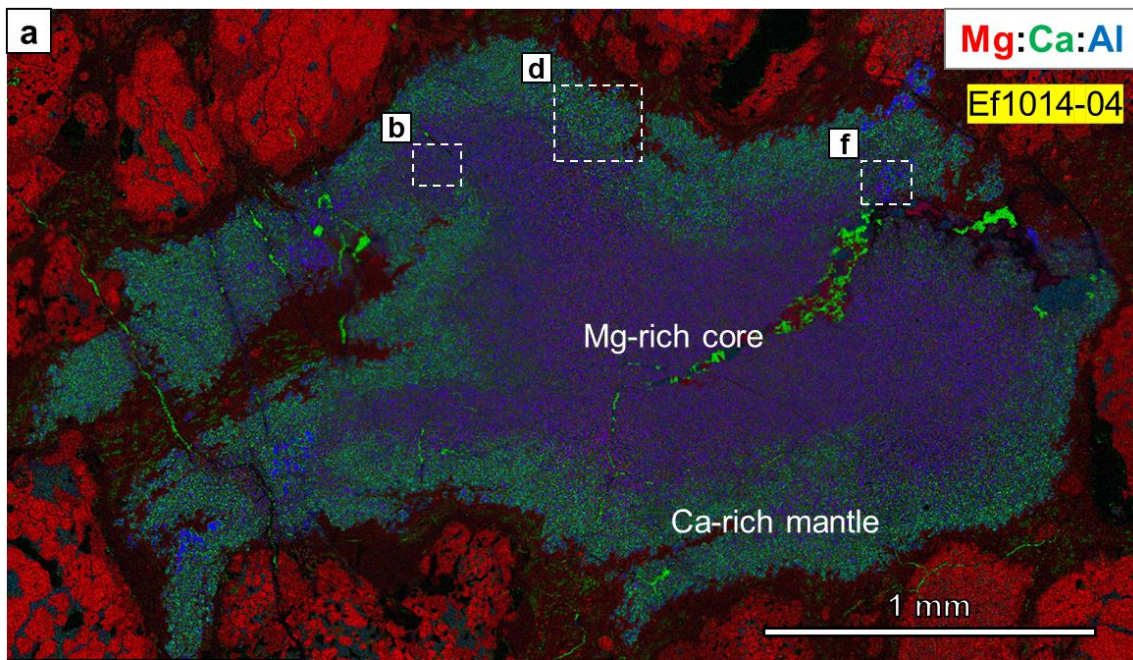


Fig. 2. Combined EDS X-ray elemental map in Mg (red), Ca (green), and Al (blue) (a), and BSE images (b-g) of a mineralogically zoned FGI Ef1014-04 from the Efremovka chondrite. (a) The compositional zoning of this FGI is clearly illustrated by the X-ray map: a Mg-rich core and a Ca-rich mantle. The boundary between the core and mantle regions is diffuse, and it is parallel to the shape of the FGI. Some major phases of this FGI can be recognized by colors on the X-ray map: melilite in bright green, diopside in dark green, spinel in purple, and hibonite in blue.

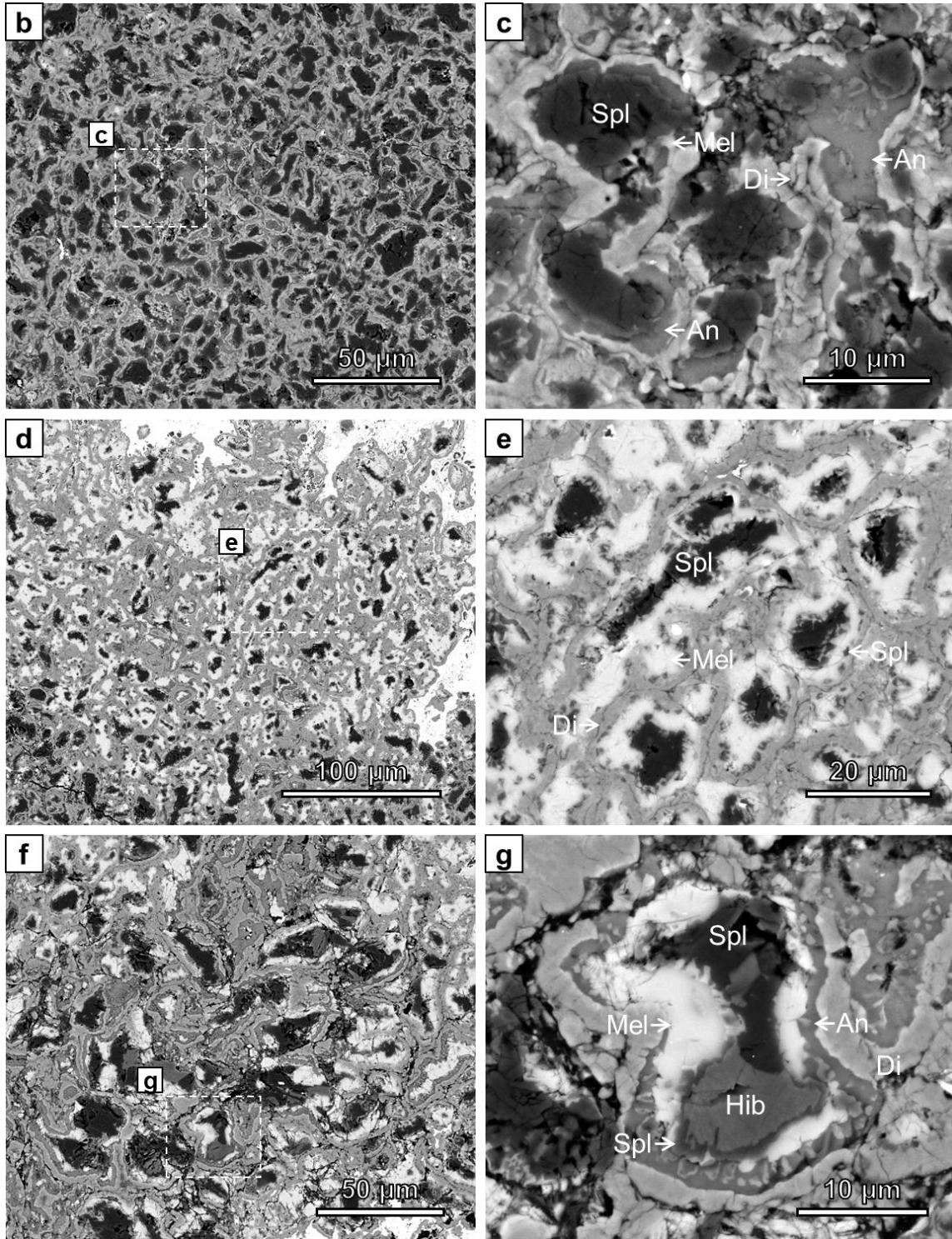


Fig.2. (continued) (b-c) Nodules in the core region are exclusively spinel-cored ones, with a spinel-anorthite-diopside layered sequence. Spinel in the core region of these nodules forms polycrystalline aggregates. The anorthite layers are usually very thin ($<1 \mu\text{m}$). Rare melilite is also present and has corroded interfaces with anorthite.

Fig.2. (*continued*) (d-e) The mantle region is composed of randomly distributed melilite-rich nodules, either with or without spinel cores. Necklace-like chains of fine-grained spinel often occur adjacent to the inner edge of diopside layers. (f-g) Clusters of hibonite-bearing nodules are observed in the outer core and mantle regions. Hibonite has a corroded or embayed interface with coexisting spinel. Spinel is pseudomorphically replacing hibonite in many cases. In contrast, no textural evidence for a replacement relationship exists between hibonite and melilite. Abbreviations: An = anorthite, Di = diopside, Hib = hibonite, Mel = melilite, Spl = spinel.

to-subhedral shape. Hibonite grains are present in the central region of the nodules and, in most cases, are enclosed, partly or completely, in spinel. Some hibonite grains have been pseudomorphically replaced by spinel and exhibit interfaces that are usually corroded or embayed. In regions where hibonite is directly in contact with melilite, the hibonite-melilite interfaces are smooth and do not show clear evidence for a replacement relationship.

Leo-H07 is a mineralogically-zoned FGI, $\sim 350 \mu\text{m}$ in size, with a trapezoidal shape, and Ca-rich and Ca-depleted regions (Fig. 3). Three zones have been identified. (1) A melilite-rich zone consisting of nodules with a spinel-melilite-anorthite-diopside sequence (Fig. 3c). Perovskite is a common phase in the core region of these nodules. The grain sizes of perovskite and spinel are $1\text{-}3 \mu\text{m}$ and $1\text{-}2 \mu\text{m}$, respectively. The thickness of melilite and diopside layers are similar ($\sim 1 \mu\text{m}$). Minor anorthite ($<1 \mu\text{m}$ in size) occurs, replacing melilite. (2) A spinel-anorthite-rich zone with spinel-anorthite-dominant nodules (Fig. 3d). Spinel forms fine-grained clusters ($\sim 1 \mu\text{m}$ for individual grains) in the core region of the nodules. The diopside layers ($\ll 1 \mu\text{m}$) are significantly thinner than the anorthite layers ($\sim 1\text{-}2 \mu\text{m}$). (3) Another spinel-anorthite-rich zone that contains nodules with a lower abundance of diopside than those in the second zone (Fig. 3e). The grain sizes of phases in zone 3 are similar to those in zone 2.

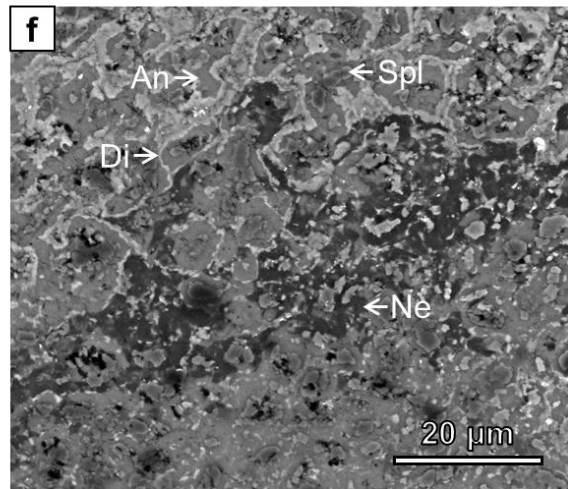
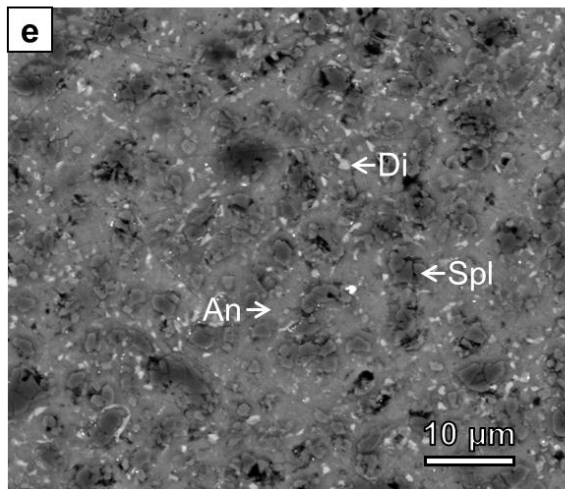
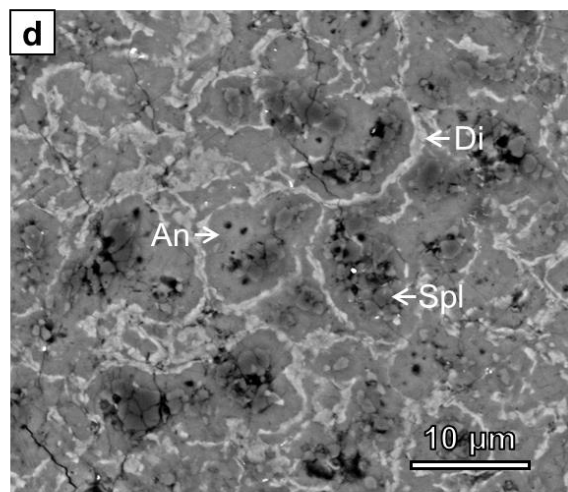
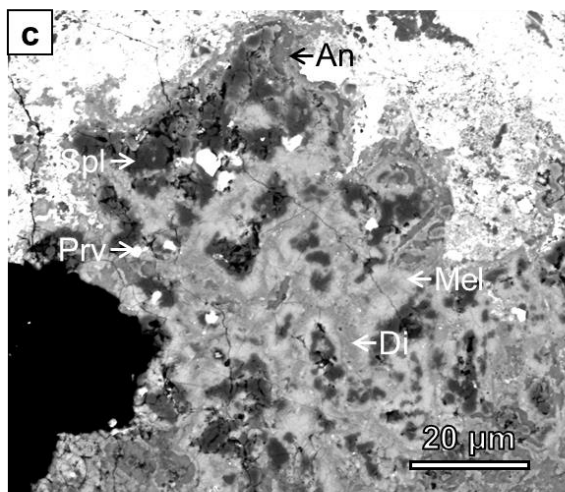
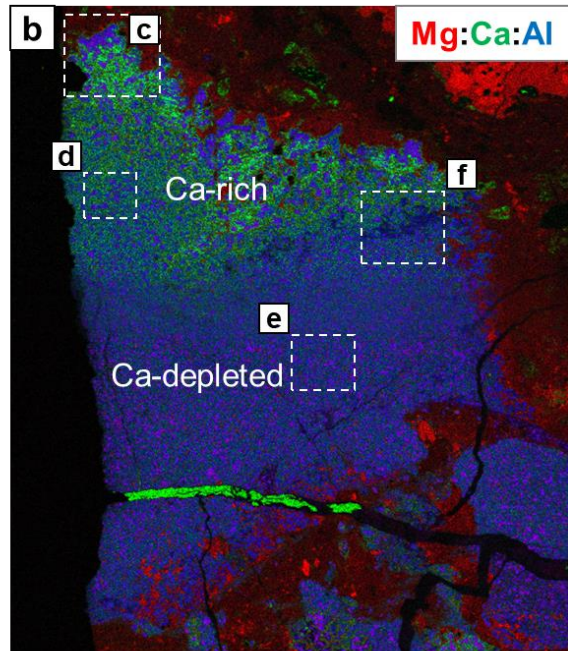
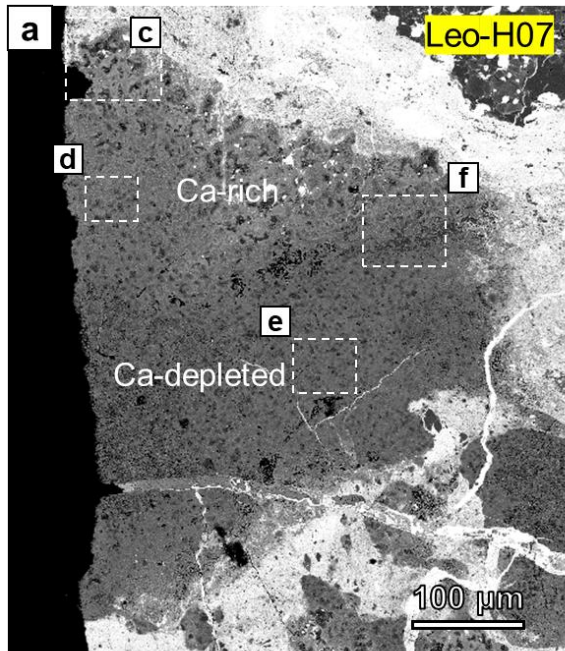


Fig. 3. BSE image (a, c-f) and combined EDS X-ray elemental map in Mg (red), Ca (green), and Al (blue) (b) of a zoned FGI Leo-H07 from Leoville. (a-b) This FGI shows a zoned structure: the upper half is more Ca-enriched, and contains a large proportion of melilite, while the lower half is depleted in Ca and contains much less melilite. On the X-ray map, major phases in Leo-H07 can be distinguished by colors: melilite in bright green, diopside in dark green, spinel in purple, anorthite in cyan, and olivine in red. Three mineralogically distinct zones have been identified and their representative nodules are shown in (c-e). The bottom region of the inclusion contains some olivine-rich assemblages, which are texturally similar to AOAs. (c) The melilite-rich zone is composed of nodules with a spinel-melilite-diopside zoning sequence from cores to rims. Perovskite is often present in the core region of these nodules. Anorthite is also present in some nodules, partly replacing melilite. (d) The spinel-anorthite-rich zone that is adjacent to the melilite-rich zone contains nodules, which are dominated by spinel and anorthite, and are separated from each other by diopside layers. The diopside layers show compositional zoning (as demonstrated by the variation in the Z contrast) and have corroded interfaces with anorthite. (e) A distinct spinel-anorthite-rich zone, which differs from the second zone in that the diopside layers often occur as isolated diopside grains. (f) Nepheline has replaced anorthite in nodules on the periphery of the FGI. Abbreviations: An = anorthite, Di = diopside, Mel = melilite, Ne = nepheline, Prv = perovskite, Spl = spinel.

The size of nodules (10-15 μm) does not vary significantly in different zones. In all the three zones, a fine-grained layer is commonly observed outside the diopside layer of individual nodules, and appears to consist of some low-Z contrast phases, which are too fine-grained to identify by SEM. Some nodules contain nepheline that has replaced anorthite (Fig. 3f). Some Ca-depleted regions that are composed of altered olivine (Fe-enriched due to metamorphism) and Fe,Ni metal (oxidized) are present on the periphery of zone 3, and may represent altered AOA-like materials. Several FGI fragments with similar mineralogy and zoning texture to that of Leo-H07 are present adjacent to Leo-H07, and are therefore probably fragments of a larger FGI, in which zones 1-3 form a concentric zoning structure.

Leo-H09 is also an irregularly-shaped FGI, 300 μm in size, with a zoned structure: a Mg-rich region and a Ca-rich region (Fig. 4a). These two regions have a diffuse contact and only a

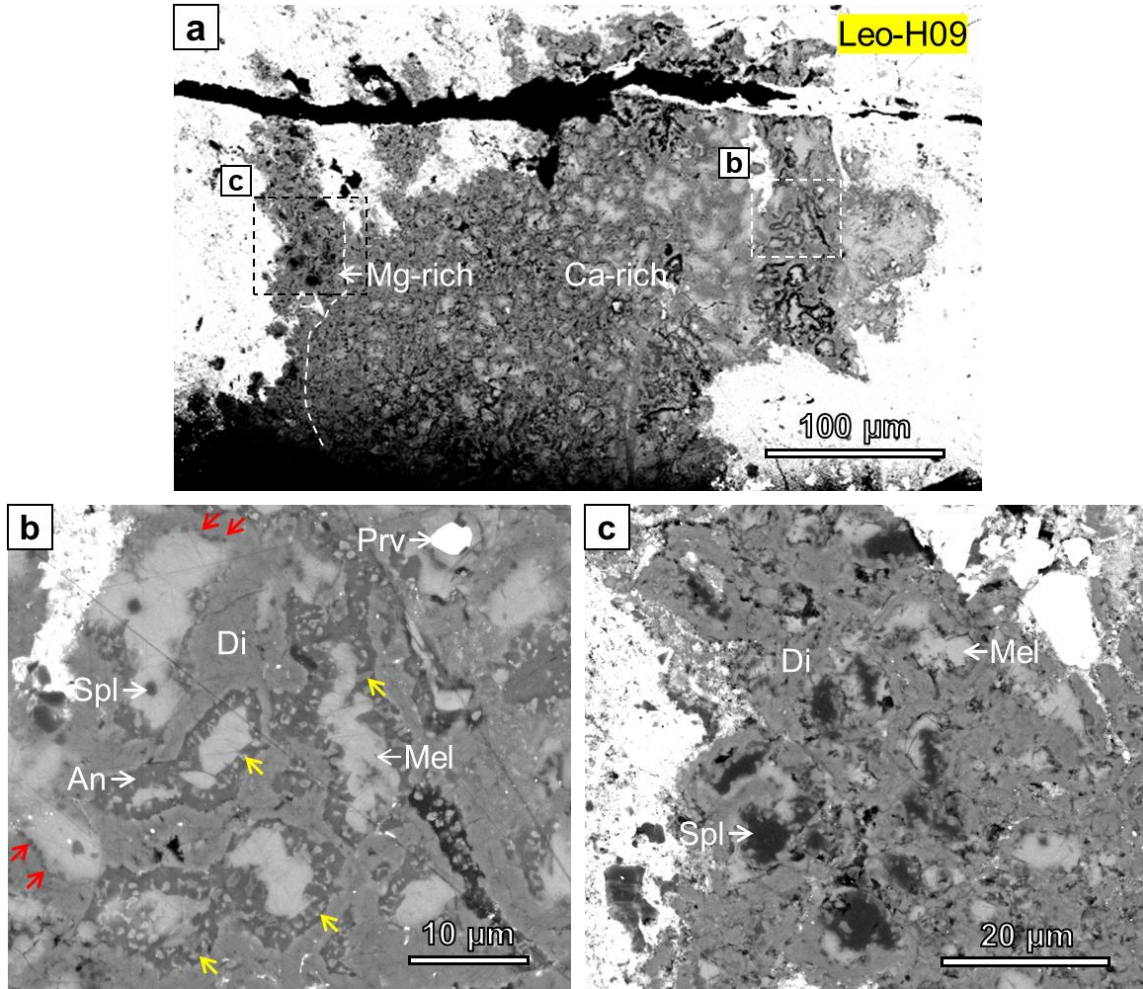


Fig. 4. BSE images of another zoned FGI Leo-H09 from Leoville. (a) This FGI has a Mg-rich region with spinel-rich nodules and a Ca-rich region with melilite-rich nodules. Their rough boundary is outlined by the white dashed line. (b) The melilite-rich nodules lack a spinel-rich core and there are often spinel grains that are enclosed in melilite. Some fine-grained spinels exist close to the interface between melilite and diopside, forming necklace-like chains (red arrows). Perovskite is a rare phase enclosed in melilite. Melilite grains in different nodules show various degrees of replacement by anorthite. In anorthite-bearing nodules, fine-grained spinel chains (indicated by yellow arrows) show Fe-enrichment and are enclosed in anorthite. (c) Spinel-cored nodules have a spinel-melilite-diopside layered sequence. Spinel cores in these nodules are polycrystalline aggregates. Abbreviations: An = anorthite, Di = diopside, Mel = melilite, Ne = nepheline, Prv = perovskite, Spl = spinel.

rough boundary can be recognized. In Leo-H09, the zonation is revealed by nodules with and without spinel cores, whereas all the nodules in Leo-H07 contain a spinel core. The dominant

nodules contain more than 50 vol% melilite, a relatively thick diopside layer (2-3 μm), and a small amount of spinel (Fig. 4b). Most of these melilite-rich nodules lack anorthite, although some nodules contain anorthite that has replaced melilite. A few spinel grains (1-2 μm) occur enclosed in melilite and smaller spinel grains (<1 μm) are concentrated along the interface between melilite and diopside, forming necklace-like chains. Fine-grained spinel chains in anorthite-bearing nodules are more Fe-enriched than spinel in the core region of nodules and are present as inclusions in anorthite (Fig. 4b). Rare perovskite grains commonly associated with spinel are found enclosed in melilite. In the Mg-rich region of the FGI, the nodules have cores of spinel aggregates (>50 volume%) that are enclosed by a melilite layer and a diopside outer layer (Fig. 4c). Fine-grained spinel is also present along the interface between melilite and diopside in these spinel-cored nodules.

3.1.3. Mineralogically heterogeneous FGIs

Some other FGIs that lack a zoning structure contain nodules with different mineralogies. Mineralogically-distinct nodules have random distribution patterns, or small aggregates of nodules with the same mineralogy are enclosed in large clusters of other types of nodules. Nodules with different mineralogies often differ in size. Three FGIs in Leoville and Efremovka show this heterogeneous characteristic: Leo-H01 (Fig. 5-6), Leo-H03 (Fig. 7), and Ef1014-05 (Fig. 8).

Leo-H01 is a rounded FGI, 1 mm in size, from Leoville (Fig. 5) that is dominated by two types of nodules: spinel-anorthite-diopside nodules and anorthite-diopside nodules (Fig. 6d-e).

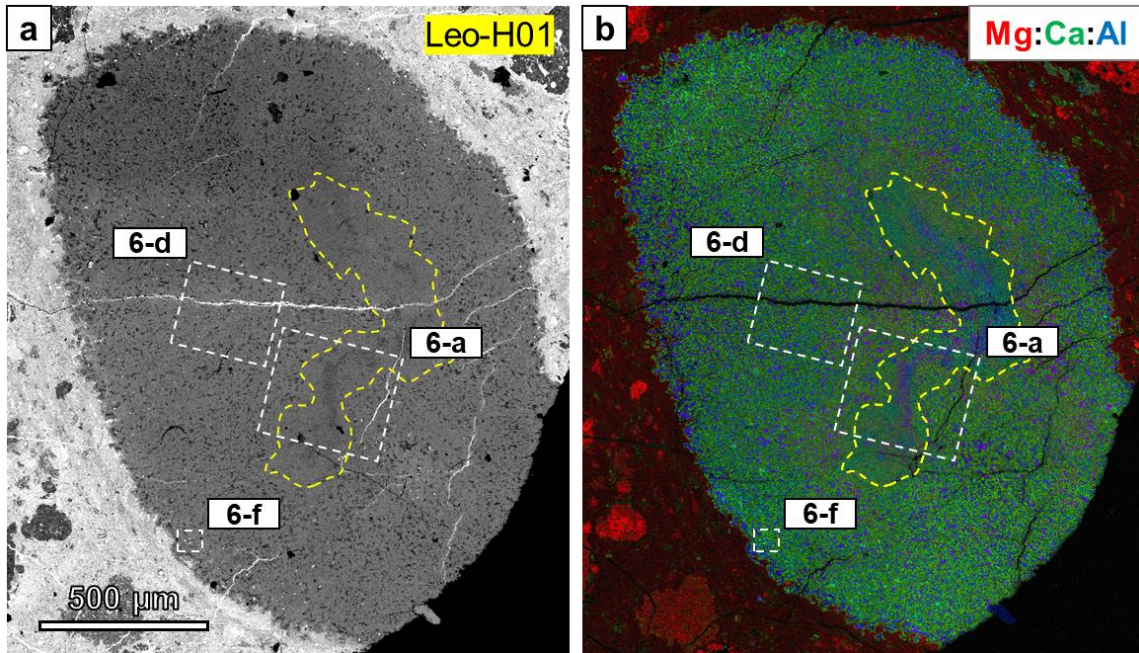


Fig. 5. BSE image (a) and combined EDS X-ray elemental map in Mg (red), Ca (green), and Al (blue) (b) of a mineralogically heterogeneous FGI Leo-H01 from Leoville. This FGI contains a sinuous aggregate with a low-Z contrast (outlined by the yellow dashed line), which is embedded in the mass of anorthite-rich nodules. The sinuous aggregate has a zoned structure: the inner region contains a lower amount of diopside and has a lower-Z contrast than the outer region. Many nodules on the periphery of the FGI contain a larger proportion of melilite than those in the interior. On the X-ray map, the color code for some major phases of this FGI is: melilite in bright green, diopside in dark green, spinel in purple, and anorthite in cyan.

These nodules are randomly distributed and vary in size from 15-25 μm . Perovskite grains (2-4 μm) are often present in the central region of these nodules. Where spinel cores are present, spinel usually forms aggregates of grains that are commonly corroded by fine-grained phases (<1 μm). These fine-grained phases are compositionally heterogeneous and are difficult to identify due to their small sizes. In the central region of Leo-H01, there is a sinuous assemblage with a low-Z contrast (Fig. 6a). This assemblage has a layered structure: the interior consists of numerous fragmented, anorthite-diopside nodules, with or without a spinel core (Fig. 6b);

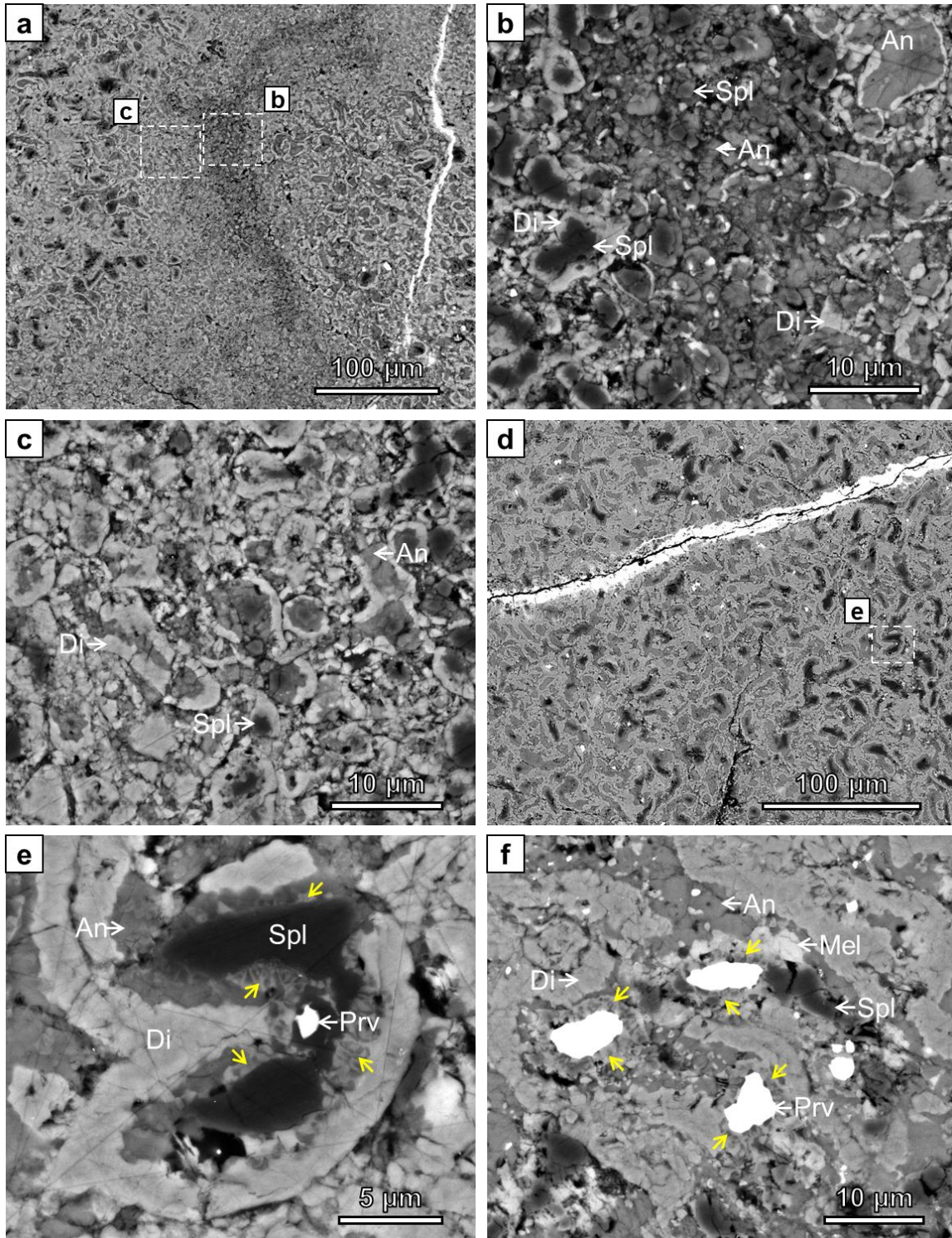


Fig. 6. BSE images of nodules from different regions of Leo-H01 showing variations in texture and mineralogy. (a) The sinuous assemblage that is located in the central region of the FGI displays a zoned structure, as demonstrated by the distinct Z contrast which is attributed to the low proportion of diopside.

Fig. 6. (*continued*) (b) Nodules in the interior of the sinuous assemblage typically contain discontinuous or discrete diopside layers. Some nodules completely lack a diopside outer layer. The size of nodules in this inner region varies from 1 to 5 μm . (c) The outer region of the sinuous assemblage is composed of nodules with thicker and more continuous diopside layers (1-2 μm), and these nodules typically have a size range of 4-8 μm . (d-e) Surrounding the sinuous assemblage are nodules with significantly larger sizes (15-25 μm). These nodules have a \pm spinel-anorthite-diopside layered sequence. Spinel cores, if present, are compacted aggregates of spinel grains and are often corroded by some fine-grained phases (marked by yellow arrows). Perovskite is a common phase in the core region of these nodules. (f) Compared with nodules in the interior of Leo-H01, those on the periphery usually have a melilite layer between anorthite and spinel. Melilite has been partly replaced by anorthite. Coarse-grained perovskite in these nodules is often enclosed by shells that are composed of a symplectic intergrowth of spinel and diopside (marked by yellow arrows). Abbreviations: An = anorthite, Di = diopside, Mel = melilite, Prv = perovskite, Spl = spinel.

and the surrounding layer is composed of nodules with similar mineralogies (Fig. 6c). The nodules in the interior typically have thin and discontinuous diopside layers ($<1 \mu\text{m}$), and in many regions, diopside occurs as isolated grains, whereas diopside in nodules from the outer layer of the sinuous assemblage forms thicker and more continuous layers (1-2 μm). The nodule sizes of the interior and outer layer of the sinuous assemblage are slightly different, with a smaller nodule size in the former (1-5 μm) than the latter (4-8 μm). The proportion of diopside in nodules from the outer layer region (30-50 vol%) is higher than in the interior region ($<20 \text{ vol}\%$), which accounts for the slightly higher-Z contrast of the outer layer region. On the periphery of Leo-H01, nodules contain a significant amount of melilite, which separates the spinel cores from anorthite (Fig. 6f). Perovskite with various sizes ($<1 \mu\text{m}$ to $\sim 10 \mu\text{m}$) is a common phase, and occurs, in most cases, in the central region of the nodules. Some coarse-grained perovskites are enclosed by shells that are composed of a symplectic intergrowth of spinel and diopside. Nodules on the periphery of this FGI have been affected by secondary

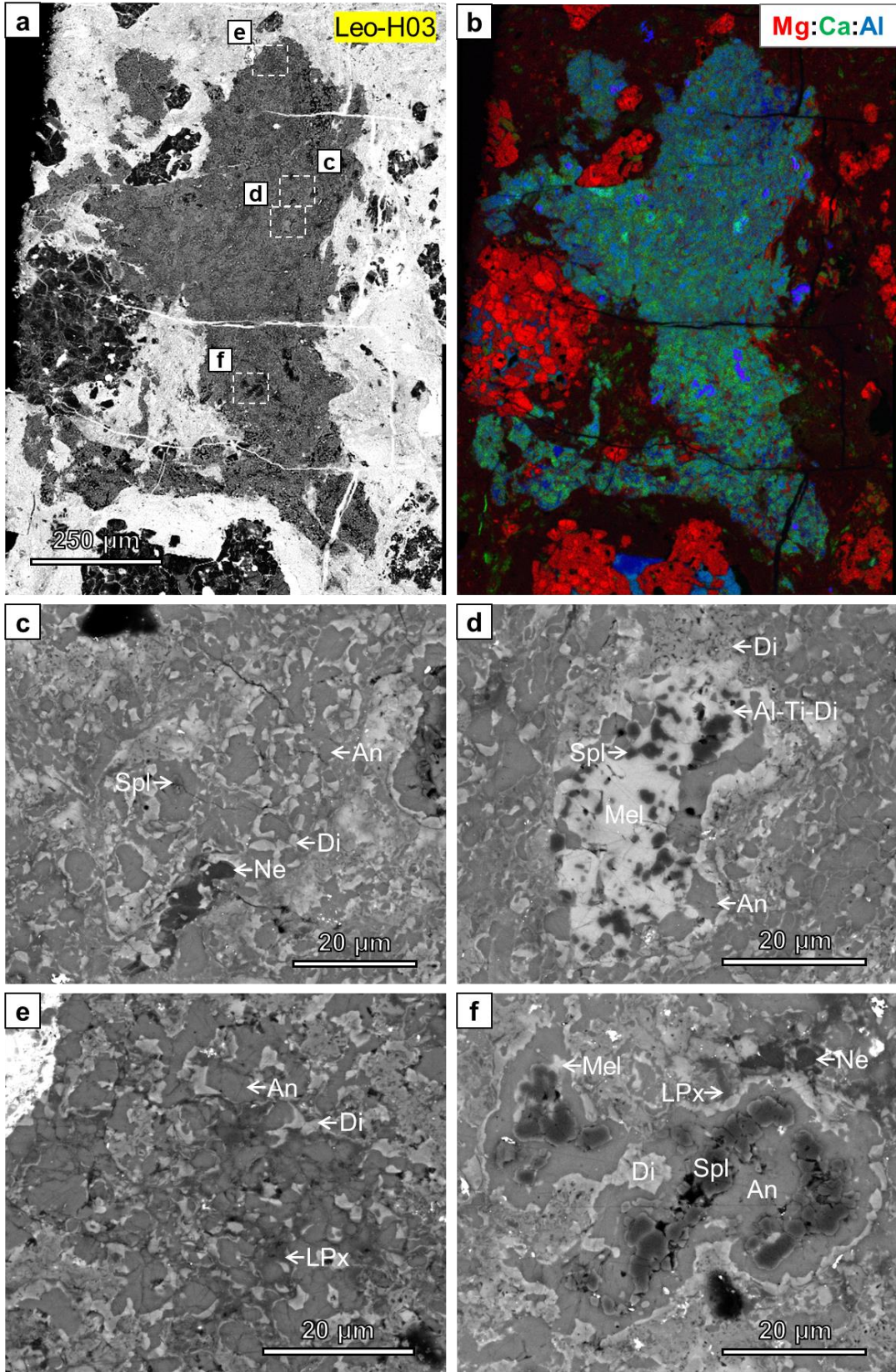


Fig. 7. BSE images (a, c-f) and combined EDS X-ray elemental map in Mg (red), Ca (green), and Al (blue) (b) of a mineralogically heterogeneous FGI Leo-H03 from Leoville. This FGI shows a remarkable textural heterogeneity as shown by the distribution of mineralogically-distinct nodules on the X-ray map. Some nodules are considerably larger than the others. On the X-ray map, the color code for some major phases of Leo-H03 is: melilite in bright green, diopside in dark green, spinel in purple, and anorthite in cyan. (c) This FGI is dominated by anorthite-rich nodules that vary significantly in size. Some of the nodules contain spinel and/or melilite. The diopside layers in many nodules are discontinuous, and sometimes diopside occurs as isolated grains. (d) Some melilite-rich nodules are present as islands within the mass of anorthite-rich nodules. In these melilite-rich nodules, melilite forms a mantle that encloses euhedral-to-subhedral spinel and Al-Ti-diopside grains. Anorthite grains have curved and sometimes embayed interfaces with melilite. The outer diopside layers are fine-grained. (e) Many anorthite-rich nodules in this FGI have an outermost low-Ca pyroxene layer. Low-Ca pyroxene layers in some nodules are in direct contact with anorthite and an outer diopside layer is discontinuous or absent. (f) There are also some large spinel-cored nodules that are texturally similar to those observed in Leo-H01. Spinel grains in the core region commonly form clusters. Finer-grained spinel is also present as inclusions in anorthite. Relict melilite that shows a replacement relationship with anorthite is sometimes observed. Abbreviations: Al-Ti-Di = Al-Ti-diopside, An = anorthite, Di = diopside, LPx = low-Ca pyroxene, Mel = melilite, Ne = nepheline, Prv = perovskite, Spl = spinel.

alteration, which produced Fe-rich spinel and nepheline.

Leo-H03 has an elongated shape with a length of about 1mm (Fig. 7a). The EDS X-ray map shows that this inclusion is mineralogical and texturally heterogeneous (Fig. 7b). Isolated or clusters of anorthite-rich nodules (3-10 μm in size) dominate this FGI. These nodules do not contain a spinel-rich core, but many have thin and discontinuous diopside layers ($<1 \mu\text{m}$), which often occur as discrete grains (Fig. 7c). Clusters of anorthite-rich nodules are $\sim 50 \mu\text{m}$ in size, and adjacent clusters are separated by layers of fine-grained diopside (3-5 μm in thickness). A few melilite-rich nodules (30-50 μm in size) are present (Fig. 7d), with randomly distributed subhedral spinel and Al-Ti-rich diopside inclusions in melilite (3-5 μm in size). Melilite is partly surrounded by a diopside layer, which is composed of fine-grained, Al-bearing diopside and some other phases that are too fine-grained to analyze by electron

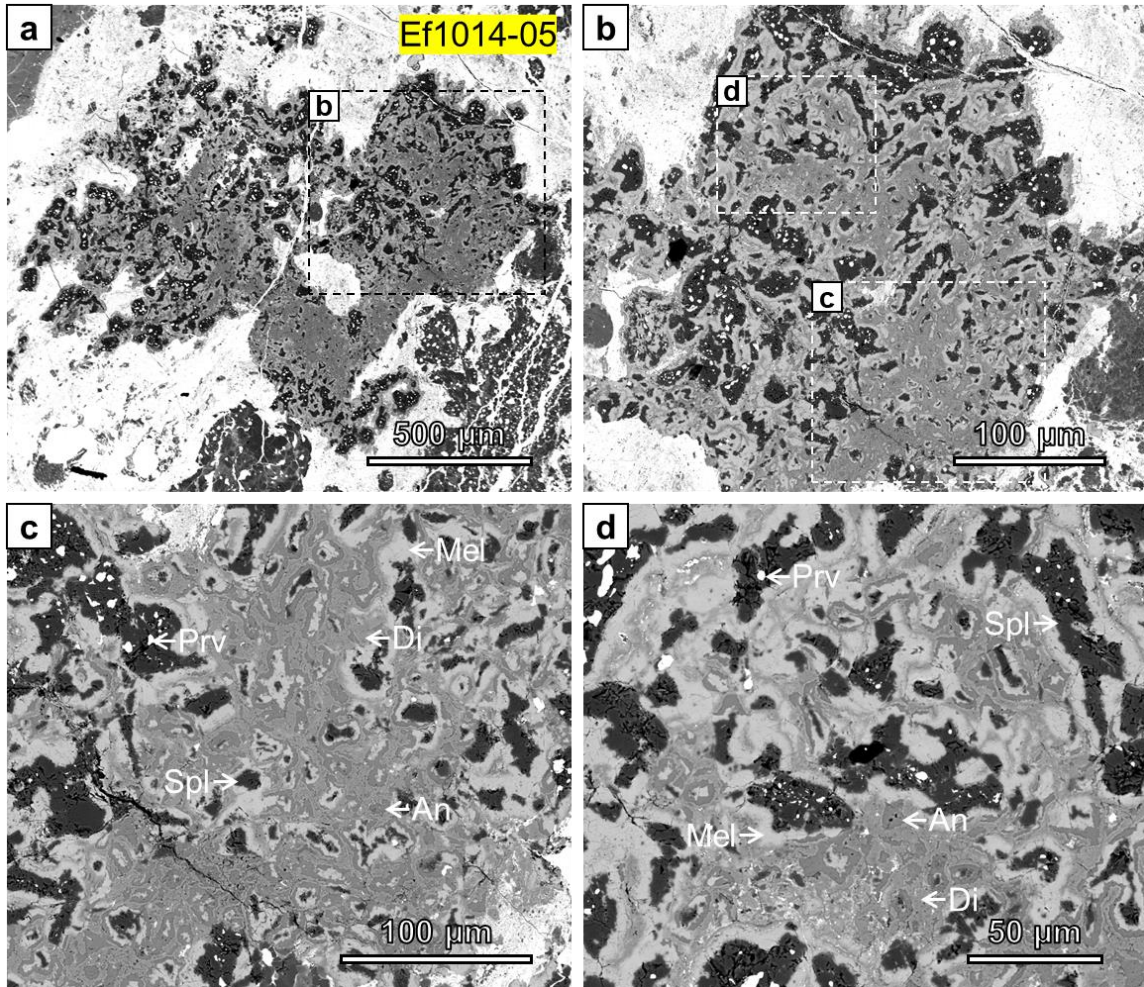


Fig. 8. BSE images of a mineralogically heterogeneous FGI Ef1014-05 from Efremovka. (a-b) This FGI has a dendritic shape and nodules show different mineralogies and sizes. (c) Aggregates of small nodules are surrounded by larger nodules. These small nodules usually contain anorthite that is replacing melilite. Some nodules have spinel cores, while others do not. (d) Large nodules have polycrystalline spinel cores, which often contain perovskite. Only a minor amount of anorthite is observed in the large nodules. Abbreviations: An = anorthite, Di = diopside, Mel = melilite, Prv = perovskite, Spl = spinel.

microprobe. Perovskite grains are also present in some melilite-rich nodules, decorating the interface between melilite and the outer diopside layers, forming necklace-like chains. Melilite in these nodules has been partially replaced to varying degrees by anorthite. Many anorthite-rich nodules contain an outermost thin layer with a low-Z contrast that is probably low-Ca

pyroxene (Fig. 7e), based on EDS analyses. In some regions, the diopside layers are nearly completely absent, and the anorthite-rich interiors of adjacent nodules are separated from each other only by low-Ca pyroxene. There are also some large nodules (25-35 μm in size) that are spinel-cored (Fig. 7f). The spinel grains in these nodules have subhedral shapes and often form aggregates. Some spinel grains are associated with anhedral Al-Ti-diopside. The diopside layers on the periphery of these nodules show compositional zonation, with higher Al_2O_3 and/or TiO_2 contents towards the center of the nodules. Nodules near the interface between the FGI and the matrix show evidence for secondary parent body alteration: nepheline partly or completely replaces anorthite.

Ef1014-05 has a dendritic shape, with a size of $\sim 150 \mu\text{m}$ (Fig. 8a). This FGI is texturally similar to Leo-H01 in that agglomerates of smaller nodules (10-15 μm in size) are surrounded by agglomerates of larger nodules (40-80 μm in size) (Fig. 8b). Mineralogically, the smaller nodules have a \pm spinel-melilite-anorthite-diopside layered sequence (Fig. 8c). In these nodules, spinel, if present, forms polycrystalline cores that contain rare perovskite grains ($\sim 1 \mu\text{m}$). Melilite has been partially to completely replaced by anorthite. All the larger nodules in Ef1014-05 contain a compacted, polycrystalline, spinel-rich core (Fig. 8d). Perovskite (up to 10 μm in size) inclusions is a much more common in the cores of these larger nodules, compared to smaller nodules. Melilite in the larger nodules is only minimally replaced by anorthite.

3.2. Mineral compositions

Representative electron microprobe analyses of spinel, melilite, anorthite, and diopside of selected FGIs in this study are reported in Tables 1-4. No systematic differences in mineral compositions have been found among the different FGIs. Spinel shows various degrees of Fe-enrichment, with Fe# ($= \text{Fe}/(\text{Fe} + \text{Mg}) \times 100$) up to ~ 8.33 . Most of the spinel grains have compositions close to the pure Mg-rich endmember, and their FeO contents are below 0.5 wt%. The Cr₂O₃ contents of spinel are between 0.18 and 0.40 wt%. The MgO contents of melilite vary significantly in different nodules, with Åk contents varying between 2.7-30.4. The Åk contents of most melilite grains are, however, in a relatively narrow range (15-20). Most of the anorthite grains contain a trace amount of Na₂O (<0.1 wt%), but some grains show more elevated Na₂O contents (up to about 0.31 wt%). Individual diopside grains display a significant variation in Al₂O₃ (3.98-20.49 wt%) and TiO₂ (<0.1 to 7.05 wt%) contents, and those grains that are located on the periphery of nodules tend to have lower Al₂O₃ and TiO₂ contents.

3.3. Microstructures

To understand the complex fine-scale textural and mineralogical variations in individual FGIs in more detail, we extracted a total of six FIB sections from nodules that show variable mineralogies in three FGIs (Leo-H05, -H07, and -H09) from the Leoville 577 thin section. The positions of these FIB sections are shown in Fig. 9.

Two of the FIB sections (FIB-02 from Leo-H07 (Fig. 9b) and FIB-04 from Leo-H05 (Fig. 9d)) were extracted from spinel-cored nodules with perovskite inclusions and a layered

Table 1. Representative electron microprobe analyses (wt%) of spinel in FGIs from Leoville.

| CAI# | Leo-H01 | | Leo-H03 | | Leo-H05 | | Leo-H07 | | Leo-H09 | |
|--------------------------------|---------|-------|---------|--------|---------|--------|---------|--------|---------|--------|
| SiO ₂ | 0.67 | 1.85 | 2.22 | 2.00 | 0.05 | 0.06 | 0.60 | 0.10 | 0.42 | 0.67 |
| TiO ₂ | 0.06 | 0.05 | 0.28 | 0.26 | 0.13 | 0.12 | 0.21 | 0.09 | 0.06 | 0.03 |
| Al ₂ O ₃ | 71.81 | 67.79 | 68.37 | 69.45 | 71.78 | 70.75 | 70.06 | 71.99 | 70.98 | 70.60 |
| V ₂ O ₃ | 0.06 | 0.33 | 0.41 | 0.38 | 0.49 | 0.47 | 0.16 | 0.15 | 0.05 | 0.09 |
| Cr ₂ O ₃ | 0.32 | 0.33 | 0.22 | 0.21 | 0.23 | 0.22 | 0.63 | 0.42 | 0.28 | 0.39 |
| FeO | 0.18 | 2.05 | 0.21 | 0.11 | 0.33 | 4.11 | 0.95 | 0.47 | 0.12 | 0.36 |
| MnO | bd | 0.01 | 0.01 | bd | bd | 0.01 | 0.01 | 0.01 | 0.01 | 0.01 |
| MgO | 28.35 | 27.02 | 26.43 | 27.14 | 28.38 | 25.36 | 27.37 | 28.04 | 28.41 | 27.86 |
| CaO | 0.37 | 0.48 | 2.49 | 2.29 | 0.11 | 0.15 | 0.37 | 0.18 | 0.39 | 0.50 |
| Na ₂ O | 0.01 | 0.05 | 0.04 | 0.02 | bd | 0.02 | 0.01 | bd | 0.02 | 0.01 |
| K ₂ O | 0.01 | 0.02 | bd | bd | bd | bd | 0.01 | 0.01 | bd | bd |
| Total | 101.84 | 99.98 | 100.68 | 101.86 | 101.51 | 101.27 | 100.38 | 101.46 | 100.73 | 100.54 |
| Cations per 4 oxygen anions | | | | | | | | | | |
| Si | 0.016 | 0.044 | 0.053 | 0.047 | 0.001 | 0.001 | 0.014 | 0.002 | 0.010 | 0.016 |
| Ti | 0.001 | 0.001 | 0.005 | 0.005 | 0.002 | 0.002 | 0.004 | 0.002 | 0.001 | 0.001 |
| Al | 1.971 | 1.903 | 1.909 | 1.916 | 1.982 | 1.989 | 1.960 | 1.987 | 1.972 | 1.959 |
| V | 0.001 | 0.006 | 0.008 | 0.007 | 0.009 | 0.009 | 0.003 | 0.003 | 0.001 | 0.002 |
| Cr | 0.006 | 0.006 | 0.004 | 0.004 | 0.004 | 0.004 | 0.012 | 0.008 | 0.005 | 0.007 |
| Fe | 0.004 | 0.041 | 0.004 | 0.002 | 0.007 | 0.082 | 0.019 | 0.009 | 0.002 | 0.007 |
| Mn | - | 0.000 | 0.000 | - | - | 0.000 | 0.000 | 0.000 | 0.000 | 0.000 |
| Mg | 0.984 | 0.959 | 0.933 | 0.947 | 0.991 | 0.902 | 0.968 | 0.979 | 0.998 | 0.978 |
| Ca | 0.009 | 0.012 | 0.063 | 0.058 | 0.003 | 0.004 | 0.009 | 0.005 | 0.010 | 0.013 |
| Na | 0.001 | 0.002 | 0.002 | 0.001 | - | 0.001 | 0.000 | - | 0.001 | 0.001 |
| K | 0.000 | 0.001 | - | - | - | - | 0.000 | 0.000 | - | - |
| Total | 2.992 | 2.976 | 2.981 | 2.986 | 2.999 | 2.994 | 2.990 | 2.994 | 3.000 | 2.983 |
| Fe# | 0.357 | 4.075 | 0.436 | 0.226 | 0.654 | 8.330 | 1.909 | 0.935 | 0.230 | 0.723 |

Note: bd = below detection limits.

Table 2. Representative electron microprobe analyses (wt%) of melilite in FGIs from Leoville.

| CAI# | Leo-H01 | | Leo-H03 | | Leo-H05 | | Leo-H07 | | Leo-H09 | |
|--------------------------------|---------|-------|---------|--------|---------|--------|---------|--------|---------|--------|
| SiO ₂ | 23.67 | 23.59 | 27.54 | 24.41 | 25.58 | 25.90 | 22.91 | 27.38 | 21.68 | 24.94 |
| TiO ₂ | 0.25 | 0.09 | 1.43 | 0.02 | 0.08 | 1.01 | 0.03 | 0.22 | 0.02 | bd |
| Al ₂ O ₃ | 34.80 | 36.92 | 26.29 | 30.81 | 31.38 | 30.99 | 32.51 | 26.75 | 35.31 | 30.78 |
| V ₂ O ₃ | 0.05 | 0.01 | 0.17 | 0.02 | 0.03 | 0.03 | 0.02 | 0.05 | bd | bd |
| Cr ₂ O ₃ | 0.01 | 0.01 | 0.02 | bd | bd | 0.01 | bd | 0.06 | bd | bd |
| FeO | 0.45 | 0.98 | 0.04 | 0.07 | 0.52 | 0.44 | 0.02 | 0.42 | 0.03 | 0.06 |
| MnO | 0.01 | 0.01 | bd | bd | 0.01 | 0.02 | bd | bd | bd | bd |
| MgO | 3.50 | 1.16 | 4.22 | 2.72 | 2.85 | 2.84 | 1.74 | 4.40 | 0.56 | 2.22 |
| CaO | 35.78 | 35.39 | 37.88 | 40.14 | 37.84 | 37.51 | 40.24 | 37.48 | 39.51 | 40.31 |
| Na ₂ O | 0.08 | 0.10 | 0.10 | 0.05 | 0.13 | 0.23 | 0.04 | 0.29 | bd | 0.09 |
| K ₂ O | 0.01 | bd | 0.01 | bd | 0.02 | 0.01 | 0.01 | 0.02 | 0.01 | bd |
| Total | 98.60 | 98.26 | 97.70 | 98.24 | 98.43 | 98.99 | 97.53 | 97.06 | 97.12 | 98.41 |
| Cations per 7 oxygen anions | | | | | | | | | | |
| Si | 1.079 | 1.077 | 1.277 | 1.135 | 1.176 | 1.183 | 1.075 | 1.279 | 1.018 | 1.156 |
| Ti | 0.008 | 0.003 | 0.050 | 0.001 | 0.003 | 0.035 | 0.001 | 0.008 | 0.001 | - |
| Al | 1.871 | 1.987 | 1.436 | 1.688 | 1.699 | 1.668 | 1.797 | 1.472 | 1.954 | 1.682 |
| V | 0.002 | 0.000 | 0.006 | 0.001 | 0.001 | 0.001 | 0.001 | 0.002 | - | - |
| Cr | 0.000 | 0.001 | 0.001 | - | - | 0.000 | - | 0.002 | - | - |
| Fe | 0.017 | 0.038 | 0.002 | 0.003 | 0.020 | 0.017 | 0.001 | 0.016 | 0.001 | 0.002 |
| Mn | 0.000 | 0.000 | - | - | 0.000 | 0.001 | - | - | - | - |
| Mg | 0.238 | 0.079 | 0.292 | 0.188 | 0.195 | 0.193 | 0.121 | 0.306 | 0.039 | 0.153 |
| Ca | 1.748 | 1.732 | 1.882 | 1.999 | 1.863 | 1.835 | 2.022 | 1.875 | 1.988 | 2.002 |
| Na | 0.007 | 0.009 | 0.009 | 0.004 | 0.011 | 0.020 | 0.004 | 0.026 | - | 0.008 |
| K | 0.001 | - | 0.001 | - | 0.001 | 0.001 | 0.001 | 0.001 | 0.001 | - |
| Total | 4.973 | 4.926 | 4.954 | 5.020 | 4.970 | 4.954 | 5.022 | 4.988 | 5.002 | 5.005 |
| Åk | 20.292 | 7.342 | 28.898 | 18.255 | 18.679 | 18.797 | 11.897 | 29.373 | 3.841 | 15.435 |

Note: bd = below detection limits.

Table 3. Representative electron microprobe analyses (wt%) of anorthite in FGIs from Leoville.

| CAI# | Leo-H01 | | Leo-H03 | | Leo-H07 | |
|--------------------------------|---------|-------|---------|-------|---------|-------|
| SiO ₂ | 42.35 | 41.16 | 42.51 | 42.86 | 42.19 | 41.64 |
| TiO ₂ | 0.04 | 0.05 | 0.02 | 0.05 | 0.15 | 0.15 |
| Al ₂ O ₃ | 35.79 | 36.41 | 35.76 | 35.70 | 34.89 | 35.34 |
| V ₂ O ₃ | 0.01 | 0.03 | 0.01 | 0.02 | 0.02 | 0.02 |
| Cr ₂ O ₃ | bd | bd | bd | bd | bd | 0.06 |
| FeO | 0.09 | 0.24 | 0.12 | 0.13 | 0.11 | 0.23 |
| MnO | bd | bd | bd | bd | bd | bd |
| MgO | 0.19 | 0.75 | 0.17 | 0.11 | 0.29 | 1.15 |
| CaO | 19.86 | 19.42 | 19.96 | 19.77 | 20.09 | 19.01 |
| Na ₂ O | 0.07 | 0.04 | 0.09 | 0.08 | 0.05 | 0.18 |
| K ₂ O | 0.01 | 0.02 | 0.01 | 0.02 | 0.01 | 0.01 |
| Total | 98.41 | 98.13 | 98.65 | 98.73 | 97.80 | 97.80 |
| Cations per 8 oxygen anions | | | | | | |
| Si | 1.996 | 1.947 | 1.999 | 2.011 | 2.004 | 1.976 |
| Ti | 0.001 | 0.002 | 0.001 | 0.002 | 0.005 | 0.005 |
| Al | 1.988 | 2.030 | 1.982 | 1.974 | 1.953 | 1.977 |
| V | 0.000 | 0.001 | 0.000 | 0.001 | 0.001 | 0.001 |
| Cr | - | - | - | - | - | 0.002 |
| Fe | 0.003 | 0.010 | 0.005 | 0.005 | 0.005 | 0.009 |
| Mn | - | - | - | - | - | - |
| Mg | 0.014 | 0.053 | 0.012 | 0.008 | 0.021 | 0.082 |
| Ca | 1.003 | 0.984 | 1.006 | 0.994 | 1.022 | 0.967 |
| Na | 0.007 | 0.004 | 0.008 | 0.007 | 0.005 | 0.017 |
| K | 0.000 | 0.001 | 0.000 | 0.001 | 0.001 | 0.000 |
| Total | 5.012 | 5.033 | 5.012 | 5.002 | 5.016 | 5.035 |

Note: bd = below detection limits.

Table 4. Representative electron microprobe analyses (wt%) of diopside in FGIs from Leoville.

| CAI# | Leo-H01 | | Leo-H03 | | Leo-H07 | | Leo-H09 | |
|--------------------------------|---------|--------|---------|--------|---------|-------|---------|--------|
| SiO ₂ | 53.57 | 43.23 | 47.08 | 49.33 | 44.90 | 53.59 | 53.32 | 46.56 |
| TiO ₂ | 0.11 | 0.17 | 2.59 | 0.09 | 1.32 | 0.27 | 0.06 | 0.55 |
| Al ₂ O ₃ | 6.21 | 20.49 | 11.90 | 8.72 | 17.36 | 3.98 | 4.02 | 14.28 |
| V ₂ O ₃ | 0.03 | 0.08 | 0.27 | 0.02 | 0.15 | 0.06 | 0.01 | 0.09 |
| Cr ₂ O ₃ | 0.01 | 0.11 | 0.05 | 0.11 | 0.25 | 0.11 | 0.04 | 0.11 |
| FeO | 0.75 | 0.64 | 0.50 | 1.03 | 0.55 | 0.42 | 0.68 | 0.15 |
| MnO | 0.01 | bd | 0.01 | bd | 0.05 | 0.05 | 0.01 | 0.01 |
| MgO | 17.17 | 14.32 | 13.33 | 17.13 | 14.00 | 18.38 | 17.95 | 16.89 |
| CaO | 22.47 | 21.96 | 24.63 | 23.55 | 20.82 | 22.86 | 23.51 | 22.49 |
| Na ₂ O | 0.09 | 0.01 | bd | 0.25 | 0.16 | 0.07 | 0.61 | 0.06 |
| K ₂ O | 0.04 | 0.01 | bd | 0.04 | 0.03 | 0.03 | 0.05 | 0.02 |
| Total | 100.46 | 101.00 | 100.35 | 100.27 | 99.60 | 99.82 | 100.26 | 101.22 |
| Cations per 6 oxygen anions | | | | | | | | |
| Si | 1.903 | 1.535 | 1.698 | 1.777 | 1.614 | 1.922 | 1.914 | 1.653 |
| Ti | 0.003 | 0.004 | 0.070 | 0.002 | 0.036 | 0.007 | 0.002 | 0.015 |
| Al | 0.260 | 0.858 | 0.506 | 0.370 | 0.735 | 0.168 | 0.170 | 0.598 |
| V | 0.001 | 0.002 | 0.008 | 0.001 | 0.004 | 0.002 | 0.000 | 0.002 |
| Cr | 0.000 | 0.003 | 0.001 | 0.003 | 0.007 | 0.003 | 0.001 | 0.003 |
| Fe | 0.022 | 0.019 | 0.015 | 0.031 | 0.017 | 0.013 | 0.020 | 0.004 |
| Mn | 0.000 | - | 0.000 | - | 0.002 | 0.002 | 0.000 | 0.000 |
| Mg | 0.910 | 0.758 | 0.717 | 0.920 | 0.751 | 0.983 | 0.961 | 0.894 |
| Ca | 0.855 | 0.836 | 0.952 | 0.909 | 0.802 | 0.879 | 0.904 | 0.856 |
| Na | 0.006 | 0.001 | - | 0.017 | 0.011 | 0.005 | 0.043 | 0.004 |
| K | 0.002 | 0.000 | - | 0.002 | 0.001 | 0.001 | 0.002 | 0.001 |
| Total | 3.963 | 4.017 | 3.968 | 4.033 | 3.981 | 3.984 | 4.018 | 4.031 |

Note: bd = below detection limits.

sequence of spinel-melilite-diopside. Spinel cores in these nodules are composed of polycrystalline grains that commonly have subhedral shapes and 120° triple junction boundaries with melilite (Fig. 10a,e). Melilite is also polycrystalline with random orientations. The grain size of spinel in FIB-02 are smaller (500-700 nm) than those in FIB-04 (1-2 μm). There is also finer-grained spinel (200-300 nm in FIB-02, and 300-500 nm in FIB-04) that is randomly distributed in the melilite and anorthite layers (Fig. 10b,e). At the interface between the spinel core and melilite in FIB-02, some perovskite grains ~ 200 nm in size occur (Fig. 10a); this interface in FIB-04 is often decorated by fine-grained, Al-Ti-diopside (100-300 nm) (Fig. 10e-f). In FIB-02, the periphery of the melilite layer has been partly replaced by a thin (250-300 nm), polycrystalline anorthite layer (Fig. 10b). The outer diopside layers in both FIB sections are polycrystalline and display variations in Al_2O_3 and TiO_2 contents. The main nodule in FIB-02 has a double layer of diopside that separates adjacent nodules and contains abundant perovskite grains (50-80 nm) (Fig. 10d) and a fine-grained assemblage that is enriched in Na, Mg, and Fe, consisting mainly of spinel nanoparticles (5-10 nm) based on HRTEM imaging (Fig. 10c).

Two FIB sections (FIB-01 (Fig. 9a) and FIB-03 (Fig. 9c)) are from melilite-rich nodules in Leo-H09. These nodules lack spinel cores and contain abundant fine-grained spinel close to the inner edge of diopside layers. In both FIB sections, the spinel grains (150 to 400 nm in size) are commonly associated with fine-grained Al-bearing diopside (20-80 nm; 5.5-7.1 wt% Al_2O_3) (Fig. 11a,d). The compositions of spinel grains in FIB-01 are less Fe-rich ($\text{Fe}\# = \sim 11.6$) than those in FIB-03 ($\text{Fe}\#$ up to ~ 43.9), and the latter also contain up to 2.7 wt% Cr_2O_3 . Rare melilite

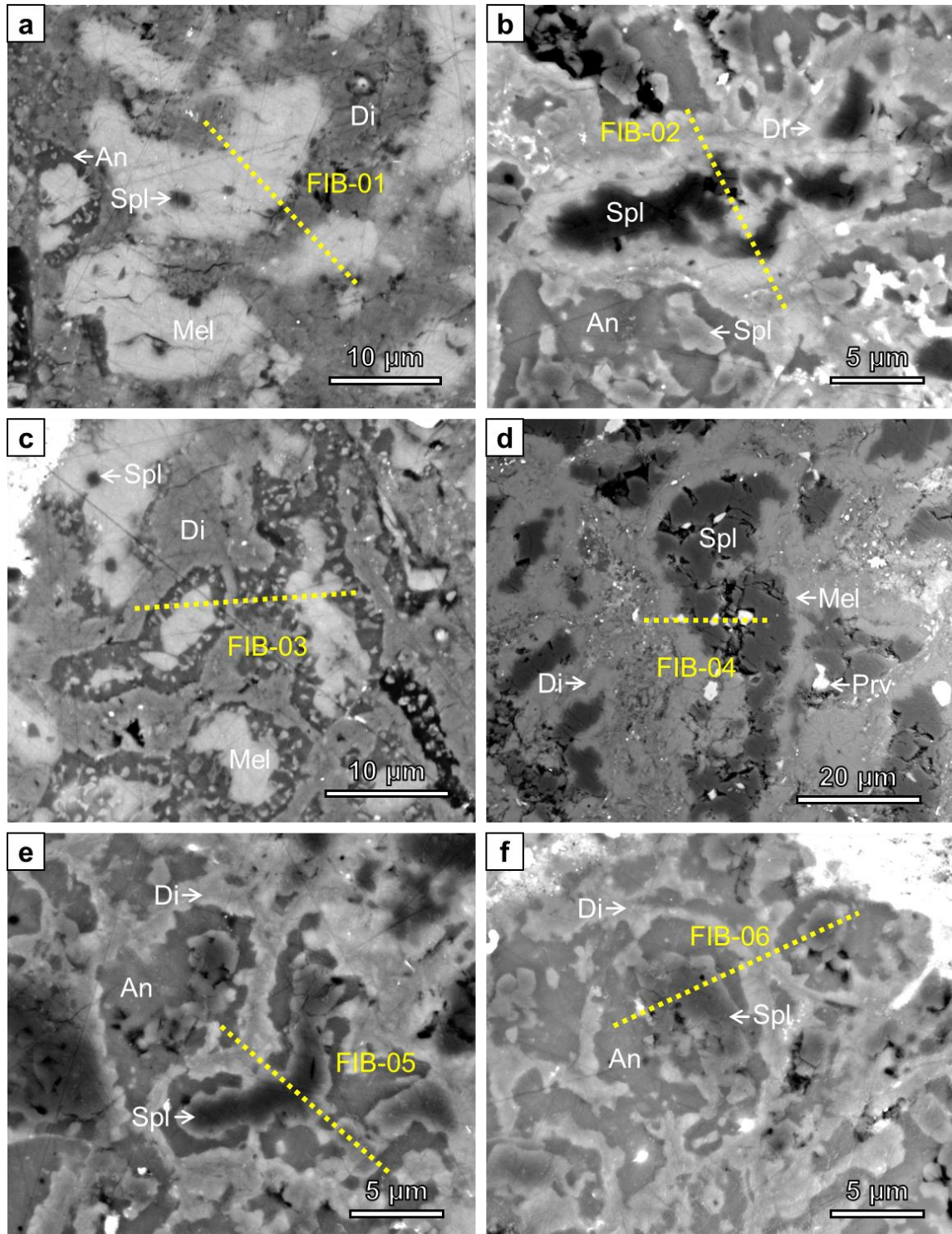


Fig. 9. The locations of the FIB sections extracted for TEM studies. FIB-01 and FIB-03 are from Leo-H09, and sample the melilite-(anorthite)-diopside layered sequence from the melilite-rich nodules. Fine-grained spinel and high-Z phases have also been sampled. FIB-02, -05, and -06 were extracted from Leo-H07, and they are across some spinel-cored nodules.

Fig. 9. (*continued*) The nodule sampled by FIB-02 has a melilite mantle, which has not been significantly replaced by anorthite, while melilite in the other two nodules has been almost completely consumed. FIB-04 is from a spinel-melilite-diopside nodule in Leo-H05. This FIB section was cut across several perovskite grains. Abbreviations: An = anorthite, Di = diopside, Mel = melilite, Prv = perovskite, Spl = spinel.

grains (~350 nm) also coexist with fine-grained spinel and Al-bearing diopside in FIB-03 (Fig. 11d). In FIB-01, a thin, 300-500 nm layer is present, consisting of a melilite-rich inner layer and diopside-rich outer layer. The melilite and diopside grains (~11.1 wt% Al₂O₃ and ~0.8 wt% TiO₂) are <100 nm in size and are sometimes associated with spinel grains (50-100 nm). This thin layer also contains a fine-grained assemblage (Fig. 11a-b) of spinel (5-10 nm) and diopside (15-20 nm) (Fig. 11c) that is texturally and compositionally similar to the fine-grained material found in FIB-02. In FIB-03, some low-Ca pyroxene grains are embedded in the diopside double layer between two adjacent nodules (Fig. 11e). Electron diffraction data for the low-Ca pyroxene are consistent with twinned clinoenstatite (CLEN) (Fig. 11f). Rare, nanometer-sized perovskite grains are also present in the diopside layer.

The last two FIB sections (FIB-05 (Fig. 9e) and FIB-06 (Fig. 9f)) were extracted from anorthite-rich nodules in Leo-H07, which have a spinel-anorthite-diopside layered sequence. In these nodules, melilite has been extensively replaced by anorthite, demonstrated by the curved and sometimes highly embayed melilite-anorthite interfaces in the TEM images. The spinel cores are polycrystalline, and a minor amount of melilite and Al-Ti-diopside occurs on the edge of spinel cores (Fig. 12a,d). The diopside layers consist of grains of variable sizes (20-250 nm) and orientations and are compositionally heterogeneous. Aluminum-Ti-rich diopside

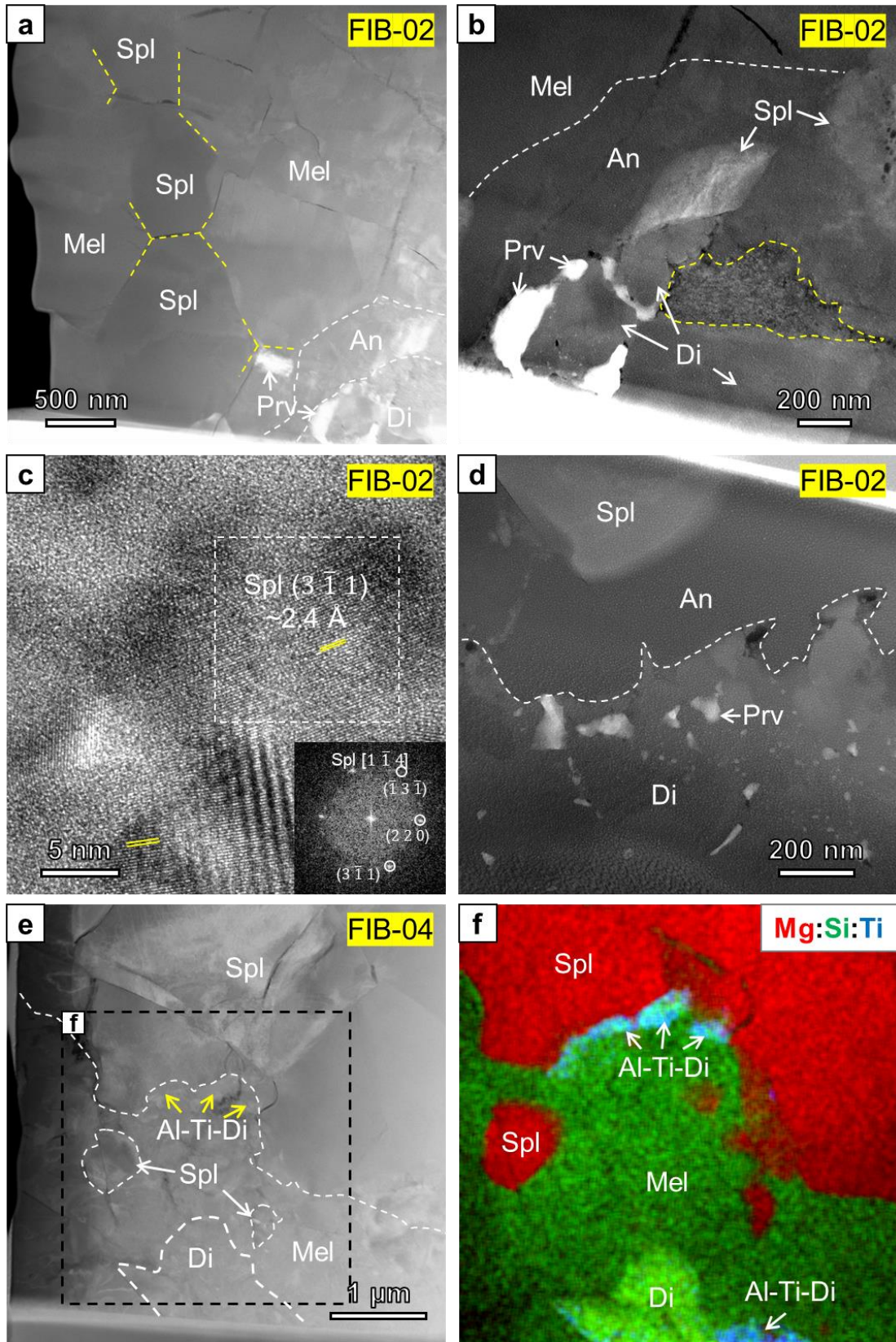


Fig. 10. TEM images of spinel-cored nodules from Leo-H07 and Leo-H05. (a-d) are from FIB-02 and (e-f) are from FIB-04. (a) DF-STEM image showing that spinel cores in FIB-02 are polycrystalline and often display 120° triple junction grain boundaries (yellow dashed lines) with melilite. Fine-grained perovskite is observed at the spinel-melilite interface. (b) DF-STEM image showing that an anorthite layer occurs between melilite and diopside. The diopside outer layer contains perovskite, spinel, and a fine-grained assemblage (outlined by the yellow dashed line). (c) HRTEM image of the fine-grained assemblage in (b) showing the presence of spinel nanoparticles. Yellow double lines indicate the d spacings of different spinel grains. The insert is an FFT pattern of the region outlined by the white box, and it is consistent with the $[1\bar{1}4]$ zone axis of spinel. (d) DF-STEM image of the diopside layers between two adjacent nodules on one side of FIB-02, which are mainly composed of fine-grained diopside and perovskite. (e) DF-STEM image and (f) combined STEM X-ray map in Mg (red), Si (green), and Ti (blue) of the interface between spinel and melilite in FIB-04. The spinel core is a polycrystalline aggregate. Some finer-grained spinel grains occur in melilite. There are fine-grained Al-Ti-rich diopsides (yellow arrows) decorating the interface between the spinel core and the melilite mantle. The interfaces between these Al-Ti-diopside and spinel are curved and embayed. There are also Al-Ti-diopside grains coexisting with Al-Ti-poor diopside in the diopside outer layer. Abbreviations: Al-Ti-Di = Al-Ti-diopside, An = anorthite, Di = diopside, Mel = melilite, Prv = perovskite, Spl = spinel.

is in direct contact with melilite or anorthite and becomes Al-Ti-poorer with increasing distance from the interface with melilite or anorthite (Fig. 12a). Like FIB-03, fine-grained CLEN is present in diopside layers in both FIB-05 (Fig. 12b-c) and FIB-06. Rare perovskite grains with anhedral shapes (~ 50 nm) are also found in the diopside layers (Fig. 12b).

4. DISCUSSION

Fine-grained, spinel-rich inclusions are agglomerates of condensed dust particles from the solar nebular gas and did not experience extensive thermal events that could have caused annealing or melting. As a consequence, FGIs are more pristine samples of nebular condensates, compared to the igneous CAIs. We can gain insights into gas-solid interactions in the early solar nebula, based on textural and mineralogic observations of FGIs. Specifically, the layered

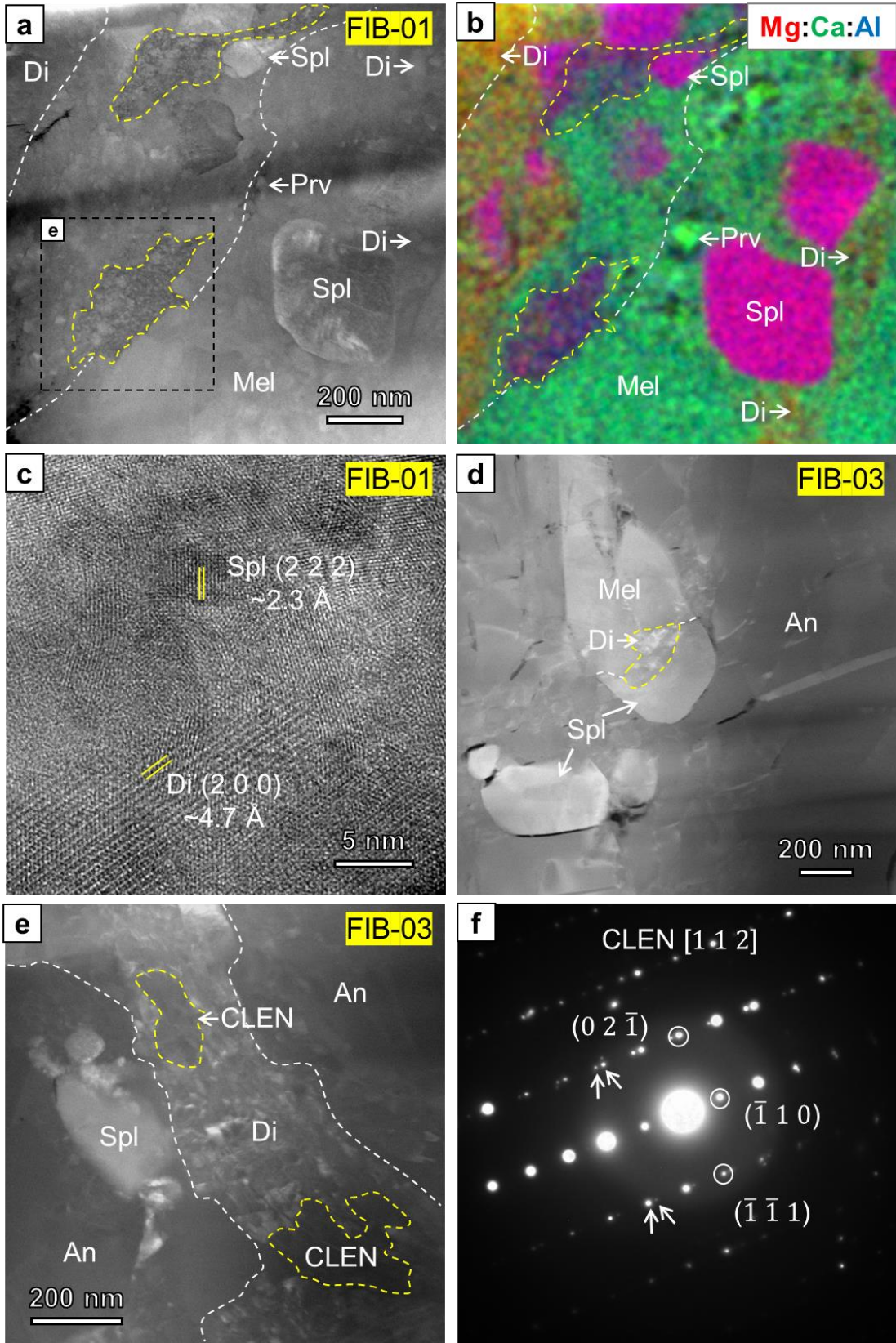


Fig. 11. TEM images of melilite-rich nodules from Leo-H09. (a) DF-STEM image of FIB-01 showing that spinel enclosed in melilite is commonly associated with Al-bearing diopside. Also shown in the image is a fine-grained, thin layer (outlined by the white dashed lines) that is present at the interface between melilite and diopside, and it has a zoned structure as demonstrated by the STEM X-ray map (b): a melilite-rich inner layer and a diopside-rich outer layer. There are some anhedral spinel grains that are randomly distributed in this layer. Also present in this layer are some fine-grained assemblages (outlined by yellow dashed lines), which are composed of spinel nanoparticles and fine-grained diopside, as illustrated by the HRTEM image (c). (d) DF-STEM image showing that spinel enclosed in anorthite (polycrystalline and often lath-shaped) in FIB-03 is commonly associated with fine-grained, Al-bearing diopside (outlined by the yellow dashed line). Rare melilite grains are also found to coexist with spinel. The white dashed lines marked the interface between spinel and melilite. (e) DF-STEM image of a diopside layer between two adjacent nodules in FIB-03 showing that some CLEN grains occur in this layer. (f) SAED pattern from a CLEN grain in (e) can be indexed as the [112] zone axis of CLEN. The paired spots as indicated by arrows on the diffraction pattern are caused by twinning. Abbreviations: An = anorthite, CLEN = clinoenstatite, Di = diopside, Mel = melilite, Prv = perovskite, Spl = spinel.

mineral sequence that is commonly observed in nodules in FGIs provides an opportunity to evaluate equilibrium thermodynamic condensation models (e.g., Yoneda and Grossman, 1995; Ebel and Grossman, 2000; Ebel, 2006).

This study is the first detailed microstructural study of FGIs in CV3 chondrites. Our new observations show that individual FGIs are heterogeneous with either mineralogic zoning (such as Leo-H07) or heterogeneously distributed nodules with various mineralogies (such as Leo-H03). Mineralogically-distinct nodules may record an evolutionary sequence of nebular condensates. Many nodules in FGIs share similarities with hibonite-rich inclusions and Fluffy Type A CAIs (FTAs), indicating that there may be genetic relationships between these different nebular materials. In the following discussion, we examine the implications of our observations for the formation of FGIs and their relationship to other types of inclusions, building on previous petrologic and isotopic studies of FGIs in CV3 chondrites by Krot et al. (2004a) and

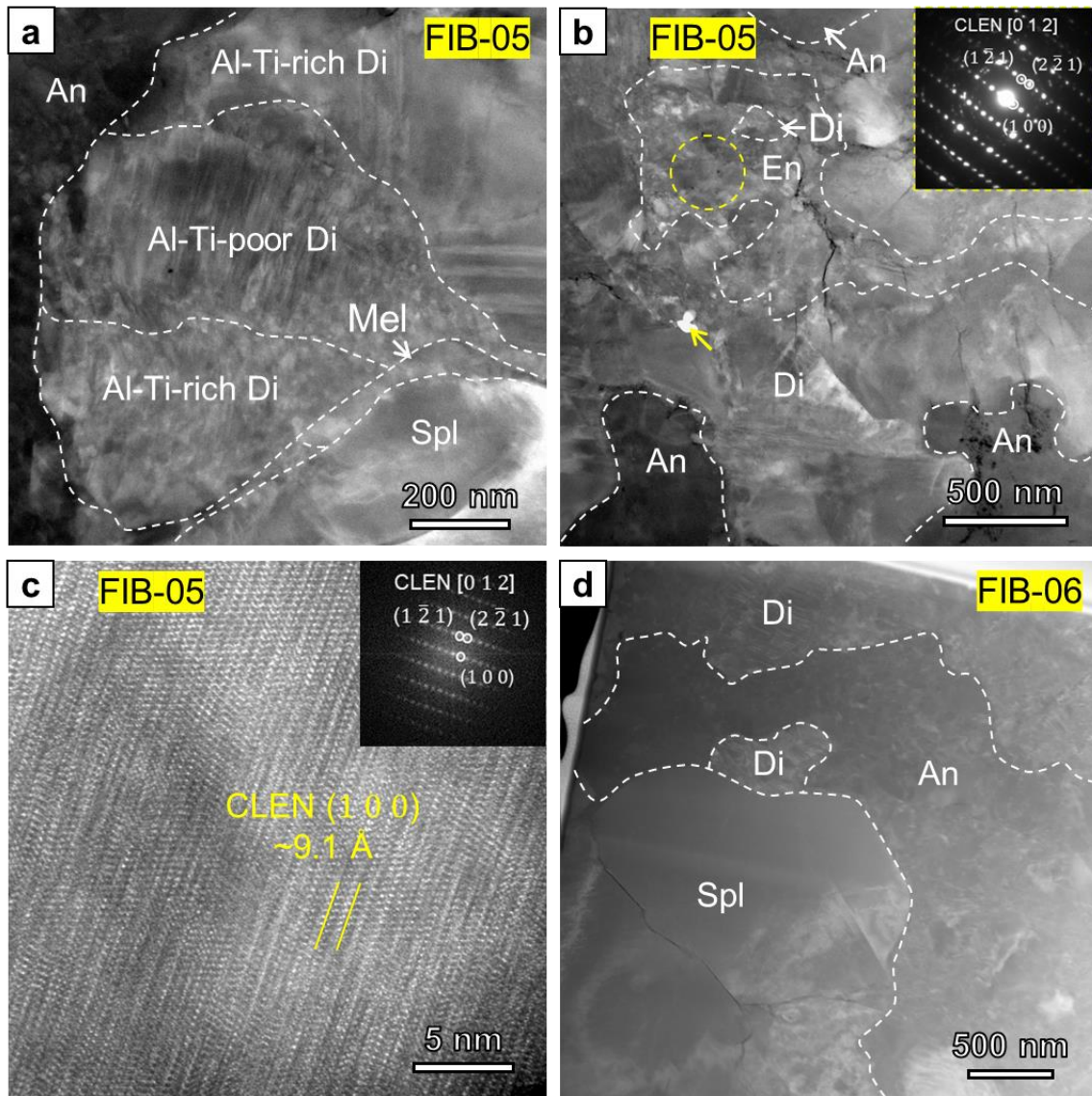


Fig. 12. TEM images of spinel-anorthite-diopside nodules in FIB-05 and -06 from Leo-H07. (a) DF-STEM images showing that highly irregular relict melilite grains are often associated with polycrystalline spinel cores. The diopside layer has a double-layered structure, separating adjacent nodules. This diopside layer is composed of randomly oriented, anhedral grains with various grain sizes. This layer is also compositionally zoned, with increasing Al_2O_3 and TiO_2 contents towards the spinel cores in the two nodules. (b) DF-STEM image showing that the diopside layer between two adjacent nodules in FIB-05 contains fine-grained enstatite. The interface between diopside and the enstatite is irregular and curved, but no replacement relationship has been observed. The SAED pattern of an enstatite grain (yellow circle in (b)) can be indexed as the $[012]$ zone axis of CLEN. There are some rare, nanometer-sized inclusions of perovskite (pointed out by the yellow arrow in (b)) in the diopside layer. (c) HRTEM image of enstatite from (b) showing that enstatite is exclusively CLEN. The insert is an FFT pattern of the HRTEM image, and it is consistent with the $[012]$ zone axis of CLEN.

Fig. 12. (*continued*) (d) DF-STEM image of FIB-06 showing that fine-grained diopside often occurs on the edge of the polycrystalline spinel cores. Abbreviations: An = anorthite, CLEN = clinoenstatite, Di = diopside, En = enstatite, Mel = melilite, Prv = perovskite, Spl = spinel.

Aléon et al. (2005).

4.1. Formational and evolutionary histories of nodules in the Leoville and Efremovka FGIs

Various condensation reactions have been proposed for FGIs (e.g., Krot et al., 2004a; Han and Brearley, 2016), based on both equilibrium thermodynamic calculations and textural relationships. Although there is still discussion on the exact formation reactions for certain phases in FGIs, there is a general consensus that hibonite, melilite, and spinel are among the first phases to condense. Reactions between these phases and the nebular gas with an evolving composition produced other less refractory phases in FGIs.

There are four major types of nodules in FGIs from Leoville and Efremovka: (1) hibonite-bearing nodules, (2) spinel-melilite-diopside nodules, (3) melilite-diopside nodules, and (4) anorthite-diopside nodules. Spinel occurs as either polycrystalline cores, or as fine-grained, necklace-like chains that are located near the inner edge of the diopside layers. The proportion and size of perovskite vary significantly in different nodules, and it is typically present in the core region of the nodules. The diopside outer layers in the nodules show compositionally zoning, with decreasing Al_2O_3 and TiO_2 contents towards the edge of the nodules. A fine-grained CLEN layer is often present outside the diopside layers, and a clear crystallographic

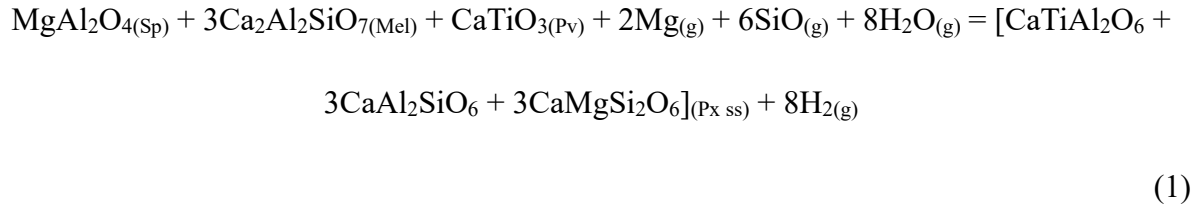
orientation relationship is observed between CLEN and adjacent diopside grains. Below, we discuss the possible condensation reactions that have been recorded in different nodules, based on the above observations. Although hibonite-spinel nodules are present in FGIs in CV chondrites, the formational history of hibonite-spinel inclusions in the CO3 chondrite ALH A77307 has been extensively discussed by Han et al. (2015, 2019), and our observations do not provide any new insights and are not discussed further here.

4.1.1. Spinel-melilite-diopside nodules

In these nodules, spinel-rich cores containing common perovskite grains are surrounded by a mantle of melilite that is, in turn, surrounded by a diopside-rich outer layer. Based on these observations, the condensation sequence should be perovskite → spinel → melilite → diopside, which is not consistent with the calculated equilibrium condensation sequences from a gas of solar composition (e.g., Yoneda and Grossman, 1995; Ebel and Grossman, 2000; Ebel, 2006). The formation of spinel prior to melilite is a long-standing problem that argues against an equilibrium condensation process (e.g., Kornacki and Fegley, 1984; Beckett and Stolper, 1994; Krot et al., 2004a). One possible mechanism for such a condensation sequence has been provided by Beckett and Stolper (1994) and Han et al. (2015). Han et al. (2015) observed a crystallographic orientation relationship between hibonite and spinel in hibonite-spinel inclusions from the ALHA77307 CO3 chondrite and proposed that epitaxial growth may have lowered the activation energy of nucleation of spinel. If this mechanism was responsible for the observed spinel-melilite layered sequence in CV3 FGIs, the lack of hibonite in these

nodules probably means that hibonite has been completely consumed by reactions with the nebular gas. Alternatively, the formation of spinel prior to melilite could be caused by condensation in a supercooled nebular gas at pressures lower than $\sim 2.5 \times 10^{-4}$ bar (e.g., Petaev and Wood, 1998, 2005; Wood, 2004; Petaev et al., 2005). In this case, disequilibrium condensation occurred, where minerals condensed incompletely before spinel. Equilibrium condensation calculations predict that melilite forms via a reaction between hibonite and the gas (e.g., Yoneda and Grossman, 1995; Ebel and Grossman, 2000; Ebel, 2006), but the commonly observed Group II REE pattern in FGIs (e.g., Tanaka and Masuda, 1973; Boynton, 1975; Davis and Grossman, 1979; Mason and Taylor, 1982; Krot et al., 2004a) are inconsistent with this formation mechanism. Group II REE patterns require a fractional condensation process where the most refractory REEs were removed by condensation into hibonite (e.g., MacPherson and Davis, 1994). It is therefore more likely that melilite in FGIs formed by direct condensation from the gas phase onto the surface of spinel grains.

The diopside layer surrounding melilite is often Al-Ti-enriched, with higher Al and Ti contents towards the nodule cores, and the interface between diopside and melilite is complex (Fig. 10). Fine-grained perovskite and spinel grains commonly occur with diopside, and very fine-grained spinel is also present. This relationship indicates that diopside at the interface with melilite formed by a reaction involving melilite, spinel, perovskite, and some gaseous species, as proposed by Han and Brearley (2017). Such a reaction can be written as:



where “Px ss” means pyroxene solid solution. The fine-grained spinel and perovskite in the outer part of the spinel-melilite-diopside nodules implies that they formed after melilite began to condense and indicates at least two generations of spinel and perovskite. Equilibrium condensation calculations (e.g., Yoneda and Grossman, 1995; Ebel and Grossman, 2000; Ebel, 2006) show spinel forms after the onset of melilite condensation, and prior to diopside condensation. Spinel remains a stable phase until the formation of feldspar (appearance temperatures of ~1300-1400 K). Therefore, fine-grained spinel intimately associated with diopside is consistent with these calculations. However, as discussed earlier, the coarser-grained spinel in the nodule cores cannot be explained by equilibrium condensation; instead, a kinetic process, either the epitaxial growth of spinel on pre-condensed hibonite, or disequilibrium condensation from a supercooled gas, must have controlled the formation of this spinel. After the formation of spinel cores, the condensates continuously adjusted to the evolving composition of the nebular gas, and spinel eventually became stable again as a condensate, forming the fine-grained spinel in the outer regions of nodules. This later generation of spinel could form by disequilibrium condensation in a supercooled gas (Petaev et al., 2005).

An alternative formation scenario for fine-grained spinel is physical migration of spinel-rich cores to a partially condensed gaseous reservoir, where fine-grained spinel condensed. As

proposed by Han and Brearley (2016), the observed disequilibrium textures in CAI-like objects in an AOA from ALHA77307 CO3 chondrite can be produced by transportation of spinel-rich cores to a different region with a partially condensed gas. There is still a debate on the mechanisms of transportation of refractory inclusions in the solar nebula (e.g., Shu et al., 1996; Cuzzi et al., 2003; Ciesla, 2007; Simon et al., 2011; Boss et al., 2012). However, models that simulate the evolutionary histories of dust particles during the transportation process (Ciesla, 2010; Boss et al., 2012) show that dust particles migrated both inward and outward through the protoplanetary disk repeatedly in a short time period ($\sim 10^5$ and ~ 200 yrs, respectively), and were exposed to high-temperature thermal events. Disequilibrium conditions during the formation of fine-grained spinel are also supported by zoning in diopside grains, with higher Al_2O_3 and TiO_2 contents adjacent to the interfaces between diopside and melilite layers. Equilibrium condensation cannot account for such a refractory-element-enriched composition, since Ti should have already condensed into perovskite prior to diopside condensation (e.g., Yoneda and Grossman, 1995; Ebel and Grossman, 2000; Ebel, 2006). The fine-grained perovskite can also be produced by the same disequilibrium process.

In FIB-04, fine-grained Al-Ti-diopside grains occur along the interface between spinel in the core region and the melilite mantle. The formation of this Al-Ti-diopside could have occurred prior to melilite condensation, but this is inconsistent with equilibrium condensation calculations and requires formation under disequilibrium conditions. Although Al-Ti-diopside is stable at a higher temperature than diopside in equilibrium condensation models (e.g., Ebel, 2006), it should form later than melilite. Condensation with partial isolation can change the

stability fields of condensates; however, diopside and melilite condensation temperatures do not change significantly with an increasing degree of isolation (Petaev and Wood, 1998). Consequently, Al-Ti-diopside at the spinel-melilite interface must have formed after condensation of melilite. One possible reaction to form Al-Ti diopside is reaction (1), discussed earlier. In this case, the source of Ti for the Al-Ti-diopside may have been pre-condensed perovskite that has been completely consumed. Alternatively, Ti in Al-Ti-diopside could have originated from the same nebular gas reservoir that had only partially condensed spinel, melilite, and perovskite, or a different gaseous reservoir that was only partially condensed, similar to the mechanism proposed by Han and Brearley (2016). The presence of fine-grained Al-Ti-diopside suggests that the formation of melilite layers did not completely isolate the spinel cores from the nebular gas, and gaseous species could still infiltrate into the nodules along pathways, such as grain boundaries.

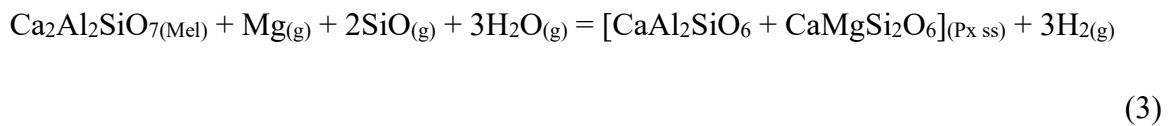
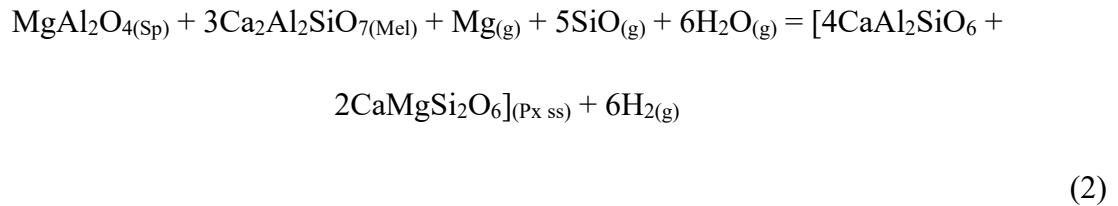
4.1.2. Melilite-diopside nodules

Some nodules are dominated by melilite and diopside and contain only minor spinel that is intimately associated with fine-grained diopside. These spinel grains are typically distributed close to the interface between melilite and diopside. A fine-grained layer exists between melilite and diopside, composed of melilite, diopside, and spinel. Perovskite is absent in these two regions. These observations suggest that condensation of spinel did not occur for these nodules, consistent with equilibrium condensation, where spinel condenses after melilite (e.g., Yoneda and Grossman, 1995; Ebel and Grossman, 2000; Ebel, 2006). However, phases (e.g.,

corundum, hibonite, and grossite) that should have condensed prior to melilite in the equilibrium condensation sequence are not observed in melilite. Although these phases may have been consumed completely by gas-solid reactions, these reactions would have produced a significant amount of spinel, which is not observed. A more plausible explanation is that the lack of spinel is the result of a disequilibrium process. There are three scenarios where such disequilibrium conditions could be achieved. First, due to the isolation of hibonite from the condensing gas, spinel failed to nucleate before the condensation of melilite. The absence of hibonite as a substrate for nucleation of spinel (Han et al., 2015) allowed melilite to condense preferentially. In this case, melilite forms by direct condensation, rather than hibonite-gas reactions. Second, spinel did condense before melilite, but it was removed from the gas before a significant amount of melilite formed. This may be caused by epitaxial growth of spinel on pre-condensed hibonite, which may have suppressed the nucleation of melilite (e.g., Han et al., 2019). Third, condensation in a supercooled gas, at pressures higher than $\sim 2.5 \times 10^{-4}$ bar, forms spinel after melilite (e.g., Petaev and Wood, 1998, 2005; Wood, 2004; Petaev et al., 2005). In these models, spinel accounts for less than 2 wt% of the condensates, in contrast to the high proportion melilite (~ 60 wt%), at a nebular pressure of 10^{-5} bar and an isolation degree of 0.1% (Fig 7 in Petaev and Wood, 1998). This is consistent with the minor amount of fine-grained spinel on the periphery of melilite layers.

Like the Al-Ti-diopside in spinel-melilite-diopside nodules, the Al-Ti-diopside in melilite-diopside nodules is intergrown with fine-grained spinel. Reaction (1) is therefore capable of producing these Al-Ti-diopside grains. On the other hand, diopside that is located further away

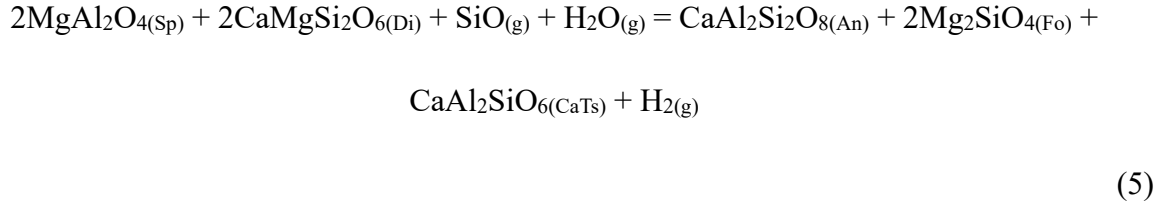
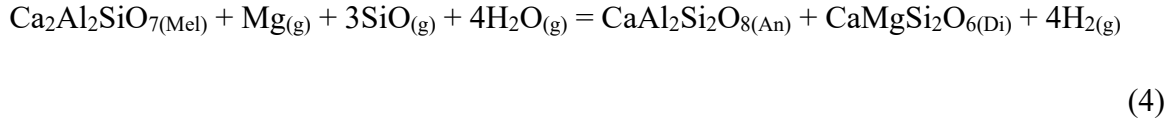
from the melilite-diopside interface has low TiO₂ contents. Therefore, slightly different reactions, as proposed by Krot et al. (2004a,b), in which melilite, spinel, and gaseous species are reactants are responsible for the formation of Ti-poor diopside:



The compositional zoning in Ti in the diopside layers can be explained by the decreasing availability of Ti, as the diopside condensation reactions proceeded, a similar formation history to diopside zoning in spinel-melilite-diopside nodules.

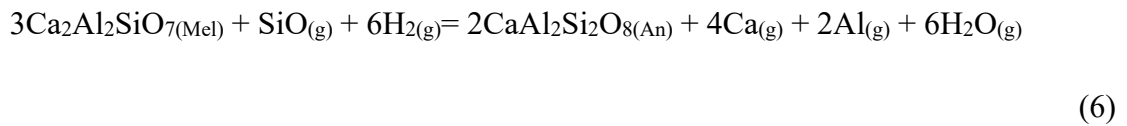
4.1.3. Anorthite-rich nodules

Anorthite-rich nodules are abundant in the FGIs that we investigated. When melilite is present, the interfaces between melilite and anorthite are highly embayed, indicating a replacement relationship. Krot et al. (2004a,b) proposed two possible reactions for the formation of anorthite in FGIs:



The textural evidence suggests these two reactions were not responsible for the formation of anorthite in FGIs. Reaction (4) should form an intergrowth of anorthite and diopside, but no diopside is associated with anorthite, even at the TEM scale. Spinel is a reactant in reaction (5), and the spinel/diopside ratio is 1:1, requiring abundant spinel for the reaction to proceed. A high proportion of spinel is present in spinel-melilite-diopside nodules, but these spinel grains do not show a replacement relationship with anorthite. For nodules that lack a spinel-rich core, spinel is much less abundant than melilite. In addition, in these nodules, fine-grained spinel is ubiquitously enclosed in anorthite that has partially replaced melilite. It is possible that these spinel grains are products of the anorthite formation reaction. However, as discussed earlier, fine-grained spinel commonly occurs in melilite-rich nodules that show minimal replacement of melilite by anorthite. Many nodules with extensive replacement of melilite by anorthite do not contain fine-grained spinel. Hence, a more likely origin for these fine-grained spinel inclusions is that they are unreacted relicts of condensates that formed by the disequilibrium condensation process proposed in Section 4.1.1. Another issue is that reaction (5) produces abundant forsterite, which is not present in the FIB sections. The evidence for the involvement of diopside in the reaction is also equivocal. The diopside layers do show significant variations

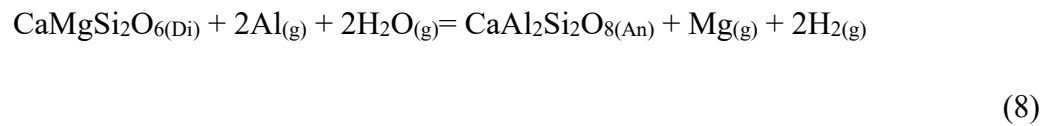
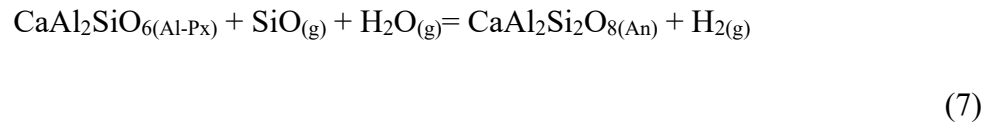
in thickness in most nodules, indicating that diopside was not consumed during the formation of anorthite in these nodules. The curved interfaces between anorthite and diopside in many nodules may be due to the reactions proposed earlier for diopside formation, rather than by a subsequent replacement reaction. Based on the textural observations, the most likely reaction is the direct, pseudomorphic replacement of melilite by anorthite. A possible reaction, based on the molar volumes of melilite (92.50 cm³/mol) and anorthite (105.05 cm³/mol) can be written as:



Given the absence of porosity in the anorthite-rich nodules, this may be an isovolumetric reaction. However, this reaction is problematic, because it requires loss of Ca and Al to the gas, which is counterintuitive because both elements are refractory. The reaction between melilite and gas should result in an almost negligible transfer of these species into the gas (e.g., Simon et al., 2005), suggesting that this reaction may not be thermodynamically viable. However, the textural observations show that no other solid phases were involved in the reaction. Therefore, Ca and Al must have been lost in some way, but the nature of these Ca and Al phases is currently unknown. The progressive inward corrosion of melilite by anorthite, despite the presence of an outer diopside layer, means that the nebular gas was not completely isolated from the nodule cores. Pathways for infiltration of gaseous species, possibly in the form of

pores, were present during the reactions.

In addition to reaction (6), other reactions may be responsible for the formation of some anorthite grains in anorthite-rich nodules. In the zoned FGI Leo-H07, mineralogically-distinct nodules likely formed by different degrees of gas-solid interaction (see Section 4.3 for a detailed discussion). The thickness of diopside layers in the three zones gradually decreases and the layers becomes discontinuous (Fig. 3). This suggests that some anorthite grains may form by progressive replacement of diopside at temperatures lower than reaction (6). This process can be illustrated by the following reactions:



In these nodules, two generations of anorthite occur: the first generation formed by replacement of melilite and the second one formed by replacement of diopside. On the other hand, some mineralogically-heterogeneous FGIs also contain anorthite-rich nodules with discontinuous diopside layers, which may have a different origin (see Section 4.3).

4.1.4. Enstatite-bearing nodules

Many nodules contain a thin enstatite layer outside the diopside layer, which is composed

exclusively of fine-grained, twinned CLEN. We have evaluated possible formation mechanisms for low-Ca pyroxene in a unique, enstatite-bearing FGI from the Efremovka CV3 chondrite in Chapter 3 and thus will not discuss its origin in detail here. The enstatite most likely formed by transformation from a protoenstatite precursor, via direct condensation or reheating in the solar nebula. The condensation of enstatite was facilitated by epitaxial nucleation onto diopside.

4.2. An evolutionary condensation sequence revealed by various nodules in FGIs

The presence of mineralogically-distinct nodules in individual FGIs, as well as the textural relationships between different phases imply an evolutionary condensation sequence in the solar nebula: (1) hibonite-bearing nodules, (2) melilite-rich nodules, (3) anorthite-rich nodules, and finally (4) AOA-like materials. Hibonite-bearing nodules, such as those in Ef1014-04, represent the most refractory endmember. Subsequent gas-solid interactions replaced hibonite by spinel, transforming hibonite-bearing nodules into spinel-cored, melilite-rich nodules. As temperatures decreased, melilite (\pm diopside) underwent replacement by anorthite, producing anorthite-rich nodules. Forsterite and Fe,Ni metal later condensed as AOA-like materials on the surface of anorthite-rich nodules. Such an evolutionary sequence may imply a genetic relationship between different types of refractory inclusions: hibonite-spinel inclusions, FTAs, FGIs, and AOAs. It is well-known that refractory inclusions show a compositional evolutionary trend that is primarily controlled by vapor-solid processes (e.g., MacPherson and Huss, 2005). This compositional trend is, however, complicated by

evaporation processes in the solar nebula, which resulted in various types of igneous CAIs. Therefore, the primary condensation trend has primarily been established based on compositional and thermodynamic modeling. For example, a genetic link between anorthite-spinel-rich inclusions, spinel-rich FTAs, and Type C inclusions was proposed by Lin and Kimura (1998), based mainly on the similarities in bulk compositions of the three types of inclusions. In the literature, textural evidence supporting a relatively complete evolutionary trend are remarkably rare: a recent study of a unique CAI from the Dominion Range 08006 CO3.00 chondrite reported a layered sequence of nine condensate phases (hibonite, grossite, perovskite, melilite, spinel, Fe,Ni metal, diopside, forsterite, and enstatite) (Simon et al., 2019). Our investigations of FGIs from CV3 chondrites provide further evidence for such an evolutionary sequence, in which mineralogically-distinct nodules in FGIs are micrometer-sized counterparts of different types of non-igneous refractory inclusions and represent snapshots of the nebular condensation process at different times. These micrometer-sized nodules may be primitive high-temperature products of condensation directly from the nebular gas, which are similar to the small, unmolten CAIs (~30-100 μm) from the ALHA77307 CO3.0 chondrite (Liu et al., 2019). A schematic cartoon of the above evolutionary condensation sequence is shown in Fig. 13.

The hibonite-bearing nodules in Ef1014-03 are texturally similar to hibonite-rich CAIs that are mostly composed of hibonite single crystals, or assemblages of hibonite and spinel \pm perovskite (e.g., Ireland et al., 1988; Sahijpal et al., 2000; Simon et al., 2006; Liu et al., 2009; Han et al., 2015). In both types of hibonite-bearing object, hibonite often shows a

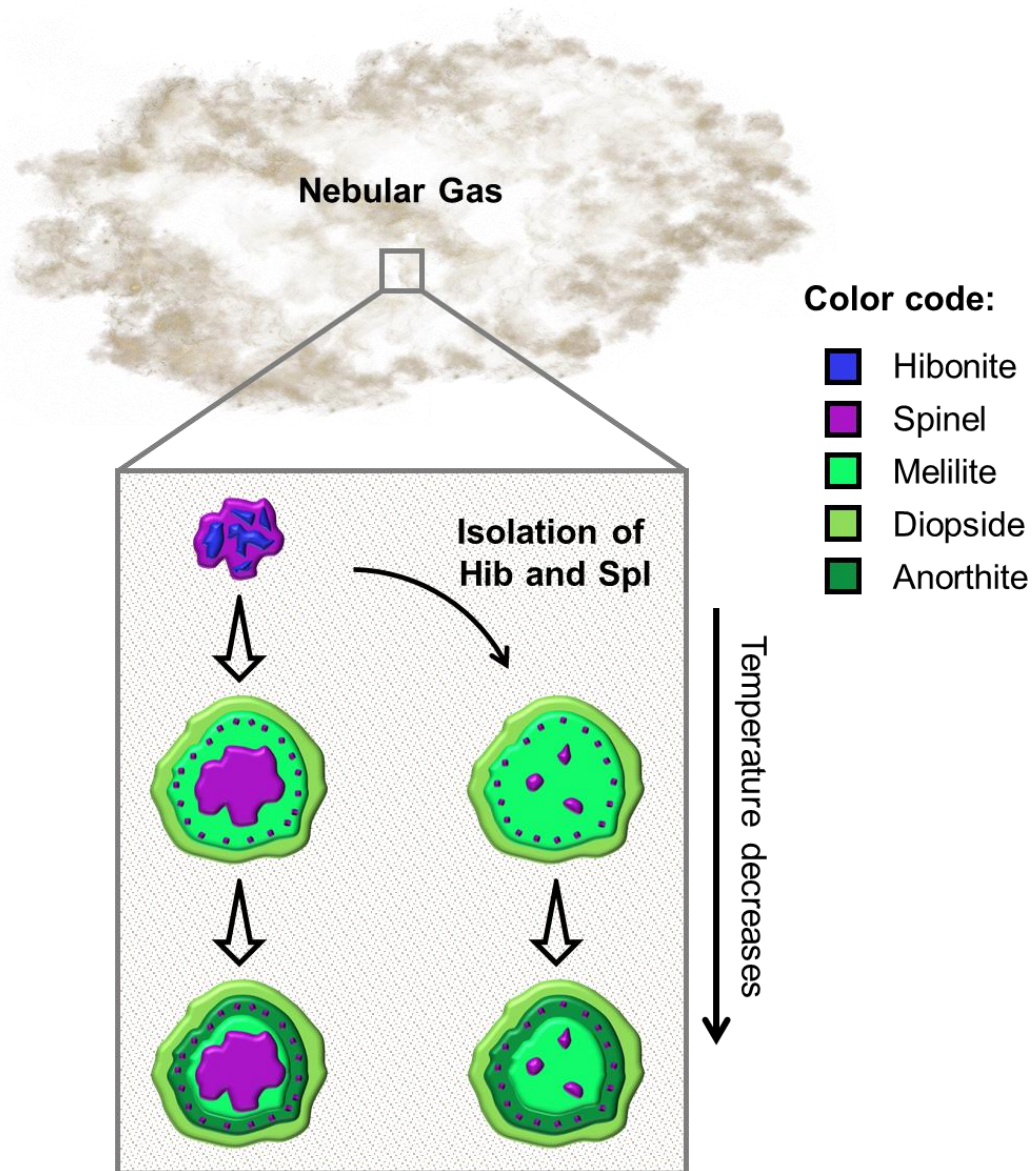


Fig. 13. Schematic cartoon illustrating the evolutionary condensation sequence that has been recorded by nodules with different mineralogies. Mineralogically-distinct nodules represent micrometer-sized counterparts of different non-igneous CAIs. Hibonite condensed at a very early stage and was pseudomorphically replaced by spinel through reaction with the nebular gas, forming hibonite-spinel nodules. These hibonite-spinel nodules later transformed into spinel-cored nodules. On the other hand, due to the formation and physical isolation of hibonite and spinel, spinel-deficient nodules formed. Fine-grained spinel condensed in the outer part of the melilite layer, under disequilibrium conditions. Further gas-solid interactions at lower temperatures resulted in progressive replacement of melilite by anorthite, producing anorthite-rich nodules. Forsterite and Fe,Ni metal (not shown in the figure) eventually condensed after nodules accreted into FGIs, forming AOA-like shells on FGIs. Abbreviations: Hib = hibonite, Spl = spinel.

pseudomorphic replacement relationship with spinel, which is consistent with previous studies proposing that spinel condensed prior to melilite due to a crystallographic control effect of hibonite (e.g., Beckett and Stolper, 1994; Simon et al., 2006; Han et al., 2015). Further interactions with the nebular gas would have transformed these hibonite-bearing or -rich objects into spinel-cored objects. The diopside layers on hibonite-bearing nodules in FGIs probably formed at a later stage, after the condensation of melilite.

Melilite-rich nodules in FGIs are texturally similar to FTAs in CV3 chondrites. The Åk contents of melilite (2.7-30.4) in these nodules are within the range for FTAs reported in the literature (e.g., MacPherson and Grossman, 1984). Some melilite-rich nodules contain a spinel-rich core, whereas others do not. Since spinel and melilite do not show a replacement relationship, this raises the possibility that melilite-rich nodules may have two different precursors. The spinel-cored, melilite-rich nodules may have been transformed directly from hibonite-bearing nodules. The formation of spinel-deficient nodules, on the other hand, may be caused by some disequilibrium process, such as physical isolation of condensates, as discussed in Section 4.1.2. In this case, hibonite-bearing nodules and spinel-deficient, melilite-rich nodules are genetically linked in that the formation of the former effectively isolated spinel from the condensing gas, which would have resulted in the absence of spinel in the latter.

After the formation of diopside, melilite was progressively replaced by anorthite, though the exact reaction is unclear. Spinel-melilite-diopside nodules transformed into spinel-anorthite-diopside nodules, while melilite-diopside nodules transformed into ones containing anorthite and diopside. Later-stage melting events of anorthite-rich nodules, together with

some ferromagnesian components, would have produced Type C CAIs and Al-rich chondrules (e.g., Lin and Kimura, 1998; MacPherson and Huss, 2005; Krot et al., 2007).

Finally, forsterite and Fe,Ni metal condensed, forming shells on FGIs. The texture, mineralogy, and composition of these shells are similar to AOAAs, and therefore they are likely to have formed by similar condensation processes in the ^{16}O -rich, CAI-forming gaseous region (e.g., Cosarinsky et al., 2008).

4.3. Agglomeration of nodules to form mineralogically zoned and heterogeneous FGIs

An important question is how these diverse nodules accreted into millimeter-sized FGIs. Nodules with different mineralogies may form in the same nebular region at different times. Alternatively, different nodules may form in different gaseous reservoirs and were later assembled.

In the single reservoir scenario, mineralogically-distinct nodules may have formed zoned FGIs, in which the core regions are more hibonite- and/or melilite-rich, with anorthite-rich mantles. In this case, the early condensed, most refractory nodules aggregated rapidly into FGIs that are several tens or hundreds of micrometers in size, which then experienced gas-solid interactions that transformed nodules on the exterior of the FGIs into anorthite-rich ones. The zoned FGI Leo-H07 (Fig. 3) is an example of an FGI that formed via this mechanism. In Leo-H07, melilite-rich nodules may be the core of a larger FGI, which was fragmented, and anorthite-rich nodules are the mantle formed by extensive gas-solid interactions. Progressive reactions between nodules and gas would have eventually eliminated the zoning structure,

resulting in mineralogically homogeneous FGIs. An important assumption in this formation mechanism is that nodules in zoned FGIs like Leo-H07 must have a rapid accretion rate before significant replacement of melilite and diopside by anorthite occurred. Experimental and theoretical studies of aggregation of spherical, micrometer-sized dust particles show that the tendency for the dust grains to stick together by van der Waals forces decreases with increasing particle size, and larger dust particles can more easily rebound or fragment during collisions (e.g., Dominik and Tielens, 1997; Poppe et al., 2000; Ueda et al., 2001; Cuzzi, 2004). Most of the nodules in Leo-H07 have a size of $\sim 10 \mu\text{m}$, and many are smaller than $5 \mu\text{m}$. It is therefore likely that these nodules clumped together rapidly into larger objects during condensation.

The single reservoir scenario could also produce heterogeneous FGIs, such as Leo-H01, Leo-H03, and Ef1014-05, in which nodules with different mineralogies and sizes are randomly distributed. The difference in accretion rates of nodules due to their different sizes may account for the mineralogically heterogeneous structure of these FGIs. Small nodules quickly formed clusters, while nodules with a larger size would have stuck together more slowly. This could have resulted in heterogeneous objects, in which either large nodules are randomly distributed within the clusters of small nodules (e.g., Leo-H03), or clusters of small nodules promoted accretion of large nodules onto the surfaces of the former, resulting in an enclosed structure (e.g., Leo-H01 and Ef1014-05). In Leo-H03, there are some melilite-rich and anorthite-rich nodules (with or without spinel cores) that are significantly larger ($20\text{-}50 \mu\text{m}$) than other nodules ($<10 \mu\text{m}$). These large nodules occur as single nodules or clumps of a few nodules, which is consistent with the hypothesis that larger nodular particles stick to each other at a

slower rate. In Leo-H01 and Ef1014-05, on the other hand, aggregates of small nodules are enclosed in a shell of large nodules. The formation of the aggregates of small nodules may have aided accretion of large nodules, promoting growth into millimeter-sized FGIs. This is consistent with experimental work, which demonstrates that collisions of dust particles on larger dust aggregates leads to net growth (Wurm et al., 2005; Kothe et al., 2010).

The size difference of nodules in heterogeneous FGIs is intimately related to the difference in mineralogy. Smaller nodules typically have an anorthite-diopside layered sequence, and when spinel cores are present, the cores are composed of single or a few grains that are less than 2 μm in size. In comparison, spinel cores in larger nodules are often dense aggregates of multiple grains with a grain size of 2-5 μm . In disequilibrium condensation, aggregation and grain growth are important mechanisms for condensates to be physically isolated from the reacting nebular gas, and could have led to the formation of coarse-grained, larger objects (Petaev and Wood, 1998). It is thus likely that aggregation and growth of spinel and melilite (for nodules without spinel cores) resulted in larger nodules in heterogeneous FGIs. Physical isolation could also generate chemical fractionation between coarse and fine condensates, with the former more enriched in refractory components, due to different gas-solid reaction rates (Petaev and Wood, 1998). This is consistent with the observation that in heterogeneous FGIs, larger nodules often contain relict melilite, whereas melilite is completely absent in smaller nodules. The physical isolation process may also serve as a mechanism by which nodules and their CAI counterparts are genetically linked. For example, FTAs in CV3 chondrites are mainly composed of numerous micrometer-sized melilite grains with reverse

zoning patterns (more gehlenite-rich towards grain rims) (e.g., MacPherson and Grossman, 1984). In the physical isolation mechanism, the formation of such large aggregates of mineral grains can be attributed to grain growth, which effectively isolated grains in the interior from extensive reactions with the gas. In this case, melilite-rich nodules and FTAs may have formed in the same reservoir, but some melilite condensates grew into large clumps, resulting in the formation of FTAs. If this is correct, the compositional similarity between FTAs and FGIs from the Ningqiang chondrite (Lin and Kimura, 1998) may be the result of the formation of anorthite-rich nodules in FGIs from melilite-rich nodules that are compositionally similar to FTAs. In other words, FTA-like nodules, but not large FTAs, are the precursor for FGIs in the Ningqiang chondrite. This conjecture may be supported by a recent high-precision ^{26}Al - ^{26}Mg mineral isochron study of an FGI and two FTAs from the Efremovka and Vigarano CV3 chondrites (Kawasaki et al., 2019), which showed that the FGI has a canonical initial $^{26}\text{Al}/^{27}\text{Al}$ ($(^{26}\text{Al}/^{27}\text{Al})_0$) value of $(5.19 \pm 0.17) \times 10^{-5}$, while the FTAs have significantly lower $(^{26}\text{Al}/^{27}\text{Al})_0$ values ($(4.703 \pm 0.082) \times 10^{-5}$ and $(4.392 \pm 0.084) \times 10^{-5}$). The formation of millimeter-sized FTAs was delayed due to grain growth of melilite.

Further evidence for a more rapid accretion of smaller nodules in the heterogeneous FGIs may come from their diopside layers, which are often discontinuous and composed of isolated grains or linear aggregates. One possible explanation for the formation of such diopside layers is rapid accretion of nodules before a significant amount of diopside condensed. Density function theory calculations by Bolser et al. (2016) suggested that island-type growth may be kinetically favorable during high-temperature condensation processes in the solar nebula. They

proposed that Wark-Lovering (WL) rims formed by nucleation of crystals initially as oriented grain islands on the surface of the CAI hosts, or on inner WL rim layers, and these islands later merged into layers. If the small nodules accreted very rapidly after the condensation of melilite, some diopside grains might grow on the surface of melilite as islands, but did not have time to form layers. An alternative explanation for discontinuous diopside layers on small nodules is replacement of diopside by anorthite, the same mechanism used for explaining the discontinuous diopside layers in the outer part of the zoned FGI Leo-H07. However, there is a notable difference between Leo-H07 and heterogeneous FGIs. In Leo-H07, diopside layers become gradually thinner and discontinuous towards the periphery of the FGI, implying an increasing degree of consumption of diopside. In contrast, when discontinuous diopside layers occur in nodules from heterogeneous FGIs, these nodules typically form clusters with rounded or irregular shapes, which are often separated from each other by thicker and more continuous diopside ribbons or bands. In comparison, larger nodules in heterogeneous FGIs typically have thicker and more intact diopside layers, and an unambiguous replacement of diopside by anorthite is absent. Consequently, it is more likely that discontinuous diopside layers observed in heterogeneous FGIs are attributable to the rapid accretion of small nodules.

In the multiple reservoir scenario, mineralogically-distinct nodules formed in different nebular regions and likely under different conditions. Physical transport brought different nodules together, producing compound objects. Physical transport has been suggested as an important mechanism for explaining the multiple thermal events experienced by CAIs and the survival of refractory inclusions in the protoplanetary disk before accretion into chondrite

parent bodies (e.g., Shu et al., 1996; Ciesla, 2010; Cuzzi et al., 2003; Boss et al., 2012; Salmeron and Ireland, 2012; Han and Brearley, 2016). For FGIs in this study, it is possible that some nodules, such as large nodules in Leo-H03, were transported to a different reservoir, where they were captured as inclusions within condensates from this reservoir. However, this mechanism poses the problem of how these micrometer-sized nodules or aggregates of nodules escaped accretion into large aggregates during transport. Additionally, this mechanism alone cannot explain why many FGIs are mineralogically homogeneous, if transport of nodules between different reservoirs is an important process.

Therefore, we suggest that nodules in mineralogically heterogeneous FGIs and some zoned FGIs in CV3 chondrites formed in the same gaseous reservoir, but at different times. This is caused by physical isolation of condensates to form large aggregates, which are more difficult to stick together during collision. On the other hand, smaller nodules quickly formed large clusters, which could then facilitate accretion of large nodules.

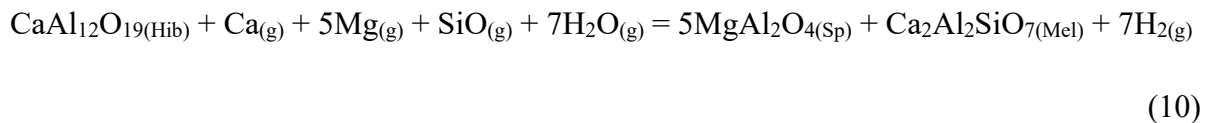
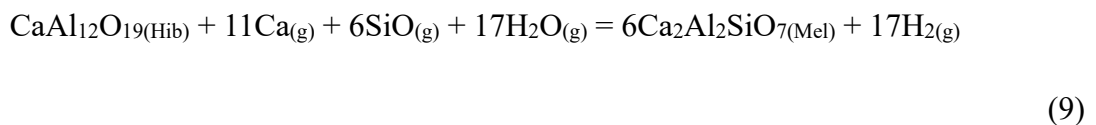
4.4. New insights into the origin of zoned FGIs in CV3 chondrites

The FGIs Leo-H07, -H09, and Ef1014-04 are unique in that they have a mineralogically-zoned structure. The mineralogical variation in Leo-H07 is similar to our proposed evolution sequence where interaction with the nebular gas resulted in an inward replacement of melilite by anorthite (see Section 4.3). Such a thermal history, however, cannot be applied to Leo-H09 and Ef1014-04. Spinel and melilite do not show any replacement relationship in these FGIs, indicating that the spinel-melilite-diopside nodules did not evolve from melilite-diopside

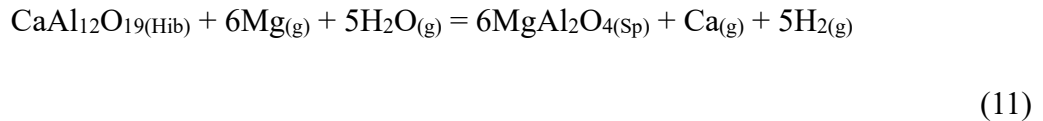
nodules, or the reverse. Texturally and mineralogically, the spinel-rich nodules and melilite-rich nodules in Leo-H09 and Ef1014-04 are similar to the core and mantle regions of zoned FGIs from Efremovka and Leoville described by Krot et al. (2004a). It is likely that Leo-H09 is a fragment of a zoned FGI, which has experienced a similar thermal history to the zoned FGIs reported by Krot et al. (2004a). The core and mantle regions in these FGIs have diffuse contacts, which is inconsistent with physical accretion of melilite-rich nodules onto anorthite-rich nodules. Instead, the formation of the zonation must be attributed to gas-solid interactions. Below we evaluate the formation mechanism of zoned FGIs proposed by Krot et al. (2004a), using the textural observations of Leo-H09 and Ef1014-04.

The zoned FGIs reported by Krot et al. (2004a) have a melilite-free core and a coarser-grained, melilite-rich mantle. These authors suggested that the melilite-rich mantle formed by re-heating and sublimation of precursor spinel-cored nodules. However, there are several problems with such a model. First, according to their proposed reactions, spinel cores are generally involved in the formation of melilite in the mantle region. However, in melilite-rich nodules in Leo-H09 and Ef1014-04, a replacement relationship between spinel and melilite was not observed. Second, if spinel and/or diopside were consumed to form melilite, we should see a decrease in the abundance of spinel and diopside from core to mantle. However, the diopside layers in the mantle regions of all these zoned FGIs are often thicker than those in the core regions. Third, these authors also proposed a reaction between spinel and anorthite to produce melilite. Again, there is no evidence for the consumption of spinel to form melilite. Moreover, anorthite should be the only solid phase involved in the melilite-forming reaction,

based on our TEM observations of Leo-H09. This reaction would start to produce melilite on the outer margin of anorthite, because it is where the gas first came into contact with anorthite. Such a structure has never been observed. Fourth, it is difficult to explain the presence of coarse-grained perovskite located in the center of nodules in the mantle regions of the zoned FGIs. In the center of nodules from the core regions, there is no evidence for the presence of a Ti-rich phase that could react to form perovskite. Even if we consider that the source of Ti comes from the gas, it is still difficult to envision why perovskite would form preferentially in the center of the nodules. Finally, Ef1014-04 contains abundant hibonite-bearing nodules in the melilite-rich mantle region, which cannot be explained by the sublimation mechanism. The hibonite grains are commonly enclosed in spinel, and they have been partly replaced by the latter. In regions where hibonite is in contact with melilite, hibonite does not show evidence of embayment by melilite, indicating a lack of replacement relationship. According to the equilibrium thermodynamic calculations (e.g., Yoneda and Grossman, 1995; Ebel and Grossman, 2000; Ebel, 2006), hibonite should be progressively replaced by melilite and spinel via the following reactions:



However, our observations show that melilite was probably not involved in the reaction. An alternative and more likely reaction is:



In this case, if hibonite in the melilite-rich mantle region of Ef1014-04 formed by a sublimation reaction that is the reverse to reaction (11), we should expect to see the formation of hibonite from the edge of the spinel grains, rather than from the interior.

Therefore, we propose that the melilite-rich mantles in the zoned FGIs reported by Krot et al. (2004a) were more likely to be produced by a separate condensation event. The core regions formed first and experienced gas-solid interactions that partly or completely replaced melilite by anorthite. These objects were later transported to a different region, where the melilite-rich mantle condensed. Since the nodules in the mantles are texturally similar to the spinel-deficient, melilite-rich nodules in unzoned FGIs, it is like that both nodules formed by similar disequilibrium processes, in which isolation of condensates (hibonite and spinel) occurred.

5. CONCLUSIONS

Our SEM and TEM observations of FGIs from the Leoville and Efremovka CV3 chondrites reveal many complex mineralogical and textural variations on the microscale,

which have not been reported previously and provide new insights into the formational and evolutionary histories of these FGIs. The importance of disequilibrium condensation in the formation of FGIs is emphasized in this study: the presence of spinel-cored and melilite-dominant nodules, and the two different occurrences of spinel imply that physical isolation of condensates may have played an important role. Some of the textural relationships in this study cannot be explained easily by the gas-solid reactions proposed in previous studies. For example, the replacement of melilite by anorthite is more consistent with a direct, pseudomorphic reaction.

The presence of mineralogically-distinct nodules and their similarities with other types of non-igneous refractory inclusions imply an evolutionary condensation sequence. In this case, nodules are micrometer-sized counterparts of non-igneous CAIs and may represent snapshots of nebular condensation processes at different times. For example, hibonite-bearing and melilite-rich nodules are counterparts of hibonite-spinel inclusions and FTAs, respectively. Mineralogically-distinct nodules in individual FGIs likely formed in the same gaseous reservoir, but due to the aggregation and growth of condensates, different nodules gained different sizes, which is intimately related to the mineralogies of these nodules: spinel and melilite cores in large nodules are more polycrystalline and compact than small nodules. This size difference has resulted in a difference in the accretion rate: small nodules accreted into clusters more rapidly than large nodules.

Finally, some of the zoned FGIs (Leo-H09 and Ef1014-04) in this study are similar to those FGIs reported by Krot et al. (2004a). Our new observations of these zoned FGIs, such as

the lack of a replacement relationship between spinel and melilite, and between hibonite and melilite, suggest that the zoning structure is more likely to be produced by two separate condensation events in different nebular regions.

ACKNOWLEDGEMENTS

This work was funded by NASA Cosmochemistry grants NNX15AD28G to A. J. Brearley (PI). We thank Dr. Elena Dobrică and Dr. Ying-Bing Jiang for their help with the TEM operations, and Mike Spilde for his assistance with the electron microprobe analysis. We also appreciate the very helpful suggestions from Dr. Steven Simon. Electron microbeam analysis and FIB section preparation were carried out in the Electron Microbeam Analysis Facility, Department of Earth and Planetary Sciences and Institute of Meteoritics, University of New Mexico. The facility is supported by funds from the State of New Mexico, NSF, and NASA.

REFERENCES

- Aléon J., Krot A. N., McKeegan K. D., MacPherson G. J. and Ulyanov A. A. (2005) Fine-grained, spinel-rich inclusions from the reduced CV chondrite Efremovka: II. Oxygen isotopic compositions. *Meteorit. Planet. Sci.* **40**, 1043–1058.
- Beckett J. R. and Stolper E. (1994) The stability of hibonite, melilite and other aluminous phases in silicate melts: Implications for the origin of hibonite-bearing inclusions from carbonaceous chondrites. *Meteoritics* **29**, 41–65.
- Bolser D., Zega T. J., Asaduzzaman A., Bringuier S., Simon S. B., Grossman L., Thompson M. S. and Domanik K. J. (2016) Microstructural analysis of Wark-Lovering rims in the Allende and Axtell CV3 chondrites: Implications for high-temperature nebular processes. *Meteorit. Planet. Sci.* **51**, 743–756.

- Bonal L., Quirico E., Bourot-Denise M. and Montagnac G. (2006) Determination of the petrologic type of CV3 chondrites by Raman spectroscopy of included organic matter. *Geochim. Cosmochim. Acta* **70**, 1849–1863.
- Boss A. P., Alexander C. M. O. and Podolak M. (2012) Cosmochemical consequences of particle trajectories during FU Orionis outbursts by the early Sun. *Earth Planet. Sci. Lett.* **345–348**, 18–26.
- Boynton W. V., Wark D. A. and Ulyanov A. A. (1986) Trace elements in Efremovka fine-grained inclusion E14: Evidence for high temperature, oxidizing fractionations in the solar nebula. *Lunar Planet. Sci.* **17**, 78–79.
- Boynton W. V. (1975) Fractionation in the solar nebula: condensation of yttrium and the rare earth elements. *Geochim. Cosmochim. Acta* **39**, 569–584.
- Brearley A. J. (2014) Nebular versus parent body processing. In *Treatise on Geochemistry: Second Edition* (eds. H. D. Holland and K. K. Turekian). Elsevier, Oxford. pp. 309–334.
- Brearley A. J. and Krot A. N. (2013) Metasomatism in the early solar system: The record from chondritic meteorites. In *Metasomatism and the chemical transformation of rock* (eds. D. E. Harlov and A. Austrheim). Springer, Berlin Heidelberg. pp. 659–789.
- Che S. and Brearley A. J. (2020) Microstructures of low-Ca pyroxene in fine-grained CAIs from CV3 chondrites: Implications for mechanisms and conditions of formation. *Submitted*.
- Ciesla F. J. (2007) Outward transport of high-temperature materials around the midplane of the solar nebula. *Science* **318**, 613–615.
- Ciesla F. J. (2010) The distributions and ages of refractory objects in the solar nebula. *Icarus* **208**, 455–467.
- Connelly J. N., Bizzarro M., Krot A. N., Nordlund Å., Wielandt D. and Ivanova M. A. (2012) The absolute chronology and thermal processing of solids in the solar protoplanetary disk. *Science* **338**, 651–655.
- Cosarinsky M., Leshin L. A., MacPherson G. J., Guan Y. and Krot A. N. (2008) Chemical and oxygen isotopic compositions of accretionary rim and matrix olivine in CV chondrites: Constraints on the evolution of nebular dust. *Geochim. Cosmochim. Acta* **72**, 1887–1913.
- Cuzzi J. N. (2004) Blowing in the wind: III. Accretion of dust rims by chondrule-sized particles

in a turbulent protoplanetary nebula. *Icarus* **168**, 484–497.

Cuzzi J. N., Davis S. S. and Dobrovolskis A. R. (2003) Blowing in the wind. II. Creation and redistribution of refractory inclusions in a turbulent protoplanetary nebula. *Icarus* **166**, 385–402.

Davis A. M. and Grossman L. (1979) Condensation and fractionation of rare earths in the solar nebula. *Geochim. Cosmochim. Acta* **43**, 1611–1632.

Dominik C. and Tielens A. G. G. M. (1997) The physics of dust coagulation and the structure of dust aggregates in space. *Astrophys. J.* **480**, 647–673.

Ebel D. S. (2006) Condensation of rocky material in astrophysical environments. In *Meteorites and the Early Solar System II* (eds. D. S. Lauretta and H. Y. McSween). University of Arizona Press, Tucson. pp. 253–277.

Ebel D. S. and Grossman L. (2000) Condensation in dust-enriched systems. *Geochim. Cosmochim. Acta* **64**, 339–366.

Fagan T. J., Krot A. N., Keil K. and Yurimoto H. (2004) Oxygen isotopic alteration in Ca-Al-rich inclusions from Efremovka: Nebular or parent body setting? *Meteorit. Planet. Sci.* **39**, 1257–1272.

Gattacceca J., Bonal L., Sonzogni C. and Longerey J. (2020) CV chondrites: More than one parent body. *Earth Planet. Sci. Lett.* **547**, 116467.

Han J. and Brearley A. J. (2016) Microstructural constraints on complex thermal histories of refractory CAI-like objects in an amoeboid olivine aggregate from the ALHA77307 CO3.0 chondrite. *Geochim. Cosmochim. Acta* **183**, 176–197.

Han J. and Brearley A. J. (2015) Microstructural evidence for complex formation histories of amoeboid olivine aggregates from the ALHA77307 CO3.0 chondrite. *Meteorit. Planet. Sci.* **50**, 904–925.

Han J. and Brearley A. J. (2017) Microstructures and formation history of melilite-rich calcium-aluminum-rich inclusions from the ALHA77307 CO3.0 chondrite. *Geochim. Cosmochim. Acta* **201**, 136–154.

Han J., Brearley A. J. and Keller L. P. (2015) Microstructural evidence for a disequilibrium condensation origin for hibonite-spinel inclusions in the ALHA77307 CO3.0 chondrite. *Meteorit. Planet. Sci.* **50**, 2121–2136.

- Han J., Jacobsen B., Liu M.-C., Brearley A. J., Matzel J. E. and Keller L. P. (2019) Origin of ^{16}O -rich fine-grained Ca-Al-rich inclusions of different mineralogy and texture. *Geochemistry* **79**, 125543.
- Han J., Liu M.-C., Matsuda N., Park C. and Keller L. P. (2020) Mg isotopic compositions of fine-grained Ca-Al-rich inclusions from reduced CV3 chondrites and implications on the timescale of nebular condensation. *Lunar Planet. Sci.* **51**, 2895.
- Ireland T. R., Fahey A. J. and Zinner E. K. (1988) Trace-element abundances in hibonites from the Murchison carbonaceous chondrite: Constraints on high-temperature processes in the solar nebula. *Geochim. Cosmochim. Acta* **52**, 2841–2854.
- Kawasaki N., Park C., Sakamoto N., Park S. Y., Kim H. N., Kuroda M. and Yurimoto H. (2019) Variations in initial $^{26}\text{Al}/^{27}\text{Al}$ ratios among fluffy Type A Ca–Al-rich inclusions from reduced CV chondrites. *Earth Planet. Sci. Lett.* **511**, 25–35.
- Kawasaki N., Wada S., Park C., Sakamoto N. and Yurimoto H. (2020) Variations in initial $^{26}\text{Al}/^{27}\text{Al}$ ratios among fine-grained Ca-Al-rich inclusions from reduced CV chondrites. *Geochim. Cosmochim. Acta* **279**, 1–15.
- Kita N. T., Ushikubo T., Knight K. B., Mendybaev R. A., Davis A. M., Richter F. M. and Fournelle J. H. (2012) Internal ^{26}Al - ^{26}Mg isotope systematics of a Type B CAI: Remelting of refractory precursor solids. *Geochim. Cosmochim. Acta* **86**, 37–51.
- Komatsu M., Krot A. N., Petaev M. I., Ulyanov A. A., Keil K. and Miyamoto M. (2001) Mineralogy and petrography of amoeboid olivine aggregates from the reduced CV3 chondrites Efremovka, Leoville and Vigarano: Products of nebular condensation, accretion and annealing. *Meteorit. Planet. Sci.* **36**, 629–641.
- Kornacki A. S. and Wood J. A. (1984) Petrography and classification of Ca, Al-rich and olivine-rich inclusions in the Allende CV3 chondrite. *J. Geophys. Res.* **89**, B573.
- Kothe S., Güttler C. and Blum J. (2010) The physics of protoplanetesimal dust agglomerates. V. Multiple impacts of dusty agglomerates at velocities above the fragmentation threshold. *Astrophys. J.* **725**, 1242–1251.
- Kracher A., Keil K., Kallemeyn G. W., Wasson J. T., Clayton R. N. and Huss G. I. (1985) The Leoville (CV3) accretionary breccia. *J. Geophys. Res.* **90**, 123.
- Krot A. N., MacPherson G. J., Ulyanov A. A. and Petaev M. I. (2004a) Fine-grained, spinel-rich inclusions from the reduced CV chondrites Efremovka and Leoville: I. Mineralogy,

petrology, and bulk chemistry. *Meteorit. Planet. Sci.* **39**, 1517–1553.

- Krot A. N., Petaev M. I., Russell S. S., Itoh S., Fagan T. J., Yurimoto H., Chizmadia L., Weisberg M. K., Komatsu M., Ulyanov A. A. and Keil K. (2004b) Amoeboid olivine aggregates and related objects in carbonaceous chondrites: Records of nebular and asteroid processes. *Chemie der Erde* **64**, 185–239.
- Krot A. N., Petaev M. I. and Yurimoto H. (2004c) Amoeboid olivine aggregates with low-Ca pyroxenes: A genetic link between refractory inclusions and chondrules? *Geochim. Cosmochim. Acta* **68**, 1923–1941.
- Krot A. N., Yurimoto H., Hutcheon I. D., Libourel G., Chaussidon M., Tissandier L., Petaev M. I., MacPherson G. J., Paque-Heather J. and Wark D. (2007) Type C Ca, Al-rich inclusions from Allende: Evidence for multistage formation. *Geochim. Cosmochim. Acta* **71**, 4342–4364.
- Lin Y. and Kimura M. (1998) Anorthite-spinel-rich inclusions in the Ningqiang carbonaceous chondrite: genetic links with type A and C inclusions. *Meteorit. Planet. Sci.* **33**, 435–446.
- Lin Y., Kimura M., Miao B., Dai D. and Monoi A. (2006) Petrographic comparison of refractory inclusions from different chemical groups of chondrites. *Meteorit. Planet. Sci.* **41**, 67–81.
- Liu M.-C., Han J., Brearley A. J. and Hertwig A. T. (2019) Aluminum-26 chronology of dust coagulation and early solar system evolution. *Sci. Adv.* **5**, 1–9.
- Liu M. C., McKeegan K. D., Goswami J. N., Marhas K. K., Sahijpal S., Ireland T. R. and Davis A. M. (2009) Isotopic records in CM hibonites: Implications for timescales of mixing of isotope reservoirs in the solar nebula. *Geochim. Cosmochim. Acta* **73**, 5051–5079.
- MacPherson G. J. (2014) Calcium-aluminum-rich inclusions in chondritic meteorites. In *Treatise on Geochemistry: Second Edition* (eds. H. D. Holland and K. K. Turekian). Elsevier, Oxford. pp. 139–179.
- MacPherson G. J., Bullock E. S., Janney P. E., Kita N. T., Ushikubo T., Davis A. M., Wadhwa M. and Krot A. N. (2010) Early solar nebula condensates with canonical, not supracanonical, initial $^{26}\text{Al}/^{27}\text{Al}$ ratios. *Astrophys. J. Lett.* **711**, 117–121.
- MacPherson G. J. and Davis Andrew M. (1994) Refractory inclusions in the prototypical CM chondrite, Mighei. *Geochim. Cosmochim. Acta* **58**, 5599–5625.

- Macpherson G. J. and Grossman L. (1984) “Fluffy” Type A Ca-, Al-rich inclusions in the Allende meteorite. *Geochim. Cosmochim. Acta* **48**, 29–46.
- MacPherson G. J. and Huss G. R. (2005) Petrogenesis of Al-rich chondrules: Evidence from bulk compositions and phase equilibria. *Geochim. Cosmochim. Acta* **69**, 3099–3127.
- MacPherson G. J., Kita N. T., Ushikubo T., Bullock E. S. and Davis A. M. (2012) Well-resolved variations in the formation ages for Ca-Al-rich inclusions in the early Solar System. *Earth Planet. Sci. Lett.* **331–332**, 43–54.
- MacPherson G. J., Krot A. N., Ulyanov A. a. and Hicks T. (2002) A comprehensive study of pristine, fine-grained, spinel-rich inclusions from the Leoville and Efremovka CV3 chondrites, I: petrology. *Lunar Planet. Sci.* **33**, 1526.
- Mason B. and Taylor S. R. (1982) Inclusions in the Allende Meteorite. *Smithson. Contrib. to Earth Sci.*, 1–30.
- Petaev M. I., Krot A. N. and Wood J. A. (2005) Nebular condensation under incomplete equilibrium: Implications for the fine-grained spinel-rich CAIs. *Lunar Planet. Sci.*, 1238.
- Petaev M. I. and Wood J. A. (2005) Meteoritic constraints on temperatures, pressures, cooling rates, chemical compositions, and modes of condensation in the solar nebula. In *Chondrites and the protoplanetary Disk* (eds. A. N. Krot, E. R. D. Scott and B. Reipurth), vol. 341. pp. 373–406.
- Petaev M. I. and Wood J. A. (1998) The condensation with partial isolation (CWPI) model of condensation in the solar nebula. *Meteorit. Planet. Sci.* **33**, 1123–1137.
- Poppe T., Blum J. and Henning T. (2000) Analogous Experiments on the Stickiness of Micron-sized Preplanetary Dust. *Astrophys. J.* **533**, 454–471.
- Russell S. S. and Howard L. (2013) The texture of a fine-grained calcium-aluminium-rich inclusion (CAI) in three dimensions and implications for early solar system condensation. *Geochim. Cosmochim. Acta* **116**, 52–62.
- Ruzicka A., Floss C. and Hutson M. (2012) Amoeboid olivine aggregates (AOAs) in the Efremovka, Leoville and Vigarano (CV3) chondrites: A record of condensate evolution in the solar nebula. *Geochim. Cosmochim. Acta* **79**, 79–105.
- Sahijpal S., Goswami J. N. and Davis A. M. (2000) K, Mg, Ti and Ca isotopic compositions and refractory trace element abundances in hibonites from CM and CV meteorites:

- Implications for early solar system processes. *Geochim. Cosmochim. Acta* **64**, 1989–2005.
- Salmeron R. and Ireland T. R. (2012) Formation of chondrules in magnetic winds blowing through the proto-asteroid belt. *Earth Planet. Sci. Lett.* **327–328**, 61–67.
- Shu F. H., Shang H. and Lee T. (1996) Toward an astrophysical theory of chondrites. *Science* **271**, 1545–1552.
- Simon J. I., Hutcheon I. D., Simon S. B., Matzel J. E. P., Ramon E. C., Weber P. K., Grossman L. and DePaolo D. J. (2011) Oxygen isotope variations at the margin of a CAI records circulation within the solar nebula. *Science* **331**, 1175–1178.
- Simon J. I., Young E. D., Russell S. S., Tonui E. K., Dyl K. A. and Manning C. E. (2005) A short timescale for changing oxygen fugacity in the solar nebula revealed by high-resolution ^{26}Al - ^{26}Mg dating of CAI rims. *Earth Planet. Sci. Lett.* **238**, 272–283.
- Simon S. B., Grossman L., Hutcheon I. D., Phinney D. L., Weber P. K. and Fallon S. J. (2006) Formation of spinel-, hibonite-rich inclusions found in CM2 carbonaceous chondrites. *Am. Mineral.* **91**, 1675–1687.
- Simon S. B., Krot A. N., Nagashima K., Kööp L. and Davis A. M. (2019) Condensate refractory inclusions from the CO3.00 chondrite Dominion Range 08006: Petrography, mineral chemistry, and isotopic compositions. *Geochim. Cosmochim. Acta* **246**, 109–122.
- Tanaka T. and Masuda A. (1973) Rare-earth elements in matrix, inclusions, and chondrules of the Allende meteorite. *Icarus* **19**, 523–530.
- Ueda T., Murakami Y., Ishitsu N., Kawabe H., Inoue R., Nakamura T., Sekiya M. and Takaoka N. (2001) Collisional destruction experiment of chondrules and formation of fragments in the solar nebula. *Earth, Planets Sp.* **53**, 927–935.
- Ulyanov A. A. (1984) On the origin of fine-grained Ca, Al-rich inclusions in the Efremovka carbonaceous chondrite. *Lunar Planet. Sci.*, 872–873.
- Wang Y. and Hsu W. (2009) Petrology and mineralogy of the Ningqiang carbonaceous chondrite. *Meteorit. Planet. Sci.* **44**, 763–780.
- Wood J. A. (2004) Formation of chondritic refractory inclusions: The astrophysical setting. *Geochim. Cosmochim. Acta* **68**, 4007–4021.
- Wurm G., Paraskov G. and Krauss O. (2005) Growth of planetesimals by impacts at ~ 25 m/s.

Icarus **178**, 253–263.

Yoneda S. and Grossman L. (1995) Condensation of CaO–MgO–Al₂O₃–SiO₂ liquids from cosmic gases. *Geochim. Cosmochim. Acta* **59**, 3413–3444.

CHAPTER 3

Microstructures of enstatite in fine-grained CAIs from CV3 chondrites: Implications for mechanisms and conditions of formation

Abstract

Enstatite is a ubiquitous phase in chondritic meteorites, interplanetary dust particles, and cometary samples. In equilibrium condensation models, enstatite is predicted to condense via a reaction between pre-condensed forsterite and gaseous SiO. However, previous studies have shown that some enstatites in chondrite matrices and AOAs do not have a genetic relationship with forsterite, arguing against formation by the predicted forsterite-gas reaction. Here we report the occurrence of enstatite in a unique, fine-grained, spinel-rich inclusion (FGI) Ef1014-01 in the Efremovka CV3 chondrite. Enstatite in this FGI is present as an outer layer on spinel-anorthite-diopside nodules and separates the FGI from an amoeboid olivine aggregate (AOA)-like material. Enstatite shows elevated CaO and Al₂O₃ contents (up to a few weight percent). Four FIB sections were extracted from this FGI to investigate the microstructures of enstatite and its relationship with other phases using TEM techniques. The TEM observations show that the enstatite is dominantly low-temperature clinoenstatite (LCLN), which displays abundant twinning, and is sometimes associated with thin orthoenstatite (OREN) lamellae. Clinoenstatite grains commonly have a crystallographic orientation relationship with adjacent diopside, but do not exhibit any replacement relationship with forsterite in the AOA-like

material surrounding the FGI. Investigations of several other fine-grained CAIs from the Efremovka and Leoville CV3 chondrites show that enstatite is more common in these inclusions than previously thought and typically forms discontinuous layers or islands on the diopside layers.

Based on SEM and TEM observations, we suggest that the LCLLEN-OREN intergrowths in Ef1014-01 formed by transformation from a protoenstatite (PEN) precursor, which may be a product of direct condensation or reheating in the solar nebula. The crystallographic orientation relationship between enstatite and diopside suggests that epitaxial growth of enstatite occurred, lowering the activation energy for nucleation and facilitating direction condensation of enstatite from the gas phase, rather than by reaction of the gas with forsteritic olivine. The microstructures of enstatite are indicative of an extremely rapid cooling rate ($\sim 10^4$ K/h) that is within the range of chondrule cooling rates. Such a rapid cooling rate may imply that the cooling rates of FGIs are indeed much higher than other types of refractory inclusions. Alternatively, the rapid cooling rate may not reflect the primary cooling of the FGIs, but is the result of rapid cooling after a short-lived secondary reheating event in the solar nebula.

A fractionated gas with a lower Mg/Si ratio than the solar value is required to condense enstatite. Such a gas could be produced by isolation of pre-condensed forsterite or repeated evaporation-recondensation processes. The presence of both enstatite-bearing and enstatite-free CAIs in CV3 chondrites suggests that at least two gaseous reservoirs with different Mg/Si ratios were present in the CAI-forming regions.

1. INTRODUCTION

Calcium-aluminum-rich inclusions (CAIs) are submillimeter-to-centimeter sized refractory objects that represent the oldest material formed in the solar nebula (e.g., Amelin et al., 2002; Connelly et al., 2012). Some of these refractory inclusions exhibit igneous characteristics (both texturally and compositionally) that indicate an origin by melting and crystallization of pre-existing solar nebular condensates (e.g., MacPherson and Grossman, 1979; Stolper, 1982; Wark and Lovering, 1982; Wark et al., 1987; Beckett and Stolper, 1994; Simon et al., 1999; MacPherson et al., 2010, 2012; Kita et al., 2012). However, others seem to have largely preserved their primitive condensation textures, and do not show strong evidence for post-formation thermal processing at temperatures higher than their solidus (e.g., MacPherson et al., 1983; Beckett and Stolper, 1994; MacPherson and Grossman, 1984; Krot et al., 2004a).

Fine-grained, spinel-rich inclusions (FGIs) are a group of CAIs whose textures indicate that they did not experience remelting and show evidence for an origin by direct condensation (e.g., Boynton, 1975; Davis and Grossman, 1979; MacPherson and Davis, 1994; Krot et al., 2004a). They are characterized by aggregates of nodules separated from each other by sinuous diopside layers; the detailed mineralogy of individual nodules varies, but a layered sequence of spinel-anorthite-Al-rich diopside is commonly observed. This aggregate structure is distinct from once molten CAIs, such as Type B CAIs (e.g., Stolper, 1982; Beckett, 1986; MacPherson and Davis, 1993; Simon and Grossman, 2006). Another strong line of evidence for a condensation origin comes from their Rare Earth Element (REE) abundance patterns. For

example, FGIs from CV chondrites show volatility-fractionated group II REE patterns (e.g., Tanaka and Masuda, 1973; Grossman and Ganapathy, 1976), which can only be explained by fractional condensation from a gaseous reservoir (Boynton, 1975; Grossman and Ganapathy, 1976; Davis and Grossman, 1979). Therefore, studies of FGIs can provide valuable information on condensation processes in the solar nebula. The bulk compositions of some FGIs overlap with those of Type C CAIs, which are igneous inclusions composed mainly of anorthite, Al-Ti-diopside, spinel, and melilite (e.g., Beckett and Grossman, 1988; Lin and Kimura, 1998; Krot et al., 2004a). Consequently, FGIs are possible candidates for the precursor material that has been melted to form Type C CAIs. In fact, the bulk compositions of different types of CAIs show an evolutionary trend that has been explained as a result of vapor-solid processes (MacPherson and Huss, 2005). The genetic relationship between some FGIs and Type C CAIs is part of such an evolutionary trend.

Here we report mineralogic and petrologic observations of an enstatite-bearing FGIs (Ef1014-01) from the Efremovka CV3 chondrite. We also investigate several other FGIs containing finer-grained enstatite from Efremovka and Leoville. Enstatite with an ^{16}O -rich composition has been previously reported in amoeboid olivine aggregates (AOAs) from CR, CB, CH, CM, CV, CO, and several ungrouped carbonaceous chondrites (Krot et al., 2004b, 2005), and in the matrix of the Kakangari K-grouplet chondrite (Nagashima et al., 2015). However, enstatite has never been reported previously in CAIs, and its proposed formation reactions are entirely based on thermodynamic calculations. Therefore, this study can provide new insights into the possible gas-solid reactions and condensation conditions in the local

nebular environment.

2. ANALYTICAL METHODS

Three 1 inch-round polished thin sections, two from the Efremovka meteorite (#1014 and an un-numbered section) and one from the Leoville meteorite (UNM 577) were examined for this study. All three thin sections are from the Meteorite Collection of the Institute of Meteoritics, University of New Mexico (UNM). Backscattered electron (BSE) images and full spectral X-ray maps were obtained on a FEI Quanta 3D DualBeam[®] field emission gun scanning electron microscope/focused ion beam (FEG-SEM/FIB) instrument in the Department of Earth and Planetary Sciences (EPS) at UNM. This FEG-SEM is fitted with an EDAX Apollo 40 SDD Energy Dispersive Spectroscopy (EDS) system with Genesis software. Full thin section BSE and X-ray map mosaics were produced using ImageJ software, by combining multiple image fields. These mosaics were then used to locate refractory inclusions and chondrules on the thin sections. The petrology and mineralogy of individual objects were characterized in detail by high-resolution BSE imaging and X-ray mapping. The instrument operating conditions for BSE imaging and X-ray mapping were: an accelerating voltage of 15 kV and beam current of 11 nA.

The major and minor element compositions of phases in Ef1014-01 were obtained by wavelength dispersive spectrometry (WDS) on a JEOL JXA-8200 electron probe microanalyzer (EPMA) at UNM. All analyses were obtained at an accelerating voltage of 15 kV, a beam current of 20 nA, and a spot size of 1 μm . Taylor Company Microprobe Standards

were used for calibration: Na on albite, Mg, Si, and Fe on olivine, Al and K on orthoclase, S on pyrite, Ca on diopside, Ti on titanite, V on V-metal, Cr on chromite, Mn on spessartine, Ni on Ni-metal. In addition, an almandine oxygen standard and an apatite-F (Wilberforce) standard were also used for Al and P, respectively. The detection limits for Fe and Ni are ~ 0.02 , while those for all the other elements are ~ 0.01 . Data were reduced using the modified ZAF correction procedure in Probe for EPMA.

A total of four FIB sections were extracted from Ef1014-01 using the FEI Quanta 3D FEG-SEM/FIB instrument equipped with an Omniprobe micromanipulator, using the method described by Han and Brearley (2015). The microstructures of the FIB sections were then characterized on a JEOL 2010 transmission electron microscope (TEM) instrument and a JEOL 2010F FASTEM field emission gun scanning TEM (STEM/TEM) instrument at UNM. The TEM techniques we used include bright-field TEM (BF-TEM), dark-field scanning TEM (DF-STEM), electron diffraction, and high-resolution TEM (HRTEM). We also performed quantitative microanalyses and X-ray elemental mapping on the JEOL 2010F using an Oxford Instruments AZtec microanalysis system with an Oxford Instruments X-Max 80N 80 mm² SDD EDS detector. The Cliff–Lorimer thin film approximation was used for quantification using theoretical k-factors.

3. RESULTS

3.1. SEM observations

The fine-grained, enstatite-bearing, spinel-rich CAI Ef1014-01 is an aggregate that is

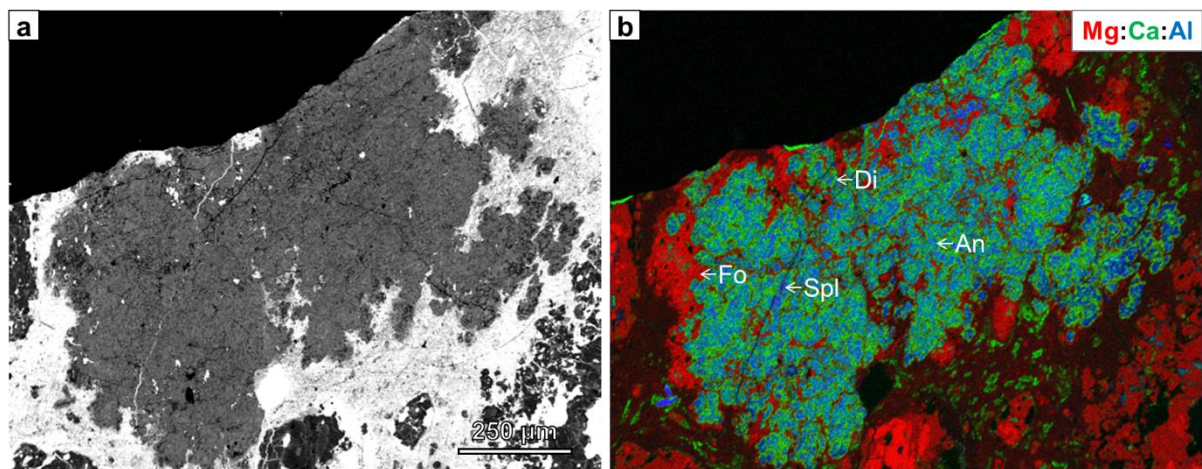


Fig. 1. SEM and EDS X-ray maps of the enstatite-bearing CAI Ef1014-01 from Efremovka. (a) BSE image of Ef1014-01, and (b) combined X-ray elemental map in Mg (red), Ca (green), and Al (blue) showing the distribution of anorthite, diopside, and spinel. The CAI is composed of spinel-anorthite-diopside nodules that are enclosed by a forsterite-rich shell. Abbreviations: An = anorthite, Di = Al-Ti-bearing diopside, Fo = forsterite, Spl = spinel.

composed of numerous spinel-rich nodules (Fig. 1). This CAI is about 750 μm wide and has an irregular shape. Individual nodules (20-50 μm in diameter) are composed of spinel enclosed by anorthite, which is surrounded by concentric layers of Al-bearing diopside (2-8 μm thick) and enstatite (1-5 μm thick) (Fig. 2a). The spinel grains (1-2 μm in size) have anhedral-to-subhedral shapes and show various degrees of Fe-enrichment. Spinel is present either as isolated grains or as aggregates interconnected by Al-Ti-rich diopside grains (1-2 μm in size). These Al-Ti diopside grains have irregular shapes, which often have curved or embayed outlines. The interface between Al-Ti diopside and spinel is often sharp, but becomes less well-defined where spinel is enriched in Fe at grain edges due to the similarity in contrast between diopside and spinel in Z-contrast STEM images. Anorthite, with a grain size of 2 to 5 μm , is the most abundant phase in the nodules. In addition to spinel grains that are partly

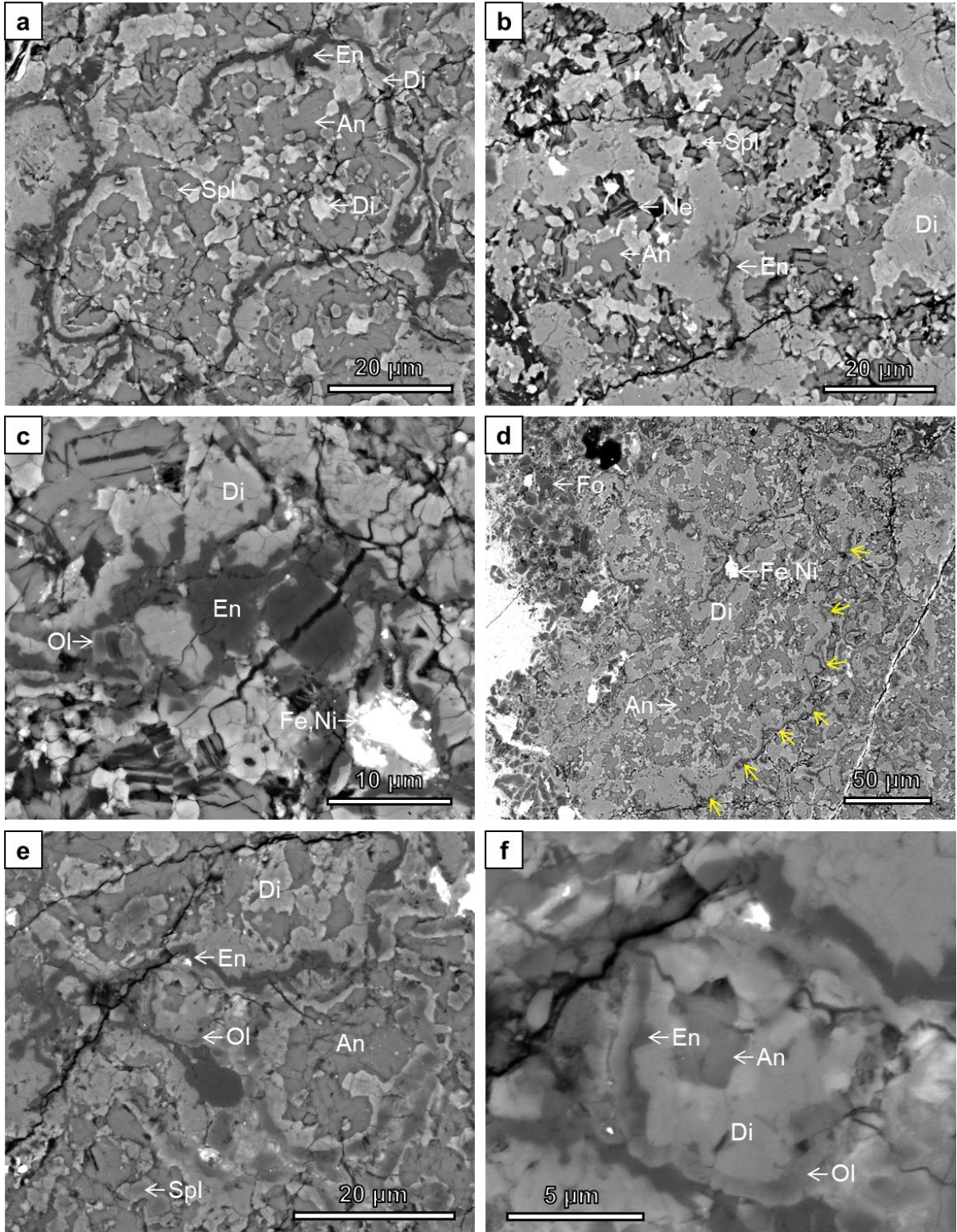


Fig. 2. Backscattered electron SEM images showing the mineralogy of spinel-rich nodules. (a) In individual nodules, spinel and Al-Ti-rich diopside grains are enclosed in an anorthite mantle, which in turn is surrounded by diopside and enstatite layers.

Fig. 2. (*continued*) (b) Anorthite commonly shows alteration by nepheline along some crystallographically-controlled planes, or along the interface of anorthite with diopside. (c) Enstatite grains from adjacent nodules often coalesce into coarse-grained enstatite. Olivine and Fe,Ni metal grains are observed in between enstatite layers. (d) Enstatite sometimes forms an extended layer surrounding several nodules. An example is shown in this image, where the extended layer is marked by yellow arrows. (e) Some enstatite grains appear to have been replaced by olivine, which is more obvious in (f) where a relict enstatite layer is present between diopside and olivine. Abbreviations: An = anorthite, Di = Al-Ti-bearing diopside, En = enstatite, Fe,Ni = Fe,Ni-rich metal, Fo = forsterite, Ne = nepheline, Ol = olivine, Spl = spinel.

interconnected by Al-Ti-diopside, anorthite also contains nm-sized Al-Ti diopside inclusions (<500 nm). Anorthite grains in different nodules show variable degrees of alteration by nepheline, which has replaced anorthite either along crystallographically-controlled planes, or along the interface of anorthite with diopside (Fig. 2b). Surrounding the anorthite mantle is an Al-bearing diopside layer whose thickness varies in different places. This diopside layer shows compositional zoning, with Al and Ti enrichment towards the interface with the anorthite. Diopside layers from adjacent nodules often coalesce to form compact aggregates. The enstatite layer is usually a few μm thick and has a curved interface with the diopside layer. When adjacent nodules both have enstatite layers, large regions of enstatite ($\sim 6\text{-}10\ \mu\text{m}$ in size) are often present (Fig. 2c). Such enstatite layers are ubiquitous in Ef1014-01; however, an enstatite layer is not present on every nodule, and sometimes, enstatite forms an extended layer surrounding several nodules (Fig. 2d). In the right half of the CAI, there is a region where enstatite appears to have been partially replaced by olivine (Fig. 2e). This relationship is most evident in Figure 2f, where there is a relict enstatite layer on the left periphery of an anorthite-diopside-rich nodule.

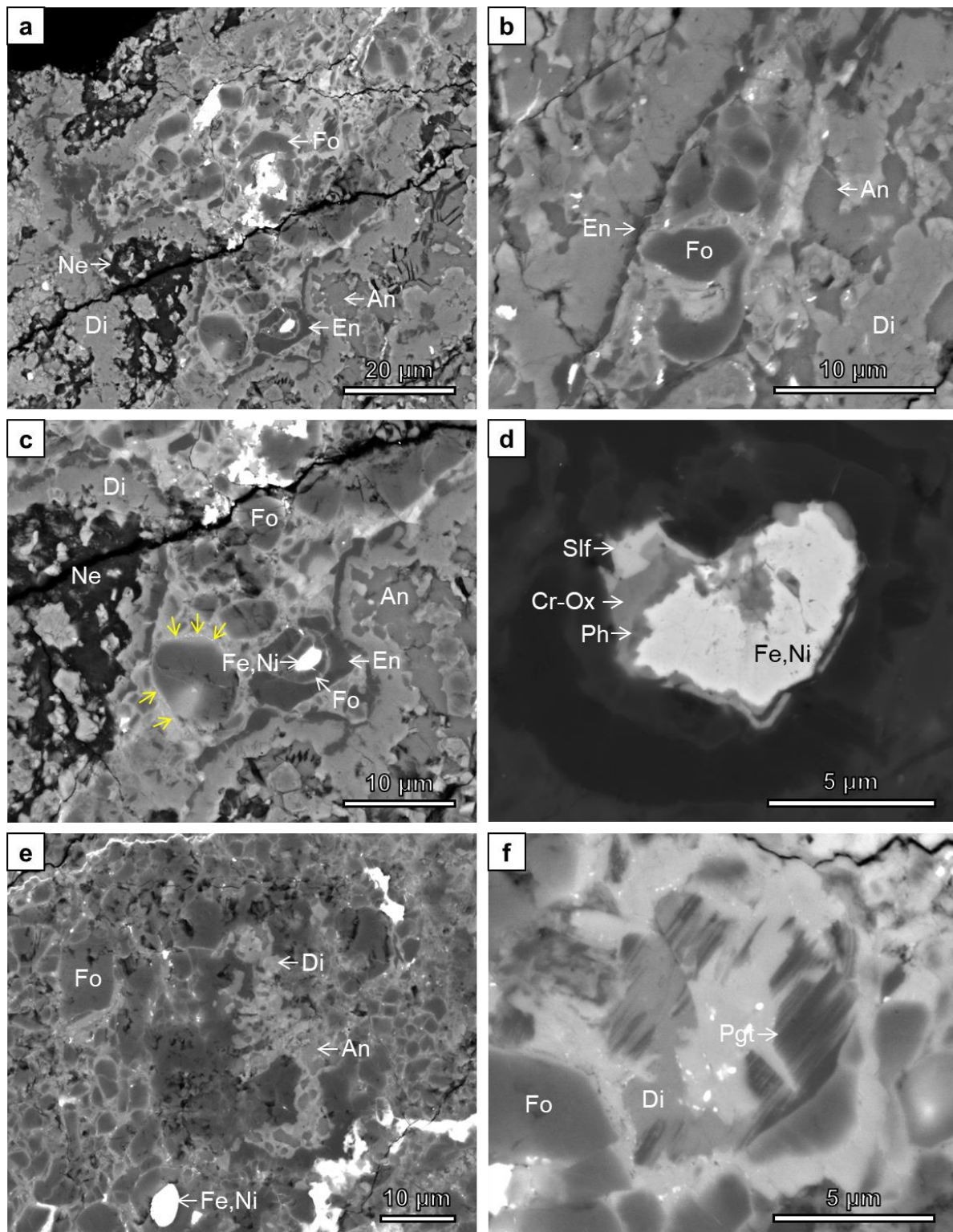


Fig. 3. Backscattered electron SEM images of the AOA-like material surrounding Ef1014-01. (a) The major phases in the AOA-like material are forsterite and Fe,Ni metal. High-Z contrast phases interstitial to forsterite and metal grains are secondary alteration products.

Fig. 3. (*continued*) (b) Many forsterite grains have Fe-rich rims and sometimes Fe-rich olivine overgrowths. These features can be attributed to metamorphism on the parent body. (c) Olivine grains often have a thin layer that is composed of nm-sized, Fe-rich oxides (indicated by yellow arrows). Some rare enstatite grains are also present in the AOA-like material, forming shells enclosing olivine and Fe,Ni metal. (d) Fe,Ni metal grains commonly have alteration rims that are mainly composed of Cr-rich oxides, Fe,Ni sulfides, and phosphates. (e) The AOA-like material contains sinuous CAI-like assemblages of anorthite and Al-Ti-diopside. (f) Some diopside grains in the AOA-like material contain pigeonite exsolution lamellae. Abbreviations: An = anorthite, Di = Al-Ti-bearing diopside, Cr-Ox = Cr-rich oxides, En = enstatite, Fe,Ni = Fe,Ni-rich metal, Fo = forsterite, Ne = nepheline, Pgt = pigeonite, Ph = phosphates, Slf = sulfides.

Outside the enstatite layer is an AOA-like material that is mainly composed of anhedral-to-subhedral olivine (3-10 μm) and anhedral Fe,Ni metal (2-15 μm) (Fig. 3a). A ferromagnesian material with a high-Z contrast, together with abundant nm-sized, Fe-rich oxide grains (probably products of parent body alteration or terrestrial weathering), is present interstitial to olivine and Fe,Ni metal grains. Olivine displays a significant degree of Fe-enrichment, and some olivine grains have fayalitic olivine overgrowths (Fig. 3b). The nm-sized, Fe-rich oxides are often distributed on the olivine rims, forming a thin layer (Fig. 3c). Some rare metal-olivine nodules are present in the AOA-like material, and sometimes they are poikilitically enclosed by relatively coarse-grained enstatite (up to 3 μm) (Fig. 3c). The coarse-grained Fe,Ni metal grains have alteration rims (1-3 μm thick) that contain Cr-rich oxides, Fe,Ni sulfides, and phosphates (Fig. 3d). The AOA-like material also contains CAI-like assemblages that are composed of anorthite and Al-Ti diopside, and resemble spinel-rich nodules in the host CAI (Fig. 3e, f). Individual diopside grains (~ 2 μm) are also present in the AOA-like material and contain pigeonite exsolution lamellae (Fig. 3g, h).

3.2. Mineral compositions

Representative electron microprobe analyses of spinel, anorthite, diopside, enstatite, and olivine from Ef1014-01 are reported in Table 1-5. Spinel commonly shows elevated FeO contents (up to 8.58 wt%) due to metamorphism. Anorthite contains up to 1.8 wt% Na₂O, which is probably caused by alkali metasomatism. Diopside shows compositional zoning in individual nodules, with decreasing TiO₂ and Al₂O₃ contents towards the enstatite layers. The TiO₂ and Al₂O₃ contents of diopside range between 0.03-7.85 wt% and 1.67-23.79 wt%, respectively. Enstatite contains 1.52 wt% CaO on average, and many grains contain elevated Al₂O₃ (up to 2.14 wt%) and FeO contents (up to Fs_{3.1}). Only a minor amount of MnO was detected in enstatite: 0.01-0.1 wt%. Olivine in the AOA-like material is forsteritic olivine with Fa contents between ~3.8 and ~11.8, which is likely the result of parent body thermal metamorphism.

3.3. Microstructures

The positions selected for FIB section extraction are shown in Fig. 4. Two FIB sections (FIB-01 and -02) were extracted from the interface between two adjacent nodules with enstatite layers (Fig. 4a-d), one was from the contact between a nodule (FIB-03) and the AOA-like material (Fig. 4e, f), and the final section (FIB-04) was from a junction of several nodules where a coarse-grained Fe,Ni metal is present (Fig. 4g).

The FIB section FIB-01 sampled the interface between two adjacent nodules, where Al-diopside grains occur between the enstatite layers. The STEM mosaic image shows that the

Table 1. Representative electron microprobe analyses (wt%) of spinel in Ef1014-01.

| Spot# | 1 | 2 | 3 | 4 |
|--------------------------------|--------|-------|--------|--------|
| SiO ₂ | 0.03 | 0.10 | 0.05 | 0.03 |
| TiO ₂ | 0.33 | 1.00 | 0.03 | 0.18 |
| Al ₂ O ₃ | 68.57 | 69.62 | 69.43 | 67.29 |
| V ₂ O ₃ | 0.33 | 0.29 | 0.16 | 0.20 |
| Cr ₂ O ₃ | 0.29 | 0.24 | 0.27 | 0.27 |
| FeO | 6.11 | 2.27 | 2.83 | 7.99 |
| MnO | 0.02 | 0.01 | 0.01 | 0.04 |
| MgO | 23.65 | 24.01 | 25.63 | 21.29 |
| CaO | 0.01 | 0.05 | 0.01 | 0.02 |
| Na ₂ O | 0.02 | 0.01 | 0.14 | 0.03 |
| K ₂ O | 0.01 | 0.01 | 0.01 | 0.01 |
| Total | 100.36 | 99.60 | 101.57 | 101.35 |

Cations per 4 oxygen anions

| | | | | |
|-------|--------|--------|-------|--------|
| Si | 0.001 | 0.002 | 0.001 | 0.001 |
| Ti | 0.006 | 0.017 | 0.001 | 0.003 |
| Al | 1.984 | 1.952 | 1.965 | 1.981 |
| V | 0.006 | 0.005 | 0.003 | 0.004 |
| Cr | 0.005 | 0.004 | 0.005 | 0.005 |
| Fe | 0.125 | 0.146 | 0.057 | 0.209 |
| Mn | 0.000 | 0.000 | 0.000 | 0.001 |
| Mg | 0.865 | 0.864 | 0.918 | 0.793 |
| Ca | 0.001 | 0.002 | 0.001 | 0.001 |
| Na | 0.001 | 0.000 | 0.006 | 0.001 |
| K | 0.000 | 0.000 | 0.000 | 0.000 |
| Total | 2.995 | 2.994 | 2.957 | 2.998 |
| Fe# | 12.650 | 14.443 | 5.829 | 20.852 |

Note: bd = below detection limits.

Table 2. Representative electron microprobe analyses (wt%) of anorthite in Ef1014-01.

| Spot# | 1 | 2 | 3 | 4 | 5 |
|--------------------------------|--------|--------|--------|--------|--------|
| SiO ₂ | 41.27 | 41.68 | 39.42 | 41.14 | 40.06 |
| TiO ₂ | 0.06 | 0.03 | 0.07 | 0.04 | 0.09 |
| Al ₂ O ₃ | 38.30 | 37.03 | 38.41 | 36.42 | 36.97 |
| V ₂ O ₃ | 0.11 | 0.01 | 0.03 | 0.01 | 0.02 |
| Cr ₂ O ₃ | 0.00 | 0.00 | 0.03 | 0.01 | bd |
| FeO | 0.51 | 0.31 | 0.77 | 0.98 | 0.22 |
| MnO | 0.02 | 0.00 | 0.00 | 0.00 | 0.00 |
| MgO | 0.43 | 0.21 | 0.90 | 0.99 | 0.36 |
| CaO | 19.10 | 19.18 | 18.51 | 15.97 | 17.77 |
| Na ₂ O | 0.10 | 0.99 | 0.05 | 1.80 | 1.19 |
| K ₂ O | 0.02 | 0.02 | bd | 0.34 | 0.03 |
| Total | 100.90 | 101.47 | 101.18 | 101.71 | 101.70 |

| Cations per 8 oxygen anions | | | | | |
|-----------------------------|-------|-------|-------|-------|-------|
| Si | 1.916 | 1.946 | 1.880 | 1.950 | 1.992 |
| Ti | 0.002 | 0.001 | 0.002 | 0.002 | 0.003 |
| Al | 2.095 | 2.037 | 2.105 | 2.035 | 2.016 |
| V | 0.004 | 0.001 | 0.001 | 0.000 | 0.001 |
| Cr | 0.000 | 0.000 | 0.001 | 0.000 | - |
| Fe | 0.020 | 0.012 | 0.030 | 0.039 | 0.008 |
| Mn | 0.001 | 0.000 | 0.000 | 0.000 | 0.000 |
| Mg | 0.029 | 0.015 | 0.062 | 0.070 | 0.025 |
| Ca | 0.950 | 0.959 | 0.972 | 0.811 | 0.881 |
| Na | 0.009 | 0.090 | 0.005 | 0.166 | 0.107 |
| K | 0.001 | 0.001 | - | 0.021 | 0.002 |
| Total | 5.027 | 5.062 | 5.058 | 5.094 | 5.034 |

Note: bd = below detection limits.

Table 3. Representative electron microprobe analyses (wt%) of diopside in Ef1014-01.

| Spot# | 1 | 2 | 3 | 4 | 5 |
|--------------------------------|--------|--------|--------|--------|--------|
| SiO ₂ | 54.10 | 53.99 | 46.36 | 49.56 | 36.85 |
| TiO ₂ | 0.03 | 0.08 | 2.13 | 0.88 | 7.42 |
| Al ₂ O ₃ | 1.67 | 2.51 | 12.09 | 8.74 | 23.79 |
| V ₂ O ₃ | 0.01 | 0.01 | 0.21 | 0.10 | 0.64 |
| Cr ₂ O ₃ | 0.02 | 0.02 | 0.06 | 0.03 | 0.12 |
| FeO | 0.50 | 0.82 | 1.68 | 1.24 | 0.52 |
| MnO | bd | 0.01 | bd | 0.01 | 0.01 |
| MgO | 19.27 | 20.22 | 14.53 | 15.88 | 7.76 |
| CaO | 25.57 | 22.51 | 23.74 | 23.65 | 24.34 |
| Na ₂ O | 0.01 | bd | 0.02 | 0.03 | 0.13 |
| K ₂ O | bd | bd | 0.01 | 0.02 | 0.01 |
| Total | 101.79 | 101.12 | 101.64 | 101.16 | 102.00 |

| Cations per 6 oxygen anions | | | | | |
|-----------------------------|-------|-------|-------|-------|-------|
| Si | 1.929 | 1.925 | 1.667 | 1.780 | 1.329 |
| Ti | 0.001 | 0.002 | 0.058 | 0.024 | 0.201 |
| Al | 0.070 | 0.105 | 0.512 | 0.370 | 1.011 |
| V | 0.000 | 0.000 | 0.006 | 0.003 | 0.019 |
| Cr | 0.000 | 0.001 | 0.002 | 0.001 | 0.003 |
| Fe | 0.015 | 0.024 | 0.050 | 0.037 | 0.016 |
| Mn | - | 0.000 | - | 0.000 | 0.000 |
| Mg | 1.024 | 1.075 | 0.779 | 0.850 | 0.417 |
| Ca | 0.977 | 0.860 | 0.915 | 0.910 | 0.940 |
| Na | 0.001 | - | 0.002 | 0.002 | 0.009 |
| K | - | - | 0.000 | 0.001 | 0.000 |
| Total | 4.017 | 3.993 | 3.991 | 3.979 | 3.946 |

Note: bd = below detection limits.

Table 4. Representative electron microprobe analyses (wt%) of enstatite in Ef1014-01.

| Spot# | 1 | 2 | 3 | 4 | 5 |
|--------------------------------|--------|--------|--------|--------|--------|
| SiO ₂ | 57.97 | 57.71 | 56.79 | 58.19 | 59.12 |
| TiO ₂ | 0.04 | 0.02 | 0.02 | 0.06 | bd |
| Al ₂ O ₃ | 1.19 | 0.90 | 2.14 | 1.91 | 0.75 |
| V ₂ O ₃ | bd | bd | bd | 0.02 | 0.02 |
| Cr ₂ O ₃ | 0.32 | 0.37 | 0.39 | 0.32 | 0.06 |
| FeO | 1.21 | 1.42 | 2.19 | 1.07 | 0.48 |
| MnO | 0.06 | 0.07 | 0.10 | 0.09 | 0.01 |
| MgO | 36.22 | 38.62 | 38.43 | 36.58 | 40.49 |
| CaO | 3.02 | 1.26 | 1.12 | 1.74 | 0.48 |
| Na ₂ O | 0.16 | 0.24 | 0.54 | 0.05 | bd |
| K ₂ O | 0.03 | 0.03 | 0.03 | 0.01 | bd |
| Total | 100.47 | 100.87 | 102.08 | 100.34 | 101.85 |
| Cations per 6 oxygen anions | | | | | |
| Si | 1.963 | 1.944 | 1.901 | 1.962 | 1.956 |
| Ti | 0.001 | 0.000 | 0.000 | 0.001 | 0.000 |
| Al | 0.047 | 0.036 | 0.085 | 0.076 | 0.029 |
| V | - | - | - | 0.000 | 0.000 |
| Cr | 0.009 | 0.010 | 0.010 | 0.009 | 0.002 |
| Fe | 0.034 | 0.040 | 0.061 | 0.030 | 0.013 |
| Mn | 0.002 | 0.002 | 0.003 | 0.003 | 0.000 |
| Mg | 1.828 | 1.939 | 1.918 | 1.838 | 1.997 |
| Ca | 0.109 | 0.046 | 0.040 | 0.063 | 0.017 |
| Na | 0.011 | 0.016 | 0.035 | 0.003 | - |
| K | 0.001 | 0.001 | 0.001 | 0.000 | - |
| Total | 4.005 | 4.034 | 4.055 | 3.985 | 4.015 |
| En | 98.16 | 97.98 | 96.90 | 98.39 | 99.34 |
| Wo | 5.55 | 2.25 | 1.99 | 3.26 | 0.84 |

Note: bd = below detection limits.

Table 5. Representative electron microprobe analyses (wt%) of olivine in Ef1014-01.

| Spot# | 1 | 2 | 3 | 4 | 5 |
|--------------------------------|--------|--------|--------|--------|--------|
| SiO ₂ | 40.04 | 39.08 | 40.44 | 40.99 | 40.67 |
| TiO ₂ | 0.00 | 0.03 | 0.03 | bd | 0.02 |
| Al ₂ O ₃ | 0.12 | 0.87 | 0.37 | 0.11 | 0.13 |
| V ₂ O ₃ | 0.02 | 0.02 | bd | 0.02 | 0.02 |
| Cr ₂ O ₃ | 0.02 | 0.11 | 0.01 | bd | 0.06 |
| FeO | 8.77 | 11.34 | 6.04 | 3.94 | 9.72 |
| MnO | 0.15 | 0.18 | 0.16 | 0.15 | 0.20 |
| MgO | 51.21 | 47.73 | 53.31 | 56.25 | 49.18 |
| CaO | 0.17 | 0.39 | 0.29 | 0.19 | 0.31 |
| Na ₂ O | 0.01 | 0.03 | 0.02 | bd | bd |
| K ₂ O | bd | 0.01 | bd | bd | bd |
| Total | 100.73 | 100.11 | 101.03 | 101.92 | 100.57 |
| Cations per 4 oxygen anions | | | | | |
| Si | 0.973 | 0.968 | 0.969 | 0.965 | 0.992 |
| Ti | 0.000 | 0.000 | 0.000 | - | 0.000 |
| Al | 0.003 | 0.025 | 0.011 | 0.003 | 0.004 |
| V | 0.000 | 0.000 | - | 0.000 | 0.000 |
| Cr | 0.000 | 0.002 | 0.000 | - | 0.001 |
| Fe | 0.178 | 0.235 | 0.121 | 0.077 | 0.198 |
| Mn | 0.003 | 0.004 | 0.003 | 0.003 | 0.004 |
| Mg | 1.856 | 1.762 | 1.903 | 1.974 | 1.788 |
| Ca | 0.005 | 0.010 | 0.008 | 0.005 | 0.008 |
| Na | 0.000 | 0.001 | 0.001 | - | - |
| K | - | 0.000 | - | - | - |
| Total | 3.020 | 3.009 | 3.016 | 3.027 | 2.996 |
| Fa | 8.76 | 11.77 | 5.97 | 3.78 | 9.98 |

Note: bd = below detection limits.

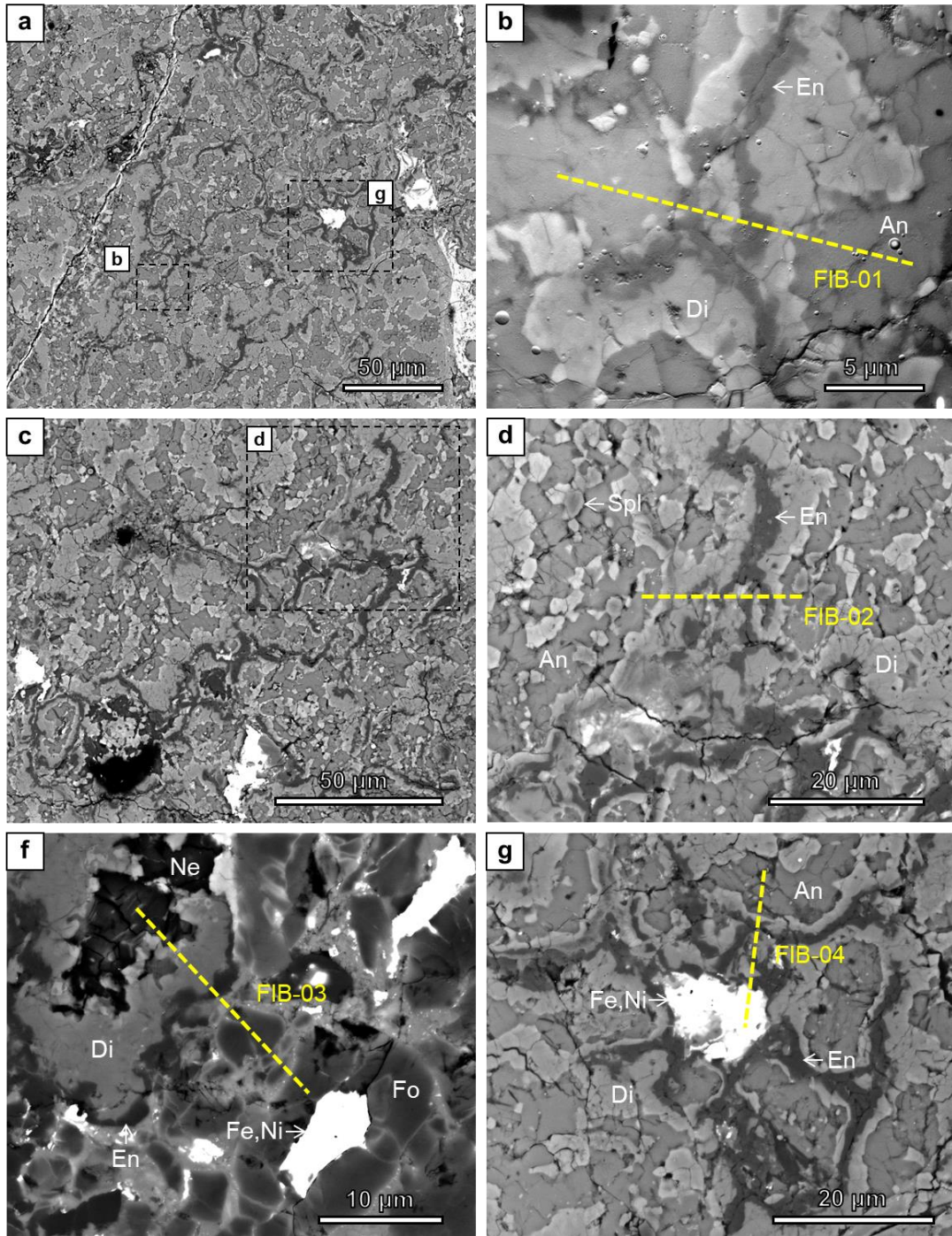


Fig. 4. The positions of FIB sections subtracted from Ef1014-01. FIB-01, -02, and -04 were extracted from the interfaces between two adjacent nodules. The enstatite layers in FIB-02 are separated by some olivine-rich aggregates with fine-grained interstitial phases, whereas in FIB-04, a Fe,Ni-rich metal assemblage occurs between the enstatite layers. FIB-03 is from the boundary between a nodule and the surrounding AOA-like material. Abbreviations: An = anorthite, Di = Al-Ti-bearing diopside, En = enstatite, Fe,Ni = Fe,Ni-rich metal, Fo = forsterite, Ne = nepheline, Spl = spinel.

interface is actually between three nodules, with the third one present below the thin section surface (Fig. 5a). A diopside layer with variable thickness (<0.1 to 2 μm) is always present between the anorthite-rich core and the enstatite layer. The interfaces between anorthite and diopside, and enstatite are curved and irregular. There are some places where the boundary between diopside and enstatite is sharp and often tooth-shaped (Fig. 6a); however, in other places, a clear boundary is not easy to recognize (Fig. 6b, c). Both the diopside and enstatite layers are composed of aggregates of subhedral grains that are usually 0.5-1 μm in size, and commonly show evidence of planar defects, with enstatite exhibiting a higher abundance of defects than diopside (Fig. 6d). Where individual diopside and enstatite grains are in contact, the planar defects in the two phases are subparallel to one another. Electron diffraction patterns from adjacent diopside and enstatite grains (Fig. 6e) show that: (1) enstatite is dominantly the clinoenstatite polymorph (CLEN) with weak streaking along the a^* direction, indicating that the planar defects are parallel to (100); and (2) enstatite and diopside have a crystallographic orientation relationship, with $[0\bar{2}1]_{\text{En}} // [\bar{1}\bar{1}1]_{\text{Di}}$ and $(100)_{\text{En}}$ subparallel to $(\bar{1}10)_{\text{Di}}$. The planar defects are likely to be stacking faults, but it was not possible to tilt these particular grains into the optimum crystallographic orientation to confirm that this is the case using HRTEM imaging.

The FIB section FIB-02 also samples the interface between two nodules with enstatite layers. In addition to diopside in between the enstatite layers, some AOA-like materials are also present. The STEM mosaic image of the FIB section reveals a complex relationship between enstatite and diopside (Fig. 5b). Similar to FIB-01, the interfaces between enstatite

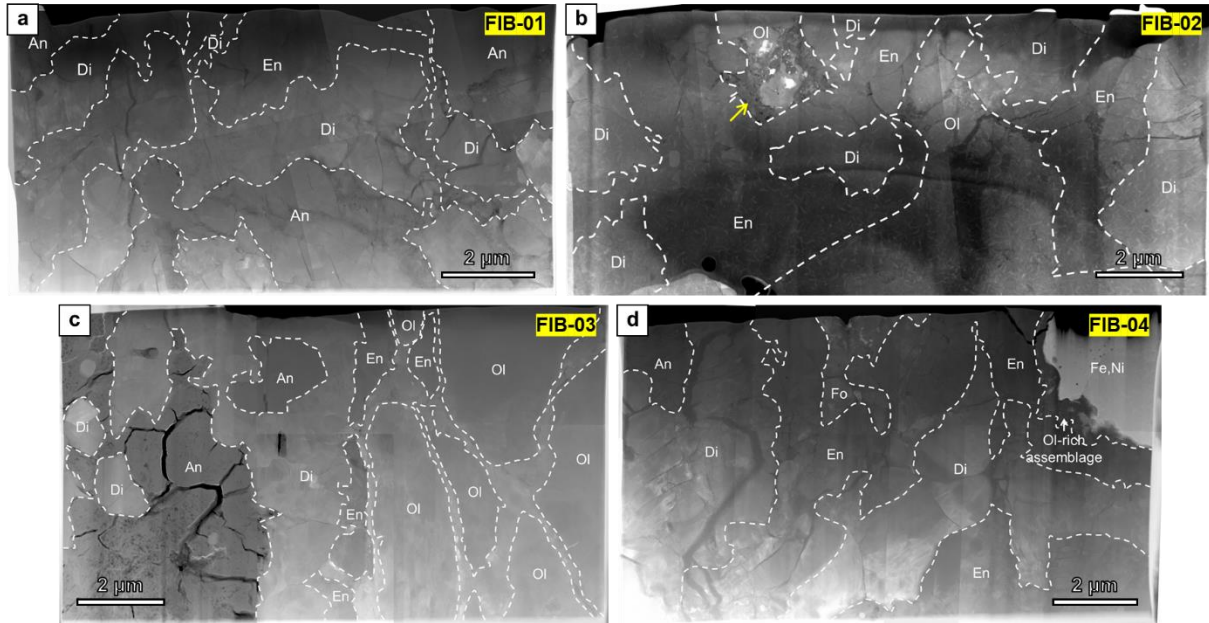


Fig. 5. Dark-field STEM mosaics of the four FIB sections extracted from Ef1014-01. The white dashed lines in the images outline the interfaces between different phases. (a) In FIB-01, a third nodule below the sample surface is revealed by the FIB section. The thickness of the enstatite layer varies significantly. (b) FIB-02 is from the interface between two adjacent nodules. Forsterite-rich assemblages (marked by the yellow arrow) occur between enstatite layers. (c) FIB-03 was extracted from the interface between a nodule and the outside AOA-like material showing the complex relationship between enstatite and other phases. Enstatite forms a thin, discontinuous layer separating the nodule from the olivine-rich assemblage. The AOA-like material is mainly composed of coarse-grained, Fe-rich olivine, which has been significantly affected by secondary alteration. (d) FIB-04 is from the boundary between a nodule and a Fe,Ni metal grain. Enstatite forms an irregular-shaped layer, separating the nodule from the metal grain. A thin layer of an olivine-rich assemblage occurs between enstatite and the metal grain. Abbreviations: An = anorthite, Di = Al-Ti-bearing diopside, En = enstatite, Fe,Ni = Fe,Ni metal, Fo = forsterite, Ol = olivine.

and diopside are curved and irregular (Fig. 7a). Pigeonite exsolution lamellae (based on EDS analysis) are sometimes observed in diopside (Fig. 7a), but they are absent in other grains. The AOA-like material is present in between enstatite layers in the upper left of the FIB section. This material is composed of Fe-rich olivine (up to 1 μm ; $\sim\text{Fa}_{19.5}$), Cr-bearing, hercynitic spinel ($\sim 10\text{ nm}$; $\sim 7.7\text{ wt}\%$ Cr_2O_3), sulfides (pyrrhotite and pentlandite, with grain sizes ranging from

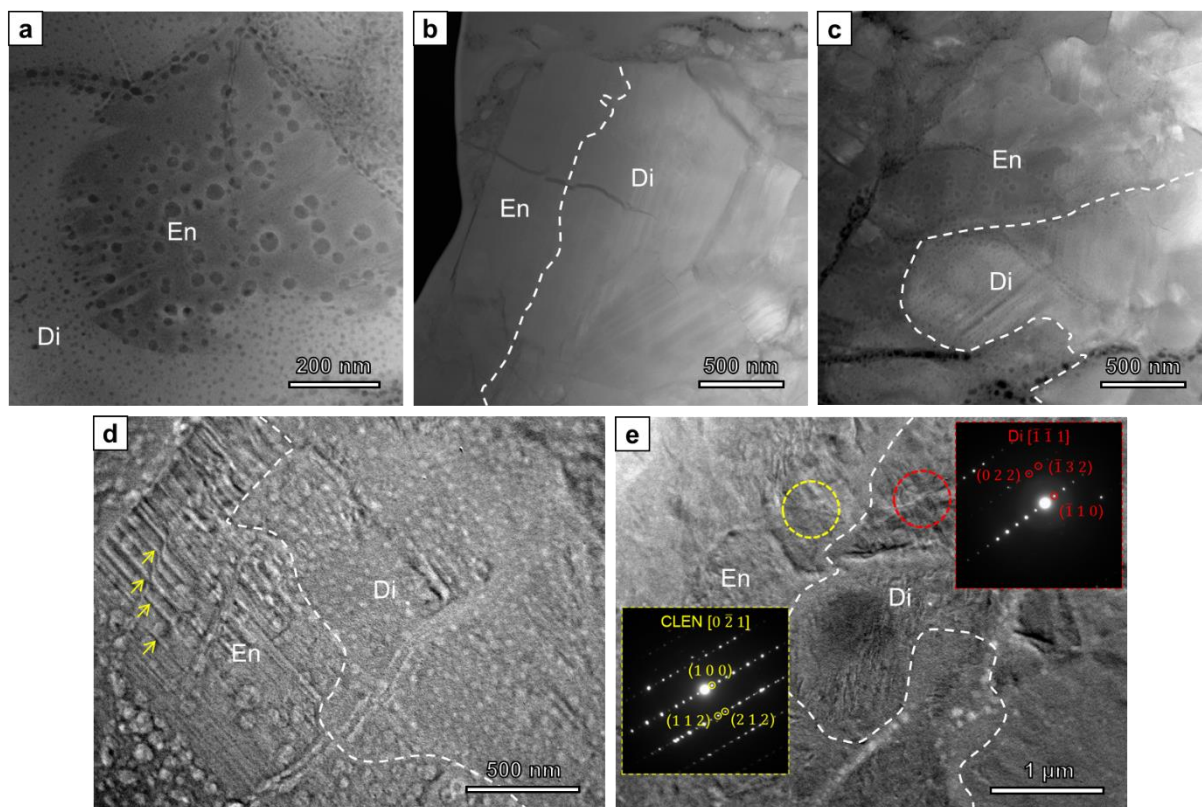


Fig. 6. Dark-field STEM (a-c) and BF-TEM images (d-e) showing the interfaces between enstatite and diopside in FIB-01. An interface can be easily recognized in some places, and it sometimes shows a tooth-shaped outline (a). In other places, however, a clear boundary is difficult to identify. (d) Enstatite sometimes contains planar defects that are the result of stacking disorder (indicated by yellow arrows), whose abundance varies significantly even in individual grains. The enstatite layer is clearly composed of polycrystalline grains with variable orientations (c). (e) Selected area electron diffraction patterns of adjacent enstatite (indexed as CLEN) and diopside grains show a crystallographic orientation relationship between the two phases. The exact crystallographic relation is, however, difficult to interpret because the FIB section does not sample a good zone axis of enstatite. The bubbles in (a), (c), and (d) are artifacts caused by redeposition during the FIB preparation. Abbreviations: CLEN = clinoenstatite, Di = Al-Ti-bearing diopside, En = enstatite.

a few nanometers up to 100 nm), minor Ca-phosphates (~50 nm), and an interstitial Al-rich material (Fig. 7b). Olivine grains are irregular in shape and have embayed outlines when they are in contact with the Al-rich silicate material. Abundant fine-grained olivines (<30 nm) are enclosed in the Al-rich silicate material, and appear to be fragments from the large olivine

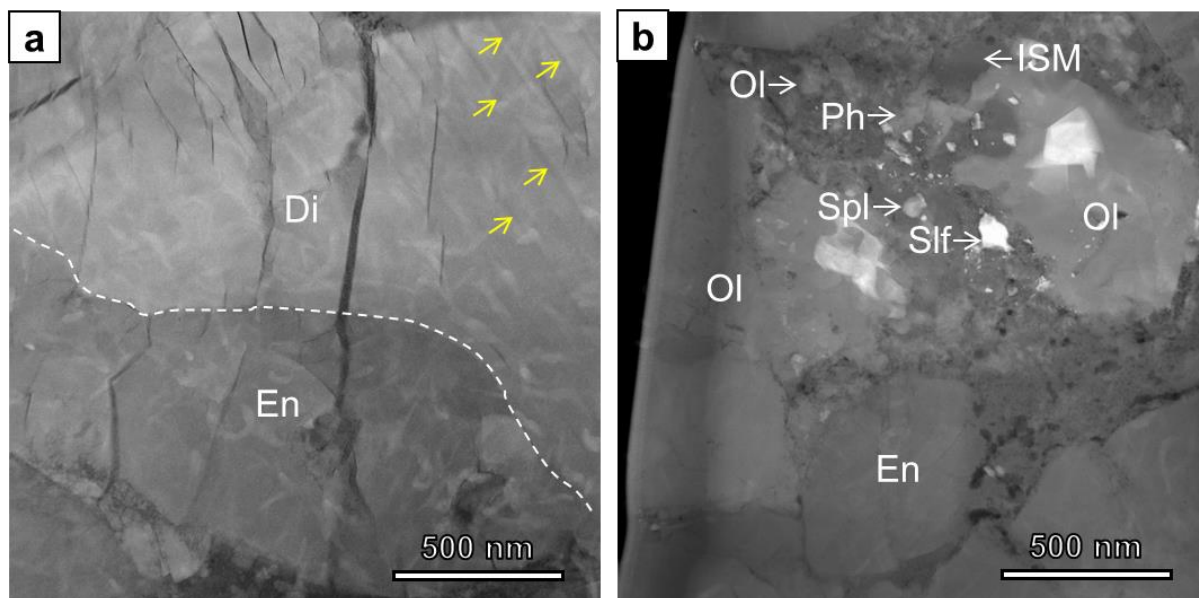


Fig. 7. Dark-field STEM images of the mineralogy and textural characteristics of FIB-02. (a) The interfaces between enstatite and diopside are often curved and irregular. Some diopside grains show thin exsolution lamellae of pigeonite (indicated by yellow arrows), which are parallel to (001) planes of diopside. (b) The AOA-like material is composed of Fe-rich olivine, Cr-bearing, hercynitic spinel, sulfides, minor Ca-phosphates, and an interstitial Al-rich silicate material. Abbreviations: Di = Al-Ti-bearing diopside, En = enstatite, ISM = interstitial Al-rich silicate, Ol = olivine, Ph = phosphates, Slf = sulfides, Spl = spinel.

grains. Enstatite grains adjacent to this Al-rich silicate material are surrounded by fine-grained, porous aggregates of enstatite (~50-150 nm).

The FIB section FIB-03 cuts across the interface between a nodule and AOA-like material that contains several rounded olivine grains. The STEM mosaic image shows that the enstatite layer is discontinuous, and the AOA-like material protrudes into the diopside layer of the nodule (Fig. 5c). The enstatite and diopside layers are composed of subhedral-to-anhedral grains (up to 0.5 μm), and their interfaces are curved (Fig. 8a). Enstatite has microstructures that are the same as observed in FIB-01, e.g., some enstatite grains show streaking in their

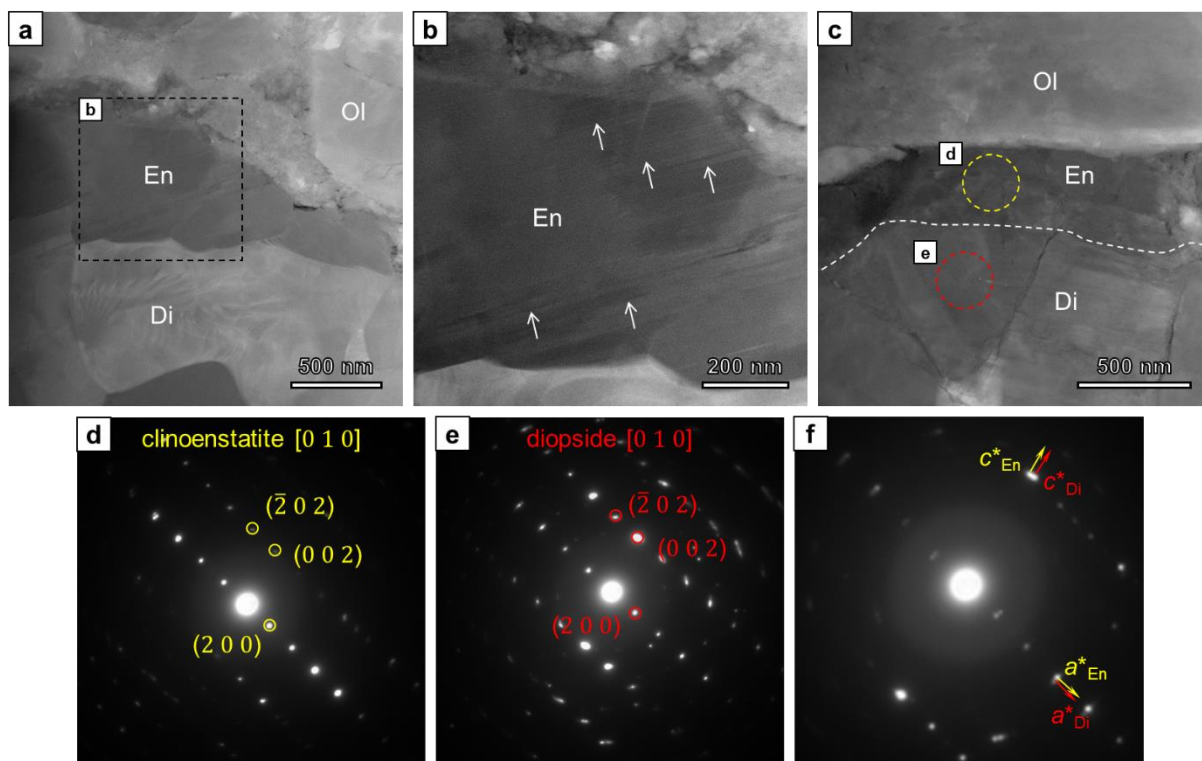


Fig. 8. Dark-field STEM images (a-c) of the enstatite layer in FIB-03, and its relationship with other adjacent phases. The enstatite layer is an aggregate of subhedral-to-anhedral grains which sometimes show planar defects parallel to (100) planes (white arrows) (b). Planar defects are, however, rare or absent in most of the grains. Selected area electron diffraction patterns of a defect-free enstatite (d) and adjacent diopside (e) showing an orientation relationship with $[010]_{\text{En}} // [010]_{\text{Di}}$, $a^*_{\text{En}} // a^*_{\text{Di}}$, and $c^*_{\text{En}} // c^*_{\text{Di}}$. (f) An electron diffraction pattern that samples both enstatite and diopside in (c) shows that their a^* and c^* axes are subparallel. Abbreviations: Di = Al-Ti-bearing diopside, En = enstatite, Ol = olivine.

electron diffraction patterns (Fig. 8b), indicating the presence of planar defects. Selected area electron diffraction patterns (Fig. 8d-f) from adjacent enstatite and diopside grains (Fig. 8c) show that: (1) enstatite is the CLEN polymorph; (2) enstatite and diopside have a crystallographic orientation relationship, with $[010]_{\text{En}} // [010]_{\text{Di}}$, $a^*_{\text{En}} // a^*_{\text{Di}}$, and $c^*_{\text{En}} // c^*_{\text{Di}}$; (3) an electron diffraction pattern from the interface between enstatite and diopside shows that the angles between their a and c crystallographic axes are $\sim 1.8^\circ$ and $\sim 1.2^\circ$, respectively. The

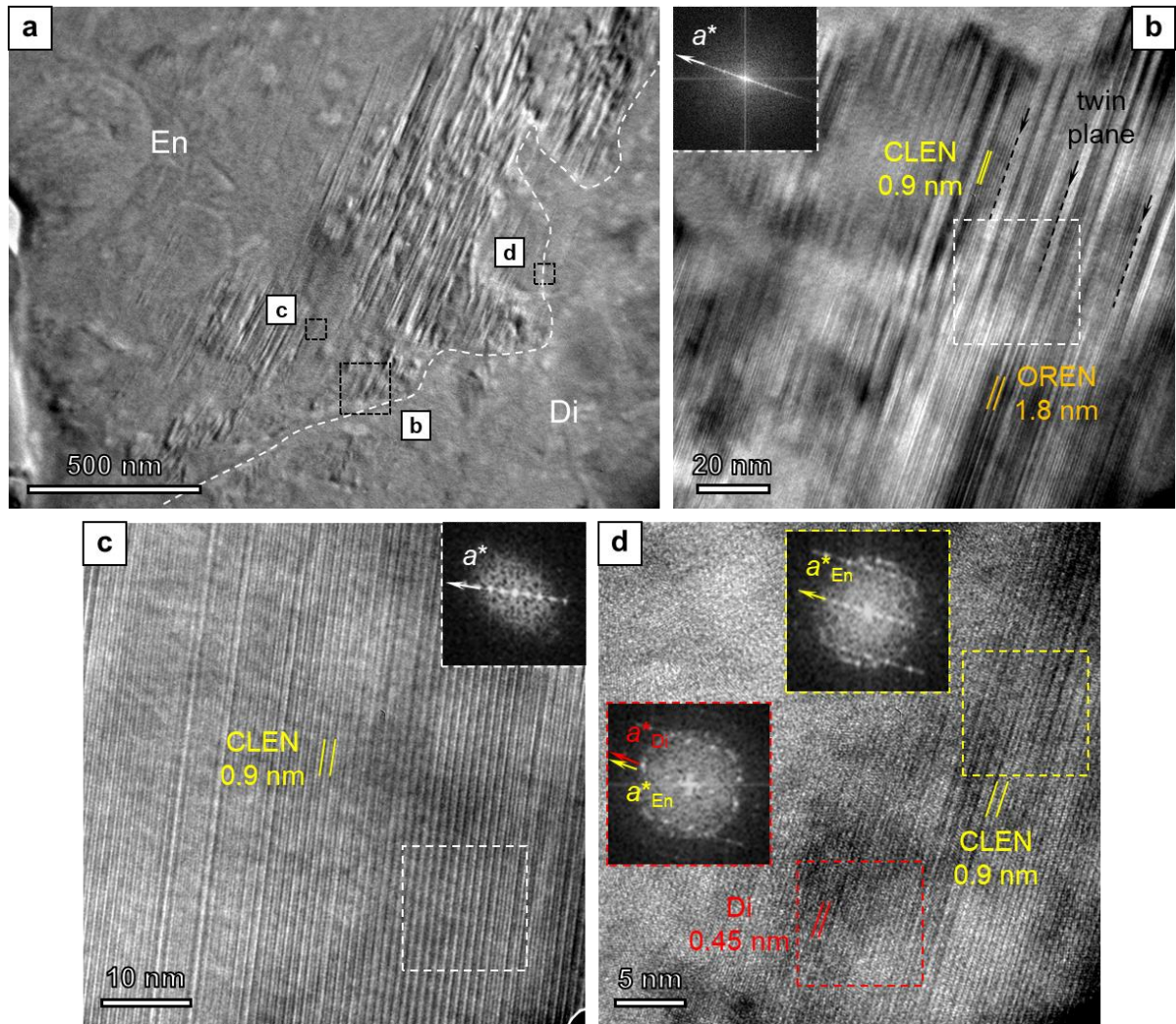


Fig. 9. Bright-field TEM image (a) and HRTEM images (b-e) of adjacent enstatite and diopside grains from the upper right region of FIB-04. (a) Enstatite shows heterogeneously distributed stacking faults parallel to (100) planes. Most of the grains contain only a few stacking faults. Some enstatite grains (dominantly CLEN; yellow double lines) show abundant twinning (black dashed lines and arrows) (b), while others show less twinning (c). FFT patterns obtained from HRTEM images from regions (white boxes) in (b) and (c) show different degrees of streaking along the a^* axis. Rare OREN lamellae (orange double lines in (b)) are also present. (d) The lattice fringes of adjacent enstatite and diopside grains are coherent, and their a^* axes are subparallel as shown in the FFT patterns. Abbreviations: CLEN = clinoenstatite, En = enstatite, Di = diopside, OREN = orthoenstatite.

AOA-like material is composed of coarse-grained forsteritic olivine (up to 3 μm ; $\sim\text{Fa}_9$) that has been altered along grain boundaries and veins to fine-grained, Fe-rich olivine (~ 100 nm;

~Fa₃₁) and Cr-bearing, hercynitic spinel (~1.9 wt% Cr₂O₃). Some fine-grained forsteritic olivine grains with irregular shapes are found interstitially to larger olivine grains, and they have similar fayalitic contents. Enstatite also has been affected by the alteration process, resulting in fragmentation of large enstatite grains, replacement by fine-grained, Fe-rich olivine, and formation of hercynitic spinel. Veins (~150 nm thick) containing elongate, Fe-rich olivine grains (10-60 nm) and Cr-rich, hercynitic spinel (~100 nm; ~30.5 wt% Cr₂O₃) are ubiquitous in coarse-grained, forsteritic olivine.

The last FIB section FIB-04 samples the interface between an enstatite-bearing nodule and a coarse-grained Fe,Ni metal phase (10 µm in size) (Fig. 5d). The Fe,Ni metal phase is an intergrowth of kamacite and taenite, based on electron diffraction patterns and EDS analyses. In BSE images, a thin layer (<1 µm) with low-Z contrast is present between the enstatite layer and the metal grain (Fig. 4h), which TEM observations show is composed of fine-grained, forsteritic olivine (<200 nm; ~Fa_{10.5}), Cr-rich, hercynitic spinel (50-200 nm; ~30.1 wt% Cr₂O₃), and minor nanometric sulfide grains (~30 nm). In the middle part of the FIB section, an AOA-like material is present between adjacent enstatite-bearing nodules, composed of coarse-grained, forsteritic olivine (500-600 nm; ~Fa₈), fine-grained, sometimes elongate, Fe-rich olivine (10-100 nm; ~Fa₂₉), hercynite (20-30 nm), sulfides (100-200 nm; mainly pentlandite), and some Fe,Ni metal grains (~100 nm). Some enstatite grains that are in contact with the AOA-like material have porous alteration rims. Bright-field and HRTEM images of enstatite show that some grains display a high density of planar defects, while others do not (Fig. 9a). Some grains are dominantly twinned CLEN (twin planes perpendicular to the a^* direction)

with 0.9 nm (100) lattice fringes. High-resolution TEM imaging shows that the planar defects are stacking faults caused by the presence of a minor amount of intergrown orthoenstatite (OREN) with 1.8 nm lattice fringes, which are distributed randomly within CLEN (Fig. 9b). The OREN slabs are commonly a few unit cells wide. The Fast Fourier Transform (FFT) of the HRTEM images shows strong streaking along the a^* direction. On the other hand, other enstatite grains are almost entirely composed of CLEN with some twinning and OREN slabs (1 or 2 unit cells wide) that are randomly distributed in the CLEN grain (Fig. 9c), and the FFT pattern shows only very weak streaking along the a^* axis. In all the enstatite grains, both $n9 \text{ \AA}$ and $(n+1)9 \text{ \AA}$ widths of LCLEN have been observed between OREN slabs. An HRTEM image from enstatite and diopside (Fig. 9d), which are in direct contact with each other, shows that they have parallel (100) lattice fringes. The FFT patterns from enstatite and diopside grains on the HRTEM image (Fig. 9d) demonstrate that their a^* axes are not exactly parallel to each other, but are misoriented by $\sim 2^\circ$.

3.4. Enstatite in fine-grained CAIs from other CV3 chondrites

The presence of enstatite in Ef1014-01 raises an interesting question of whether enstatite is a common phase in FGIs. We carried out a systematic investigation of other CAIs from Efremovka and Leoville CV3 chondrites, and found that many of them contain a thin and discontinuous enstatite layer outside the diopside layer. One example is shown in Fig. 10a from a fluffy Type A CAI in Efremovka. In this CAI, enstatite grains are present as discontinuous layers (less than $1 \mu\text{m}$ thick) or islands that are attached to the outer diopside layer. In some

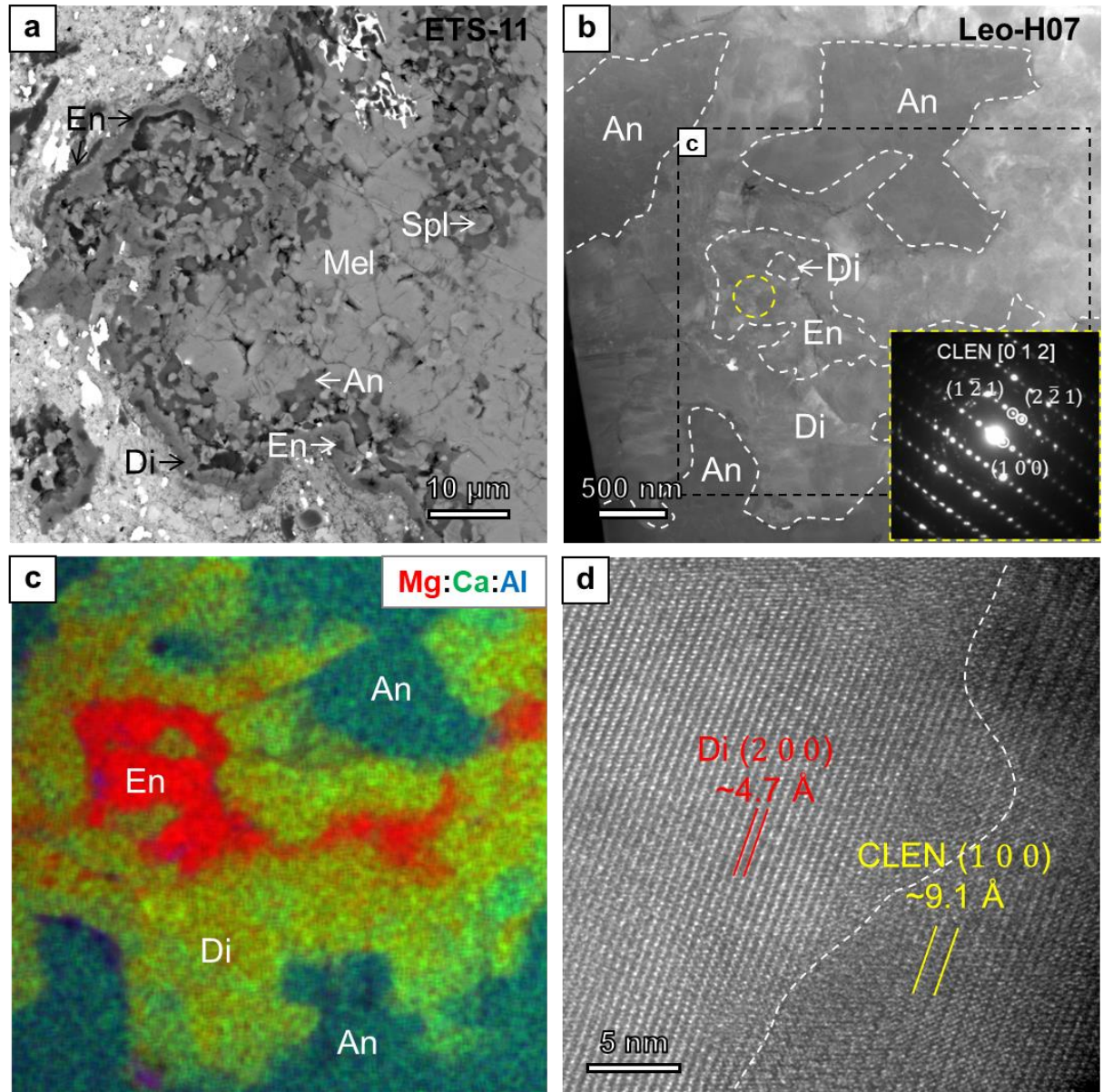


Fig. 10. SEM and TEM images showing occurrences of enstatite in other CAIs from Efremovka and Leoville. (a) BSE image of a fluffy Type A CAI ETS-11 from Efremovka showing that a discontinuous, enstatite layer is present outside the diopside layer. Dark-field STEM image (b) and combined STEM X-ray map (c) of a diopside layer between adjacent nodules in a Leoville FGI Leo-H07 showing that the layer contains a fine-grained, Mg-rich silicate layer. The insert electron diffraction pattern obtained from the yellow circle in (b) can be indexed as the clinoenstatite [012] zone axis. The diopside layer has compositional zoning, with a decreasing Al_2O_3 content towards the CLEN. (d) HRTEM image showing that clinoenstatite has a coherent interface with diopside, with their (100) planes parallel to each other. The white dashed line outlines the rough boundary between diopside and CLEN. Abbreviations: CLEN = clinoenstatite, En = enstatite, Di = diopside, Mel = melilite, Spl = spinel.

other fine-grained CAIs, we did not identify enstatite by SEM, but observed a fine-grained enstatite layer, partly surrounding the outer diopside layers. The TEM observations of a FIB section extracted from an FGI Leo-H07 in Leoville show that a thin enstatite layer occurs between two adjacent spinel-anorthite-diopside nodules (Fig. 10b-c). The HRTEM image of this enstatite layer shows that it is dominated by clinoenstatite, which has the same crystallographic orientation relationship (Fig. 10d) with diopside as observed in Ef1014-01. These observations suggest that enstatite is a more common phase in fine-grained CAIs than previously thought.

4. DISCUSSION

Enstatite has been reported in the matrices of various groups of chondrites (e.g., Müller et al., 1979; Greshake, 1997; Brearley and Jones, 1998; Nuth et al., 2005), in AOAs from carbonaceous chondrites (Krot et al., 2004b, 2005; Nagashima et al., 2015; Komatsu et al., 2018), in interplanetary dust particles (e.g., Bradley et al., 1983; Klöck et al., 1989; Ishii et al., 2008; Joswiak et al., 2009), and in comet return samples (Brownlee et al., 2006; Zolensky et al., 2006; Schmitz and Brenker, 2008). Microstructural studies of some of these enstatite occurrences using TEM techniques have revealed that these grains are mainly composed of disordered intergrowths of CLEN and OREN (e.g., Brearley, 1989, 1993; Greshake, 1997; Schmitz and Brenker, 2008; Ishii et al., 2008). In this study, we have observed the first occurrence of enstatite in FGIs. The TEM observations of microstructures in Ef1014-01 provide several important indicators for the formation mechanism of enstatite in this FGI. The

most important observations are: (1) enstatite in this FGI is dominated by twinned CLEN with minor intergrowths of OREN, and (2) it has a crystallographic orientation relationship with diopside. In the following sections, we first evaluate the possible formation mechanisms of enstatite in Ef1014-01. We then discuss the implications of the estimated cooling rate of enstatite in Ef1014-01 for the formation of this FGI. Finally, we discuss the nebular reservoirs where enstatite-bearing, fine-grained CAIs formed.

4.1. Formation mechanisms of enstatite in Ef1014-01

4.1.1. Microstructural constraints on the precursor polymorph of enstatite in Ef1014-01

The crystal structures and stability fields of five enstatite polymorphs are well-characterized in the literature: (1) protoenstatite (PEN) with space group *Pbcn* is a high-T, low-P polymorph, and it is stable at temperatures $>\sim 1250$ K (the first phase on the liquidus at 1 atm) and unquenchable; (2) high-temperature clinoenstatite (HT-CLEN, *C2/c*) is only stable at very high temperature ($>\sim 1750$ K) and very low pressure and it is also unquenchable; (3) high-pressure clinoenstatite (HP-CLEN, *C/2c*) is stable only at pressures higher than about 6 GPa; (4) low clinoenstatite (LCLEN, *P2₁/c*) is stable at low temperatures and low pressures; (5) orthoenstatite (OREN, *Pbca*) has a stability field at moderate temperatures and pressures. The stability fields of these polymorphs are illustrated in the phase diagram (Fig. 11). There are also other polytypes that form via different periodic stacking sequences of the basic 9 Å repeat units (corresponding to the *asinβ* dimension of CLEN) (Iijima and Buseck, 1975; Buseck and Iijima, 1975).

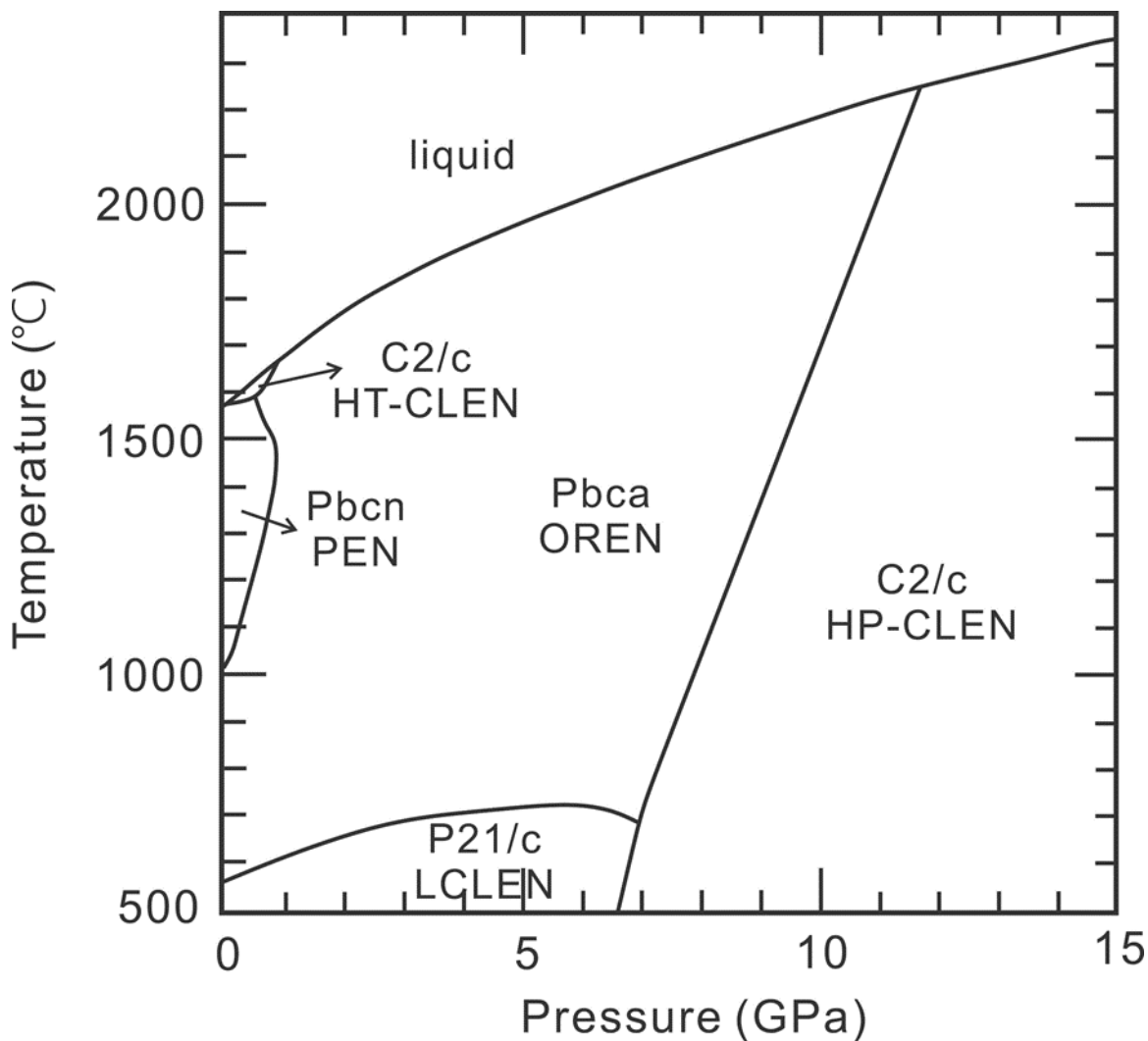


Fig. 11. Phase diagram for MgSiO₃ polymorphs. Five enstatite polymorphs are shown on the diagram, with different P-T stability fields. Based on this diagram, PEN, OREN, and LCLEN are the most likely to be stable phases under nebular conditions. Modified after Raterron et al. (2016).

The LCLEN and OREN polymorphs, as the stable phases at low temperatures and pressures, can be produced by inversion from PEN with rapid and slow cooling rates, respectively (e.g., Smyth, 1974a; Buseck and Iijima, 1975; Brearley and Jones, 1993; Jones and Brearley, 1988). The Si-O chains in PEN are structurally equivalent, and during cooling, these chains change their configurations due to the lattice distortion. The formation of new

stable phases, LCLLEN and OREN, during this transformation occurs randomly at different locations within an individual PEN crystal. The PEN-LCLLEN transformation also results in the formation of polysynthetic twinning. Clinoenstatite with both odd and even multiples of the (100) lattice spacing [$n9 \text{ \AA}$ and $(n+1)9 \text{ \AA}$] should be present intergrown with lamellae of OREN. In addition, the inversion of PEN during cooling can produce isolated faults that are 4.5 \AA in width, as demonstrated by experimental work on synthetic enstatite (Iijima and Buseck, 1975; Wang et al., 1993).

At least three other transformation mechanisms have also been proposed for the formation of LCLLEN at low pressures. (1) Inversion from HT-CLEN (e.g., Smith, 1969; Smyth, 1969, 1974b; Livi and Veblen, 1989). This process is similar to the high-to-low pigeonite transition, which involves distortion of Si-O chains. At high temperatures, high-T pyroxene phase with space group $C2/c$ has equivalent Si-O chains; rapid cooling induces a displacive transformation from a C-centered to a primitive unit cell, with the loss of equivalence of Si-O chains. During this transition, antiphase domains (APDs) often form due to the loss of a translational symmetry element during the $C \Rightarrow P$ transformation (e.g., Morimoto and Tokonami, 1969; Livi and Veblen, 1989; Bozhilov et al., 1999). (2) Transformation from OREN through shearing (e.g., Turner et al., 1960; Pollack and Ruble, 1964; Buseck and Iijima, 1975; Coe and Kirby 1975). Shearing transformation from OREN is a martensitic transformation, and each unit cell of OREN with an a lattice parameter of 18 \AA transforms to 2 unit cells of LCLLEN with a 9 \AA unit cell dimension in the a direction. The shear transformation therefore always results in LCLLEN lamellae that are even multiples of the (100) lattice spacing. The observed LCLLEN

lamellae in OREN from meteorite samples that experienced shock metamorphism have been explained by such a shear-induced mechanism (e.g., McCoy et al., 1995). (3) Crystallization from amorphous silicate dust below ~ 1063 K (e.g., Murata et al., 2009).

The enstatite in Ef1014-01 is dominantly twinned LCLEN. It only contains a minor amount of OREN that is usually present as randomly distributed thin lamellae, giving rise to stacking faults within some enstatite grains. Between the OREN slabs, both $n9 \text{ \AA}$ and $(n+1)9 \text{ \AA}$ widths of LCLEN are observed. Based on the distinguishing microstructural features of different transformation mechanisms described above, the most likely precursor polymorph for enstatite in Ef1014-01 is PEN. We can rule out HT-CLEN as the precursor, because the absence of APDs is inconsistent with a $C \Rightarrow P$ transition process. The stability field of HT-CLEN is not well constrained and only a few experiments have been conducted, which show that HT-CLEN has a stability field at 1 atm (e.g., Cameron and Papike, 1981; Feuer et al., 1989; Gasparik, 1990). HT-CLEN has never been reported in chondritic materials, indicating that it may not be stable at solar nebular pressures. Orthoenstatite cannot be the precursor because the OREN-LCLEN transformation would have only produced $n9 \text{ \AA}$ widths of LCLEN.

There are five possible processes that could have produced the PEN precursor in Ef1014-01: (1) crystallization from a pyroxene-normative melt, (2) equilibrium condensation by reaction of forsterite with the nebular gas, (3) direct condensation from the nebular gas, (4) reheating, and (5) crystallization from amorphous silicate dust. The difference between equilibrium and direct condensation is that all the reactants in the latter mechanism are gaseous species. Below we evaluate each of them using the chemical compositions and textural

observations of Ef1014-01.

4.1.2. Crystallization from a pyroxene-normative melt

Enstatite with an ^{16}O -poor composition has been reported in AOAs from CR and CM chondrites (Krot et al., 2005). These pyroxene grains are present as shells on the periphery of AOAs with compact textures, and they contain abundant Fe,Ni metal inclusions. These authors suggested that melting of a pyroxene-normative dust, condensed on the surface of AOAs, has produced the enstatite by crystallization from the melt. One of the major lines of evidence for an igneous origin is the elevated concentrations of relatively refractory elements (e.g., CaO, Al_2O_3 , and TiO_2). Enstatite in Ef1014-01 contains 1.52 wt% CaO on average, and many grains contain elevated Al_2O_3 (up to 2.14 wt%) and FeO contents (up to Fs3.1). This may point to an igneous origin, where enstatite crystallized from a melt of a pyroxene-normative dust, which accreted onto the surface of FGIs. The CLEN-dominant microstructure may then have developed during rapid cooling that followed crystallization. However, Ef1014-01 does not show any textural evidence for melting or annealing, distinct from AOAs that have a compact and equilibrated texture (Krot et al., 2004b). The elevated CaO and Al_2O_3 contents could be attributed to disequilibrium condensation, rather than crystallization from a melt. For example, the formation of diopside with increasing Al_2O_3 and TiO_2 contents towards melilite and spinel in FGIs may have formed via reactions of spinel and melilite with a partially condensed, Ti-saturated gas (Han and Brearley, 2016). It is thus likely that during disequilibrium condensation, the nebular gas may still contain a significant amount of refractory species (e.g., Ca and Al),

which were incorporated into enstatite. Therefore, we suggest that an igneous origin is a less likely formation mechanism for the PEN precursor in Ef1014-01.

4.1.3. Formation by equilibrium condensation

Equilibrium condensation calculations predict that enstatite could have condensed from a gas of solar composition via a reaction between forsterite and gaseous SiO (e.g., Yoneda and Grossman, 1995; Ebel and Grossman, 2000; Krot et al., 2004b). Indeed, enstatite has been reported in AOAs from many carbonaceous chondrites (Krot et al., 2004b, 2005; Nagashima et al., 2015), and many of these pyroxene grains are intimately associated with forsterite in the outer portions of the AOAs. The enstatite and forsterite from the AOAs commonly show similar enrichments in ^{16}O isotopes, which serves as a further line of evidence for the predicted condensation reaction. This condensation reaction has also been verified by experimental work (Imae et al., 1993; Nagahara et al., 2008).

The condensation temperatures of enstatite, at solar nebular pressures of 10^{-3} - 10^{-5} bar, are in the range of 1250 K and 1450 K (e.g., Yoneda and Grossman, 1995; Petaev and Wood, 1998; Ebel and Grossman, 2000). These temperatures are within the stability field of PEN at low pressures (e.g., ~ 1250 K to ~ 1800 K at 1 atm; Raterron et al., 2016). It is therefore very likely that the enstatite polymorph that condensed via the forsterite-SiO gas reaction was PEN, which then underwent PEN-(LCLLEN/OREN) transition to form low-T enstatite polymorphs. Experimental work on the forsterite-SiO gas reaction shows that fine-grained enstatite can be produced over the cooling time scale of the solar nebula (on the order of 10^3 yrs) (Imae et al.,

1993), which refers to the duration of the nebular thermal structure reaching a steady state (Watanabe and Nakagawa, 1988). This short time scale is consistent with the recent high-precision $^{26}\text{Al}/^{26}\text{Mg}$ measurements of FGIs in CO3 chondrites, which indicate a formation time scale of <50,000 yrs for FGIs with sizes of several tens of micrometers (Liu et al., 2019). Nonetheless, the forsterite grain size required to produce enstatite during cooling of the solar nebula has to be submicron-scale, which is much smaller than the typical sizes of forsterite in FGIs and AOAs. Kinetic calculations of cation interdiffusion also show that, at 1350 K, a timescale of $\sim 10^6$ yrs is required to convert grains of forsterite with sizes of 0.1 μm to enstatite (Gail, 2004). These studies demonstrate the difficulty in producing enstatite in FGIs via equilibrium condensation. The presence of a replacement relationship between enstatite and forsterite in many AOAs (e.g., Krot et al., 2004b, 2005) could have resulted from significant annealing of AOAs (Han and Brearley, 2015) that facilitated equilibrium condensation of enstatite. However, such annealing effects have not been observed in Ef1014-01. In addition, the absence of forsterite between the enstatite and diopside layers, even on the TEM scale, argues against condensation of forsterite prior to enstatite, unless the precursor olivine grain size was much smaller than 0.1 μm , which caused them to react much more quickly with gaseous SiO, due to their high surface to volume ratio.

4.1.4. Formation by direct condensation

Formation of enstatite in Ef1014-01 by the condensation reaction between forsterite and SiO gas has several problems, as discussed above. Further evidence against an equilibrium

condensation origin comes from the epitaxial growth relationship between enstatite and diopside in Ef1014-01. Forsterite forms via direct condensation from the nebular gas and it has a very different crystal structure from pyroxene. It is thus difficult to envisage that enstatite formed by replacing forsterite would have an epitaxial relationship with diopside. The orientation relationship between enstatite and diopside could be better explained by direct epitaxial nucleation of enstatite on diopside. In this process, enstatite may have formed by direct condensation from the gas. The structural similarities of enstatite and diopside, both monoclinic, single-chain silicates, make nucleation of condensing enstatite on a diopside substrate kinetically more favorable than the formation of olivine with isolated [SiO₄] tetrahedra (Fig. 12). This kinetic control is similar to the mechanism proposed by Han et al. (2015) to explain the absence of melilite in hibonite-spinel inclusions in the ALHA77307 CO3.0 chondrite: the epitaxial growth of spinel on hibonite may have lowered the nucleation energy of spinel compared with that of melilite. The presence of discontinuous enstatite layers and enstatite islands on some fine-grained CAIs in this study provides further insights into how the nucleation energy of enstatite was further lowered. Since the modes of epitaxial growth (layer-by-layer or island growth) depend on the surface energies of substrate and film, and the interface energy (e.g., Volmer and Weber, 1926; Stranski and Krastanov, 1938; Frank and van der Merve, 1949; Eaglesham and Cerullo, 1990), the commonly observed discontinuous enstatite layer and enstatite islands suggest that the surface energy of diopside is equal to or slightly smaller than the sum of the surface energy of enstatite and the interfacial energy. The discontinuous and island-like layers of enstatite are therefore the result of minimization of

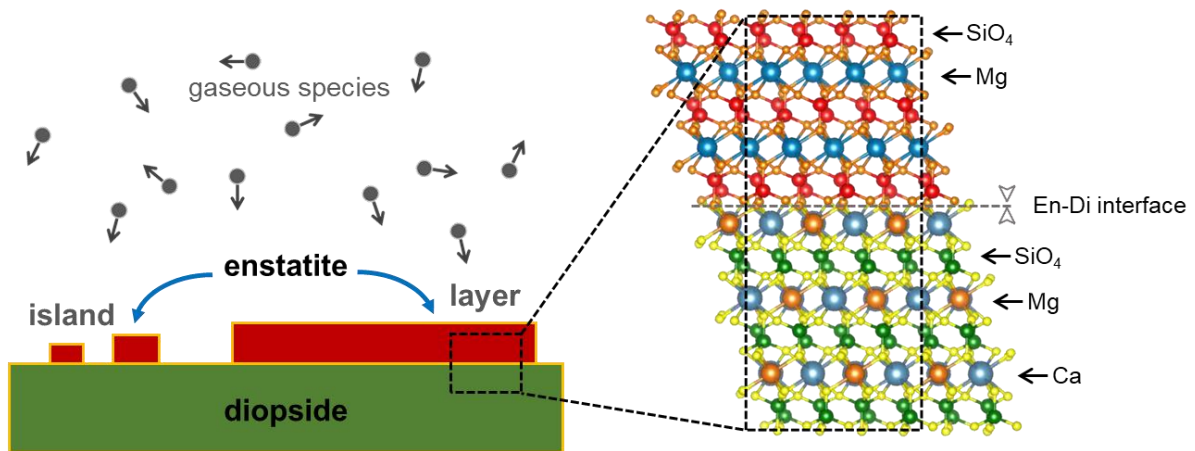


Fig. 12. A schematic cartoon illustrating the direct condensation process of enstatite on diopside. The direct condensed phase should be PEN; however, the LCLLEN structure is used here to better illustrate the epitaxial growth relationship. The similar chain structures of enstatite and diopside may have facilitated the condensation of enstatite via lowering the free energy of nucleation. It is likely that enstatite nucleated on the diopside substrate initially as islands as a result of minimization of nucleation energy and then developed into layers. The crystal structure model is drawn using the VESTA software (Momma and Izumi, 2011).

nucleation energy. Bolser et al. (2016) proposed a similar three-dimensional island growth model for the formation of Wark-Lovering rims.

The enstatite polymorph that formed by direct condensation in the solar nebula should be PEN, based on the observed microstructures and the predicted condensation temperatures of enstatite in the solar nebula (e.g., Yoneda and Grossman, 1995; Petaev and Wood, 1998; Ebel and Grossman, 2000). Although a direct condensation mechanism of metastable CLEN in the stability field of PEN was proposed for some enstatite whiskers and platelets in interplanetary dust particles (IDPs) (Bradley et al., 1983; Klöck et al., 1989; Greshake, 1997; Scott and Krot,

2005), there are notable differences between enstatite in Ef1014-01 and that from IDPs. First, axial screw dislocations that were observed in IDPs are absent in Ef1014-01 enstatite. Second, enstatite in IDPs does not show twinning. Finally, enstatite in IDPs commonly contains a high MnO content (usually >1 wt%) (e.g., Klöck et al., 1989), while enstatite in Ef1014-01 only contains a trace amount of MnO (up to 0.1 wt%). Enstatite in IDPs occurs as isolated crystals without any associated minerals, quite distinct from the occurrence of enstatite in Ef1014-01. Therefore, we can infer that enstatite grains in Ef1014-01 and IDPs had different formation mechanisms and different precursor materials.

The crystallographic orientation relationship between enstatite and diopside may have also affected the polymorph (LCLLEN or OREN) that formed preferentially during the PEN inversion. The crystal structures of LCLLEN and diopside are more similar (e.g., both are monoclinic, and they have similar lattice parameters (LCLLEN: a 9.62 Å, b 8.83 Å, c 5.19 Å, and β 71.67° (Morimoto et al., 1960); diopside: a 9.75 Å, b 8.90 Å, c 5.25 Å, and β 105.63° (Cameron et al., 1973) compared with OREN. In this case, the enstatite-diopside epitaxial growth relationship may have favored the formation of LCLLEN during the PEN inversion.

4.1.5. Formation by reheating

The PEN precursor for enstatite in Ef1014-01 could alternatively be the result of a reheating event that occurred after the primary condensation process. The reheating must have occurred in a high-temperature nebular environment, since the transformation from LCLLEN and OREN to PEN requires temperatures above 1250 and 1275 K at 1 atm, respectively (Smyth,

1974a). The LCLLEN-to-PEN transition is a temperature-controlled and time-invariant process, while the OREN-to-PEN transition is time-dependent (up to several days; Smyth, 1974a). Therefore, the latter transition is kinetically more sluggish than the former and consequently requires more prolonged reheating in the solar nebula.

Previous studies have shown that CAIs have been thermally processed multiple times in the early stage of the solar nebula. For example, recent Al-Mg isotopic studies of FGIs from pristine CO3 and CV3 chondrites showed that a significant variation in the initial $^{26}\text{Al}/^{27}\text{Al}$ ratio, $(^{26}\text{Al}/^{27}\text{Al})_0$, is present in these CAIs, which may imply multiple thermal events over an extended time period (e.g., MacPherson et al., 2010; Kawasaki et al., 2019; Liu et al., 2019; Simon et al., 2019; Wada et al., 2019; Han et al., 2020). These thermal events could have occurred during a FU Orionis outburst. In this case, CAIs could have traversed radially both inward and outward in less than 200 years, and have been exposed to temperatures from ~ 60 K to ~ 1550 K (e.g., Boss et al., 2012). Reheating could also be caused by vertical transportation in the protoplanetary disk (Aléon, 2016). In this model, CAIs are transported by turbulence or disk winds during outward transport in the viscously expanding protoplanetary disk. Those CAIs that reach the optically thin surface of the protoplanetary disk may have been exposed to protosolar and interstellar radiations, resulting in reheating to the CAI solidus. The above two transportation models that may be responsible for reheating are illustrated in Fig. 13.

4.1.6. Crystallization from amorphous silicate dust material

Enstatite may also form via crystallization from circumstellar amorphous silicate dust

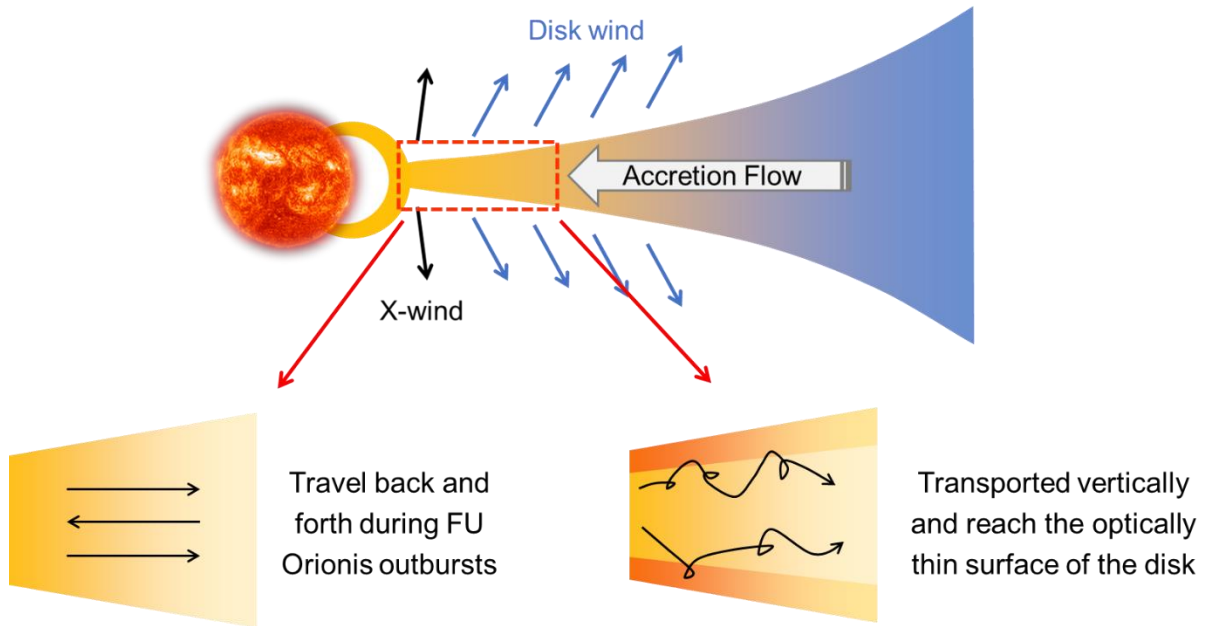


Fig. 13. A carton figure illustrating possible transportation processes in the protoplanetary disk that could have caused reheating of Ef1014-01. This FGI could have traversed radially (both inward and outward) and vertically in a short time period, and have been exposed to high-temperature thermal processing.

(e.g., Rietmeijer, 1986; Brearley, 1989, 1993; Nuth et al., 2005; Murata et al., 2009; Matsuno et al., 2012). Most annealing experiments using synthetic amorphous Mg-Si-O silicate smokes reveal that enstatite could be produced by a reaction between metastable forsterite and tridymite during a prolonged annealing process (e.g., 4 hrs at 1000K, Rietmeijer, 1986).

Disequilibrium condensation is likely to have occurred during the formation of refractory inclusions, as argued by Han and Brearley (2016), who investigated the reaction textures of a CAI-bearing AOA from the ALHA77307 CO3.0 chondrite. However, the formation conditions for amorphous smokes and CAIs are very different in that the former requires a rapidly supercooled gas that would prevent the nucleation and growth of crystalline materials (e.g.,

Rietmeijer et al., 1986; Rietmeijer and Nuth, 1991; Brearley, 1993). The microstructures and compositions of enstatite in Ef1014-01 also argue against formation from amorphous silicate dust. Firstly, forsterite grains that are commonly observed to coexist with enstatite in chondrite matrices are absent in Ef1014-01, though pre-existing forsterite may have been completely consumed. Secondly, a long period of annealing is required to crystallize enstatite from amorphous silicates. The predominance of twinned LCLLEN in the enstatite grains from Ef1014-01 is consistent with a rapid cooling history, as will be discussed in Section 4.2. Thirdly, 120° triple grain boundary junctions indicative of annealing are not observed in the CAI. Fourthly, the observed enstatite-diopside orientation relationship cannot be explained by such a mechanism which should have produced randomly orientated grains due to heterogeneous nucleation of forsterite grains. Finally, enstatite in Ef1014-01 contains only a trace amount of MnO (<0.1 wt%), while enstatite with a crystallization origin in the matrix of ALNH77307 CO3 chondrite, for example, contains up to 2 wt% MnO (e.g., Kornacki and Wood, 1984; Brearley, 1993). We therefore exclude crystallization from amorphous silicate dust as the formation mechanism for the enstatite in Ef1014-01.

4.2. Implications of the cooling rate of enstatite in Ef1014-01

Enstatite in Ef1014-01 is almost pure LCLLEN with only a minor amount of OREN (most grains contain <5 vol% OREN). The experimental data on cooling rates of enstatite formed by inversion from PEN (Brearley and Jones, 1988, 1993; Jones and Brearley, 1988) predict that the cooling rate for the Ef1014-01 enstatite should be $\sim 10^4$ K/h. The cooling rates of fine-

grained CAIs have not been estimated previously, but cooling rates of some other refractory inclusions can be used as a reference. Cooling rates of 0.5 to 50 K/h have been inferred for Type B CAIs (e.g., Stolper, 1982; MacPherson et al., 1984; Beckett et al., 1990; Davis et al., 1992; Richter et al., 2006). For AOAs, cooling rates can be deduced using the compositions and grain sizes of forsterite, as well as grain sizes of Fe,Ni metal: the estimated values are from 0.002 K/h up to 100 K/h (e.g., Petaev and Wood, 2005; Sugiura et al., 2009). This range of cooling rates partly overlaps the experimental values (~ 0.02 K/h at 10^{-4} bar) for producing enstatite layers around forsterite, via forsterite-gas reactions (Imae et al., 1993). Compared to other types of refractory inclusions, the cooling rate for enstatite in Ef1014-01 is significantly higher and is within the range of chondrule cooling rates (10 - 10^4 K/h) (e.g., Planner and Keil, 1982; Brearley and Jones, 1988; Jones and Brearley, 1988; Weinbruch and Müller, 1995; Lofgren 1996; Hewins et al. 2005).

An important question is whether such a rapid cooling rate is viable during the nebular condensation process. Quantitative constraints on the nebular cooling rates during condensation have been provided by studies of metal grains, which inferred slow cooling rates (e.g., 1-100 K/h in Petaev and Wood (2005); 0.5K/yr in Berg et al. (2009)). The Petaev and Wood (2005) results were obtained from metal grains embedded in AOAs, which may have experienced post-condensation thermal events, such as annealing, thus their relatively high cooling rates represent, at best, an upper limit. On the other hand, metal grains in Berg et al. (2009) are refractory metal nuggets whose components have been suggested to be among the earliest condensed species from the nebular gas (e.g., Palme and Wlotzka, 1976; Blander et al.,

1980). It is possible that the slow cooling rates from their study may be more applicable to the nebular condensation process. Even if we take the high values from Petaev and Wood (2005), they are still orders of magnitude lower than the cooling rates deduced from this study. It is consequently reasonable to consider that the rapid cooling rate may be related to reheating that occurred after the primary condensation process, as discussed in Section 4.1.5. However, the cooling rates during the transport processes that may have caused reheating are not well constrained. It is thus unclear if nebular transport processes are capable of generating rapid cooling rates.

To summarize, the microstructures of enstatite in Ef1014-01 require a high cooling rate. This could be achieved if condensation of FGIs occurred either at much higher cooling rates than other types of refractory inclusions, or at similar cooling rates, but the FGIs experienced a subsequent reheating event, followed by rapid cooling. No experimental work has been conducted to constrain the cooling rates of FGIs. On the other hand, we do not know the exact cooling rates related to transport in the solar nebula. We therefore cannot differentiate between these two thermal histories based on our observations. However, given the complex thermal histories of CAIs in the solar nebula and the importance of transport in producing mineralogically-diverse refractory inclusions, the likelihood of reheating is significant and seems more compatible with the estimated rapid cooling rate than during the primary condensation process.

4.3. The nebular reservoirs of enstatite-bearing, fine-grained CAIs

Some fine-grained CAIs (e.g., FGIs and FTAs) from Leoville and Efremovka contain enstatite, which occurs as outer layers. It is therefore likely that these fine-grained CAIs were formed in the same nebular reservoir as Efl014-01. The SiO partial pressure has a significant effect on the condensation of enstatite (e.g., Ebel and Grossman, 2000). Therefore, one way to directly condense enstatite is to condense from a nebular gas with a non-solar composition: for example, condensation in a fractionated gas with a Mg/Si ratio lower than the solar value (Petaev and Wood, 1998; Ebel et al., 2003; Krot et al., 2004b, 2005). Theoretical calculations suggest that such a fractionated gas could be produced by isolation of forsterite from the condensing gas by either physical removal or coarsening of pre-condensed forsterite (Petaev and Wood, 1998; Ebel et al., 2003; Krot et al., 2004b, 2005). The ubiquitous AOAs with rare occurrences of enstatite in various groups of chondrites (e.g., Krot et al., 2004b,c) may serve as an isolated forsterite reservoir. Alternatively, a fractionated gas could be produced by repeated evaporation-recondensation processes, based on experimental work (Nagahara and Ozawa, 2003). After the condensation of enstatite, CAIs were transported to a different region where the AOA-like material began to condense on the CAI exterior.

There are also many fine-grained CAIs that do not have an enstatite outer layer. For these FGIs, the lack of enstatite may be partly due to the fact that enstatite is too fine-grained to be characterized by SEM. Another, perhaps more probable reason is that the local partial pressure of SiO was not be high enough to stabilize enstatite; instead, forsterite condensed on the diopside layer. For these CAIs, it is reasonable to argue that even though diopside provided

favorable nucleation sites for enstatite, the SiO partial pressure was still too low for enstatite to condense. The presence of two groups of FGIs, one with enstatite and one without, in CV3 chondrites implies at least two different gaseous reservoirs existed in the solar nebula, and these CAIs were later transported to the CV3 chondrite accretion region.

Some nodules in Ef1014-01 do not have enstatite layers; instead, enstatite forms an extended layer surrounding several nodules. This observation suggests that these nodules accreted together rapidly, preventing enstatite from condensing onto the individual nodules. The formation of such “accretionary units” may have facilitated accretion of other nodules and promoted growth into millimeter-sized FGIs (Wurm et al., 2005; Kothe et al., 2010).

5. CONCLUSIONS

In this study, we have documented microstructural observations of the first occurrence of enstatite in FGIs. Enstatite in the FGI Ef1014-01 is dominantly twinned LCLLEN with a minor amount of intergrown, thin OREN lamellae. Enstatite has a crystallographic orientation relationship with the adjacent diopside. We also observed enstatite with similar microstructural features in some other fine-grained CAIs from Leoville and Efremovka. Based on the compositions and textural observations, we suggest that the precursor phase for enstatite in Ef1014-01 is PEN, which formed by either direct condensation or reheating in the solar nebula. The crystallographic orientation relationship between enstatite and diopside suggests that the nucleation of enstatite on diopside was kinetically more favorable than that of forsterite. The high proportion of LCLLEN in enstatite indicates a rapid cooling rate of close to 10^4 K/h, which

may have been achieved during the condensation process or during the physical transport. The formation of enstatite in fine-grained CAIs requires a fractionated gas, which may be produced by isolation of forsterite or by repeated evaporation-recondensation processes.

ACKNOWLEDGEMENTS

This work was funded by NASA Cosmochemistry grants NNX15AD28G to A. J. Brearley (PI). We thank Dr. Elena Dobrică and Dr. Ying-Bing Jiang for their help with the TEM operations, and Mike Spilde for his assistance with the electron microprobe analysis. We are grateful to Dr. Steven Simon for helpful discussions and suggestions. Electron microbeam analysis and FIB section preparation were carried out in the Electron Microbeam Analysis Facility, Department of Earth and Planetary Sciences and Institute of Meteoritics, University of New Mexico. The facility is supported by funds from the State of New Mexico, NSF, and NASA.

REFERENCES

- Aléon J. (2016) Oxygen isotopes in the early protoplanetary disk inferred from pyroxene in a classical type B CAI. *Earth Planet. Sci. Lett.* **440**, 62–70.
- Amelin Y., Krot A. N., Hutcheon I. D. and Ulyanov A. A. (2002) Lead isotopic ages of chondrules and calcium-aluminum-rich inclusions. *Science* **297**, 1678–1683.
- Beckett J. R. and Grossman L. (1988) The origin of type C inclusions from carbonaceous chondrites. *Earth Planet. Sci. Lett.* **89**, 1–14.
- Beckett J. R., Spivack A. J., Hutcheon I. D., Wasserburg G. J. and Stolper E. M. (1990) Crystal

chemical effects on the partitioning of trace elements between mineral and melt: An experimental study of melilite with applications to refractory inclusions from carbonaceous chondrites. *Geochim. Cosmochim. Acta* **54**, 1755–1774.

Beckett J. R. and Stolper E. (1994) The stability of hibonite, melilite and other aluminous phases in silicate melts: Implications for the origin of hibonite-bearing inclusions from carbonaceous chondrites. *Meteoritics* **29**, 41–65.

Berg T., Maul J., Schönhense G., Marosits E., Hoppe P., Ott U. and Palme H. (2009) Direct evidence for condensation in the early solar system and implications for nebular cooling rates. *Astrophys. J.* **702**, 172–176.

Blander M., Fuchs L. H., Horowitz C. and Land R. (1980) Primordial refractory metal particles in the Allende meteorite. *Geochim. Cosmochim. Acta* **44**, 217–223.

Bolser D., Zega T. J., Asaduzzaman A., Bringuier S., Simon S. B., Grossman L., Thompson M. S. and Domanik K. J. (2016) Microstructural analysis of Wark-Lovering rims in the Allende and Axtell CV3 chondrites: Implications for high-temperature nebular processes. *Meteorit. Planet. Sci.* **51**, 743–756.

Boss A. P., Alexander C. M. O'D. and Podolak M. (2012) Cosmochemical consequences of particle trajectories during FU Orionis outbursts by the early Sun. *Earth Planet. Sci. Lett.* **345–348**, 18–26.

Boynton W. V. (1975) Fractionation in the solar nebula: Condensation of yttrium and the rare earth elements. *Geochim. Cosmochim. Acta* **39**, 569–584.

Bozhilov K. N., Green H. W. and Dobrzhinetskaya L. (1999) Clinoenstatite in Alpe Arami peridotite: Additional evidence of very high pressure. *Science* **284**, 128–132.

Bradley J. P., Brownlee D. E. and Veblen D. R. (1983) Pyroxene whiskers and platelets in interplanetary dust: Evidence of vapour phase growth. *Nature* **301**, 473–477.

Brearley A. J. (1993) Matrix and fine-grained rims in the unequilibrated CO3 chondrite, ALHA77307: Origins and evidence for diverse, primitive nebular dust components. *Geochim. Cosmochim. Acta* **57**, 1521–1550.

Brearley A. J. (1989) Nature and origin of matrix in the unique type 3 chondrite, Kakangari. *Geochim. Cosmochim. Acta* **53**, 2395–2411.

Brearley A. J. and Jones R. H. (1988) An experimental study of the ortho/clino transition in

low-Ca pyroxenes and its application to thermal histories of chondritic meteorites. *Eos (Washington, DC)*. **69**, 1506.

Brearley A. J. and Jones R. H. (1993) Chondrite thermal histories from low-Ca pyroxene microstructures: Autometamorphism vs. prograde metamorphism revisited. *Lunar Planet. Sci* **24.**, 185.

Brearley A. J. and Jones R. H. (1998) Chondritic meteorites. In *Planetary Materials* (ed. J. J. Papike). Mineralogical Society of America, Washington. pp. 3–1–3–398.

Brownlee D., Tsou P., Aléon J., Alexander C. M. O'D., Araki T., Bajt S., Baratta G. A., Bastien R., Bland P., Bleuet P., Borg J., Bradley J. P., Brearley A., Brenker F., Brennan S., Bridges J. C., Browning N. D., Brucato J. R., Bullock E., Burchell M. J., Busemann H., Butterworth A., Chaussidon M., Chevront A., Chi M., Cintala M. J., Clark B. C., Clemett S. J., Cody G., Colangeli L., Cooper G., Cordier P., Daghlian C., Dai Z., D'Hendecourt L., Djouadi Z., Dominguez G., Duxbury T., Dworkin J. P., Ebel D. S., Economou T. E., Fakra S., Fairey S. A. J., Fallon S., Ferrini G., Ferroir T., Fleckenstein H., Floss C., Flynn G., Franchi I. A., Fries M., Gainsforth Z., Gallien J.-P., Genge M., Gilles M. K., Gillet P., Gilmour J., Glavin D. P., Gounelle M., Grady M. M., Graham G. A., Grant P. G., Green S. F., Grossemy F., Grossman L., Grossman J. N., Guan Y., Hagiya K., Harvey R., Heck P., Herzog G. F., Hoppe P., Hörz F., Huth J., Hutcheon I. D., Ignatyev K., Ishii H., Ito M., Jacob D., Jacobsen C., Jacobsen S., Jones S., Joswiak D., Jurewicz A., Kearsley A. T., Keller L. P., Khodja H., Kilcoyne A. L. D., Kissel J., Krot A., Langenhorst F., Lanzirotti A., Le L., Leshin L. A., Leitner J., Lemelle L., Leroux H., Liu M.-C., Luening K., Lyon I., MacPherson G., Marcus M. A., Marhas K., Marty B., Matrajt G., McKeegan K., Meibom A., Mennella V., Messenger K., Messenger S., Mikouchi T., Mostefaoui S., Nakamura T., Nakano T., Newville M., Nittler L. R., Ohnishi I., Ohsumi K., Okudaira K., Papanastassiou D. A., Palma R., Palumbo M. E., Pepin R. O., Perkins D., Perronnet M., Pianetta P., Rao W., Rietmeijer F. J. M., Robert F., Rost D., Rotundi A., Ryan R., Sandford S. A., Schwandt C. S., See T. H., Schlutter D., Sheffield-Parker J., Simionovici A., Simon S., Sitnitsky I., Snead C. J., Spencer M. K., Stadermann F. J., Steele A., Stephan T., Stroud R., Susini J., Sutton S. R., Suzuki Y., Taheri M., Taylor S., Teslich N., Tomeoka K., Tomioka N., Toppani A., Trigo-Rodríguez J. M., Troadec D., Tsuchiyama A., Tuzzolino A. J., Tyliszczak T., Uesugi K., Velbel M., Vellenga J., Vicenzi E., Vincze L., Warren J., Weber I., Weisberg M., Westphal A. J., Wirick S., Wooden D., Wopenka B., Wozniakiewicz P., Wright I., Yabuta H., Yano H., Young E. D., Zare R. N., Zega T., Ziegler K., Zimmerman L., Zinner E. and Zolensky M. (2006) Comet 81P/Wild 2 under a microscope. *Science* **314**, 1711 LP – 1716.

Buseck P. R. and Iijima S. (1975) High resolution electron microscopy of enstatite. II: Geological Application. *Am. Mineral.* **60**, 771–784.

- Cameron M. and Papike J. J. (1981) Structural and chemical variations in pyroxenes. *Am. Mineral.* **66**, 1–50.
- Cameron M., Sueno S., Prewitt C. T. and Papike J. J. (1973) High-Temperature crystal chemistry of acmite, diopside, hedenbergite, jadeite, spodumene, and Ureyite. *Am. Mineral.* **58**, 594–618.
- Coe R. S. and Kirby S. H. (1975) The orthoenstatite to clinoenstatite transformation by shearing and reversion by annealing: Mechanism and potential applications. *Contrib. to Mineral. Petrol.* **52**, 29–55.
- Connelly J. N., Bizzarro M., Krot A. N., Nordlund Å., Wielandt D. and Ivanova M. A. (2012) The absolute chronology and thermal processing of solids in the solar protoplanetary disk. *Science* **338**, 651–655.
- Davis A. M. and Grossman L. (1979) Condensation and fractionation of rare earths in the solar nebula. *Geochim. Cosmochim. Acta* **43**, 1611–1632.
- Davis A. M., Simon S. B. and Grossman L. (1992) Melilite composition trends during crystallization of Allende Type B1 refractory inclusion melts. *Lunar Planet. Sci.* **23**, 281.
- Eaglesham D. J. and Cerullo M. (1990) Dislocation-free Stranski-Krastanow growth of Ge on Si(100). *Phys. Rev. Lett.* **64**, 1943–1946.
- Ebel D. S., Engler A. and Kurat G. (2003) Pyroxene chondrules from olivine-depleted, dust-enriched systems. *Lunar Planet. Sci.* **34**, 2059.
- Ebel D. S. and Grossman L. (2000) Condensation in dust-enriched systems. *Geochim. Cosmochim. Acta* **64**, 339–366.
- Feuer H., Schröpfer L., Fuess H. and Jefferson D. A. (1989) High resolution transmission electron microscope study of exsolution in synthetic pigeonite. *Eur. J. Mineral.* **1**, 507–516.
- Frank F. C., Van Der Merwe J. H. and Mott N. F. (1949) One-dimensional dislocations. II. Misfitting monolayers and oriented overgrowth. *Proc. R. Soc. London. Ser. A. Math. Phys. Sci.* **198**, 216–225.
- Gail H.-P. (2004) Radial mixing in protoplanetary accretion disks IV. Metamorphosis of the silicate dust complex. *Astron. Astrophys.* **413**, 571–591.

- Gasparik T. (1990) A thermodynamic model for the enstatite-diopside join. *Am. Mineral.* **75**, 1080–1091.
- Greshake A. (1997) The primitive matrix components of the unique carbonaceous chondrite Acfer 094: A TEM study. *Geochim. Cosmochim. Acta* **61**, 437–452.
- Grossman L. and Ganapathy R. (1976) Trace elements in the Allende meteorite—II. Fine-grained. Ca-rich inclusions. *Geochim. Cosmochim. Acta* **40**, 967–977.
- Han J. and Brearley A. J. (2016) Microstructural constraints on complex thermal histories of refractory CAI-like objects in an amoeboid olivine aggregate from the ALHA77307 CO3.0 chondrite. *Geochim. Cosmochim. Acta* **183**, 176–197.
- Han J. and Brearley A. J. (2015) Microstructural evidence for complex formation histories of amoeboid olivine aggregates from the ALHA77307 CO3.0 chondrite. *Meteorit. Planet. Sci.* **50**, 904–925.
- Han J., Brearley A. J. and Keller L. P. (2015) Microstructural evidence for a disequilibrium condensation origin for hibonite-spinel inclusions in the ALHA77307 CO3.0 chondrite. *Meteorit. Planet. Sci.* **50**, 2121–2136.
- Han J., Liu M.-C., Matsuda N., Park C. and Keller L. P. (2020) Mg isotopic compositions of fine-grained Ca-Al-rich inclusions from reduced CV3 chondrites and implications on the timescale of nebular condensation. *Lunar Planet. Sci.* **51**, 2895.
- Hewins R. H., Connolly H. C., Lofgren G. E. and Libourel G. (2005) Experimental constraints on chondrule formation. In *Chondrites and the Protoplanetary Disk* (eds. A. N. Krot, E. R. D. Scott, and B. Reipurth). Astronomical Society of the Pacific Conference Series. p. 286.
- Iijima S. and Buseck P. R. (1975) High resolution electron microscopy of enstatite I: Twinning, polymorphism and polytypism. *Am. Mineral.* **60**, 758–770.
- Imae N., Tsuchiyama A. and Kitamura M. (1993) An experimental study of enstatite formation reaction between forsterite and Si-rich gas. *Earth Planet. Sci. Lett.* **118**, 21–30.
- Ishii H. A., Bradley J. P., Dai Z. R., Chi M., Kearsley A. T., Burchell M. J., Browning N. D. and Molster F. (2008) Comparison of comet 81P/Wild 2 dust with interplanetary dust from comets. *Science* **319**, 447–450.
- Jones R. H. and Brearley A. J. (1988) Kinetics of the clinopyroxene-orthopyroxene transition:

Constraints on the thermal histories of chondrules and type 3-6 chondrites. *Meteoritics* **23**, 277.

Joswiak D. J., Brownlee D. E., Matrajt G., Westphal A. J. and Snead C. J. (2009) Kosmochloric Ca-rich pyroxenes and FeO-rich olivines (Kool grains) and associated phases in Stardust tracks and chondritic porous interplanetary dust particles: Possible precursors to FeO-rich type II chondrules in ordinary chondrites. *Meteorit. Planet. Sci.* **44**, 1561–1588.

Kawasaki N., Park C., Sakamoto N. and Yurimoto H. (2019) Variations in initial ^{26}Al abundances among fine-grained Ca-Al-rich inclusions in the reduced CV chondrites. *Annual Meeting of the Meteoritical Society* **82**, 6021.

Kita N. T., Ushikubo T., Knight K. B., Mendybaev R. A., Davis A. M., Richter F. M. and Fournelle J. H. (2012) Internal ^{26}Al - ^{26}Mg isotope systematics of a Type B CAI: Remelting of refractory precursor solids. *Geochim. Cosmochim. Acta* **86**, 37–51.

Klöck W., Thomas K. L., McKay D. S. and Palme H. (1989) Unusual olivine and pyroxene composition in interplanetary dust and unequilibrated ordinary chondrites. *Nature* **339**, 126–128.

Kornacki A. S. and Wood J. A. (1984) Petrography and classification of Ca, Al-rich and olivine-rich inclusions in the Allende CV3 chondrite. *J. Geophys. Res.* **89**, B573.

Kothe S., Güttler C. and Blum J. (2010) The physics of protoplanetary dust agglomerates. V. Multiple impacts of dusty agglomerates at velocities above the fragmentation threshold. *Astrophys. J.* **725**, 1242–1251.

Krot A. N., Fagan T. J., Nagashima K., Petaev M. I. and Yurimoto H. (2005) Origin of low-Ca pyroxene in amoeboid olivine aggregates: Evidence from oxygen isotopic compositions. *Geochim. Cosmochim. Acta* **69**, 1873–1881.

Krot A. N., MacPherson G. J., Ulyanov A. A. and Petaev M. I. (2004a) Fine-grained, spinel-rich inclusions from the reduced CV chondrites Efremovka and Leoville: I. Mineralogy, petrology, and bulk chemistry. *Meteorit. Planet. Sci.* **39**, 1517–1553.

Krot A. N., Petaev M. I. and Yurimoto H. (2004b) Amoeboid olivine aggregates with low-Ca pyroxenes: A genetic link between refractory inclusions and chondrules? *Geochim. Cosmochim. Acta* **68**, 1923–1941.

Krot A. N., Petaev M. I., Russell S. S., Itoh S., Fagan T. J., Yurimoto H., Chizmadia L., Weisberg M. K., Komatsu M., Ulyanov A. A. and Keil K. (2004c) Amoeboid olivine

aggregates and related objects in carbonaceous chondrites: Records of nebular and asteroid processes. *Chemie der Erde* **64**, 185–239.

Lin Y. and Kimura M. (1998) Anorthite-spinel-rich inclusions in the Ningqiang carbonaceous chondrite: genetic links with type A and C inclusions. *Meteorit. Planet. Sci.* **33**, 435–446.

Liu M.-C., Han J., Brearley A. J. and Hertwig A. T. (2019) Aluminum-26 chronology of dust coagulation and early solar system evolution. *Sci. Adv.* **5**, 1–9.

Livi K. J. T. and Veblen D. R. (1989) Transmission electron microscopy of interfaces and defects in intergrown pyroxenes. *Am. Mineral.* **74**, 1070–1083.

Lofgren G. E. (1996) A dynamic crystallization model for chondrule melts. In *Chondrules and the Protoplanetary Disk*, 187–196.

MacPherson G. J., Bar-Matthews M., Tanaka T., Olsen E. and Lawrence G. (1983) Refractory inclusions in the Murchison meteorite. *Geochim. Cosmochim. Acta* **47**, 823–839.

MacPherson G. J., Bullock E. S., Janney P. E., Kita N. T., Ushikubo T., Davis A. M., Wadhwa M. and Krot A. N. (2010) Early solar nebula condensates with canonical, not supracanonical, initial $^{26}\text{Al}/^{27}\text{Al}$ ratios. *Astrophys. J. Lett.* **711**, 117–121.

Macpherson G. J. and Grossman L. (1984) “Fluffy” Type A Ca-, Al-rich inclusions in the Allende meteorite. *Geochim. Cosmochim. Acta* **48**, 29–46.

Macpherson G. J. and Grossman L. (1979) Melted and non-melted coarse-grained Ca-Al-rich inclusions in Allende. *Meteoritics* **14**, 479.

MacPherson G. J., Kita N. T., Ushikubo T., Bullock E. S. and Davis A. M. (2012) Well-resolved variations in the formation ages for Ca-Al-rich inclusions in the early Solar System. *Earth Planet. Sci. Lett.* **331–332**, 43–54.

MacPherson G. J., Paque J. M., Stolper E. and Grossman L. (1984) The origin and significance of reverse zoning in melilite from Allende Type B inclusions. *J. Geol.* **92**, 289–305.

Matsuno J., Tsuchiyama A., Koike C., Chihara H., Ohi S., Imai Y. and Noguchi R. (2012) Crystallization experiments of SiO₂-rich amorphous silicate: Application to SiO₂-rich circumstellar dust and GEMS. *Astrophys. J.* 753.

McCoy T. J., Keil K., Bogard D. D., Garrison D. H., Casanova I., Lindstrom M. M., Brearley A. J., Kehm K., Nichols R. H. and Hohenberg C. M. (1995) Origin and history of impact-

- melt rocks of enstatite chondrite parentage. *Geochim. Cosmochim. Acta* **59**, 161–175.
- Momma K. and Izumi F. (2011) VESTA 3 for three-dimensional visualization of crystal, volumetric and morphology data. *J. Appl. Cryst.* **44**, 1272–1276.
- Morimoto N., Appleman D. E. and Evans. H. T. (1960) The crystal structures of clinoenstatite and pigeonite. *Zeitschrift für Krist.* **114**, 120–147.
- Morimoto N. and Tokonami M. (1969) Domain structure of pigeonite and clinoenstatite. *Am. Mineral.* **54**, 725–740.
- Müller W. F., Kurat G. and Kracher A. (1979) Chemical and crystallographic study of cronstedtite in the matrix of the Cochabamba (CM2) carbonaceous chondrite. *Tschermaks Mineral. und Petrogr. Mitteilungen* **26**, 293–304.
- Murata K., Chihara H., Koike C., Noguchi T., Takakura T., Imai Y. and Tsuchiyama A. (2009) Crystallization experiments on amorphous magnesium silicate. II. Effect of stacking faults on infrared spectra of enstatite. *Astrophys. J.* **698**, 1903–1906.
- Nagahara H., Kita N. T., Ozawa K. and Morishita Y. (2008) Condensation of major elements during chondrule formation and its implication to the origin of chondrules. *Geochim. Cosmochim. Acta* **72**, 1442–1465.
- Nagahara H. and Ozawa K. (2003) Was the diversity of chondrule compositions achieved by evaporation and condensation processes? *Annual Meeting of the Meteoritical Society* **66**, 5240.
- Nagashima K., Krot A. H. and Yurimoto H. (2004) Stardust silicates from primitive meteorites. *Nature* **428**, 921–924.
- Nagashima K., Krot A. N. and Huss G. R. (2015) Oxygen-isotope compositions of chondrule phenocrysts and matrix grains in Kakangari K-grouplet chondrite: Implication to a chondrule-matrix genetic relationship. *Geochim. Cosmochim. Acta* **151**, 49–67.
- Nuth J. A., Brearley A. J. and Scott E. R. D. (2005) Microcrystals and amorphous material in comets and primitive meteorites: Keys to understanding processes in the early solar system. In *Chondrites and the Protoplanetary Disk* (eds. A. N. Krot, E. R. D. Scott, and B. Reipurth). San Francisco: Astronomical Society of the Pacific. pp. 675–700.
- Palme H. and Wlotzka F. (1976) A metal particle from a Ca,Al-rich inclusion from the meteorite Allende, and the condensation of refractory siderophile elements. *Earth Planet.*

Sci. Lett. **33**, 45–60.

Petaev M. I. and Wood J. A. (2005) Meteoritic constraints on temperatures, pressures, cooling rates, chemical compositions, and modes of condensation in the solar nebula. In *Chondrites and the protoplanetary Disk* pp. 373–406.

Petaev M. I. and Wood J. A. (1998) The condensation with partial isolation (CWPI) model of condensation in the solar nebula. *Meteorit. Planet. Sci.* **33**, 1123–1137.

Planner H. N. and Keil K. (1982) Evidence for the three-stage cooling history of olivine-porphyrific fluid droplet chondrules. *Geochim. Cosmochim. Acta* **46**, 317–330.

Pollack S. S. and Ruble W. D. (1964) X-ray identification of ordered and disordered orthoenstatite. *Am. Mineral.* **49**, 983–992.

Raterron P., Frayse G., Girard J. and Holyoke C. W. (2016) Strength of orthoenstatite single crystals at mantle pressure and temperature and comparison with olivine. *Earth Planet. Sci. Lett.* **450**, 326–336.

Richter F. M., Mendybaev R. A. and Davis A. M. (2006) Conditions in the protoplanetary disk as seen by the type B CAIs. *Meteorit. Planet. Sci.* **41**, 83–93.

Rietmeijer F. J. M. and Nuth J. A. (1991) Tridymite and maghemite formation in an Fe-SiO smoke. *Lunar Planet. Sci.* **21**, 591–599.

Rietmeijer F. J. M., Nuth J. A. and Mackinnon I. D. R. (1986) Analytical electron microscopy of Mg-SiO smokes: A comparison with infrared and XRD studies. *Icarus* **66**, 211–222.

Schmitz S. and Brenker F. E. (2008) Microstructural indications for protoenstatite precursor of cometary MgSiO₃ pyroxene: A further high-temperature component of comet Wild 2. *Astrophys. J.* **681**, L105–L108.

Scott E. R. D. and Krot A. N. (2005) Thermal processing of silicate dust in the solar nebula: Clues from primitive chondrite matrices. *Astrophys. J.* **623**, 571–578.

Simon S. B., Davis A. M. and Grossman L. (1999) Origin of compact type A refractory inclusions from CV3 carbonaceous chondrites. *Geochim. Cosmochim. Acta* **63**, 1233–1248.

Simon S. B., Krot A. N. and Nagashima K. (2019) Oxygen and Al-Mg isotopic compositions of grossite-bearing refractory inclusions from CO3 chondrites. *Meteorit. Planet. Sci.* **54**,

1362–1378.

Smith J. V. (1969) Magnesium pyroxenes at high temperature: Inversion in clinoenstatite. *Nature* **222**, 256–257.

Smyth J. R. (1969) Orthopyroxene-high-low clinopyroxene inversions. *Earth Planet. Sci. Lett.* **6**, 406–407.

Smyth J. R. (1974a) Experimental study on the polymorphism of enstatite. *Am. Mineral.* **59**, 345–352.

Smyth J. R. (1974b) The high temperature crystal chemistry of clinohypersthene. *Am. Mineral.* **59**, 1069–1082.

Stolper E. (1982) Crystallization sequences of Ca-Al-rich inclusions from Allende: An experimental study. *Geochim. Cosmochim. Acta* **46**, 2159–2180.

Stranski I. N. and Krastanov L. (1938) Theory of orientation separation of ionic crystals. *Ber. Akad. Wiss. Wien* **146**, 797.

Sugiura N., Petaev M. I., Kimura M., Miyazaki A. and Hiyagon H. (2009) Nebular history of amoeboid olivine aggregates. *Meteorit. Planet. Sci.* **44**, 559–572.

Tanaka T. and Masuda A. (1973) Rare-earth elements in matrix, inclusions, and chondrules of the Allende meteorite. *Icarus* **19**, 523–530.

Turner F. J., Heard H. and Griggs D. T. (1960) Experimental deformation of enstatite and accompanying inversion to clinoenstatite. In *Report of 21st International Geological Congress, Copenhagen* pp. 399–408.

Volmer M. and Weber A. (1926) Novel growth mechanism in heteroepitaxial semiconductor growth. *Z. phys. Chem* **119**, 277.

Wada S., Kawasaki N. and Yurimoto H. (2019) Oxygen and Al-Mg isotope systematics of a hibonite-melilite-rich fine-grained CAI in the reduced CV chondrite Northwest Africa 8613. *Annual Meeting of the Meteoritical Society* **82**, 6028.

Wang Y. G., Yu Y. D., Ye H. Q. and Huang W. K. (1993) HRTEM study of planar defects and polytypes in MgSiO₃. *J. Mater. Sci.* **28**, 4037–4042.

Wark D. A., Boynton W. V., Keays R. R. and H P. (1987) Trace element and petrologic clues

to the formation of forsterite-bearing Ca-Al-rich inclusions in the Allende meteorite. *Geochim. Cosmochim. Acta* **51**, 607–622.

Wark D. A. and Lovering J. F. (1982) The nature and origin of type B1 and B2 Ca-Al-rich inclusions in the Allende meteorite. *Geochim. Cosmochim. Acta* **46**, 2581–2594.

Watanabe S. and Nakagawa Y. (1988) Cooling of the solar nebula. *Prog. Theor. Phys. Suppl.* **96**, 130–140.

Weinbruch S. and Müller W. F. (1995) Constraints on the cooling rates of chondrules from the microstructure of clinopyroxene and plagioclase. *Geochim. Cosmochim. Acta* **59**, 3221–3230.

Wurm G., Paraskov G. and Krauss O. (2005) Growth of planetesimals by impacts at ~25 m/s. *Icarus* **178**, 253–263.

Yoneda S. and Grossman L. (1995) Condensation of CaO–MgO–Al₂O₃–SiO₂ liquids from cosmic gases. *Geochim. Cosmochim. Acta* **59**, 3413–3444.

Zolensky M. E., Zega T. J., Yano H., Wirick S., Westphal A. J., Weisberg M. K., Weber I., Warren J. L., Velbel M. A., Tsuchiyama A., Tsou P., Toppani A., Tomioka N., Tomeoka K., Teslich N., Taheri M., Susini J., Stroud R., Stephan T., Stadermann F. J., Snead C. J., Simon S. B., Simionovici A., See T. H., Robert F., Rietmeijer F. J. M., Rao W., Perronnet M. C., Papanastassiou D. A., Okudaira K., Ohsumi K., Ohnishi I., Nakamura-Messenger K., Nakamura T., Mostefaoui S., Mikouchi T., Meibom A., Matrajt G., Marcus M. A., Leroux H., Lemelle L., Le L., Lanzirotti A., Langenhorst F., Krot A. N., Keller L. P., Kearsley A. T., Joswiak D., Jacob D., Ishii H., Harvey R., Hagiya K., Grossman L., Grossman J. N., Graham G. A., Gounelle M., Gillet P., Genge M. J., Flynn G., Ferroir T., Fallon S., Ebel D. S., Dai Z. R., Cordier P., Clark B., Chi M., Butterworth A. L., Brownlee D. E., Bridges J. C., Brennan S., Brearley A., Bradley J. P., Bleuet P., Bland P. A. and Bastien R. (2006) Mineralogy and petrology of comet 81P/Wild 2 nucleus samples. *Science* **314**, 1735–1739.

CHAPTER 4

A microstructural study of forsterite-bearing, fine-grained, spinel-rich inclusions from the Leoville CV3 chondrite: Implications for the transportation process in the formation regions of refractory inclusions

Abstract

Fine-grained, spinel-rich inclusions (FGIs) are commonly observed to be enclosed by forsterite-rich amoeboid olivine aggregates (AOAs). On the other hand, forsterite is virtually absent in the interior of FGIs. Here we have carried out a microstructural study using transmission electron microscope (TEM) on three mineralogically-zoned, forsterite-bearing FGIs from the Leoville CV3 chondrite. These FGIs are mineralogically and texturally similar, and thus are probably fragments of a larger, concentrically zoned FGI. Three zones have been identified in these FGIs and forsterite is present in all the zones, but showing different occurrences. The innermost zone is composed of a complex intergrowth of forsterite, anorthite, and diopside. A careful examination of the textural relationships reveals that anorthite is commonly enclosed by layers of intergrown forsterite and diopside. There are also forsterite-deficient assemblages that are concentrated in the outer part of the intergrowth zone. In the sinuous zone, forsterite is present interstitially between spinel, and is closely associated with fine-grained Al-diopside. The outermost zone is an AOA-like zone that consists of spinel-anorthite-diopside nodules enclosed in forsterite-rich shells.

The textural relationships observed under TEM suggest that different reactions controlled the formation of forsterite in different zones in forsterite-bearing FGIs. The phase boundaries of these reactions are strongly affected by the pressure conditions, based on previous thermodynamic calculations. This pressure-dependent feature enables us to constrain the pressure conditions for the formation of different zones. We suggest that the zoning structure of these FGIs can be explained by formation in different regions with successively lower pressures, which implies a transportation process along a negative pressure gradient in the protoplanetary disk. Based on the models of the temperature and pressure structures of the solar nebula, there are three possible transportation pathways: radial, vertical, and oscillatory. These forsterite-bearing FGIs, therefore, are unique samples that have recorded the early transportation process in the formation regions of refractory inclusions.

1. INTRODUCTION

Fine-grained, spinel-rich inclusions (FGIs) are a type of calcium-aluminum-rich inclusions (CAIs) that are ubiquitous in CV3 chondrites and are characterized by aggregation of rounded nodules commonly separated from each other by sinuous diopside layers. Compared with coarse-grained CAIs, e.g., Type As and Type Bs, in CV3 chondrites, FGIs do not show textural evidence for significant melting (e.g., Krot et al., 2004a; Aléon et al., 2005) and they display volatility-fractionated group II rare earth element (REE) patterns which can only be explained by fractional condensation (e.g., Boynton, 1975; Grossman and Ganapathy, 1976; Davis and Grossman, 1979). These non-igneous CAIs have bulk compositions that are

plotted close to those of igneous counterparts on the CaO-MgO-Al₂O₃-SiO₂ (CMAS) diagram, and thus a genetic link may exist between different types of CAIs (e.g., Lin and Kimura, 1998; Lin et al., 2006; Krot et al., 2004b; MacPherson, 2014). However, FGIs have received much less attention than their coarse-grained counterparts, partly due to the fine-grained nature of primary phases in these CAIs and their susceptibility to secondary alteration. There are many petrographic studies on FGIs, which have revealed various textural relationships (e.g., MacPherson and Davis, 1994; Lin and Kimura, 1998; MacPherson et al., 2002; Krot et al., 2004a; Weisberg et al., 2004; Russell and Howard, 2013; Han et al., 2019). There are, however, considerable variations in the primary mineralogy and texture between different FGIs, which clearly indicates that different FGIs may have experienced different thermal histories in the solar nebula. A further complexity is that FGIs are often found to be associated with amoeboid olivine aggregates (AOAs) that are mainly composed of forsteritic olivine and Fe,Ni metal, which may imply a genetic relationship between them (e.g., Komatsu et al., 2001; Fagan et al., 2004; Krot et al., 2002, 2004a,b; Aléon et al., 2005; Weisberg et al., 2007; Yurimoto et al., 2008; Ruzicka et al., 2012; Han and Brearley, 2016). Additionally, textural observations of FGIs and associated AOAs often point to a condensation sequence that is inconsistent with the equilibrium condensation calculations (e.g., Krot et al., 2004a,b; Han and Brearley, 2016; Han et al., 2019). Some of these textural inconsistencies may be attributed to formation under different nebular conditions (e.g., Petaev and Wood, 1998; Petaev et al., 2003).

In this study, we reported a suite of three mineralogically-zoned FGIs from the Leoville CV3 chondrite, which contain forsterite with different occurrences. It is likely that forsterite in

different zones of these FGIs formed by different mechanisms and under different conditions. Such FGIs have never been reported in the literature and thus can potentially provide new insights into mechanisms and conditions of the nebular condensation processes.

2. ANALYTICAL METHODS

A 1 inch-round polished thin section Leoville 577 from the Leoville meteorite (from the Meteorite Collection of the Institute of Meteoritics, University of New Mexico (UNM)) were examined in this study. The backscattered electron (BSE) images and full spectral X-ray maps of the thin sections were obtained on a FEI Quanta 3D DualBeam[®] field emission gun scanning electron microscope/focused ion beam (FEG-SEM/FIB) instrument fitted with an EDAX Apollo 40 mm² SDD Energy Dispersive Spectroscopy (EDS) system with Genesis software at UNM. Full thin section BSE and X-ray map mosaics were produced using ImageJ software, by combining multiple image fields. These mosaics were then used to locate refractory inclusions on the thin section. The petrology and mineralogy of individual objects were characterized in detail by high-resolution BSE imaging and X-ray mapping. The instrument operation conditions for BSE imaging and X-ray mapping were: an accelerating voltage of 15 kV, and beam current of 11 nA.

The major and minor elements of phases in the FGIs Leo-H08, -H10, and -H11 were obtained on a wavelength dispersive spectrometry (WDS) on a JEOL JXA-8200 electron probe microanalyzer (EPMA) at UNM. All analyses were obtained at an accelerating voltage of 15 kV, a beam current of 20 nA, and a spot size of 1 μm . Taylor Company Microprobe Standards

were used for calibration: Na on albite, Mg, Si, and Fe on olivine, Al and K on orthoclase, S on pyrite, Ca on diopside, Ti on titanite, V on V-metal, Cr on chromite, Mn on spessartine, Ni on Ni-metal. In addition, an almandine oxygen standard and an apatite-F (Wilberforce) standard were also used for Al and P, respectively. The detection limits for Fe and Ni are ~0.02 wt%, while those for all the other elements are ~0.01 wt%. Data were reduced using the modified ZAF correction procedure in Probe for EPMA.

A total of three FIB sections were extracted, with two from Leo-H08 and one from Leo-H11, using the FEI Quanta 3D FEG-SEM/FIB instrument equipped with an Omniprobe 200 micromanipulator, using the method described by Han and Brearley (2015). The microstructures of the FIB sections were then characterized on a JEOL 2010F FASTEM field emission gun scanning TEM (TEM/STEM) instrument at UNM. The samples were studied using several techniques including bright-field TEM (BF-TEM), dark-field scanning TEM (DF-STEM), electron diffraction, and high-resolution TEM (HRTEM). We also performed quantitative microanalyses and X-ray elemental mapping in STEM mode using an Oxford Instruments AZtec Energy Dispersive X-ray Spectroscopy system with Oxford Instruments XMax 80N 80 mm² SDD detector on the JEOL 2010F FASTEM at UNM. The Cliff–Lorimer thin film approximation was used for quantification of the EDS data using theoretical k-factors.

3. RESULTS

3.1. SEM observations

The three forsterite-bearing FGIs (Leo-H08, -H10, and -H11) in this study are

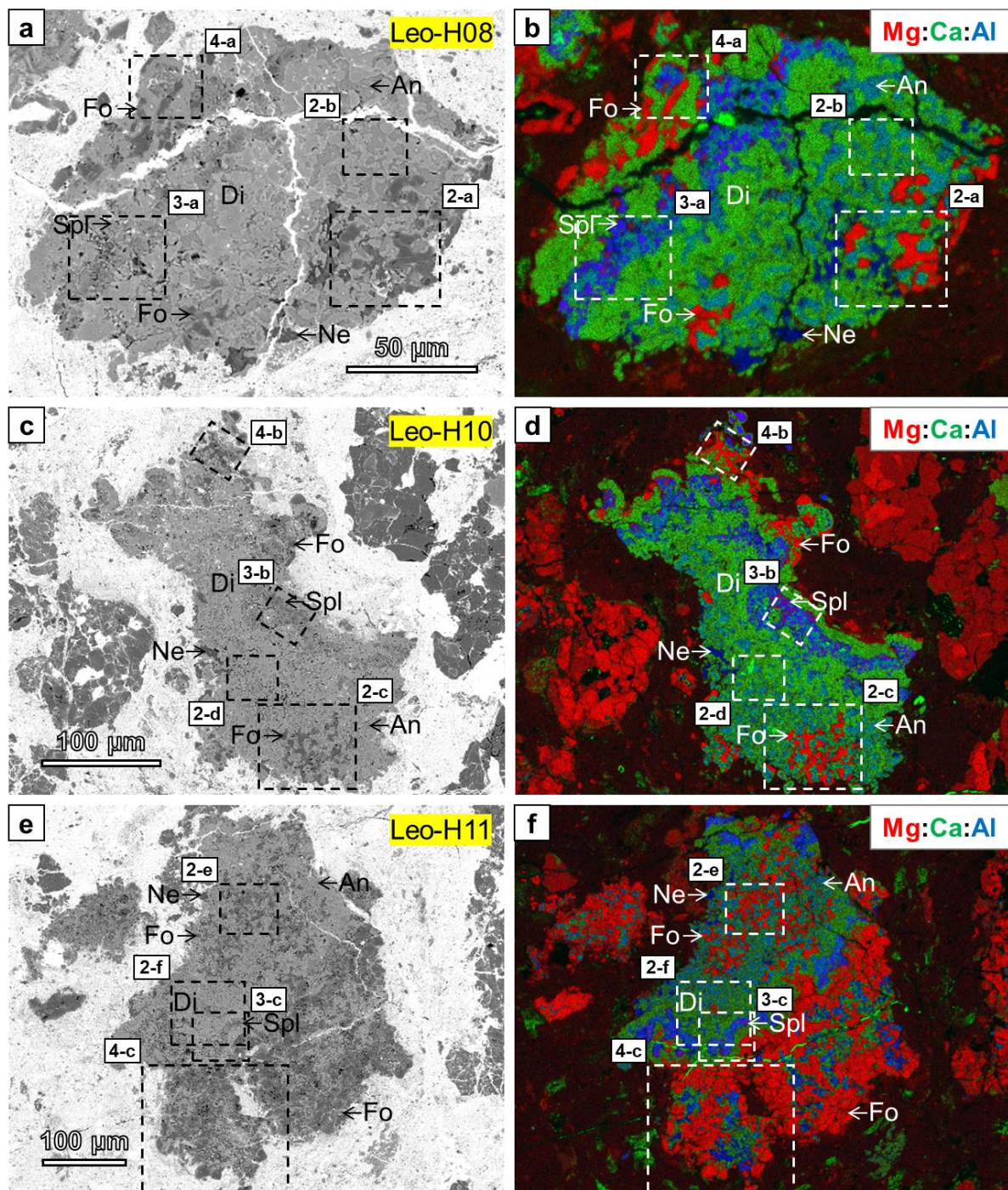


Fig. 1. BSE images (a, c, e) and combined EDS elemental X-ray maps in Mg (red), Ca (green), and Al (blue) (b, d, f) of three mineralogically-zoned, forsterite-bearing FGIs from the Leoville chondrite. These FGIs are mineralogically and texturally similar and are therefore likely to be fragments of a larger FGI. Three zones are present in these FGIs: (1) intergrowth zone, (2) sinuous zone, and (3) AOA-like zone. The relationships between the three zones are mostly obvious in Leo-H11, which displays a concentric zoning structure. Forsterite is present in all the zones, but has different contexts.

Fig. 1. (*continued*) The detailed mineralogies and textural relationships are shown in Fig. 2-4. Abbreviations: An = anorthite, Di = diopside, Fo = forsterite, Ne = nepheline, Spl = spinel.

mineralogically and texturally very similar (Fig. 1): they all contain three mineralogically-distinct zones, in which forsterite has different occurrences. It is therefore very likely that these FGIs are fragments of a larger FGI that displays a concentric zoning structure: from inner to outer parts, an intergrowth zone, a sinuous zone, and an AOA-like zone. As a result, we describe the SEM observations of these FGIs together.

The intergrowth zone is mainly composed of anorthite, diopside, and forsterite (Fig. 2). These phases often show a complex intergrowth relationship: anorthite is enclosed in layers of intergrown forsterite and diopside with similar grain sizes (5-7 μm), forming anorthite-rich nodules (10-15 μm in size). Forsterite-bearing nodules typically form clusters (Fig. 2a,c,e) and are surrounded by nodules that do not contain forsterite (Fig. 2b,d,f). The sizes of these two types of nodules do not differ significantly. Spinel is a rare phase in the intergrowth zone and occurs as fine-grained (<1 μm) Fe-bearing inclusions in anorthite.

Nodules in the sinuous zone are usually interconnected, forming sinuous-shaped assemblages with a spinel-anorthite-diopside layered sequence (Fig. 3). Spinel grains with anhedral shapes are typically 2-5 μm in size and occur as randomly distributed inclusions in anorthite. Some spinel grains show Fe-enrichment, probably caused by thermal metamorphism on the chondrite parent body. Fine-grained forsterite (<2 μm) is present as an interstitial phase to spinel grains and spinel often shows embayed interfaces with forsterite. Rare melilite is also present in the interior of the sinuous zone, as thin layers (<1 μm in thickness) partly

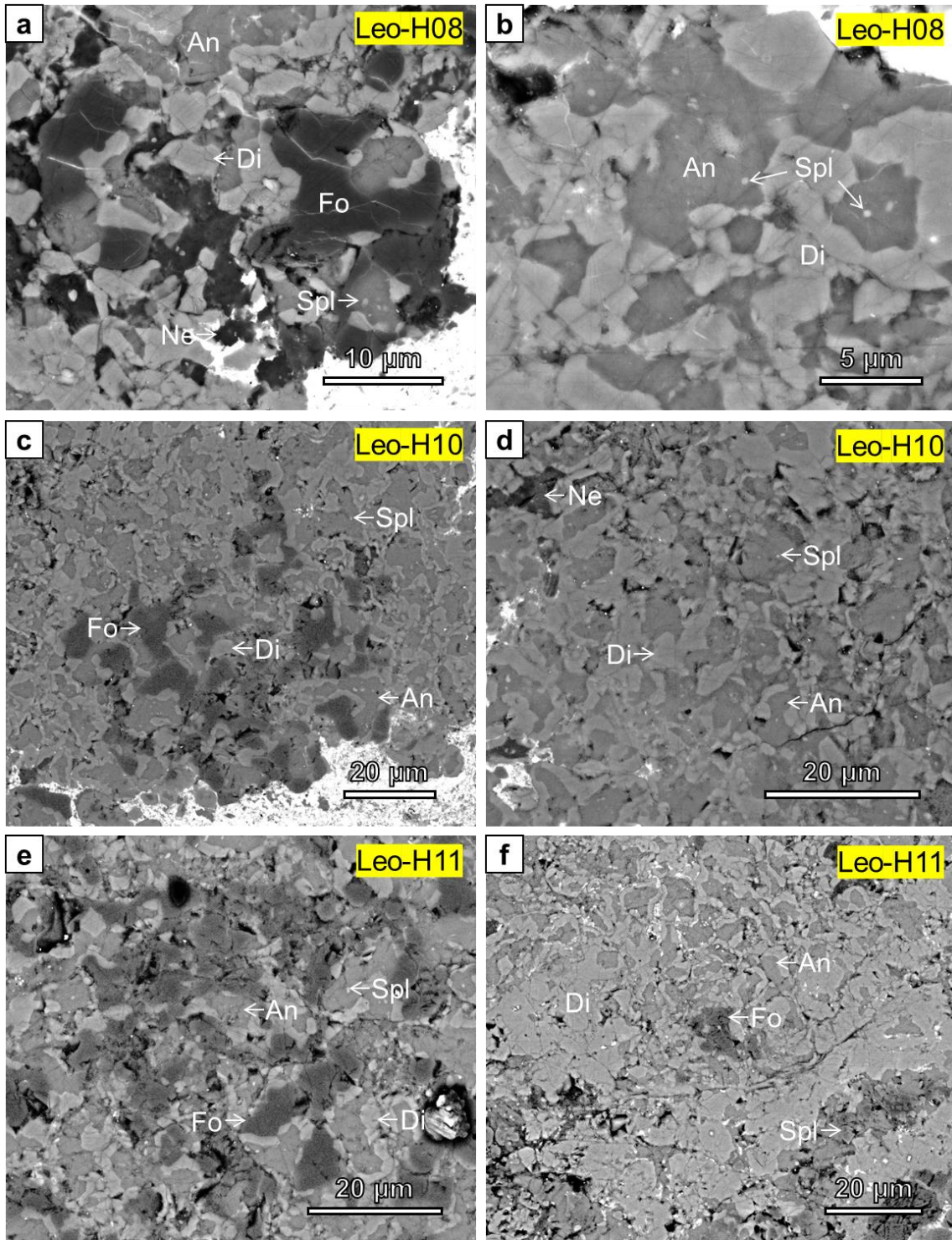


Fig. 2. BSE images of the intergrowth zones in the forsterite-bearing FGIs. (a, c, e) Forsterite commonly coexist with diopside, and these two phases form layers surrounding anorthite. There lacks clear evidence for replacement relationships between forsterite and the other two phases. Spinel nanoparticles are present as inclusions in anorthite.

Fig. 2. (*continued*) (b, d, f) Clusters of forsterite-bearing nodules are surrounded by nodules that do not contain forsterite. Fine-grained spinel also occurs in forsterite-absent nodules. The shapes and sizes of nodules do not differ significantly between the two types of nodules. Abbreviations: An = anorthite, Di = diopside, Fo = forsterite, Ne = nepheline, Spl = spinel.

surrounding spinel. The diopside layers (10-15 μm in thickness) on the sinuous assemblages are polycrystalline, with the grain size ranging from 2-5 μm .

The AOA-like zone is composed of coarse-grained, anhedral-to-subhedral forsterite that forms compacted shells enclosing CAI-like components (Fig. 4). Equilibrium grain boundaries with 120° triple junctions are commonly seen between forsterite grains. Anorthite and diopside are the dominant phases in the CAI-like components, and they often have a layered structure, with anorthite enclosed by diopside. A minor amount of fine-grained, spinel inclusions are sometimes present in anorthite.

The major lines of evidence for secondary alteration in these FGIs are Fe-enrichment in spinel and the presence of nepheline. Nepheline is replacing anorthite in regions that are adjacent to the matrix and it commonly occurs as thin lamellae along some crystallographically-controlled planes in anorthite.

3.2. Mineral compositions

Representative electron microprobe analyses of forsterite, anorthite, and diopside are reported in Table 1-3. No systematic variations in composition have been found in anorthite and forsterite in different FGIs, and these two minerals in different zones from individual FGIs are comparable. Forsterite grains in the sinuous zones are too fine-grained and closely

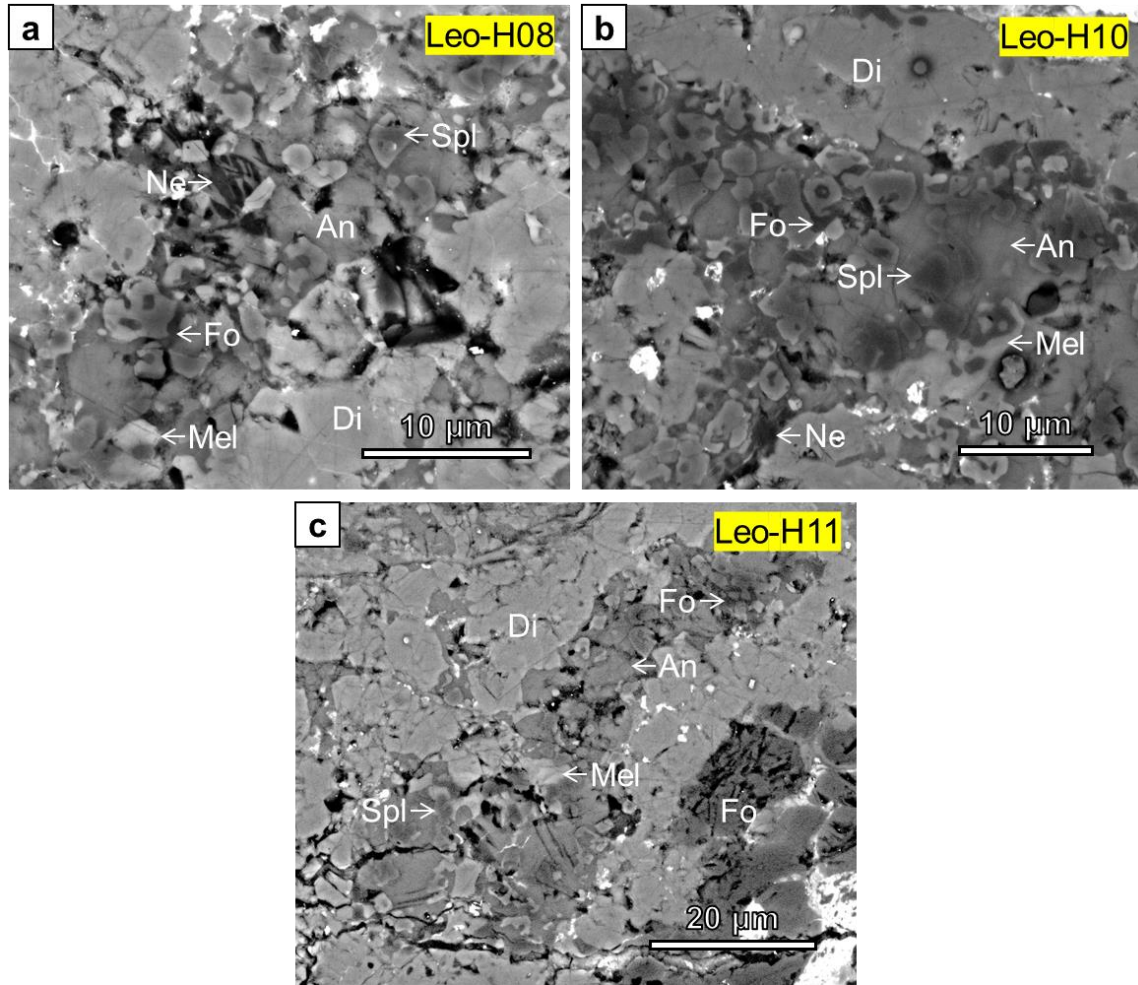


Fig. 3. BSE images of the sinuous zones in the forsterite-bearing FGIs. Nodules are interconnected to form sinuous shaped bands. Spinel grains are randomly distributed in anorthite. Interstitially to the spinel grains are fine-grained forsterite and, rarely, melilite. Curved and embayed interfaces are commonly observed between forsterite and spinel. The diopside layers are thick and polycrystalline. Nepheline as thin lamellae is replacing anorthite in regions adjacent to the matrix. Abbreviations: An = anorthite, Di = diopside, Fo = forsterite, Mel = melilite, Ne = nepheline, Spl = spinel.

associated with spinel, therefore we could not obtain meaningful microprobe data from them.

However, the TEM EDS analyses of forsterite from the sinuous zone do not show significant differences from the compositions of forsterite analyzed by the microprobe. Forsterite grains in the three FGIs show a limited range of Fa contents, from $\sim\text{Fa}_{0.2}$ to $\sim\text{Fa}_{6.8}$. The MnO and CaO

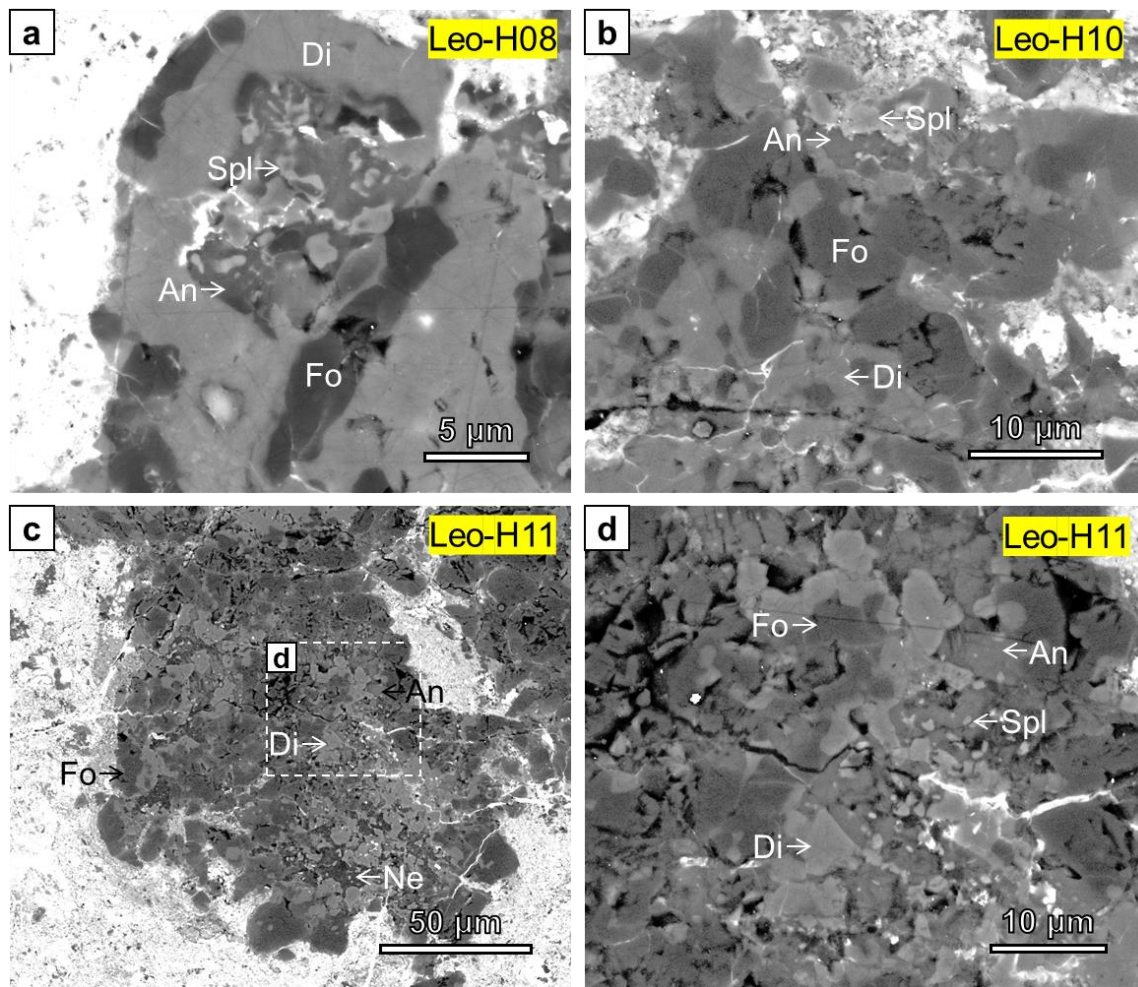


Fig. 4. BSE images of the AOA-like zones in the forsterite-bearing FGIs. Forsterite occurs as coarse-grained, compacted shells enclosing CAI-like components. The CAI-like components often form nodules that have an anorthite-diopside layered sequence. Fine-grained spinel inclusions are often found in anorthite. Abbreviations: An = anorthite, Di = diopside, Fo = forsterite, Ne = nepheline, Spl = spinel.

contents of forsterite are 0.02-0.26 wt% and 0.09-0.89 wt%, respectively (Fig. 5). Anorthite contains only a trace amount of Na₂O (<0.12 wt%).

Diopside in different zones shows a considerable variation in Al₂O₃ contents. Diopside in the intergrowth zones is significantly more enriched in Al₂O₃ (9.21-19.29 wt%), compared to diopside in the sinuous zones (2.93-6.34 wt%). The Al₂O₃ contents of diopside in the AOA-

like zones (4.52-7.95 wt%) are intermediate between the other two zones.

3.3. Microstructures

A total of three FIB sections were extracted (Fig. 6). Two of the FIB sections (FIB-01 and -03) are from the intergrowth zones in Leo-H11 and Leo-H08, respectively. Both FIB sections sample nodules with layers of intergrown diopside and forsterite. The STEM images of these FIB sections show that the forsterite-diopside interfaces are sharp and straight, and no embayment texture is observed (Fig. 7). Similarly, there is no textural evidence for a replacement relationship between forsterite and anorthite in regions where these two phases have direct contact. Rare Fe-bearing spinel nanoparticles (100-200 nm in size; Fe# = 5-7) are observed as inclusions in anorthite. The anorthite-forsterite interfaces are often decorated by spinel nanoparticles (mostly smaller than 50 nm) with elevated FeO and Cr₂O₃ contents. The crystal structure is confirmed by HRTEM analysis. The exact compositions of these spinel grains are, however, difficult to analyze due to their small sizes. Interestingly, forsterite adjacent to these spinel grains also has elevated FeO and Cr₂O₃ contents, implying that the relatively high FeO and Cr₂O₃ contents in spinel and forsterite may have a secondary parent body origin.

The other FIB section (FIB-02) was extracted from the sinuous zone in Leo-H08. This FIB section is across a nodule, in which spinel grains are randomly distributed in anorthite. Interstitial, fine-grained forsterite is also sampled by this FIB section. The STEM mosaic of the FIB section shows a complex microstructure (Fig. 8). The spinel grains enclosed in

Table 1. Representative electron microprobe analyses (wt%) of forsterite in forsterite-bearing FGIs.

| CA | Leo-H08 | | | | Leo-H10 | | | | Leo-H11 | | | |
|-----------------------------|-------------|------|----------|-----|-------------|------|----------|-----|-------------|------|----------|-----|
| | Intergrowth | | AOA-like | | Intergrowth | | AOA-like | | Intergrowth | | AOA-like | |
| Zo | | | | | | | | | | | | |
| SiO | 42.3 | 41.7 | 41. | 42. | 41.5 | 41.8 | 41. | 41. | 41.4 | 41.3 | 40. | 41. |
| Ti | 0.01 | 0.01 | 0.0 | 0.0 | 0.02 | 0.03 | bd | bd | 0.06 | 0.04 | 0.0 | bd |
| Al ₂ | 0.08 | 0.40 | 0.3 | 0.0 | 0.15 | 0.04 | 0.0 | 0.0 | 0.19 | 0.07 | 0.0 | 0.0 |
| V ₂ | 0.02 | 0.02 | 0.0 | 0.0 | 0.03 | 0.02 | 0.0 | 0.0 | 0.03 | 0.01 | 0.0 | 0.0 |
| Cr ₂ | 0.04 | 0.01 | 0.0 | 0.0 | 0.04 | 0.09 | 0.0 | 0.1 | 0.10 | 0.07 | 0.0 | 0.1 |
| Fe | 0.43 | 2.31 | 4.0 | 1.1 | 1.29 | 0.88 | 3.4 | 2.3 | 0.23 | 2.47 | 4.2 | 0.6 |
| Mn | 0.11 | 0.26 | 0.0 | 0.0 | 0.14 | 0.07 | 0.0 | 0.0 | 0.06 | 0.21 | 0.2 | 0.2 |
| Mg | 55.9 | 53.3 | 53. | 55. | 54.7 | 55.9 | 54. | 55. | 55.5 | 54.6 | 52. | 57. |
| Ca | 0.20 | 0.38 | 0.2 | 0.1 | 0.30 | 0.13 | 0.1 | 0.2 | 0.54 | 0.15 | 0.1 | 0.1 |
| Na ₂ | 0.01 | 0.01 | 0.0 | bd | bd | bd | 0.0 | 0.0 | 0.03 | 0.01 | 0.0 | 0.0 |
| K ₂ | bd | bd | 0.0 | bd | 0.01 | bd | 0.0 | bd | 0.02 | 0.01 | bd | bd |
| Tot | 99.1 | 98.4 | 99. | 99. | 98.2 | 99.1 | 99. | 99. | 98.2 | 99.1 | 97. | 99. |
| Cations per 4 oxygen anions | | | | | | | | | | | | |
| Si | 1.00 | 1.00 | 0.9 | 1.0 | 0.99 | 0.99 | 0.9 | 0.9 | 0.98 | 0.99 | 0.9 | 0.9 |
| Ti | 0.00 | 0.00 | 0.0 | 0.0 | 0.00 | 0.00 | - | - | 0.00 | 0.00 | 0.0 | - |
| Al | 0.00 | 0.01 | 0.0 | 0.0 | 0.00 | 0.00 | 0.0 | 0.0 | 0.00 | 0.00 | 0.0 | 0.0 |
| V | 0.00 | 0.00 | 0.0 | 0.0 | 0.00 | 0.00 | 0.0 | 0.0 | 0.00 | 0.00 | 0.0 | 0.0 |
| Cr | 0.00 | 0.00 | 0.0 | 0.0 | 0.00 | 0.00 | 0.0 | 0.0 | 0.00 | 0.00 | 0.0 | 0.0 |
| Fe | 0.00 | 0.04 | 0.0 | 0.0 | 0.02 | 0.01 | 0.0 | 0.0 | 0.00 | 0.05 | 0.0 | 0.0 |
| Mn | 0.00 | 0.00 | 0.0 | 0.0 | 0.00 | 0.00 | 0.0 | 0.0 | 0.00 | 0.00 | 0.0 | 0.0 |
| Mg | 1.97 | 1.91 | 1.9 | 1.9 | 1.95 | 1.98 | 1.9 | 1.9 | 1.97 | 1.95 | 1.9 | 2.0 |
| Ca | 0.00 | 0.01 | 0.0 | 0.0 | 0.00 | 0.00 | 0.0 | 0.0 | 0.01 | 0.00 | 0.0 | 0.0 |
| Na | 0.00 | 0.00 | 0.0 | - | - | - | 0.0 | 0.0 | 0.00 | 0.00 | 0.0 | 0.0 |
| K | 0.00 | 0.00 | 0.0 | - | 0.00 | - | 0.0 | - | 0.00 | 0.00 | - | - |
| Tot | 2.99 | 2.98 | 3.0 | 2.9 | 2.99 | 3.00 | 3.0 | 3.0 | 2.99 | 3.00 | 3.0 | 3.0 |
| Fa | 0.42 | 2.36 | 4.0 | 1.1 | 1.30 | 0.87 | 3.4 | 2.3 | 0.23 | 2.47 | 4.3 | 0.6 |

Note: bd = below detection limits.

Table 2. Representative electron microprobe analyses (wt%) of anorthite in forsterite-bearing FGIs.

| CAI# | Leo-H08 | | | Leo-H10 | | | Leo-H11 | | |
|--------------------------------|-------------|----------|-------|-------------|----------|-------|-------------|----------|-------|
| | Intergrowth | Sinuuous | AOA | Intergrowth | Sinuuous | AOA | Intergrowth | Sinuuous | AOA |
| Zones | | | | | | | | | |
| SiO ₂ | 41.53 | 40.66 | 41.94 | 42.27 | 43.49 | 42.02 | 42.47 | 41.87 | 42.35 |
| TiO ₂ | 0.04 | 0.07 | 0.02 | 0.09 | 0.08 | bd | 0.03 | 0.01 | bd |
| Al ₂ O ₃ | 36.28 | 36.02 | 35.05 | 35.92 | 32.69 | 36.60 | 36.22 | 36.21 | 36.46 |
| V ₂ O ₃ | 0.02 | 0.01 | 0.01 | bd | 0.01 | 0.02 | 0.01 | 0.02 | bd |
| Cr ₂ O ₃ | bd | 0.02 | bd | 0.04 | bd | bd | 0.02 | bd | bd |
| FeO | 1.05 | 1.06 | 1.17 | 0.45 | 0.58 | 0.38 | 0.27 | 0.73 | 0.09 |
| MnO | 0.01 | bd | bd | bd | 0.01 | 0.01 | bd | 0.01 | bd |
| MgO | 0.31 | 0.58 | 0.47 | 0.98 | 2.18 | 0.17 | 0.28 | 0.35 | 0.16 |
| CaO | 19.37 | 18.72 | 19.00 | 19.66 | 19.32 | 19.72 | 19.75 | 19.51 | 19.85 |
| Na ₂ O | 0.06 | 0.09 | 0.10 | 0.08 | 0.09 | 0.07 | 0.11 | 0.08 | 0.12 |
| K ₂ O | bd | 0.01 | bd | 0.01 | 0.01 | bd | 0.01 | 0.02 | 0.01 |
| Total | 98.67 | 97.22 | 97.76 | 99.53 | 98.46 | 98.99 | 99.16 | 98.80 | 99.04 |
| Cations per 8 oxygen anions | | | | | | | | | |
| Si | 1.959 | 1.944 | 1.994 | 1.973 | 2.052 | 1.970 | 1.987 | 1.970 | 1.980 |
| Ti | 0.001 | 0.002 | 0.001 | 0.003 | 0.003 | - | 0.001 | 0.000 | - |
| Al | 2.017 | 2.030 | 1.964 | 1.977 | 1.817 | 2.023 | 1.997 | 2.008 | 2.009 |
| V | 0.001 | 0.000 | 0.000 | - | 0.000 | 0.001 | 0.000 | 0.001 | - |
| Cr | - | 0.001 | - | 0.002 | - | - | 0.001 | - | - |
| Fe | 0.042 | 0.042 | 0.047 | 0.018 | 0.023 | 0.015 | 0.010 | 0.029 | 0.003 |
| Mn | 0.000 | - | - | - | 0.000 | 0.000 | - | 0.000 | - |
| Mg | 0.022 | 0.041 | 0.033 | 0.068 | 0.153 | 0.012 | 0.019 | 0.025 | 0.011 |
| Ca | 0.979 | 0.959 | 0.968 | 0.984 | 0.977 | 0.991 | 0.990 | 0.983 | 0.994 |
| Na | 0.005 | 0.008 | 0.009 | 0.008 | 0.008 | 0.006 | 0.010 | 0.007 | 0.011 |
| K | - | 0.001 | - | 0.001 | 0.001 | - | 0.000 | 0.001 | 0.000 |
| Total | 5.025 | 5.030 | 5.016 | 5.033 | 5.034 | 5.018 | 5.017 | 5.023 | 5.010 |

Note: bd = below detection limits.

Table 3. Representative electron microprobe analyses (wt%) of diopside in forsterite-bearing FGIs.

| CAI# | Leo-H08 | | | Leo-H10 | | | Leo-H11 | | |
|--------------------------------|-------------|----------|-------|-------------|----------|-------|-------------|----------|--------|
| | Intergrowth | Sinuuous | AOA | Intergrowth | Sinuuous | AOA | Intergrowth | Sinuuous | AOA |
| Zones | | | | | | | | | |
| SiO ₂ | 49.09 | 51.06 | 50.88 | 45.82 | 53.18 | 50.62 | 48.33 | 52.28 | 49.37 |
| TiO ₂ | 1.75 | 1.07 | 1.46 | 1.54 | 0.06 | 0.32 | 0.93 | 0.43 | 2.25 |
| Al ₂ O ₃ | 12.81 | 5.91 | 6.68 | 19.29 | 3.14 | 4.52 | 12.30 | 5.55 | 7.95 |
| V ₂ O ₃ | 0.03 | 0.02 | 0.08 | 0.05 | 0.01 | 0.05 | 0.05 | 0.03 | 0.05 |
| Cr ₂ O ₃ | 0.06 | 0.05 | 0.06 | 0.05 | 0.04 | 0.04 | 0.10 | 0.04 | 0.07 |
| FeO | 0.52 | 0.66 | 0.81 | 0.71 | 0.08 | 2.22 | 0.50 | 0.16 | 0.57 |
| MnO | 0.02 | bd | 0.02 | bd | bd | 0.01 | 0.01 | bd | bd |
| MgO | 13.23 | 16.01 | 16.34 | 9.87 | 17.82 | 17.41 | 13.40 | 16.91 | 15.48 |
| CaO | 22.72 | 24.98 | 23.05 | 21.47 | 25.12 | 23.11 | 24.44 | 25.06 | 24.37 |
| Na ₂ O | 0.04 | 0.02 | 0.02 | 0.04 | bd | 0.02 | 0.03 | bd | 0.03 |
| K ₂ O | 0.01 | 0.01 | 0.01 | 0.01 | bd | 0.01 | 0.01 | 0.01 | 0.01 |
| Total | 100.28 | 99.78 | 99.39 | 98.86 | 99.46 | 98.34 | 100.11 | 100.47 | 100.15 |
| Cations per 6 oxygen anions | | | | | | | | | |
| Si | 1.751 | 1.850 | 1.840 | 1.650 | 1.927 | 1.865 | 1.739 | 1.875 | 1.782 |
| Ti | 0.047 | 0.029 | 0.040 | 0.042 | 0.002 | 0.009 | 0.025 | 0.011 | 0.061 |
| Al | 0.538 | 0.252 | 0.285 | 0.818 | 0.134 | 0.196 | 0.522 | 0.235 | 0.338 |
| V | 0.001 | 0.001 | 0.002 | 0.002 | 0.000 | 0.002 | 0.002 | 0.001 | 0.002 |
| Cr | 0.002 | 0.001 | 0.002 | 0.002 | 0.001 | 0.001 | 0.003 | 0.001 | 0.002 |
| Fe | 0.016 | 0.020 | 0.024 | 0.021 | 0.003 | 0.068 | 0.015 | 0.005 | 0.017 |
| Mn | 0.001 | - | 0.001 | - | - | 0.000 | 0.000 | - | - |
| Mg | 0.703 | 0.865 | 0.881 | 0.530 | 0.963 | 0.956 | 0.719 | 0.904 | 0.833 |
| Ca | 0.868 | 0.970 | 0.893 | 0.828 | 0.975 | 0.912 | 0.942 | 0.963 | 0.942 |
| Na | 0.003 | 0.001 | 0.001 | 0.003 | - | 0.002 | 0.002 | - | 0.002 |
| K | 0.000 | 0.000 | 0.000 | 0.000 | - | 0.001 | 0.000 | 0.001 | 0.000 |
| Total | 3.930 | 3.991 | 3.968 | 3.896 | 4.004 | 4.013 | 3.970 | 3.995 | 3.979 |

Note: bd = below detection limits.

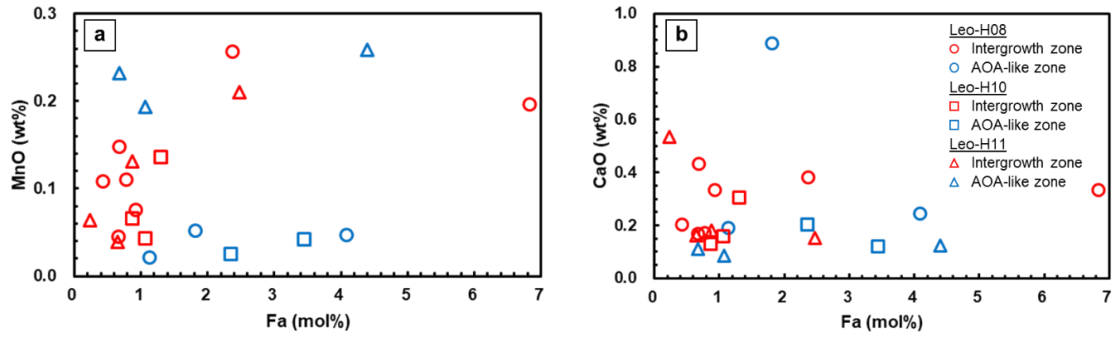


Fig. 5. Compositional plots (a) MnO vs. Fa and (b) CaO vs. Fa of forsterite in the forsterite-bearing FGIs in this study. Forsterite grains in different FGIs are compositionally similar. There are no systematic variations in the MnO and CaO contents of forsterite in the intergrowth and AOA-like zones. We failed to obtain useful microprobe data from forsterite grains in the sinuous zone, due to their fine-grained sizes. However, the STEM EDS analyses demonstrate that forsterite grains in the sinuous zone are compositionally similar to those in the other two zones.

anorthite have rounded shapes, and often form clusters. Forsterite grains (200-500 nm) are intimately associated with spinel, and their interfaces are often curved. In contrast, smooth interfaces are observed between forsterite and anorthite. These forsterite grains are intimately associated with fine-grained, Al-rich diopsides (10.5-12.1 wt% Al₂O₃; 100-200 nm in size). There are also some fine-grained, Al-rich diopside grains (11.1-13.3 wt% Al₂O₃; 300-500 nm in size) that occur on the edge of spinel but do not coexist with forsterite.

4. DISCUSSION

4.1. The origins of forsterite in the forsterite-bearing FGIs

The equilibrium thermodynamic calculations predict that forsterite should have condensed directly from a gas of solar composition via the following reaction (e.g., Yoneda

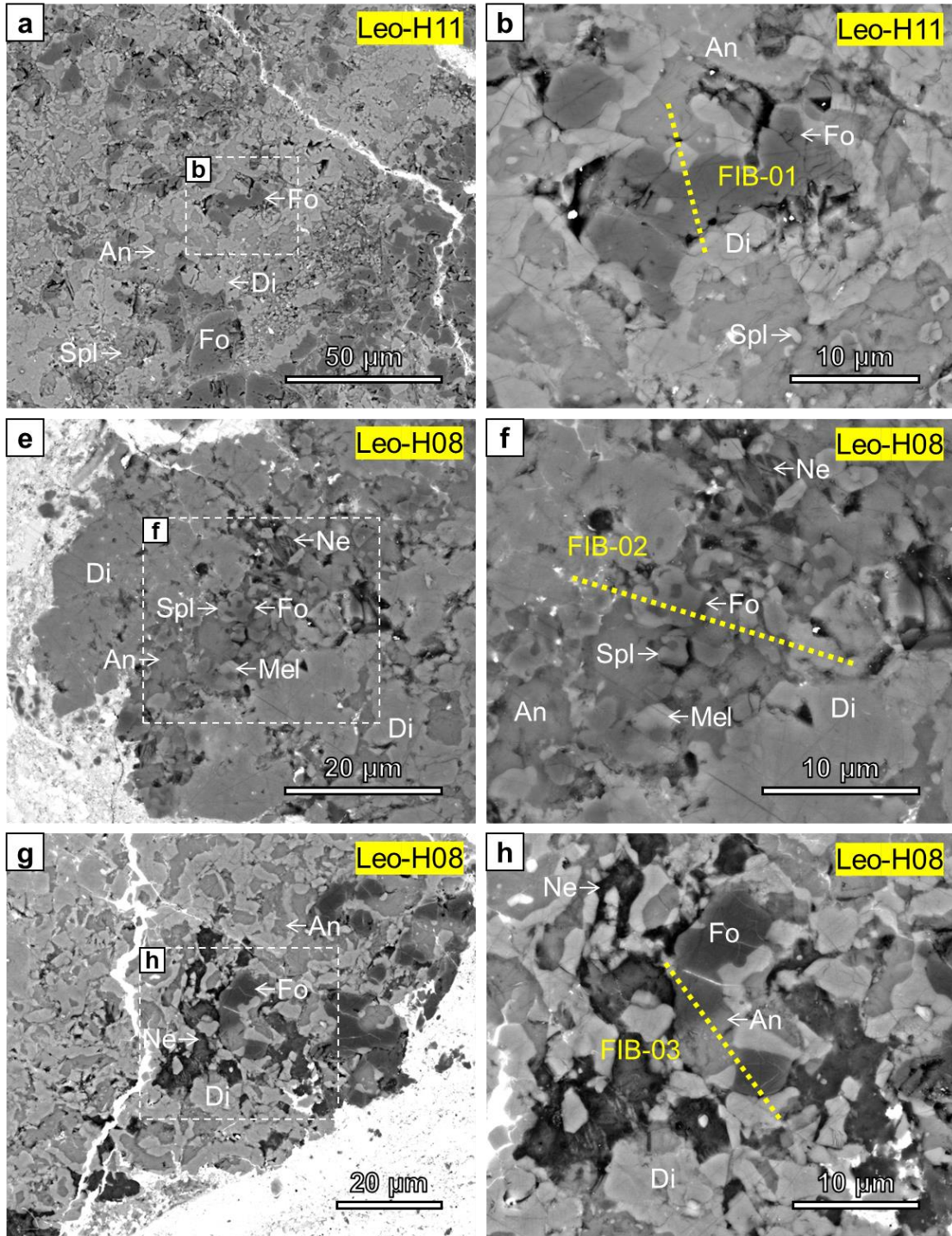
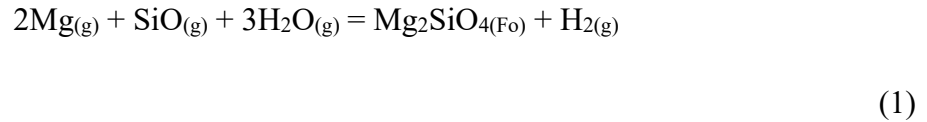


Fig. 6. BSE images showing the positions where the three FIB sections were extracted. FIB-01 and FIB-03 are from the intergrowth zones in Leo-H11 and Leo-H08, respectively. They sample the forsterite-bearing nodules. FIB-02 is from the sinuous zone in Leo-H08 and is across several spinel grains with interstitial, fine-grained forsterite. Abbreviations: An = anorthite, Di = diopside, Fo = forsterite, Mel = melilite, Ne = nepheline, Spl = spinel.

and Grossman, 1995; Ebel and Grossman, 2000; Ebel, 2006):



and its condensation temperature is between that of diopside and anorthite. In these calculations, diopside is produced from melilite, and anorthite forms by a reaction between pre-condensed diopside and spinel. The textural relationships observed in FGIs are, however, inconsistent with such a condensation sequence (e.g., Krot et al., 2004a, b). Nodules with an anorthite mantle and an outer diopside layer are commonly observed, and forsterite, together with Fe,Ni metal and, rarely, low-Ca pyroxene, forms a compact shell surrounding aggregates of nodules. This forsterite-rich shell is texturally and compositionally similar to AOAs (e.g., Krot et al., 2004b; Fagan et al., 2004; Ruzicka et al., 2012). These textural observations suggest that forsterite condenses after diopside and anorthite.

Two mechanisms have been proposed to explain this disconnect between theoretical calculations and observations. Type B and C CAIs are anorthite-normative and forsterite-deficient, and it is likely that their precursors contained a considerable amount of anorthite. The anorthite in the precursors may have been produced by a reaction between melilite, spinel, and gas (Beckett and Grossman, 1988; MacPherson and Huss, 2000), which occurred at a temperature higher than that for the condensation of forsterite. Such a mechanism can be applied to FGIs. An alternative mechanism is based on a thermodynamic calculation that

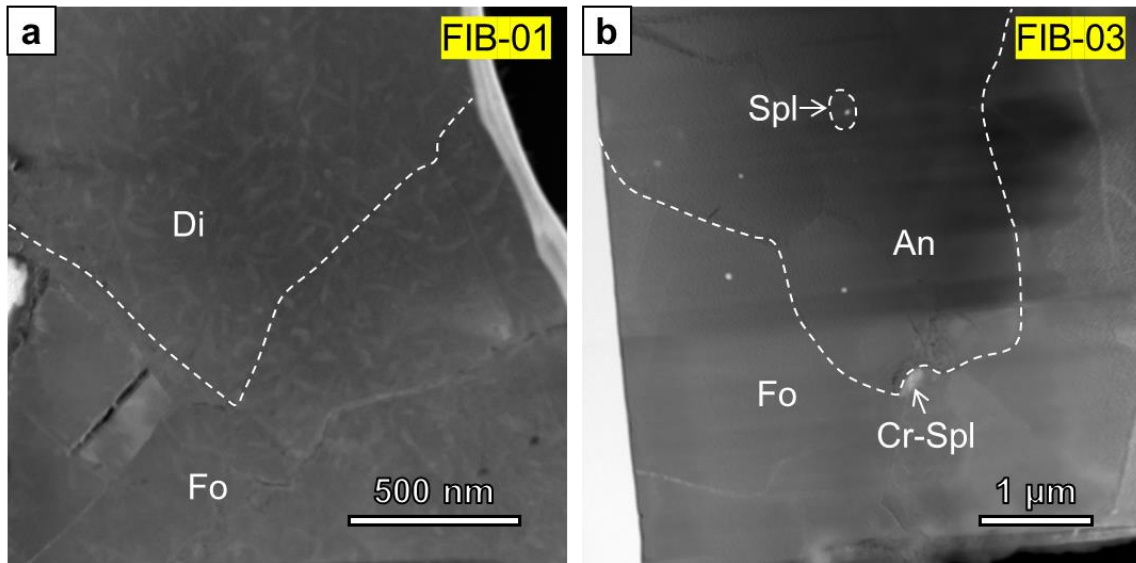


Fig. 7. DF-STEM images of FIB-01 and FIB-03 from the intergrowth zones showing the textural relationships between forsterite, diopside and anorthite. The interfaces between these phases are smooth and no replacement relationships are observed. Fine-grained spinel inclusions are sometimes present in anorthite. There are also some Cr-bearing spinel nanoparticles distributed at the forsterite-anorthite interfaces. Abbreviations: An = anorthite, Di = diopside, Fo = forsterite, Spl = spinel.

assumes continuous isolation of pre-condensed phases from the gas (Petaev and Wood, 1998; Petaev et al., 2003; Krot et al., 2004b). These authors showed that the relative condensation sequence of forsterite and anorthite is reversed at a pressure lower than $\sim 5 \times 10^{-5}$ bar. The temperature gap of condensation between forsterite and anorthite increases with decreasing pressure.

The forsterite-bearing FGIs in Leoville contain forsterite grains with different contexts, and therefore, understanding their formational mechanisms and conditions can potentially provide new insights into the condensation processes experienced by FGIs.

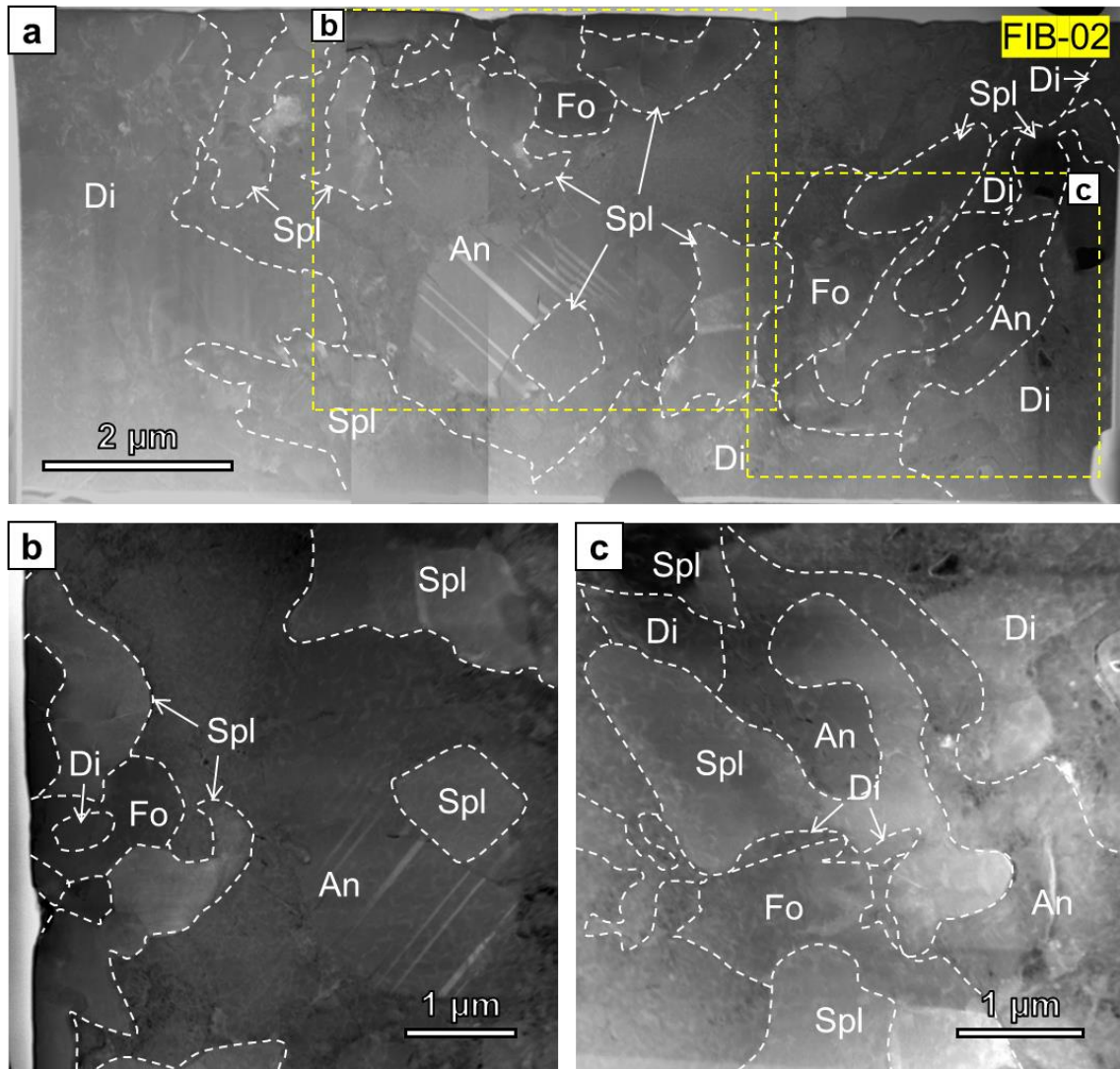


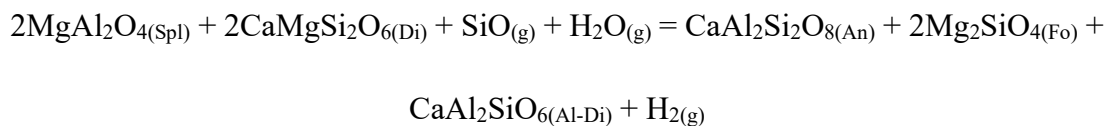
Fig. 8. DF-STEM images of FIB-02 from the sinuous zone in Leo-H08. (a) STEM mosaic of FIB-02 showing the complex textural relationships. Spinel grains are randomly distributed in anorthite. (b-c) Forsterite often has curved or embayed interfaces with spinel and is commonly associated with fine-grained, Al-rich diopside. These diopside grains are sometimes surrounded by forsterite. There are also some Al-rich diopside grains that grow on the edge of spinel, but do not coexist with forsterite. One example is the diopside grain in the upper left corner of figure (c). Abbreviations: An = anorthite, Di = diopside, Fo = forsterite, Spl = spinel.

4.1.1. Forsterite in the intergrowth zones

Concentric nodules that usually consist of spinel, anorthite, and diopside are the basic

components of FGIs (e.g., Krot et al., 2004a,b; Fagan et al., 2004; Aléon et al., 2005). Some FGIs have a sinuous texture, with the spinel cores in adjacent nodules connected to each other (e.g., Lin and Kimura, 1998), though the basic concentric sequence remains the same as that in the more common type of FGIs. An intergrowth assemblage of anorthite + diopside + forsterite has been previously reported in an FGI L3535-5 from Leoville (Krot et al., 2004b), but its formation mechanism was not discussed in that paper.

The intergrowth zones in Leo-H08, -H10, and -H11 have a complex texture; a careful examination on the textural relationships, however, reveals that anorthite is often enclosed by diopside which forms an interconnected layer with various thickness. Fine-grained spinel grains, though not abundant, are commonly observed as inclusions in anorthite. This is confirmed by the TEM observations of FIB-04, which shows that spinel grains with rounded shapes are enclosed in anorthite. On the other hand, forsterite is intimately associated with diopside. On the STEM images, the interfaces between anorthite, diopside, and forsterite are mostly smooth, rather than highly curved or embayed, which indicates that these phases probably do not have replacement relationships. A condensation reaction that can produce an assemblage of anorthite, diopside, and forsterite was previously proposed by Krot et al. (2004b):

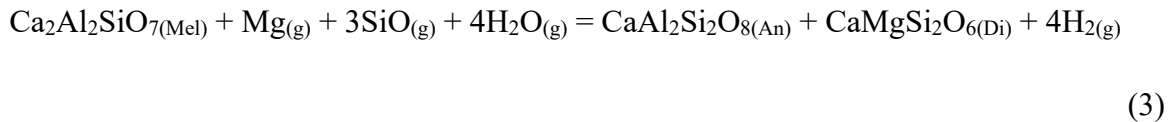


(2)

and based on their thermodynamic calculations, this reaction occurs at a higher temperature than the melilite replacement reactions which produce a fine-grained mixture of spinel, Al-diopside, and \pm anorthite. This reaction was proposed to explain the textural observations of some spinel-anorthite-diopside nodules that are enclosed in AOAs (e.g., Fig. 24d in Krot et al., 2004b). Although there are textural similarities between these nodules and the intergrowth zones in Leoville FGIs, it is obvious that forsterite associated with the nodules is part of the surrounding AOA shells, which is in contrast with the occurrence of forsterite in the intergrowth zones. Assume the precursor for the anorthite + diopside + forsterite assemblage is a nodule with spinel-melilite nodules, reaction (2) should produce either a symplectic texture, or a layered texture. The symplectic intergrowth of anorthite and diopside is commonly observed in CAI-like nodules with a spinel-melilite-diopside layered sequence from AOAs (e.g., Krot et al., 2004a; Han and Brearley, 2016). In these CAI-like nodules, the symplectite is present as a thin layer between the spinel core and melilite, implying that the formational reaction of the anorthite-diopside symplectite possibly involves spinel and melilite, instead of diopside, as reactants. In the second scenario, where the reaction produces a layered texture, the occurrence of forsterite in the intergrowth zones appears to be consistent with reaction (2). However, there are two lines of evidence that argue against reaction (2) as the formation mechanism for the intergrowth zones. First, a significant amount of spinel should have been consumed in the formation reaction of forsterite, according to reaction (2). However, in assemblages that do not contain forsterite, spinel is only present as rare, fine-grained inclusions that are enclosed in anorthite. This indicates that many of the assemblages in the intergrowth

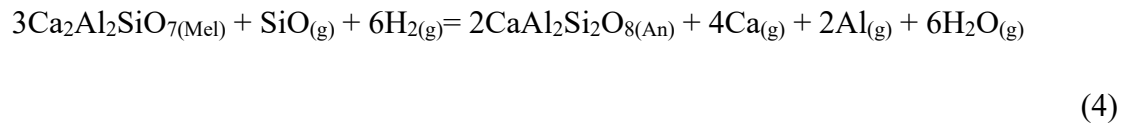
zones were not produced by reaction (2). In addition, if reaction (2) is responsible for the formation of the intergrowth zones, we might observe a corrosion texture between anorthite and relict spinel. The absence of such a texture contradicts reaction (2), though it is likely that all the spinel grains have been completely consumed.

An alternative and more likely hypothesis is that anorthite, diopside, and forsterite formed by different condensation reactions. Anorthite is likely to have formed by replacing pre-condensed melilite. Krot et al. (2004a,b) proposed another reaction for the formation of anorthite in FGIs:

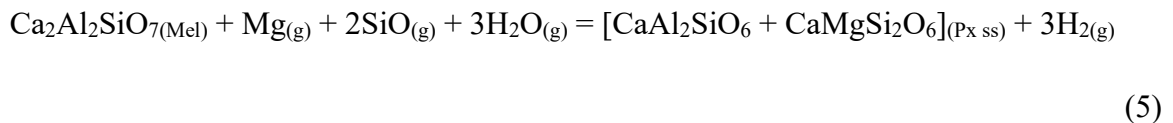


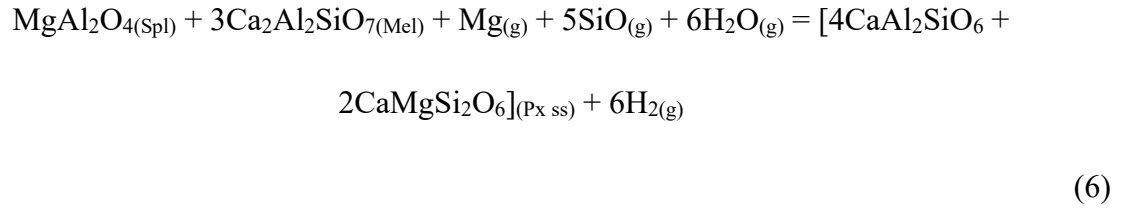
It is difficult to evaluate this reaction using the textural observations of the intergrowth zones, since all the pre-condensed melilite has been completely replaced. We can, however, gain some insights from other FGIs in Leoville. Many FGIs in Leoville contain nodules with various mineralogy, i.e., phases in the layered sequence of individual nodules vary. These nodules often show an evolutionary condensation trend, with melilite being progressively replaced by anorthite. A careful examination of the textural relation between melilite, anorthite, and diopside reveals that the diopside layer does not show a significant variation in thickness, which implies that diopside was not a product in the anorthite formation reaction. The textural observations of these nodules are more consistent with a pseudomorphic replacement reaction.

We can write an empirical reaction, based on the molar volumes of melilite and anorthite, which are 92.50 and 105.05 cm³/mol (WWW-MINCRYST), respectively. Since porosity is rarely observed in anorthite-rich nodules, it is possible that the formation reaction of anorthite is an isovolumetric reaction. A possible reaction is written as:



In this reaction, Ca and Al are lost into the gas, which is counterintuitive since Ca and Al are refractory, and the metasomatic reaction between melilite and gas should result in a relatively negligible transfer of these species into the gas (e.g., Simon et al., 2005). Therefore, the above reaction may not be thermodynamically viable. However, as suggested by the textural observations, no other solid phases were involved in the reaction, which implies that Ca and Al must have been lost during the reaction, but the nature of these Ca and Al phases is currently unknown. We suggest that reaction (4) can be applied to the intergrowth zones in forsterite-bearing FGIs. In this case, the precursor assemblages probably contained melilite and diopside, with a layered texture. Diopside is a product of reactions between melilite, ±spinel, and nebular gas, which are represented by the following reactions proposed by Krot et al. (2004a, b):





During the subsequent gas-solid metasomatism in the solar nebula, melilite was progressively replaced by anorthite. The hypothesis that anorthite formation reaction occurred after the formation of the diopside layers is consistent with the thermodynamic modeling of Krot et al. (2004b).

The smooth interfaces between forsterite and diopside observed under the TEM indicate that forsterite formed by direct condensation via reaction (1). Reaction (1), (5), and (6) may have occurred contemporaneously, resulting in the coexistence of forsterite and diopside. Thermodynamic calculations by Krot et al. (2004b) show that, on the P-T diagram, the three reactions curves overlap at a pressure higher than $\sim 3 \times 10^{-4}$ bar (Fig. 9a). The gap between the curves becomes smaller with an increasing proportion of Ca-Tschermakite (CATS) in the pyroxene solid solution. Diopside in the intergrowth zones contains up to 19.29 wt% Al_2O_3 , and most of the grains have a composition of ~ 11.5 wt% Al_2O_3 , which corresponds to $\sim \text{Di}_{76}\text{CATS}_{24}$, which meets the requirement to make the three reactions proceed simultaneously.

The chronology of anorthite and forsterite formation may provide a further constraint on the formation condition of the intergrowth zones. As suggested by Krot et al. (2004a), the condensation sequence of anorthite and forsterite is pressure dependent, and forsterite condensed prior to anorthite at pressures higher than $\sim 5 \times 10^{-5}$ bar. The proportion of forsterite

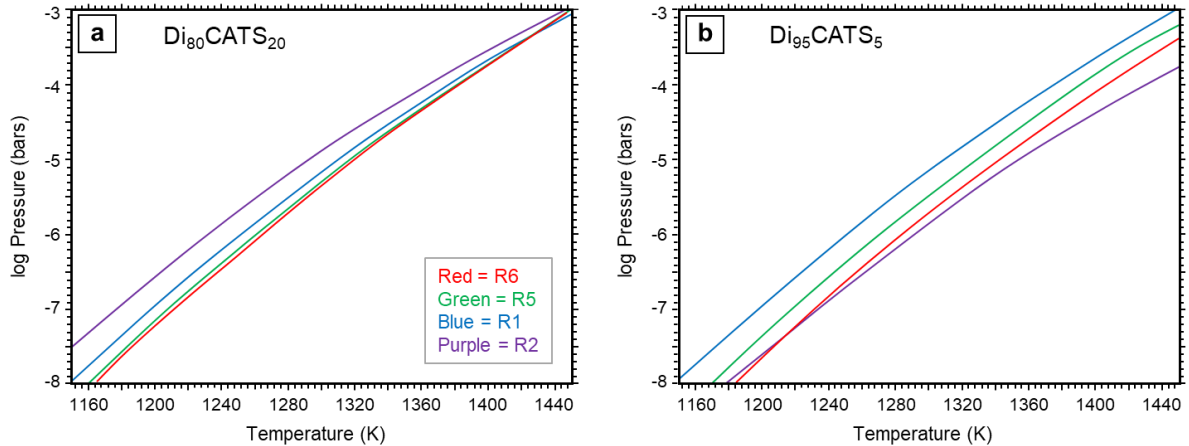


Fig. 9. Equilibrium condensation curves for the formation of diopside and forsterite illustrating the effect of pressure on the relative sequence of different reactions. The condensation sequence of forsterite and diopside is strongly controlled by pressure: higher pressures favor contemporaneous condensation, while lower pressures cause forsterite to condense after diopside. The Al_2O_3 contents of diopside also affect the relative sequence of the forsterite formation reaction (reaction (2) as represented by the purple curve) in that this reaction occurs at higher temperatures with decreasing Al_2O_3 contents of diopside. The compositions of diopside are (a) $\text{Di}_{80}\text{CATS}_{20}$ and (b) $\text{Di}_{95}\text{CATS}_5$, respectively. Diagrams are modified from Krot et al. (2004a,b).

in the intergrowth zones decreases towards the interface with the sinuous zones. For these forsterite-deficient assemblages, the forsterite condensation was clearly delayed, relatively to the condensation of diopside and anorthite. It is thus likely that during the formation of the outer portion of the intergrowth zones, the local nebular pressure dropped below $\sim 5 \times 10^{-5}$ bar (Fig. 9a), which is the reverse point for condensation of anorthite and forsterite (Petaev and Wood, 1998; Petaev et al., 2003; Krot et al., 2004b).

Therefore, we suggest that forsterite-rich assemblages in the core region of the intergrowth zones formed under high nebular pressures ($> \sim 3 \times 10^{-4}$ bar), where diopside and forsterite condensed in the same period of time; forsterite-deficient assemblages in the outer

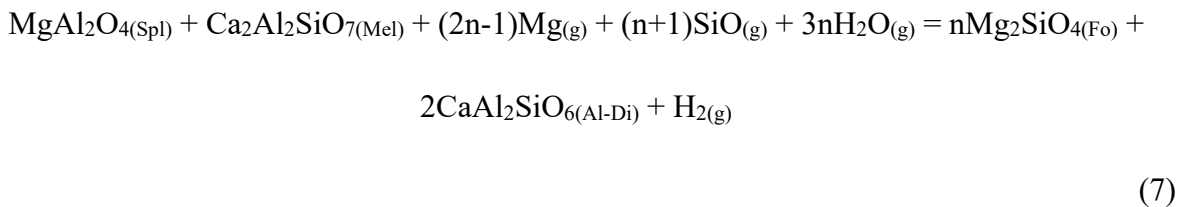
part formed at a relatively lower nebular pressure ($\sim 5 \times 10^{-5}$ bar), and the forsterite condensation was delayed under this condition.

4.1.2. Forsterite in the sinuous zones

The sinuous zones in the forsterite-bearing FGIs are texturally similar to the interconnected nodules in some FGIs and some CAI-like materials enclosed in AOAs (e.g., Krot et al., 2004a, b). Abundant spinel grains with rounded shapes are present in the sinuous zone, and they often have attached diopside globules. Relict melilite grains are commonly observed in anorthite, and sometimes they partly surround spinel grains. A notable difference of the sinuous zones from other FGIs or CAI-like materials in AOAs is that forsterite is present interstitially between spinel, and their interfaces appear to have an embayed outline on the BSE images. The detailed TEM observations of FIB-03 reveal that forsterite has a replacement relationship with spinel, and an interesting discovery is the presence of fine-grained, Al-rich diopside that is closely associated with forsterite. The diopside could be a reactant in the formation reaction of forsterite. In this scenario, diopside could have formed via reaction (6), and was subsequently consumed to form forsterite. Diopside that was produced in this way should have formed a thin layer that progressively separates spinel from melilite that was later replaced by anorthite. Indeed, such a microstructure was reported by Han and Keller (2019) in some FGIs from the Efremovka CV3 chondrite. However, many spinel grains in the forsterite-bearing FGIs are not enclosed by a diopside layer, and they are often in direct contact with anorthite, which suggests that reaction (6) did not play a major role in producing Al-rich

diopside. One explanation is that the melilite mantle surrounding spinel limited the pathways for the gas to infiltrate into the interior. In comparison, diopside layers outside the melilite grew more efficiently via interaction between melilite (and/or spinel) and the gas. If diopside is a reactant in the forsterite formation reaction, the textural observations suggest that such a reaction may be between spinel, diopside, and the gas. A possible reaction is reaction (2), in which the $\text{CaMgSi}_2\text{O}_6$ component in diopside was progressively consumed, and the diopside became increasingly more enriched in Al. One problem with this formation reaction is that, as argued earlier, the formation of anorthite in FGIs is widely consistent with a melilite pseudomorphic replacement reaction. There is no clear textural evidence for anorthite to be a product in the forsterite formation. However, we cannot completely rule out this formation mechanism. Reaction (2), if occurred, may have played a minor role in the formation of forsterite in the sinuous zones.

An alternative scenario for the origin of Al-rich diopside associated with forsterite is that it is a byproduct of the forsterite formation reaction. Such a reaction may be between spinel and melilite. Depending on the local availability of Mg in the nebular gas, the relative proportions of forsterite and Al-diopside in the products may vary:



where “n” represents the number of moles of forsterite that form from one mole of spinel. This means that the Mg of forsterite came from both spinel and the nebular gas. Based on the TEM observations, forsterite is much more abundant than the associated diopside; therefore, the major Mg source for forsterite should be the gas. We did not calculate the P-T conditions for reaction (7), but it is reasonable to postulate that it occurred at a similar temperature to reaction (6). This is because fine-grained Al-diopside that is not associated with forsterite is also present in the sinuous zones. If forsterite was produced by reaction (7), it is likely that the interactions between spinel and melilite happened in a relatively short period of time, before melilite was extensively replaced by anorthite.

Although we cannot distinguish between the two scenarios mentioned above, we can qualitatively constrain the formation time of forsterite in the sinuous zones. As shown by the thermodynamic calculations in Krot et al. (2004a,b), the phase boundaries of the diopside formation reactions are highly dependent on the Al_2O_3 contents of diopside. For example, for diopside with a high Al content ($\text{Di}_{80}\text{CATS}_{20}$), reaction (2) occurs at a lower temperature than reaction (1); decreasing the Al content in diopside moves the reaction (2) curve towards the high-temperature side of the phase diagram. Textural observations of the sinuous zones suggest that forsterite is rarely present as an outer layer on the interconnected nodules, which implied that reaction (1) did not precede the reactions that produced forsterite in the interior of the nodules. This is consistent with the Al_2O_3 contents of diopside in the sinuous zones: the Al_2O_3 contents are between 2.93 and 6.34 wt%, and most of the grains have an Al_2O_3 content of ~4.5-5.0 wt%, which corresponds to $\sim\text{Di}_{90}\text{CATS}_{10}$. The thermodynamic calculations predict that,

with this diopside composition, the possible formation reactions for forsterite in the sinuous zones (reaction (2) and (7)) occur at significantly higher temperatures than reaction (1) (Fig. 9b). The absence of forsterite surrounding the sinuous zones also suggests that the direct condensation reaction of forsterite (reaction (1)) was delayed and occurred after the formation of anorthite (reaction (4)). This implies a pressure condition of $<\sim 5 \times 10^{-5}$ bar, based on the thermodynamic calculations of Krot et al. (2004a). Therefore, the sinuous zones must have formed at a relatively low nebular pressure condition ($<\sim 5 \times 10^{-5}$ bar).

4.1.3. Forsterite in the AOA-like zones

The AOA-like zones in Leoville forsterite-bearing FGIs are similar to many AOA-CAI compound objects reported in the literature (e.g., Komatsu et al., 2001; Chizmadia et al., 2002; Krot et al., 2004a; Fagan et al., 2004; Weisberg et al., 2004; Ruzicka et al., 2012; Han and Brearley, 2016). The Ca-Al-rich assemblages in the AOA-like zones have a similar appearance with the sinuous zones; however, the former contains a less amount of spinel grains, and no forsterite is observed to coexist with spinel. The Al_2O_3 contents of diopside in the AOA-like zones (4.52-7.95 wt%) are slightly higher than that in the sinuous zones, and most of the diopside grains in the AOA-like zones contain ~ 7 wt% of Al_2O_3 ($\sim \text{Di}_{84}\text{CATS}_{15}$). This diopside composition suggests that reactions (2) and (7) may occur after reaction (1) (Fig. 9a), based on the thermodynamic diagram constructed for FGIs with diopside showing different Al_2O_3 contents (Krot et al., 2004a,b). This reaction sequence, combined with the inefficiency of the formation reactions for forsterite associated with spinel, due to the isolation of the nodule

interior from the gas by the melilite mantle, may have inhibited the formation of forsterite in the Ca-Al-rich assemblages. The presence of forsterite as a compact shell surrounding the Ca-Al-rich assemblages suggests that forsterite condensed directly from the gas via reaction (1), after the formation of the Ca-Al-rich assemblages. In this case, a relatively low nebular pressure condition is required ($< \sim 3 \times 10^{-4}$ bar).

We also compared the composition of diopside in the AOA-like zones with that in AOAs from relatively pristine carbonaceous chondrites (e.g., Komatsu et al., 2001; Aléon et al., 2002; Krot et al., 2004a; Ruzicka et al., 2012; Han and Brearley, 2016), and found that their Al_2O_3 contents are comparable. In addition, no forsterite has been reported to be present in the CAI-like objects enclosed in these AOAs. Therefore, we suggest that the AOA-like zones in forsterite-bearing FGIs may have formed in the same, or at least similar, nebular regions where AOAs formed. The formation pressures of AOAs have been previously estimated to be in the range of 10^{-6} to 10^{-4} bar, in a system of solar composition (e.g., Krot et al., 2004a; Petaev and Wood, 2005; Ruzicka et al., 2012), which is consistent with our pressure estimate for the AOA-like zones. We suggest that the AOA-like zones, due to their textural and compositional similarities to AOAs, could also have formed at $\sim 10^{-6}$ - 10^{-4} bar.

4.2. The transportation process recorded in the forsterite-bearing FGIs

In this section, we discuss the transportation history of the forsterite-bearing FGIs in Leoville. As discussed in the previous section, the presence of three texturally distinct zones and the different textural relationships of forsterite with other phases indicates that the three

zones likely formed in different nebular regions. We will demonstrate that these regions may differ in both physical conditions and gas compositions.

The lack of textural evidence for a replacement relation between forsterite and other phases in the intergrowth zones implies that forsterite probably formed by direct condensation from the gas via reaction (1). Forsterite and diopside in this zone may have formed contemporaneously due to their coexisting relationship. Based on the pressure dependence of the forsterite and diopside condensation reactions, and the compositions of diopside, we estimated the required pressure condition for the formation of the intergrowth zones to be higher than $\sim 3 \times 10^{-4}$ bar. An additional pressure constraint comes from the zoning structure of the intergrowth zones: forsterite-rich assemblages are surrounded by forsterite-deficient ones. Such a structure can be easily accounted for by decreasing the nebular pressure to a value below $\sim 5 \times 10^{-5}$ bar. For the sinuous zones, the diopside has lower Al_2O_3 contents, and the phase boundaries of reaction curves on the P-T diagram change accordingly. The most important effect of the changing diopside composition is shifting of reaction (2) towards much higher temperatures, compared to reaction (1). This compositional change also increases the temperature gap between reactions (1) and (6). Since reactions (6) and (7) may have occurred at similar temperatures, the temperature gap between reactions (1) and (7) may also become larger with increasing Al_2O_3 contents of diopside. Consequently, the formation of forsterite could have initiated preferentially in the inner region of the sinuous zones. The absence of forsterite surrounding the sinuous zones suggests pressures lower than $\sim 5 \times 10^{-5}$ bar. The AOA-like zones eventually formed on the surface of the sinuous zones. Similar to AOAs in

carbonaceous chondrites, the AOA-like zones may have formed at the same pressure range of $\sim 10^{-6}$ - 10^{-4} bar.

The oscillatory compositional variations of diopside in different zones (from $\sim \text{Di}_{76}\text{CATS}_{24}$, to $\sim \text{Di}_{90}\text{CATS}_{10}$, and back to $\sim \text{Di}_{84}\text{CATS}_{15}$) also support a scenario where zones formed in different nebular regions. The canonical equilibrium condensation models (e.g., Yoneda and Grossman, 1995; Ebel and Grossman, 2000; Ebel, 2006) predict that the proportion of CATS molecules falls steeply with decreasing temperature. Similarly, in the model of disequilibrium condensation with partial isolation, the Tschermakite content of diopside decreases nonlinearly with decreasing temperature (e.g., Petaev and Wood, 1998). Neither equilibrium nor disequilibrium condensation in the same gaseous reservoir cannot produce the observed compositional variations in forsterite-bearing FGIs. Consequently, condensation in separate regions in the solar nebula is a more reasonable scenario. Condensation and transportation in different gaseous reservoirs have been proposed as a very important process for refractory inclusions from the ALHA77307 CO3.0 chondrite (Han and Brealey, 2016; Han et al., 2019). In these studies, transport of condensates into a region with a partially condensed gas is capable of explaining the elevated Al and Ti contents of diopside in CAIs and related objects. In fact, the survival of refractory inclusions and the high abundance of these objects in carbonaceous chondrites have proved the important role of transportation process in the early solar nebula (e.g., Lin et al. 2006; Krot et al. 2009; Rubin, 2011; Brownlee et al. 2012; Scott and Krot, 2014; Scott et al., 2018). Some popular transport agents include X-wind (e.g., Shu et al., 1996), disk winds (e.g., Salmeron and Ireland, 2012; Bjerkeli et al., 2016; Van

Kooten et al., 2016), centrifugal ejection (Liffman et al., 2016), and disk turbulence (e.g., Cuzzi et al., 2003; Ciesla, 2007, 2010).

To understand how the forsterite-bearing FGIs transported in the solar nebula, we need to consider the temperature and pressure structures of the protoplanetary disk (PPD), and their temporal evolution. Both the temperature and pressure have a negative radial gradient in the PPD (e.g., Weidenschilling, 1977; Boss et al., 1998; Wood, 2000; Haghhighipour and Boss, 2003; Davis, 2005; Ciesla and Charnley, 2006; Ciesla, 2007, 2009; Boss and Ciesla, 2014). The radial thermal structure was set by the balance between the thermal energy production rate due to viscous dissipation of the disk and the rate at which this energy can be lost from the disk surface (e.g., Boss, 1998; Ciesla and Charnley, 2006). The pressure gradient varies with the gas density, and dependent on the choice of turbulence parameter (e.g., Laughlin and Bodenheimer, 1994; Calvet et al., 2000; Stone et al., 2000) and the modeling method (Wood, 2000), different trends may be generated. The temperature and pressure also vary in the vertical direction. Based on a quasi-steady model of the evolving nebula, Davis (2005) showed that the temperature of the inner solar nebula, which is controlled by vigorous viscous heating on the midplane, decreases rapidly towards the disk surface to a local minimum, beyond which the gradient is reversed due to the increasingly intense radiation heating from the protosun. On the other hand, the gas pressure drops monotonically with increasing height from the midplane (e.g., Pringle, 1981; Cuzzi and Weidenschilling et al., 2006; Ciesla, 2007; Lewis, 2004). There are also temporal variations in the temperature and pressure conditions during the evolution of the PPD. The details of the variation trends are greatly influenced by the assumption of the

initial conditions of the disk as well as model parameters; however, the general trends are similar. Using a simplified viscous accretion disk model, Boss and Ciesla (2014) simulated the long-term physical evolution of the PPD, and they found that the temperature decreased dramatically within the first 1 Myr of the disk evolution, while the decrease in pressure was more steady.

We can gain some insights into the pathways of forsterite-bearing FGIs during their transport process, based on the temperature and pressure structures of the PPD. The pressure constraints on the formation of different zones in the forsterite-bearing FGIs suggest that these FGIs may have travelled along a negative pressure gradient, and the zoning structure was produced by condensation in gaseous reservoirs with successively lower pressures. Based on the pressure structure of the PPD, both radial and vertical transport are likely. The moderately steep pressure gradient implies that only a small transport distance (<5 AU radially (Boss and Ciesla, 2014); <4 AU vertically in the inner disk (Ciesla, 2007)) is necessary to explain the pressure range of forsterite-bearing FGIs. The oscillatory variation in the Al_2O_3 contents of diopside in different zones can be explained if the ambient temperature decreased first and then increased, since a higher Al_2O_3 content may indicate condensation of diopside at a higher temperature, at which a less amount of aluminum has already condensed into solids. The vertical temperature gradient in the PPD (e.g., Davis, 2005) is consistent with such a scenario. On the other hand, radial transport requires deviations from the linear temperature profile. Recent ^{26}Al - ^{26}Mg isotopic studies show that there is a significant spread in the initial $^{26}\text{Al}/^{27}\text{Al}$ ratio, $(^{26}\text{Al}/^{27}\text{Al})_0$, of pristine FGIs (e.g., Liu et al., 2019; Kawasaki et al., 2020; Han et al.,

2020). Assuming a homogeneous distribution pattern of ^{26}Al in the PPD, this corresponds to a time span of $\sim 0.1\text{-}0.4$ Myr, which could be caused by multiple thermal events over a short time interval. One way to produce repeated high-temperature thermal events in the PPD is via episodic accretion bursts, e.g., FU Orionis outbursts (e.g., Reipurth and Aspin, 2010; Audard et al., 2014; MacPherson, 2017), which superimposed thermal spikes on the quiescent temperature background. A simplified model by MacPherson (2017) demonstrates the capacity of these high-mass accretion events to evaporate or melt dusty materials, which later condensed or crystallized to form CAIs. It is therefore likely that during the outward transport of forsterite-bearing FGIs, the AOA-like zones formed in a reservoir which was moderately enriched in refractory elements (e.g., Al) because of a thermal outburst event. An alternative scenario is an oscillatory movement in a marginally gravitationally unstable solar nebula. In such a solar nebula, refractory inclusions may have experienced repeated migration both inward and outward in a relatively short period of time, and have been exposed to a wide range of nebular conditions (e.g., Boss, 2007, 2008; Boss et al., 2012). During this process, a large proportion of refractory inclusions either accreted into the protosun or experienced melting to form igneous CAIs (Fig. 2 in Boss et al., 2012), while the rest oscillated in the inner PPD before reached the outer solar nebula (Fig. 3 in Boss et al., 2012). All three mechanisms can produce the zoning structure of forsterite-bearing FGIs, and it is likely that the actual movement of the FGIs may be a combination of these processes. The forsterite-bearing FGIs are therefore unique in that they have recorded the transport process of refractory inclusions in the very early evolutionary stage of the PPD.

5. CONCLUSIONS

In this study, we investigate several mineralogically-zoned, forsterite-bearing FGIs from Leoville. Forsterite has different occurrences in the three zones identified: (1) intergrown with anorthite and diopside, (2) interstitial to spinel, and (3) forming AOA-like shells. These different textural relationships between forsterite and other phases suggest that forsterite grains in the three mineralogical zones formed by different gas-solid reactions. Based on previous thermodynamic modeling, the phase boundaries of these reactions are pressure-dependent. We propose that the mineralogical zonation in these forsterite-bearing FGIs has recorded changes in nebular pressure, which could be attributed to transport along a negative pressure gradient.

ACKNOWLEDGEMENTS

This work was funded by NASA Cosmochemistry grants NNX15AD28G to A. J. Brearley (PI). We thank Dr. Elena Dobrică and Dr. Ying-Bing Jiang for their help with the TEM operations, and Mike Spilde for his assistance with the electron microprobe analysis. We are grateful to Dr. Steven Simon for helpful discussions and suggestions. Electron microbeam analysis and FIB section preparation were carried out in the Electron Microbeam Analysis Facility, Department of Earth and Planetary Sciences and Institute of Meteoritics, University of New Mexico. The facility is supported by funds from the State of New Mexico, NSF, and NASA.

REFERENCES

- Aléon J., Krot A. N., McKeegan K. D., MacPherson G. J. and Ulyanov A. A. (2005) Fine-grained, spinel-rich inclusions from the reduced CV chondrite Efremovka: II. Oxygen isotopic compositions. *Meteorit. Planet. Sci.* **40**, 1043–1058.
- Audard M., Abraham P., Dunham M. M., Green J. D., Grosse N., Hamaguchi K., Kastner J. H., Kóspál Á., Lodato G., Romanova M. M., Skinner S. L., Vorobyov E. I. and Zhu Z. (2014) Episodic accretion in young stars. In *Protostars and Planets VI* (eds. H. Beuther, R. S. Klessen, C. P. Dullemond, and T. Henning). University of Arizona Press, Tucson. p. 387.
- Beckett J. R. and Grossman L. (1988) The origin of type C inclusions from carbonaceous chondrites. *Earth Planet. Sci. Lett.* **89**, 1–14.
- Bjerkeli P., Van Der Wiel M. H. D., Harsono D., Ramsey J. P. and Jørgensen J. K. (2016) Resolved images of a protostellar outflow driven by an extended disk wind. *Nature* **540**, 406–409.
- Boss A. P. (2007) Evolution of the solar nebula. VIII. Spatial and temporal heterogeneity of short-lived radioisotopes and stable oxygen isotopes. *Astrophys. J.* **660**, 1707–1714.
- Boss A. P. (2008) Mixing in the solar nebula: Implications for isotopic heterogeneity and large-scale transport of refractory grains. *Earth Planet. Sci. Lett.* **268**, 102–109.
- Boss A. P. (1998) Temperatures in protoplanetary disks. *Annu. Rev. Earth Planet. Sci.* **26**, 53–80.
- Boss A. P., Alexander C. M. O. and Podolak M. (2012) Cosmochemical consequences of particle trajectories during FU Orionis outbursts by the early Sun. *Earth Planet. Sci. Lett.* **345–348**, 18–26.
- Boss A. P. and Ciesla F. J. (2014) The solar nebula. In *Treatise on Geochemistry: Second Edition* (eds. H. D. Holland and K. K. Turekian). Elsevier, Oxford. pp. 37–53.
- Boynton W. V. (1975) Fractionation in the solar nebula: condensation of yttrium and the rare earth elements. *Geochim. Cosmochim. Acta* **39**, 569–584.
- Brownlee D., Joswiak D. and Matrajt G. (2012) Overview of the rocky component of Wild 2 comet samples: Insight into the early solar system, relationship with meteoritic materials

and the differences between comets and asteroids. *Meteorit. Planet. Sci.* **47**, 453–470.

Calvet N., Hartmann L. and Strom S. E. (2000) Evolution of disk accretion. In *Protostars and Planets IV* (eds. V. Mannings, A. P. Boss, and S. S. Russell). University of Arizona Press, Tucson. p. 377.

Chizmadia L. J., Rubin A. E. and Wasson J. T. (2002) Mineralogy and petrology of amoeboid olivine inclusions in CO3 chondrites: Relationship to parent-body aqueous alteration. *Meteorit. Planet. Sci.* **37**, 1781–1796.

Ciesla F. J. (2007) Outward transport of high-temperature materials around the midplane of the solar nebula. *Science* **318**, 613–615.

Ciesla F. J. (2010) The distributions and ages of refractory objects in the solar nebula. *Icarus* **208**, 455–467.

Ciesla F. J. (2009) Two-dimensional transport of solids in viscous protoplanetary disks. *Icarus* **200**, 655–671.

Ciesla F. J. and Charnley S. B. (2006) The physics and chemistry of nebular evolution. In *Meteorites and the early solar system II* (eds. D. S. Lauretta and H. Y. McSween). University of Arizona Press, Tucson. pp. 209–230.

Cuzzi J. N., Davis S. S. and Dobrovolskis A. R. (2003) Blowing in the wind. II. Creation and redistribution of refractory inclusions in a turbulent protoplanetary nebula. *Icarus* **166**, 385–402.

Cuzzi J. N. and Weidenschilling S. J. (2006) Particle-gas dynamics and primary accretion. In *Meteorites and the Early Solar System II* (eds. D. S. Lauretta and H. Y. McSween). University of Arizona Press, Tucson. pp. 353–381.

Davis A. M. and Grossman L. (1979) Condensation and fractionation of rare earths in the solar nebula. *Geochim. Cosmochim. Acta* **43**, 1611–1632.

Davis S. S. (2005) Condensation front migration in a protoplanetary nebula. *Astrophys. J.* **620**, 994–1001.

Ebel D. S. (2006) Condensation of rocky material in astrophysical environments. In *Meteorites and the Early Solar System II* (eds. D. S. Lauretta and H. Y. McSween). University of Arizona Press, Tucson. pp. 253–277.

- Ebel D. S. and Grossman L. (2000) Condensation in dust-enriched systems. *Geochim. Cosmochim. Acta* **64**, 339–366.
- Fagan T. J., Krot A. N., Keil K. and Yurimoto H. (2004) Oxygen isotopic evolution of amoeboid olivine aggregates in the reduced CV3 chondrites Efremovka, Vigarano, and Leoville. *Geochim. Cosmochim. Acta* **68**, 2591–2611.
- Grossman L. and Ganapathy R. (1976) Trace elements in the Allende meteorite—II. Fine-grained. Ca-rich inclusions. *Geochim. Cosmochim. Acta* **40**, 967–977.
- Haghighipour N. and Boss A. P. (2003) On gas drag–Induced rapid migration of solids in a nonuniform solar nebula. *Astrophys. J.* **598**, 1301–1311.
- Han J. and Brearley A. J. (2015) Microstructural evidence for complex formation histories of amoeboid olivine aggregates from the ALHA77307 CO3.0 chondrite. *Meteorit. Planet. Sci.* **50**, 904–925.
- Han J., Jacobsen B., Liu M.-C., Brearley A. J., Matzel J. E. and Keller L. P. (2019) Origin of ^{16}O -rich fine-grained Ca-Al-rich inclusions of different mineralogy and texture. *Geochemistry* **79**, 125543.
- Han J. and Keller L. P. (2019) Fine-grained, spinel-rich Ca-Al-rich inclusions from the reduced CV3 chondrite Efremovka: A genetic link to Wark-Lovering rims? *Lunar Planet. Sci.* **50**, 2902.
- Han J., Liu M.-C., Matsuda N., Park C. and Keller L. P. (2020) Mg isotopic compositions of fine-grained Ca-Al-rich inclusions from reduced CV3 chondrites and implications on the timescale of nebular condensation. *Lunar Planet. Sci.* **51**, 2895.
- Kawasaki N., Wada S., Park C., Sakamoto N. and Yurimoto H. (2020) Variations in initial $^{26}\text{Al}/^{27}\text{Al}$ ratios among fine-grained Ca-Al-rich inclusions from reduced CV chondrites. *Geochim. Cosmochim. Acta* **279**, 1–15.
- Komatsu M., Krot A. N., Petaev M. I., Ulyanov A. A., Keil K. and Miyamoto M. (2001) Mineralogy and petrography of amoeboid olivine aggregates from the reduced CV3 chondrites Efremovka, Leoville and Vigarano: Products of nebular condensation, accretion and annealing. *Meteorit. Planet. Sci.* **36**, 629–641.
- Van Kooten E. M. M. E., Wielandt D., Schiller M., Nagashima K., Thomen A., Larsen K. K., Olsen M. B., Nordlund Å., Krot A. N. and Bizzarro M. (2016) Isotopic evidence for primordial molecular cloud material in metal-rich carbonaceous chondrites. *Proc. Natl.*

Acad. Sci. **113**, 2011–2016.

Krot A. N., Amelin Y., Bland P., Ciesla F. J., Connelly J., Davis A. M., Huss G. R., Hutcheon I. D., Makide K., Nagashima K., Nyquist L. E., Russell S. S., Scott E. R. D., Thrane K., Yurimoto H. and Yin Q.-Z. (2009) Origin and chronology of chondritic components: A review. *Geochim. Cosmochim. Acta* **73**, 4963–4997.

Krot A. N., MacPherson G. J., Ulyanov A. A. and Petaev M. I. (2004a) Fine-grained, spinel-rich inclusions from the reduced CV chondrites Efremovka and Leoville: I. Mineralogy, petrology, and bulk chemistry. *Meteorit. Planet. Sci.* **39**, 1517–1553.

Krot A. N., McKeegan K. D., Leshin L. A., MacPherson G. J. and Scott E. R. D. (2002) Existence of an ^{16}O -rich gaseous reservoir in the solar nebula. *Science* **295**, 1051–1054.

Krot A. N., Petaev M. I. and Yurimoto H. (2004b) Amoeboid olivine aggregates with low-Ca pyroxenes: A genetic link between refractory inclusions and chondrules? *Geochim. Cosmochim. Acta* **68**, 1923–1941.

Laughlin G. and Bodenheimer P. (1994) Nonaxisymmetric evolution in protostellar disks. *Astrophys. J.* **436**, 335.

Lewis J. S. (2004) *Physics and chemistry of the solar system*. 2nd Edition, Academic Press, San Diego.

Liffman K., Cuello N. and Paterson D. A. (2016) A unified framework for producing CAI melting, Wark-Lovering rims and bowl-shaped CAIs. *Mon. Not. R. Astron. Soc.* **462**, 1137–1163.

Lin Y. and Kimura M. (1998) Anorthite-spinel-rich inclusions in the Ningqiang carbonaceous chondrite: Genetic links with type A and C inclusions. *Meteorit. Planet. Sci.* **33**, 435–446.

Lin Y., Kimura M., Miao B., Dai D. and Monoi A. (2006) Petrographic comparison of refractory inclusions from different chemical groups of chondrites. *Meteorit. Planet. Sci.* **41**, 67–81.

Liu M.-C., Han J., Brearley A. J. and Hertwig A. T. (2019) Aluminum-26 chronology of dust coagulation and early solar system evolution. *Sci. Adv.* **5**, 1–9.

MacPherson G. J. (2014) Calcium-aluminum-rich inclusions in chondritic meteorites. In *Treatise on Geochemistry: Second Edition* (eds. H. D. Holland and K. K. Turekian). Elsevier, Oxford. pp. 139–179.

- MacPherson G. J. (2017) Once a CAI, always a CAI: Flare-up-induced episodic fractionation and melting in the early solar nebula. *Lunar Planet. Sci.*, 2719.
- MacPherson G. J. and Davis A. M. (1994) Refractory inclusions in the prototypical CM chondrite, Mighei. *Geochim. Cosmochim. Acta* **58**, 5599–5625.
- Macpherson G. J. and Huss G. R. (2000) Convergent evolution of CAIs and chondrules: Evidence from bulk compositions and a cosmochemical phase diagram. *Lunar Planet. Sci.*, 1796.
- MacPherson G. J., Krot A. N., Ulyanov A. a. and Hicks T. (2002) A comprehensive study of pristine, fine-grained, spinel-rich inclusions from the Leoville and Efremovka CV3 chondrites, I: petrology. *Lunar Planet. Sci.* **33**, 1526.
- Petaev M. I. and Wood J. A. (1998) The condensation with partial isolation (CWPI) model of condensation in the solar nebula. *Meteorit. Planet. Sci.* **33**, 1123–1137.
- Petaev M. I., Wood J. A., Meibom A., Krot A. N. and Keil K. (2003) The ZONMET thermodynamic and kinetic model of metal condensation. *Geochim. Cosmochim. Acta* **67**, 1737–1751.
- Pringle J. E. (1981) Accretion discs in astrophysics. *Annu. Rev. Astron. Astrophys.* **19**, 137–160.
- Reipurth B. and Aspin C. (2010) FUors and early stellar evolution eds. H. A. Harutyunian, A. M. Mickaelian, and Y. Terzian. *Evol. Cosm. Objects through their Phys. Act.*, 19–38.
- Rubin A. E. (2011) Origin and alteration of amoeboid olivine inclusions in CK3 and CV3 chondrites. *Annu. Meet. Meteorit. Soc.* **74**, 5189.
- Russell S. S. and Howard L. (2013) The texture of a fine-grained calcium-aluminium-rich inclusion (CAI) in three dimensions and implications for early solar system condensation. *Geochim. Cosmochim. Acta* **116**, 52–62.
- Ruzicka A., Floss C. and Hutson M. (2012) Amoeboid olivine aggregates (AOAs) in the Efremovka, Leoville and Vigarano (CV3) chondrites: A record of condensate evolution in the solar nebula. *Geochim. Cosmochim. Acta* **79**, 79–105.
- Salmeron R. and Ireland T. R. (2012) Formation of chondrules in magnetic winds blowing through the proto-asteroid belt. *Earth Planet. Sci. Lett.* **327–328**, 61–67.

- Scott E. R. D. and Krot A. N. (2014) Chondrites and their components. In *Treatise on Geochemistry: Second Edition* (eds. H. D. Holland and K. K. Turekian). Elsevier, Oxford. pp. 65–137.
- Scott E. R. D., Krot A. N. and Sanders I. S. (2018) Isotopic dichotomy among meteorites and its bearing on the protoplanetary disk. *Astrophys. J.* **854**, 164.
- Shu F. H., Shang H. and Lee T. (1996) Toward an astrophysical theory of chondrites. *Science* **271**, 1545–1552.
- Simon J. I., Young E. D., Russell S. S., Tonui E. K., Dyl K. A. and Manning C. E. (2005) A short timescale for changing oxygen fugacity in the solar nebula revealed by high-resolution ^{26}Al - ^{26}Mg dating of CAI rims. *Earth Planet. Sci. Lett.* **238**, 272–283.
- Stone J. M., Gammie C. F., Balbus S. A. and Hawley J. F. (2000) Transport processes in protostellar disks. In *Protostars and Planets IV* (eds. V. Mannings, A. P. Boss, and S. S. Russell). University of Arizona Press, Tucson. p. 589.
- Weidenschilling S. J. (1977) Aerodynamics of solid bodies in the solar nebula. *Mon. Not. R. Astron. Soc.* **180**, 57–70.
- Weisberg M. K., Connolly H. C. and Ebel D. S. (2004) Petrology and origin of amoeboid olivine aggregates in CR chondrites. *Meteorit. Planet. Sci.* **39**, 1741–1753.
- Weisberg M. K., Kita N. T., Ushikubo T., Connolly H. C., Ebel D. S., Spicuzza M. J. and Valley J. W. (2007) Petrologic-Isotopic Study of Amoeboid Olivine Aggregates in CR Chondrites. *Lunar Planet. Sci.* **38**, 1588.
- Wood J. A. (2000) Pressure and temperature profiles in the solar nebula. *Space Sci. Rev.* **92**, 87–93.
- Yoneda S. and Grossman L. (1995) Condensation of CaO–MgO–Al₂O₃–SiO₂ liquids from cosmic gases. *Geochim. Cosmochim. Acta* **59**, 3413–3444.
- Yurimoto H., Krot A. N., Choi B.-G., Aleon J., Kunihiro T. and Brearley A. J. (2008) Oxygen isotopes of chondritic components. *Rev. Mineral. Geochemistry* **68**, 141–186.

CHAPTER 5

The role of fluid chemistry in the alteration of melilite-rich CAIs and their Wark-Lovering rims from the Allende CV3 chondrite

Abstract

We conduct a systematic investigation of melilite-rich, calcium-aluminum-rich inclusions (CAIs) from the Allende meteorite. Our SEM observations show that melilite in these CAIs has been partially to completely replaced by a layered sequence of grossular, Ca-rich feldspar, and feldspathoids. Based on our thermodynamic modeling, such an alteration sequence can be explained by formation of secondary phases on a $\mu\text{CaO}-\mu\text{SiO}_2$ gradient. The complex alteration structures, such as the presence of two occurrences of grossular, provide further evidence for microscale heterogeneities in the fluid chemistry. Some pore-filling feldspathoids may have recorded a progressive change in the fluid chemistry.

The commonly observed mineral sequence of Wark-Lovering (WL) rims on altered Allende CAIs is: an innermost spinel-rich layer, a feldspathoid layer, an olivine layer, and an outermost diopside layer. The diopside layer in the rims are often replaced by Fe-rich olivine starting from the interface between diopside and anorthite layers. We apply the microchemical environment hypothesis to the alteration of diopside: matrix materials, due to their fine-grained size, reacted with the fluid more rapidly than anorthite, resulting in a faster rate of pH increase of the local fluid. Based on the pH-dependent dissolution behavior of diopside, we suggest that

diopside dissolved preferentially at its interface with anorthite due to the lower local pH conditions. The presence of ilmenite inclusions in the WL rims is probably related to a late stage of alteration when the fluid pH became alkaline enough for ilmenite to be stable.

1. INTRODUCTION

Calcium-aluminum-rich inclusions (CAIs) are submillimeter-to-centimeter sized refractory objects that represent the oldest material formed in the solar nebula (e.g., Amelin et al., 2002; Connelly et al., 2012). These objects have recorded primary thermal processes in the early solar nebula, including condensation (e.g., Yoneda and Grossman, 1995; Ebel, 2006), partial to complete melting (e.g., Stolper, 1982; Beckett and Stolper, 1994; Simon et al., 1999), and evaporation (e.g., Davis et al., 1991, 1999; Bullock et al., 2012; Mendybaev et al., 2012). Studies of these primary processes can place constraints on the chemical and physical conditions of the protoplanetary disk; in some CV3 chondrites, especially the oxidized subgroups, CAIs, however, have experienced secondary alteration (i.e., aqueous alteration, metasomatism, and metamorphism) that has modified the primary mineralogy and textures of the CAIs to different degrees. Although there is still some discussion on the location of where the secondary alteration in chondrites occurred (e.g., Bischoff, 1998; Brearley, 2003; Ciesla et al., 2003), many lines of evidence suggest that this processing took place largely on chondrite parent bodies (e.g., Krot et al., 1995, 1998; Brearley, 2006; Brearley and Krot, 2013).

The secondary alteration features of CAIs have been studied extensively in CV3 chondrites (e.g., Hutcheon and Newton, 1981; Hashimoto and Grossman, 1987; McGuire and

Hashimoto, 1989; Lin et al., 2005; Fagan et al., 2007; Ushikubo et al., 2007; Ford and Brearley, 2008, 2010; Ishii et al., 2010; Krot et al., 2007, 2008, 2010; Brearley and Krot, 2013; Fintor et al., 2014; Brearley and Jones, 2018) due to their large abundance in this group of chondrites (3.0 vol%; Scott and Krot, 2014). However, because of the heterogeneity of secondary minerals, few studies have investigated the alteration features in CAIs systematically. For example, secondary Na- and Cl-bearing minerals (nepheline, sodalite, wadalite, and Na-melilite) show a zonal distribution in Allende Type B1 CAIs, where nepheline and sodalite are present on the periphery of the CAIs, while wadalite and Na-melilite occur almost exclusively in the inner regions (Brearley and Krot, 2013). Similar distribution patterns of secondary mineralization have also been reported in fine-grained, spinel-rich inclusions (McGuire and Hashimoto, 1989). Such a zonation could partly be accounted for by primary mineralogical zoning in the CAI; however, our recent work has shown that other factors, including the grain size of primary minerals and fluid chemistry, can also play a significant role in producing a mineralogical zonation during secondary alteration (Che and Brearley, 2021). An additional complexity of alteration in CAIs comes from the fine-grained nature of many secondary phases. Petrographic studies using only scanning electron microscopy (SEM) may not always be adequate to fully identify complex intergrowths of fine-grained secondary minerals.

Many CAIs are surrounded by Wark-Lovering (WL) rims, which are refractory, multilayered rim sequences that may have formed contemporaneously with, or after, the formation of the host CAIs. Several distinct mechanisms have been proposed for the formation of such rims (e.g., Wark and Lovering, 1977; Ruzicka, 1997; Wark and Boynton, 2001; Simon

et al., 2005; Keller et al., 2013). Previous oxygen isotopic studies on WL rims surrounding CAIs from CV3 chondrites demonstrate that WL rims often show isotopic heterogeneities (e.g., Simon et al., 2011; Bodénan et al., 2014; Krot et al., 2017) which may have been caused by fluid-rock interactions on the parent body. The typically finer-grained sizes of WL rim phases, compared with the host CAI phases, render them more susceptible to secondary alteration. Since WL rims are the regions where secondary alteration of CAIs started, they often show more extensive alteration than the host CAIs. However, there are no systematic petrological studies on the alteration effects of WL rims in the literature. In addition, many phases in the altered WL rims are too fine-grained to be accurately characterized using SEM, and therefore TEM studies would potentially provide more detailed information.

In this paper, we conduct a systematic study of secondary alteration in melilite-rich CAIs from the Allende CV3 chondrite. Melilite is one of the primary CAI phases that are most susceptible to secondary alteration (e.g., MacPherson et al., 1988; Tomeoka et al., 1992; Nomura and Miyamoto, 1998), and a sequence of melilite breakdown reactions as revealed by secondary mineral zonation have been reported by several authors (e.g., Ford et al., 2010; Brearley and Krot, 2013; Fintor et al., 2014; Brearley and Jones, 2018). We also investigate the microstructures of altered WL rims to gain further insights into the role of fluid in the secondary alteration of the Allende chondrite.

2. ANALYTICAL METHODS

Several 1 inch-round polished thin sections, three from the Allende meteorite (ALNH,

ALNG, and ALNA3) and one from the Efremovka meteorite (un-numbered thin section) were examined in this study. All the thin sections are from the Meteorite Collection of the Institute of Meteoritics, University of New Mexico (UNM). The backscattered electron (BSE) images and full spectral X-ray maps of the thin sections were obtained on a FEI Quanta 3D DualBeam[®] field emission gun scanning electron microscope/focused ion beam (FEG-SEM/FIB) instrument fitted with an EDAX Apollo 40 mm² SDD Energy Dispersive Spectroscopy (EDS) system with Genesis software at UNM. Full thin section BSE and X-ray map mosaics were produced using ImageJ software, by combining multiple image fields. These mosaics were then used to locate CAIs on the thin section. The petrology and mineralogy of individual objects were characterized in detail by high-resolution BSE imaging and X-ray mapping. The instrument operation conditions for BSE imaging and X-ray mapping were: an accelerating voltage of 15 kV, and beam current of 11 nA.

A total of two FIB sections from two CAIs were prepared from the Allende thin sections using the FEI Quanta 3D FEG-SEM/FIB instrument and were extracted using an Omniprobe 200 micromanipulator, using the method described by Han and Brearley (2015). The microstructures of the FIB sections were then characterized on a JEOL 2010F FASTEM field emission gun scanning TEM (TEM/STEM) instrument at UNM. The samples were studied using several techniques including bright-field TEM (BF-TEM), dark-field scanning TEM (DF-STEM), electron diffraction, and high-resolution TEM (HRTEM). We also performed quantitative microanalyses and X-ray elemental mapping in STEM mode using an Oxford Instruments AZtec Energy Dispersive X-ray Spectroscopy system with Oxford Instruments

XMax 80N 80 mm² SDD detector on the JEOL 2010F FASTEM at UNM. The Cliff–Lorimer thin film approximation was used for quantification of the EDS data using theoretical k-factors.

3. RESULTS

3.1. SEM observations

3.1.1. Slightly altered melilite-rich CAIs

Several Allende melilite-rich CAIs show a low degree of secondary alteration, with secondary phases restricted to a narrow region inside their WL rims. The Type B1 CAI ALNA3-01 represents such a slightly altered melilite-rich CAI (Fig. 1). It is composed of an Al-Ti-rich diopside + anorthite-rich core and a melilite-rich mantle. There are also abundant, rounded Fe,Ni metal grains (~10-50 μm) enclosed in diopside, anorthite, and melilite. Some of these metal grains have been partially to completely altered to sulfides. Melilite on the periphery of this CAI has been replaced by a secondary mineral sequence of grossular-Ca-rich feldspar-nepheline (Fig. 1b). Such a sequence occurs within a 50 μm distance of the WL rim. Porosity is well-developed in the alteration sequence; however, the density, size, and shape of pores differ significantly in different layers. Pores in Ca-rich feldspar are often abundant and the largest (up to 5 μm), and sometimes show elongate shapes. The grossular layer has less pores with a smaller size (<1 μm , mostly nanometer-sized). Pores in the nepheline layer are nanometer-sized and mostly concentrated on the interfaces between nepheline and Ca-rich feldspar, while grain boundaries between individual nepheline grains are deficient in pores. Grossular is typically the phase on the alteration front, but we also observe direct contact of

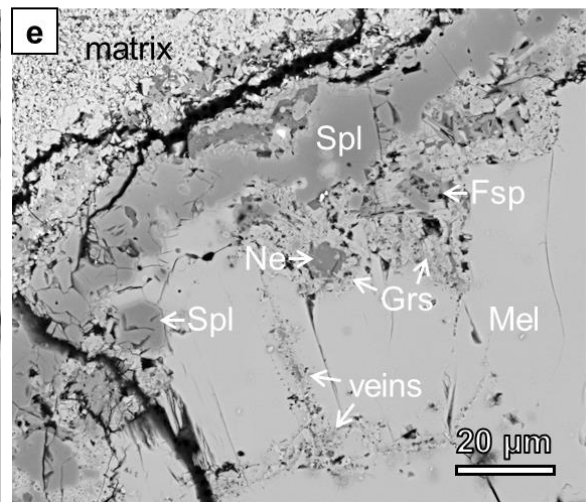
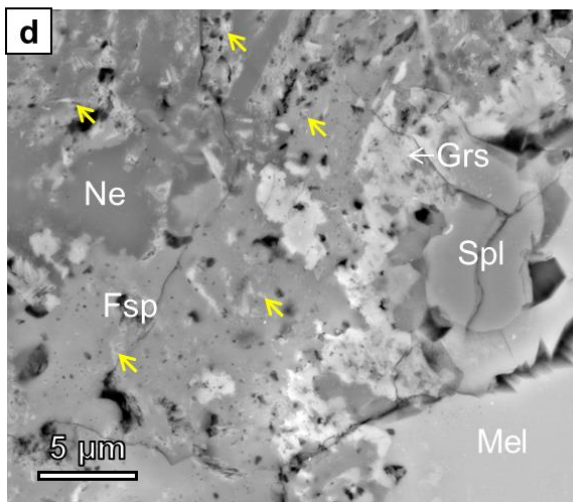
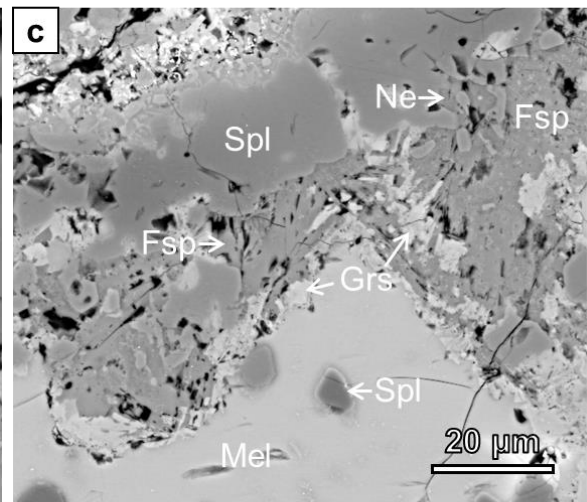
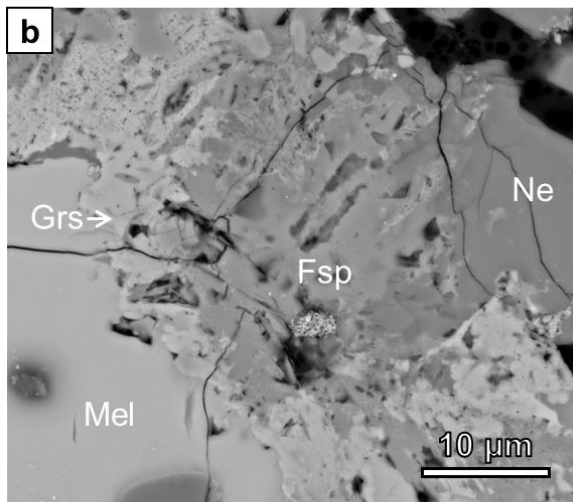
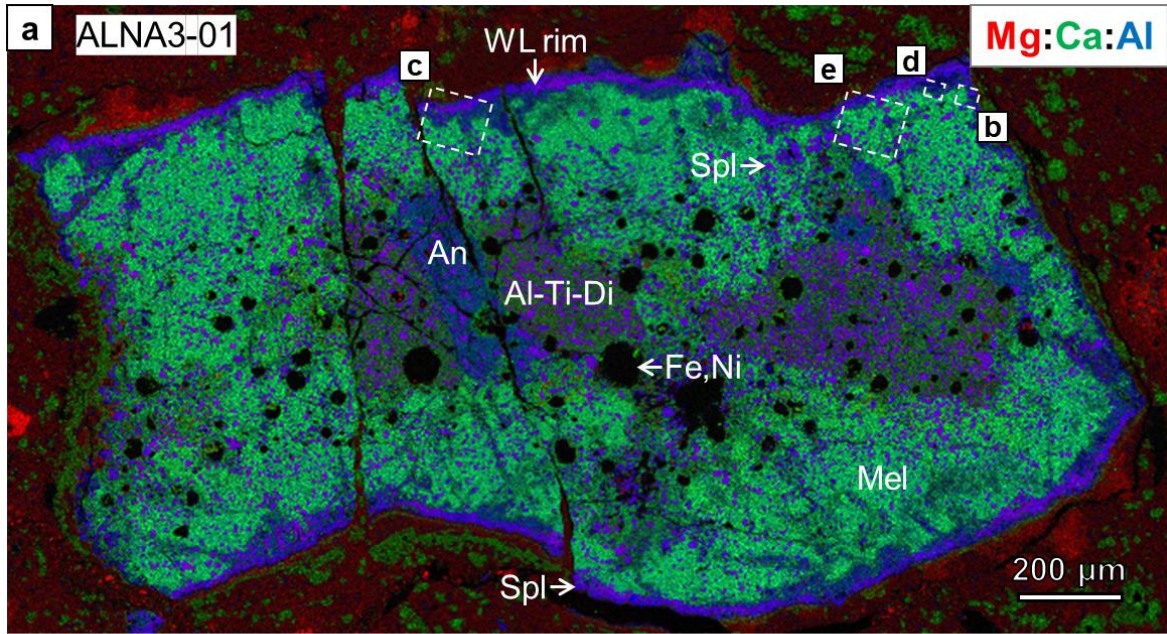


Fig. 1. Combined X-ray elemental map in Mg (red), Ca (green), and Al (blue) (a) and BSE images (b-e) of a slightly altered Type B1 CAI ALNA3-01 from Allende. This CAI contains abundant rounded Fe,Ni metal grains that have been partly or completely altered to sulfides. (b) Melilite on the periphery of this CAI has been replaced by a secondary sequence of grossular-Ca-rich feldspar-nepheline, which forms a narrow alteration zone inside the WL rim. (c) Some grossular grains have been partially replaced by Ca-rich feldspar. Both lath-shaped and fine-grained, massive Ca-rich feldspars are observed. (d) Some fine-grained, fibrous high-Z phases (indicated by yellow arrows) are commonly observed to be interstitial to Ca-rich feldspar. (e) Secondary veins in melilite also have a layered structure, with an outer grossular layer and an inner Ca-rich feldspar layer. These veins are connected to the secondary alteration sequence on the periphery of the CAI. Abbreviations: Al-Ti-Di = Al-Ti-rich diopside, An = anorthite, Di = diopside, Fe,Ni = Fe,Ni-rich metal, Fsp = Ca-rich feldspar, Grs = grossular, Mel = melilite, Ne = nepheline, Spl = spinel.

Ca-rich feldspar and nepheline with melilite in local regions. Close to the melilite alteration front, there are two occurrences of grossular aggregates with different grain sizes (2-5 μm and $<1 \mu\text{m}$). The coarser-grained grossular is commonly located more adjacent to the melilite alteration front, giving way to finer-grained grossular. There is also a difference in porosity in the two occurrences of grossular: more abundant pores are observed along grain boundaries of fine-grained grossular. Some grossular grains have been partially replaced by lamellae of Ca-rich feldspar (Fig. 1c). Two occurrences of Ca-rich feldspar that are closely associated with each other have been observed: lath-shaped and fine-grained, massive. Besides grossular, there are some fine-grained, fibrous, high-Z phases ($<1 \mu\text{m}$) that are interstitial to Ca-rich feldspar (Fig. 1d). Nepheline is not always present in the alteration sequence of melilite, and when present, it usually occurs as thin lamellae replacing Ca-rich feldspar, or as a pore-filling phase. In ALNA3-01, secondary phases are also present along veins, and in most cases, these veins have a zoning structure, with an inner Ca-rich feldspar layer and an outer grossular layer (Fig. 1e).

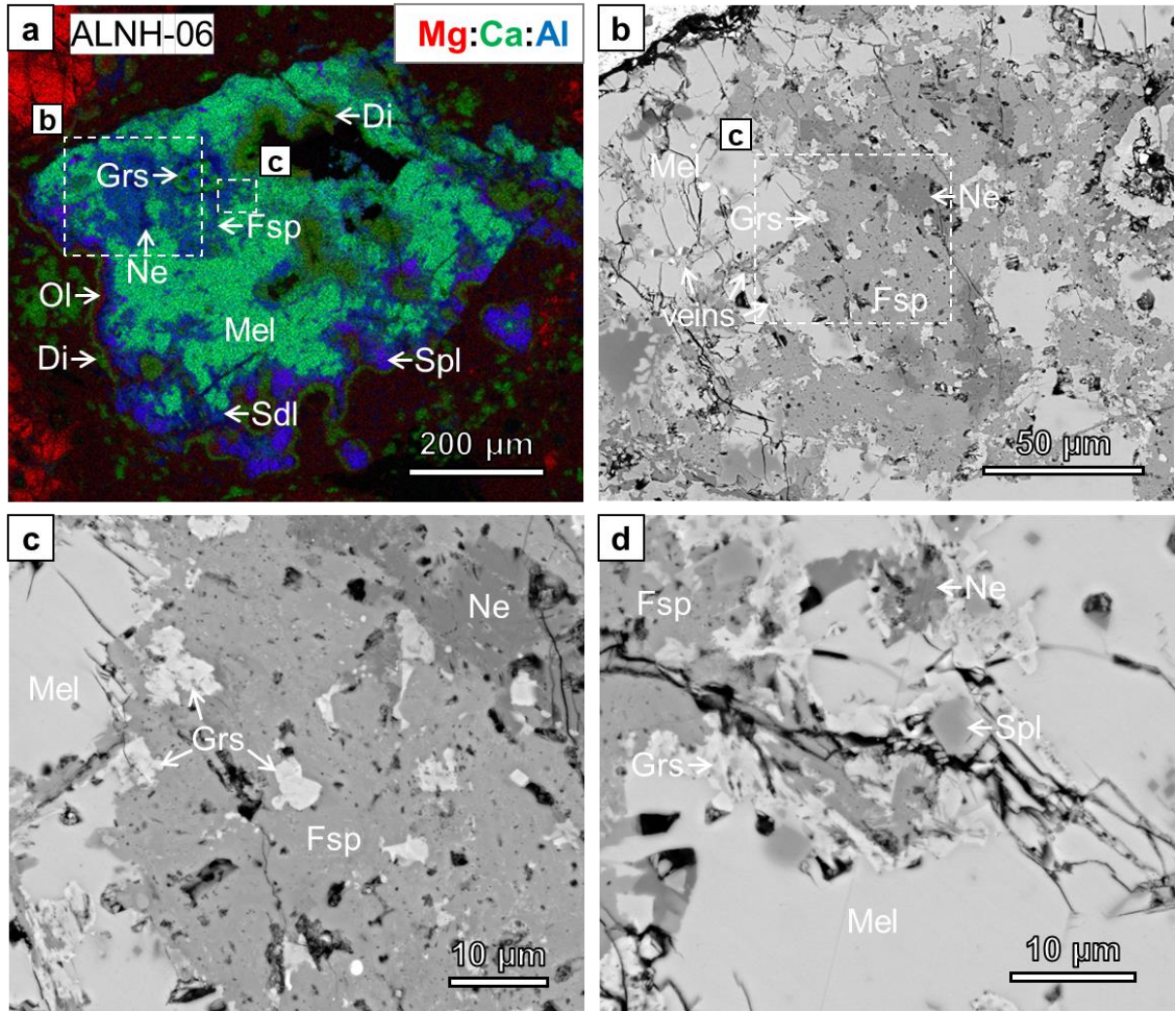


Fig. 2. Combined X-ray elemental map in Mg (red), Ca (green), and Al (blue) (a) and BSE images (b-d) of a moderately altered compact Type A CAI ALNH-06 from Allende showing the textural relationships between melilite and secondary phases. (b-c) A general alteration sequence of grossular, Ca-rich feldspar, and feldspathoids is observed in melilite. Grossular forms thin layers while Ca-rich feldspar is the dominant secondary phase. Grossular islands are present interstitial to Ca-rich feldspar. Feldspathoids are sometimes in direct contact with melilite or grossular. (d) Grossular often shows a replacement relationship with Ca-rich feldspar. Abbreviations: Di = diopside; Fsp = Ca-rich feldspar; Grs = grossular; Mel = melilite; Ne = nepheline, Ol = Fe-rich olivine; Sdl = sodalite, Spl = spinel.

3.1.2. Moderately altered melilite-rich CAIs

Some melilite-rich CAIs show more intense secondary alteration, with formation of

significant amounts of secondary phases. Examples include ALNH-06 and ALNG-01, both of which are compact Type A CAIs. In these CAIs, melilite has been replaced by a secondary layered zone of grossular-Ca-rich feldspar-feldspathoids (nepheline \pm sodalite) (Fig. 2-3), which is similar to those observed in slightly altered CAIs. The major difference is that the alteration zone in ALNH-06 and ALNG-01 is wider and develops into the inner regions of the CAIs. In the alteration sequence, grossular usually forms thin and discontinuous layers, separating melilite from Ca-rich feldspar (Fig. 2b-c, 3b-c). Grossular ($<5 \mu\text{m}$) and Ca-rich feldspar ($<5 \mu\text{m}$) often show highly embayed interfaces, and sawtooth interfaces are commonly observed (Fig. 2d and 3d), suggesting grossular has been partially replaced by Ca-rich feldspar. Calcium-rich feldspar is the dominant secondary phase replacing melilite in ALNH-06 and ALNG-01, and similar to slightly altered CAIs, this feldspar phase shows both lath-shaped and fine-grained, massive occurrences. Grossular grains ($<5 \mu\text{m}$) with a rounded shape are often present as islands in the Ca-rich feldspar layers (e.g., Fig. 2c and 3c). A high porosity has been observed in Ca-rich feldspar layers, and many of the pores are filled by feldspathoids and some fine-grained phases. Feldspathoids (from $<1 \mu\text{m}$ to $\sim 5 \mu\text{m}$) are typically the phases furthest from the melilite alteration front, though they also occur as patches that are randomly distributed in grossular and Ca-rich feldspar layers (e.g., Fig. 2d and 3c). Porosity is less developed in feldspathoid layers, compared with grossular and Ca-rich feldspar. Veins that are several micrometers thick and show the same layered sequence as the major alteration zones are also observed. These veins are extended from the major alteration zones into less altered melilite grains (Fig. 2b).

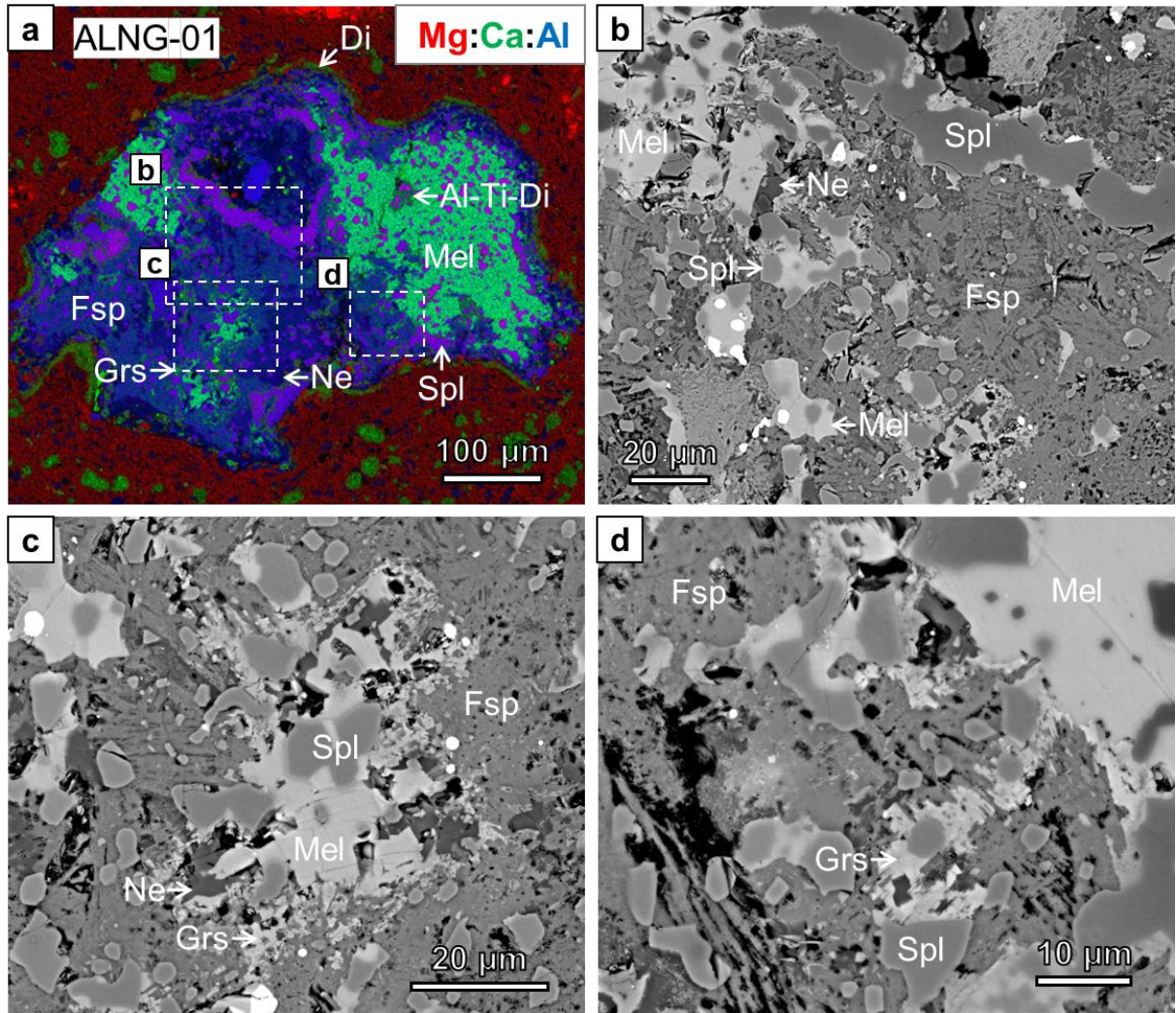
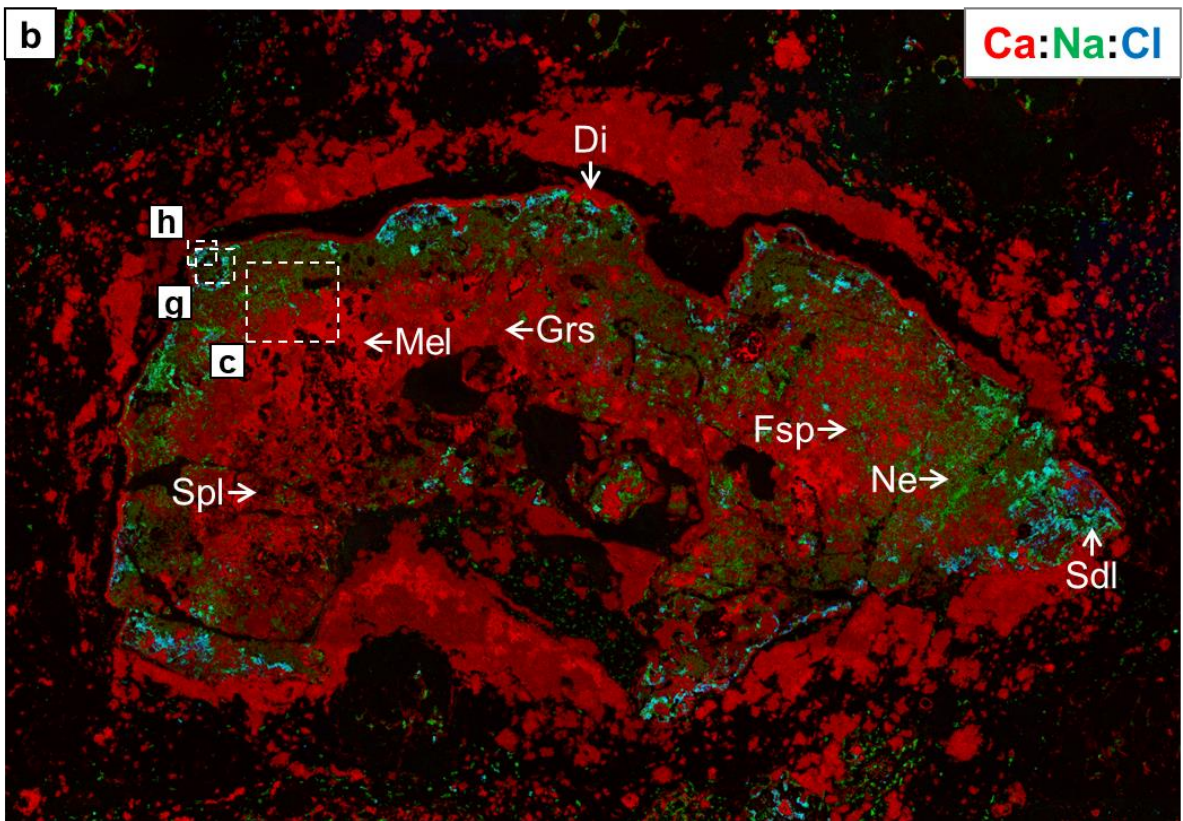
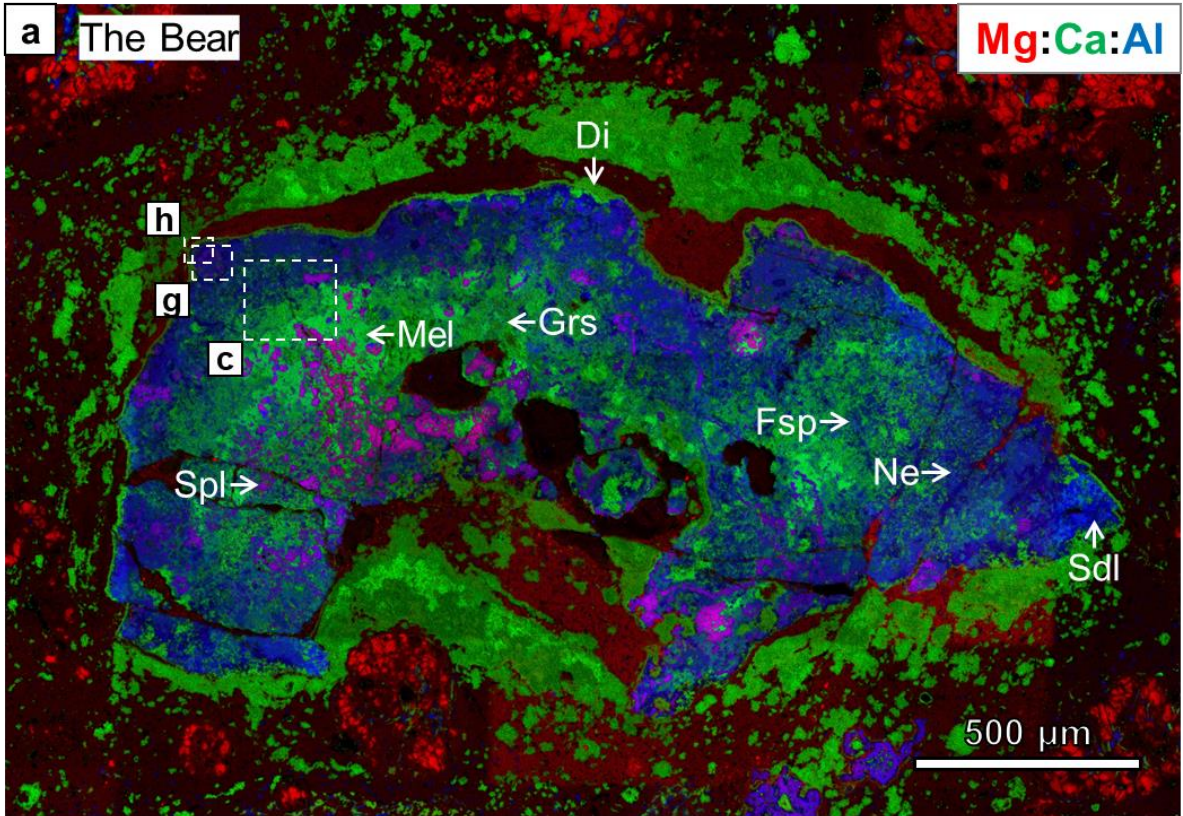


Fig. 3. Combined X-ray elemental map in Mg (red), Ca (green), and Al (blue) (a) and BSE images (b-d) of a moderately altered compact Type A CAI ALNG-01 from Allende. (b-c) Melilite in the CAI has been replaced by an alteration sequence of grossular-Ca-rich feldspar-nepheline. There are two forms of Ca-rich feldspar in this CAI: lath-shaped and fine-grained, massive. Nepheline can also have direct contact with melilite and grossular locally. (d) Grossular has highly embayed interfaces with Ca-rich feldspar and often has been partially replaced by lamellae of Ca-rich feldspar. Abbreviations: Al-Ti-Di = Al-Ti-rich diopside, Di = diopside, Fsp = Ca-rich feldspar, Grs = grossular, Mel = melilite, Ne = nepheline, Spl = spinel.

3.1.3. Extensively altered melilite-rich CAIs

There are a few melilite-rich CAIs that show extensive alteration, resulting in nearly

complete replacement of melilite. Since these CAIs show very similar alteration styles, here we only describe a large (~1.5 mm in size) compact Type A CAI “The Bear” (Fig. 4) from the ALNG thin section. Most of the primary melilite grains have been replaced by a secondary zonation of grossular-Ca-rich feldspar-nepheline-sodalite. The thickness of this secondary zone varies in different regions, but is typically ~300 μm . The grossular layer is about 150 μm in thickness, and grains closer to the melilite alteration front are coarser-grained (up to 5 μm) and have a higher porosity along grain boundaries than those further away (<1 μm) (Fig. 4d-e). Calcium-rich feldspar occurs as randomly distributed patches in the grossular layer and is often replacing grossular, as implied by their highly embayed interfaces. Nepheline is also commonly observed in this layer and often shows a replacement relationship with Ca-rich feldspar along crystallographically controlled planes (e.g., Fig. 4e). Porosity, with a typical pore size of <1 μm , is high in the grossular layer, and some pores are filled with Ca-rich feldspar and nepheline. The Ca-rich feldspar layer has an average thickness of ~100 μm and is an intimate intergrowth of lath-shaped and fine-grained, massive crystals (Fig. 4f). A significant amount of nepheline is present in this layer, commonly replacing Ca-rich feldspar grains. There are also grossular grains forming irregular-shaped blotches in the Ca-rich feldspar layer, and the interfaces between grossular and Ca-rich feldspar are highly curved and often embayed. Similar to melilite-rich CAIs that show less degrees of alteration, the Ca-rich feldspar layer in this CAI contains abundant fine-grained, fibrous high-Z phases (<1 μm) that are interstitial to Ca-rich feldspar and nepheline. Many of the pores in the Ca-rich feldspar layer are significantly larger (typically between 2 and 5 μm) than those in the grossular layer.



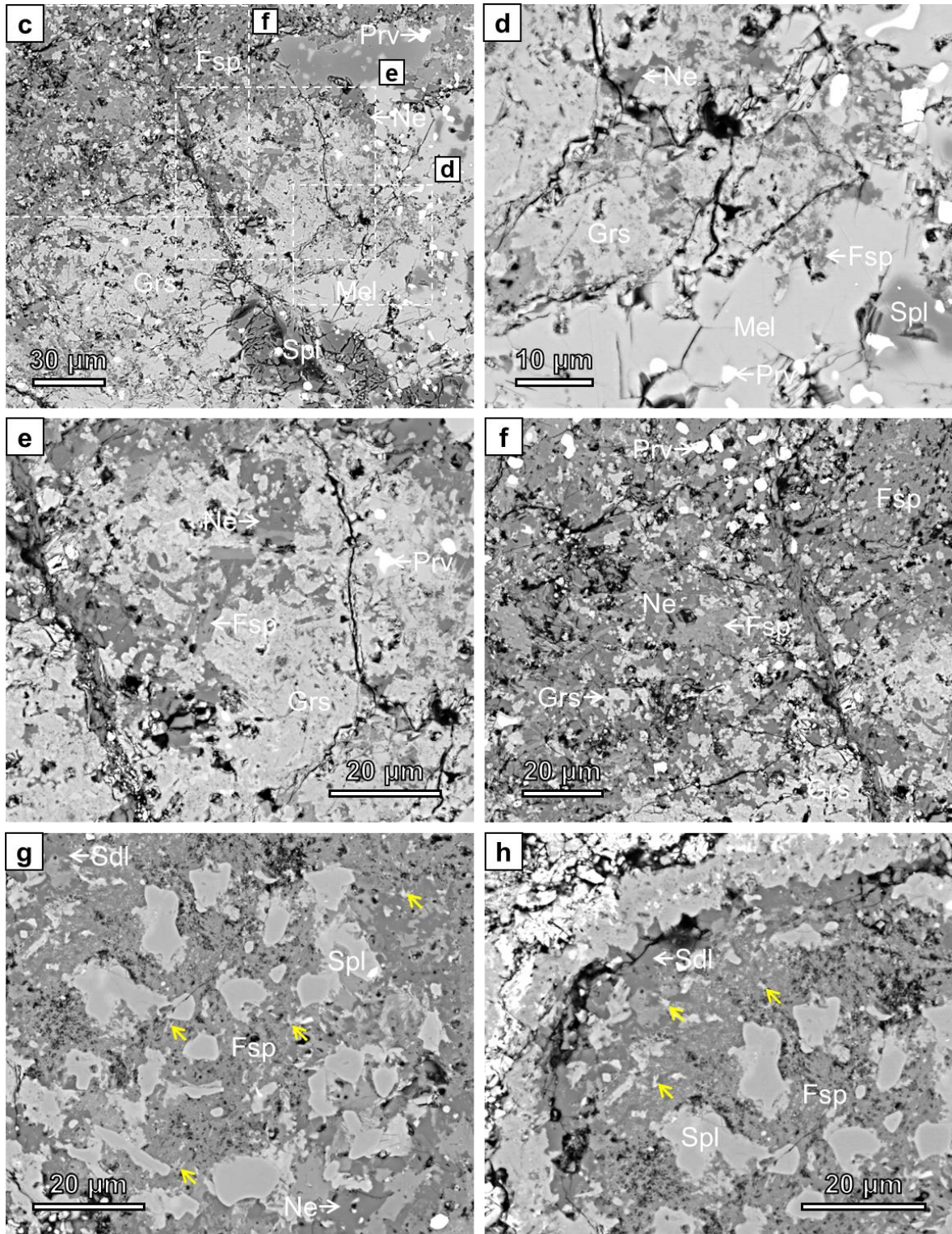


Fig. 4. Combined X-ray elemental maps (a-b) and BSE images (c-h) of an extensively altered compact Type A CAI “The Bear” from Allende. (a-b) X-ray maps showing the secondary zonation of grossular-Ca-rich feldspar-nepheline-sodalite. Only a minor amount of melilite is preserved in the inner region.

Fig. 4. (*continued*) (c-h) Higher-magnification BSE images showing the detailed textures of the alteration sequence. (d-e) The grossular layer is composed of a coarse-grained and compact inner layer and a fine-grained outer layer. Porosity is more well-developed in the fine-grained layer. Many grossular grains have been partially to completely replaced by Ca-rich feldspar. (e-f) The Ca-rich feldspar layer contains two occurrences of feldspar: lath-shaped and fine-grained. Both occurrences of feldspar show replacement relationships with nepheline. Grossular islands are also present in this layer. (g-h) Sodalite forms a thin layer on the periphery of the CAI inside the WL rim. There are abundant fine-grained fibrous phases (indicated by yellow arrows) that are interstitial to Ca-rich feldspar and feldspathoids. Abbreviations: Di = diopside, Fsp = Ca-rich feldspar, Grs = grossular, Mel = melilite, Ne = nepheline, Prv = perovskite, Sdl = sodalite, Spl = spinel.

Pores with both elongate and rounded shapes have been observed. The boundary between the nepheline and Ca-rich feldspar layers is not well-defined, because these two phases are usually intimately associated. However, the relative proportion of nepheline increases significantly towards the periphery of the CAI. A low porosity is observed along boundaries between nepheline grains, and between nepheline and Ca-rich feldspar (Fig. 4g). Sodalite is most commonly concentrated in regions within ~30 μm from the WL rim (Fig. 4b,h), although it is also present as a minor phase in other secondary layers. Similar to the nepheline layer, the sodalite layer has a dramatically lower porosity, compared to grossular and Ca-rich feldspar layers.

3.1.4. The alteration features of WL rims on melilite-rich CAIs

The WL rims surrounding melilite-rich CAIs from Allende often show more extensive alteration, compared with the interiors of the CAI hosts. These rims are typically composed of four mineral layers: spinel, feldspathoids (nepheline \pm sodalite), Fe-rich olivine ($\sim\text{Fa}_{20-22}$ based on EDS), and diopside (Fig. 5a-b). The spinel layer is coarse-grained (2-10 μm), and the spinel

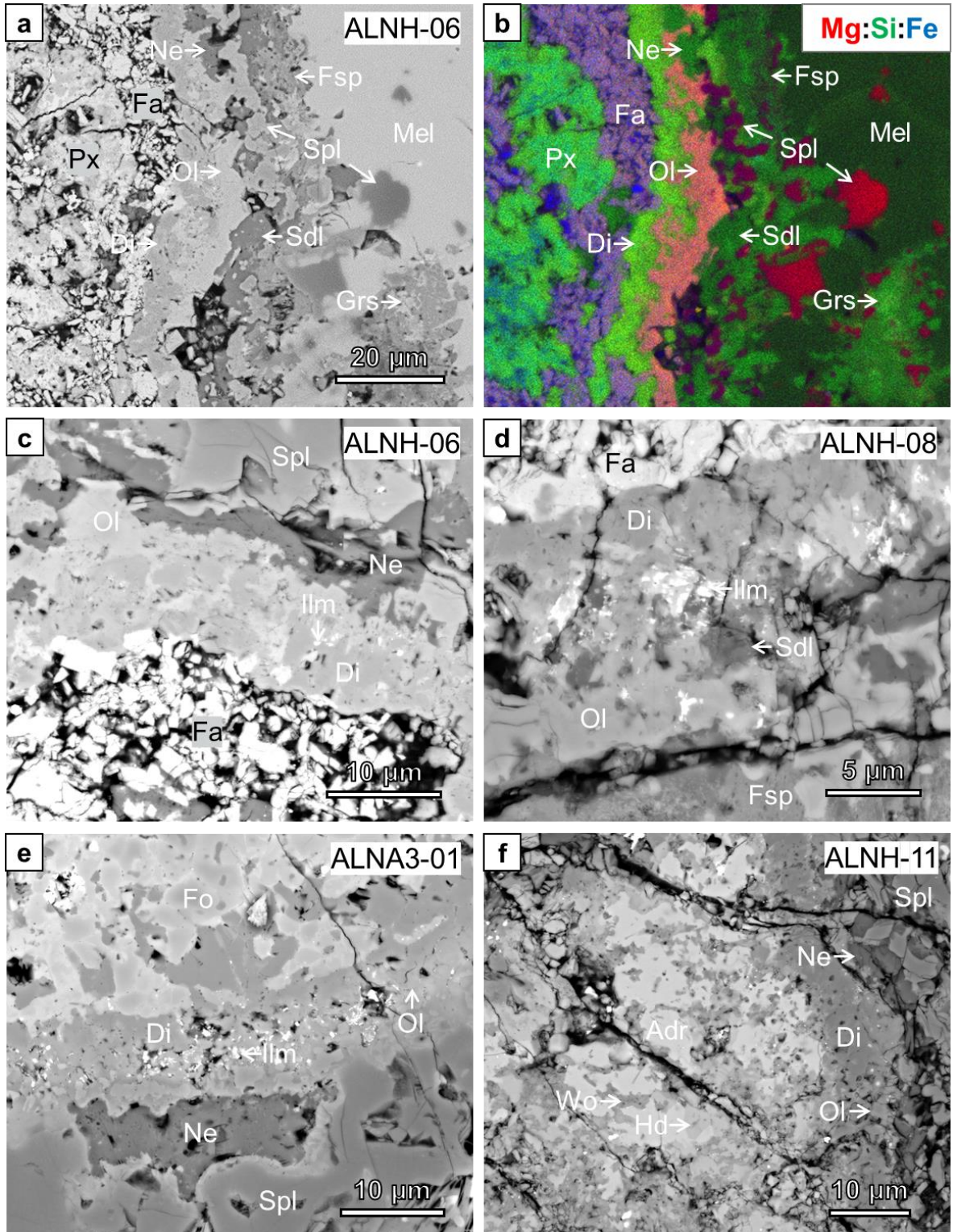


Fig. 5. BSE images (a, c-f) and combined X-ray elemental map in Mg (red), Si (green), and Fe (blue) (b) of WL rims from several Allende melilite-rich CAIs. Four basic layers have been identified: spinel, feldspathoids (nepheline \pm sodalite), Fe-rich olivine, and diopside.

Fig. 5. (*continued*) (a-b) The boundaries between diopside and Fe-rich olivine layers are highly curved and often embayed. (c) Fe-rich olivine is replacing diopside from the inner edge of the diopside layers, forming a mesh texture. (d) Abundant ilmenite grains with random distribution are observed in Fe-rich olivine layers. (e-f) The diopside layer are often overgrown by forsteritic olivine that has been partially altered to Fe-rich olivine, and Ca-Fe-rich assemblages of andradite, Ca-Fe-rich pyroxene (ferroan diopside - hedenbergite pyroxene), and wollastonite. Abbreviations: Adr = andradite, Di = diopside, Fa = fayalitic olivine, Fo = forsteritic olivine, Fsp = Ca-rich feldspars, Grs = grossular, Hd = hedenbergite, Ilm = ilmenite, Ne = nepheline, Ol = Fe-rich olivine, Px = Ca-rich pyroxene, Spl = spinel, Wo = wollastonite.

grains are partially enclosed by melilite from the host CAIs. Feldspathoids usually form thin (<5 μm) and discontinuous layers with a low porosity. Many feldspathoid grains are present as patches interstitial to coarse-grained spinel. Fine-grained spinel ($\sim 1 \mu\text{m}$) showing Fe-enrichment is sometimes observed enclosed in feldspathoids. The average thickness of Fe-rich olivine layers is around 3 μm . Abundant, randomly distributed ilmenite inclusions that are less than 1 μm in size have been observed in Fe-rich olivine layers (e.g., Fig. 5c-d). Porosity is observed in Fe-rich olivine layers, but it is more well-developed than the feldspathoid layers. The number of pores increases significantly on the interfaces between Fe-rich olivine and diopside layers. Such interfaces are highly curved and often embayed. Diopside grains are partially to completely replaced by Fe-rich olivine preferentially along the inner boundary of diopside layers, forming a mesh texture (e.g., Fig. 5c) similar to that commonly observed in terrestrial olivine-rich rocks that have been partly serpentinized. Diopside typically has a grain size of $\sim 4 \mu\text{m}$, though finer-grained diopside (1-2 μm) is present locally with a high porosity along grain boundaries. The diopside layers are often overgrown by forsterite olivine (< $\sim \text{Fa}_{10}$ based on EDS) that has been partially altered to Fe-rich olivine (< $\sim \text{Fa}_{34-37}$ based on EDS) (Fig.

5e). Outside the WL rims on some melilite-rich CAIs, there is sometimes an alteration assemblage that is mainly composed of andradite, Ca,Fe-rich pyroxene (ferroan diopside - hedenbergite pyroxene), and wollastonite (Fig. 5f). Andradite is the dominant phase (>60 %) in these assemblages, and has a grain size of $\sim 3 \mu\text{m}$. Andradite is separated from the diopside WL rim layers by thin layers of Ca,Fe-rich pyroxene. The diopside WL rim layers shows a clear replacement relationship with Ca,Fe-rich pyroxene. Wollastonite is intimately associated with Ca,Fe-rich pyroxene, and sometimes encloses andradite.

3.2. Microstructures

Two FIB sections were lifted out from the CAIs in this study. The first one (FIB-04) is from the interior of an extensively altered Allende CAI (ALNG-01). The second one (FIB-02) is from a WL rim of a moderately altered CAI (ALNA3-01) from Allende. The positions of FIB sections are shown in Fig. 6.

The FIB section FIB-04 was extracted to investigate the microstructure of fine-grained, fibrous high-Z phases that are commonly observed in the melilite alteration sequence. The TEM observations show that the fine-grained, massive Ca-rich feldspars in this FIB section are anorthite (Fig. 7a-b) and are dominantly nanometer-sized crystals, though some grains are coarser ($\sim 20\text{-}30 \text{ nm}$). Porosity is well-developed. There are abundant needle-like or fibrous spinel, with a $\text{Fe}\# (= \text{Fe}/(\text{Fe} + \text{Mg}) \times 100)$ of ~ 29 . Some of the fibrous spinel grow on relatively coarse-grained spinel ($\sim 1 \mu\text{m}$, $\text{Fe}\# = \sim 23$) (Fig. 7c-d). There are also some rounded spinel grains ($\sim 250 \text{ nm}$) that intergrow with the fibrous spinel.

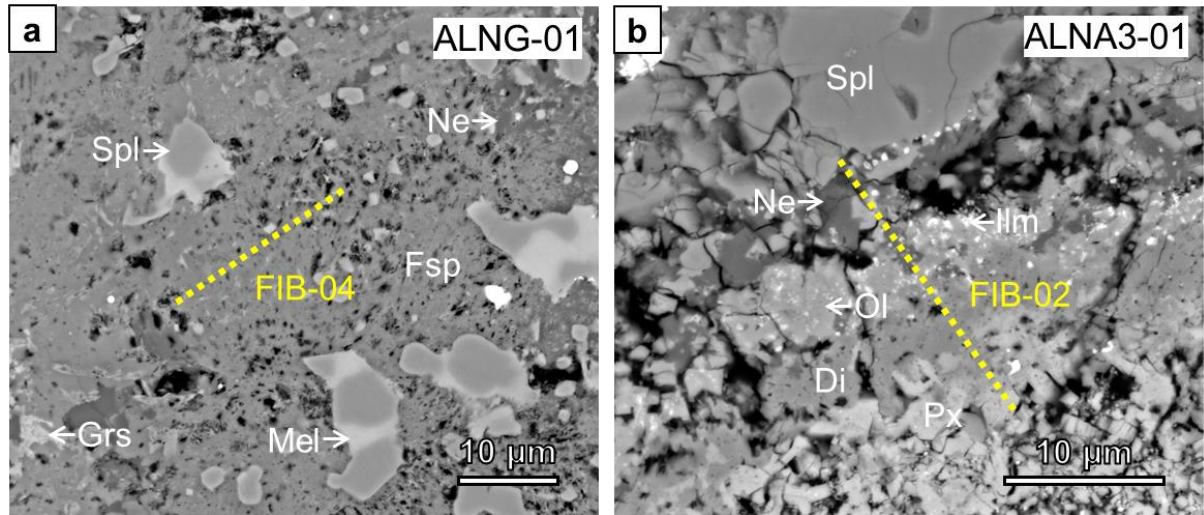


Fig. 6. The positions of the FIB sections for this study. (a) FIB-04 is from the fine-grained Ca-rich feldspar in ALNG-01 from Allende, and (b) FIB-02 was extracted from the WL rim on ALNA3-01 from Allende. Abbreviations: Di = diopside, Fsp = Ca-rich feldspar, Grs = grossular, Ilm = ilmenite, Mel = melilite, Ne = nepheline, Ol = Fe-rich olivine, Px = Ca-rich pyroxene, Spl = spinel.

The FIB section FIB-02 samples a sequence of spinel-nepheline-Fe-rich olivine-diopside. The DF-STEM mosaic image of the FIB section (Fig. 8a) reveals a complex alteration structure. The spinel layer contains several rounded perovskite grains (~300 nm) that have been partially altered to ilmenite. Porosity is observed along grain boundaries in the nepheline layer (Fig. 8b). There are also ilmenite grains (~120 nm) that are enclosed in nepheline or dispersed along nepheline grain boundaries. The olivine layer has a low porosity and is composed of Fe-rich olivine (Fa₂₀₋₂₅) that is typically 200 nm in size (Fig. 8c). Abundant ilmenite grains (<~150 nm) are present between olivine grains. The olivine layer extends into the diopside layer which consists of subhedral grains 300-400 nm in size (Fig. 8d). The STEM image shows that individual diopside grains are compositionally homogeneous, with thin, Fe-enriched rims (<~20 nm). Many diopside grains remain intact but their rims often contain abundant pores.

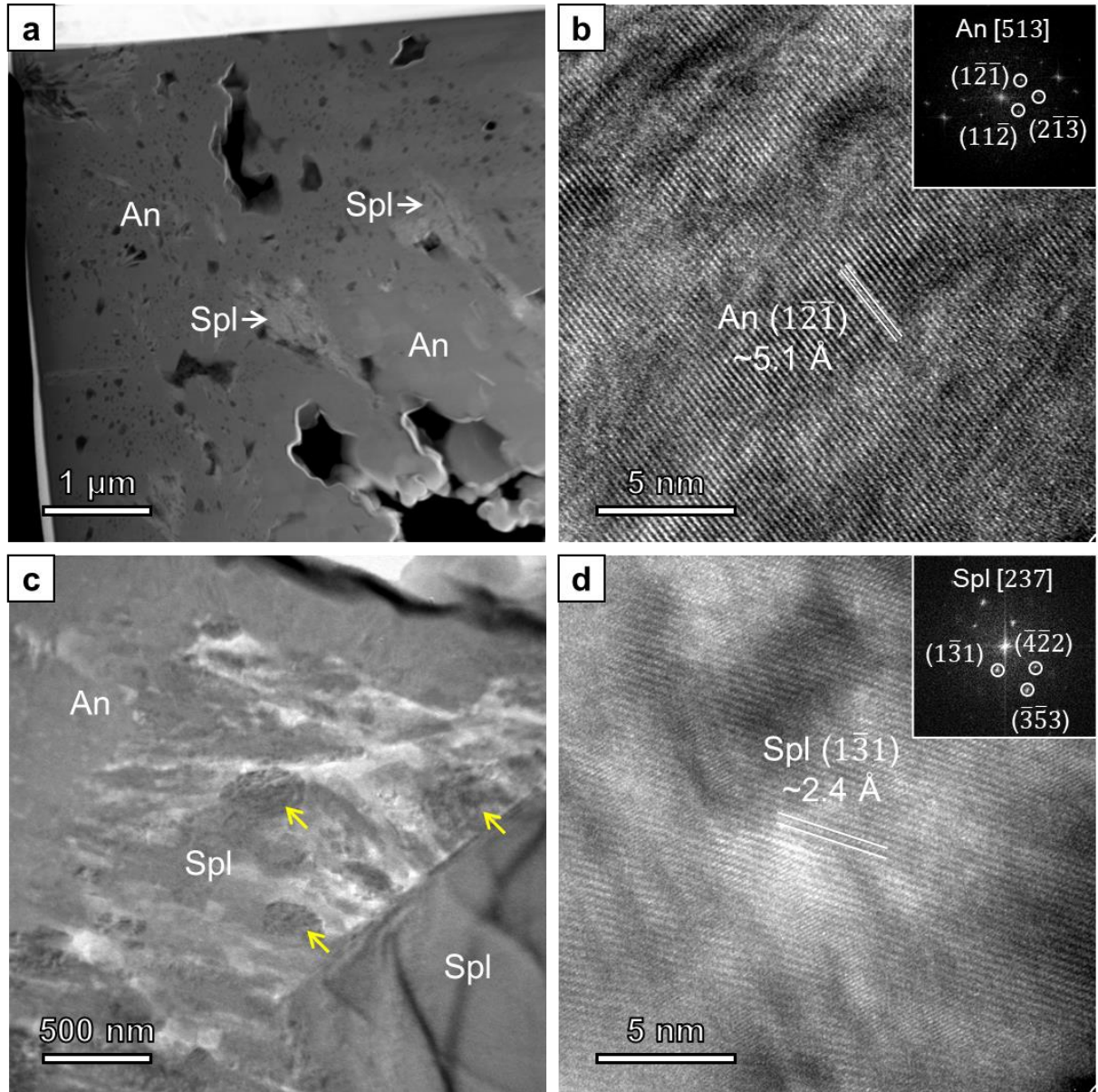


Fig. 7. TEM images of fine-grained, massive Ca-feldspar in FIB-04. (a) DF-STEM image of the Ca-feldspar grains showing that the fine-grained nature of these grains and the presence of a high density of pores. Some fibrous or needle shaped spinel grains are present. (b) HRTEM image of the fine-grained, massive Ca-feldspar showing lattice fringes that are consistent with anorthite. The insert is an FFT pattern that can be indexed as the [513] zone axis of anorthite. (c) BF-TEM image showing that fibrous spinel overgrows on coarse-grained spinel. There are also some fine-grained, rounded spinel grains (indicated by yellow arrows) coexisting with the fibrous spinel. (d) HRTEM image of a fibrous shaped spinel. The insert is the FFT pattern which can be indexed as the [237] zone axis of spinel. Abbreviations: An= anorthite, Spl = spinel.

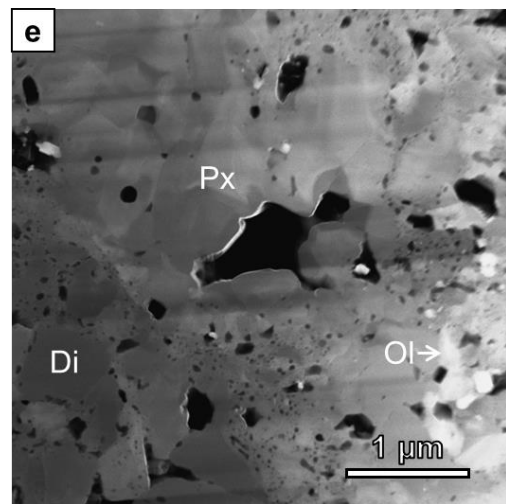
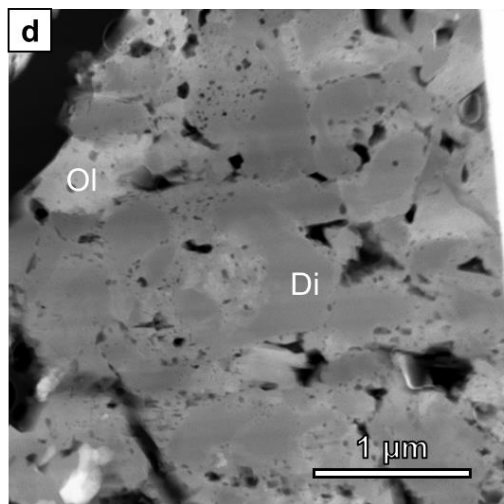
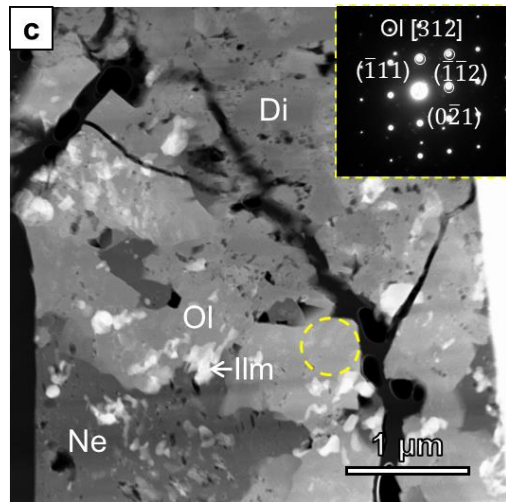
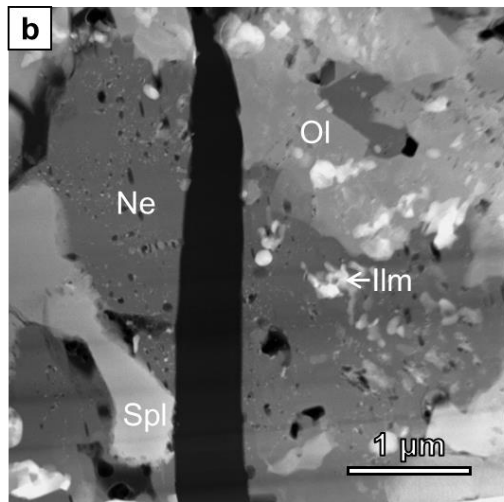
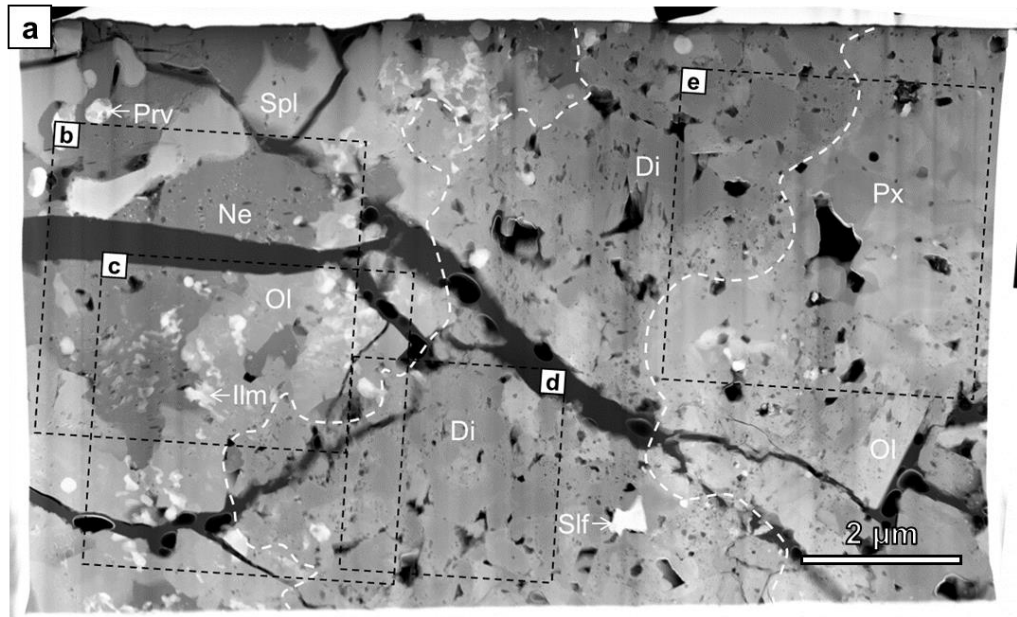


Fig. 8. Dark-field STEM images of FIB-02 that was extracted from the altered WL rim on ALNA3-01 from Allende. The inner and outer boundaries of the diopside layer are outlined by the white dashed lines in (a). The sequence of this WL rim is spinel-nepheline-Fe-rich olivine-diopside. (b) Primary anorthite has been completely altered to nepheline, and pores are present along the grain boundaries. Ilmenite nanoparticles occur as inclusions in nepheline. (c) The inner part of the diopside layer has been altered to Fe-rich olivine. A selected area diffraction pattern from the circled area can be indexed as the olivine [312] zone axis. Ilmenite is present in the Fe-rich olivine layer. (d) In the diopside layer, porosity is developed along grain boundaries and in rims of diopside grains. Some diopside grains have been pseudomorphed by Fe-rich olivine. (e) The diopside layer is overgrown by a Ca-rich pyroxene (diopside-hedenbergite solid solution) assemblage in the matrix. Abbreviations: Di = diopside, Fe,Ni = Fe,Ni-rich metal, Fo = forsteritic olivine, Ilm = ilmenite, Ne = nepheline, Ol = Fe-rich olivine, Prv = perovskite, Px = Ca-rich pyroxene, Slf = sulfides, Spl = spinel.

Some diopside grains have been pseudomorphed by Fe-rich olivine. The diopside layer is overgrown by a Ca-pyroxene ($\text{Di}_{15-70}\text{Hd}_{30-95}$) layer with low porosity that also contains lath-shaped, Fe-rich olivine (Fa_{35-40}), nepheline, and sulfides (Fig. 7e).

4. DISCUSSION

Our SEM and TEM investigations reveal that an alteration sequence of grossular-Ca-rich feldspar-feldspathoids is present in all the Allende melilite-rich CAIs. Such a sequence develops further into the interior of the CAIs with increasing degrees of alteration. It is important to understand the origin of such a sequence in the context of fluid-assisted metamorphism, which has affected all the components in CV3 chondrites. We first take advantage of chemical potential diagram to explain the formation of the alteration sequence of melilite. Then we use the microchemical environment hypothesis to explain the complex alteration microstructures of WL rims on melilite-rich CAIs.

4.1. The alteration sequence of melilite

In all the Allende melilite-rich CAIs we have studied, melilite has been replaced by the same sequence of secondary minerals. Grossular is usually the phase that is directly in contact with melilite, and further away from the grossular-melilite interface is Ca-rich feldspar. Feldspathoids are often the outermost phases in the alteration sequence. Such a grossular-Ca-rich feldspar-feldspathoids alteration sequence has been observed in all the Allende melilite-rich CAIs, with the magnitude of the alteration zone increasing with more extensive alteration. In relatively less-altered CAIs, ALNA3-01 for instance, the secondary phases are often restricted in a narrow region inside the WL rims. With an increasing degree of alteration, the alteration front progressively migrates towards the interior of the CAIs until no melilite is preserved. The interfaces between adjacent secondary phases also move inward with the alteration front. The thickness of each layer in the alteration sequence, however, does not always increase proportionally with the alteration degree. For example, the grossular layer is often thicker than the other two layers in slightly altered CAIs, while in moderately altered CAIs, grossular typically forms a thin discontinuous layer that shows significant replacement by Ca-rich feldspar. The presence of melilite-rich CAIs with different degrees of alteration suggests that the local availability of fluid may vary even on the thin section scale. Since the alteration textures we now observe represent the arrested reaction textures, different degrees of alteration may be products of either a continuous movement of fluid alteration front, or episodic fluid infiltration events.

4.1.1. The effect of chemical potential gradient

The presence of grossular inclusions in Ca-rich feldspar, together with commonly observed embayed shape of grossular-Ca-rich feldspar interface, apparently implies a replacement relationship between grossular and Ca-rich feldspar. On the other hand, the observation that Ca-rich feldspar is present in the least altered CAIs in our samples possibly indicates that grossular and some Ca-rich feldspar formed almost contemporaneously. Mineralogical layered reaction zones have been reported in many terrestrial metamorphic rocks, and it represents an arrested reaction during the metamorphic history (e.g., Fisher, 1977; Joesten, 1977; Fisher and Lasaga, 1981; Foster, 1981; Ashworth and Birdi, 1990; Guiraud et al., 2001; Carlson, 2002; Powell, 2002; Proyer, 2003; White et al., 2008; White and Powell, 2011). Such reaction zones may imply a partial equilibration process because of the chemical potential gradients of some components in these systems. One way to investigate the layered alteration structure is to establish the chemical potential relationships between reactants and products (e.g., White et al., 2008). Comparing the layered structure in our CAIs with the terrestrial skarns, it is very likely that the ubiquitous melilite-grossular-Ca-rich feldspar-feldspathoids sequence in CAIs represents a sequence of phases on a chemical potential gradient. In other words, all the secondary phases formed probably contemporaneously, but they have different stability fields with respect to the fluid chemistry.

To apply the chemical potential diagram method to our samples, it is necessary to know the nature of the medium through which the diffusion processes occurred and the chemical components involved in the diffusion. It has been inferred that Allende CAIs have experienced

metasomatic alteration, where a fluid phase was involved (see Brearley and Krot, 2013). The porosity observed in Allende CAIs clearly indicates a dissolution process which was very likely caused by the infiltration of fluid (e.g., Krot et al., 2007, 2010; Fagan et al., 2007). Additionally, petrological observations suggest that during alteration, Si, Na, Fe, and Mg were introduced, whereas Ca and Al were lost from or redistributed within the CAIs (Hashimoto and Grossman, 1987; McGuire and Hashimoto, 1989; Ford and Brearley, 2008; Krot et al., 2010; Brearley and Krot, 2013). The diffusion of these chemical components is achieved via solid-fluid exchange, and in this process, the mobile components are responsible for the establishment of chemical potential gradients. In our melilite-rich CAIs, Ca and Si are the two elements that are most relevant to the observed alteration sequence. Other components that are necessary to describe the alteration sequence include Al_2O_3 and Na_2O (sodalite was not added to the system for simplicity).

In order to construct a chemical potential diagram, we first made an orthogonal compatibility diagram with molar ratios $\text{CaO}/\text{Al}_2\text{O}_3$ and $\text{SiO}_2/\text{Al}_2\text{O}_3$ as the axes (Fig. 9a), assuming that Al_2O_3 is the least mobile component during the alteration. The presence of fibrous spinel in our FIB sections implies that Al_2O_3 is less mobile than CaO and SiO_2 , and during the alteration process, the latter two species diffused more rapidly, while Al_2O_3 precipitated closer to the alteration interface of melilite. On the other hand, Na_2O is considered as an extremely mobile component, and is therefore regarded as constant across the whole reaction zone. A qualitative $\mu\text{CaO}-\mu\text{SiO}_2$ diagram (Fig. 9b) can be constructed based on the shape of compatibility diagram, as lines in a $\mu-\mu$ diagram are orthogonal to tie lines in the

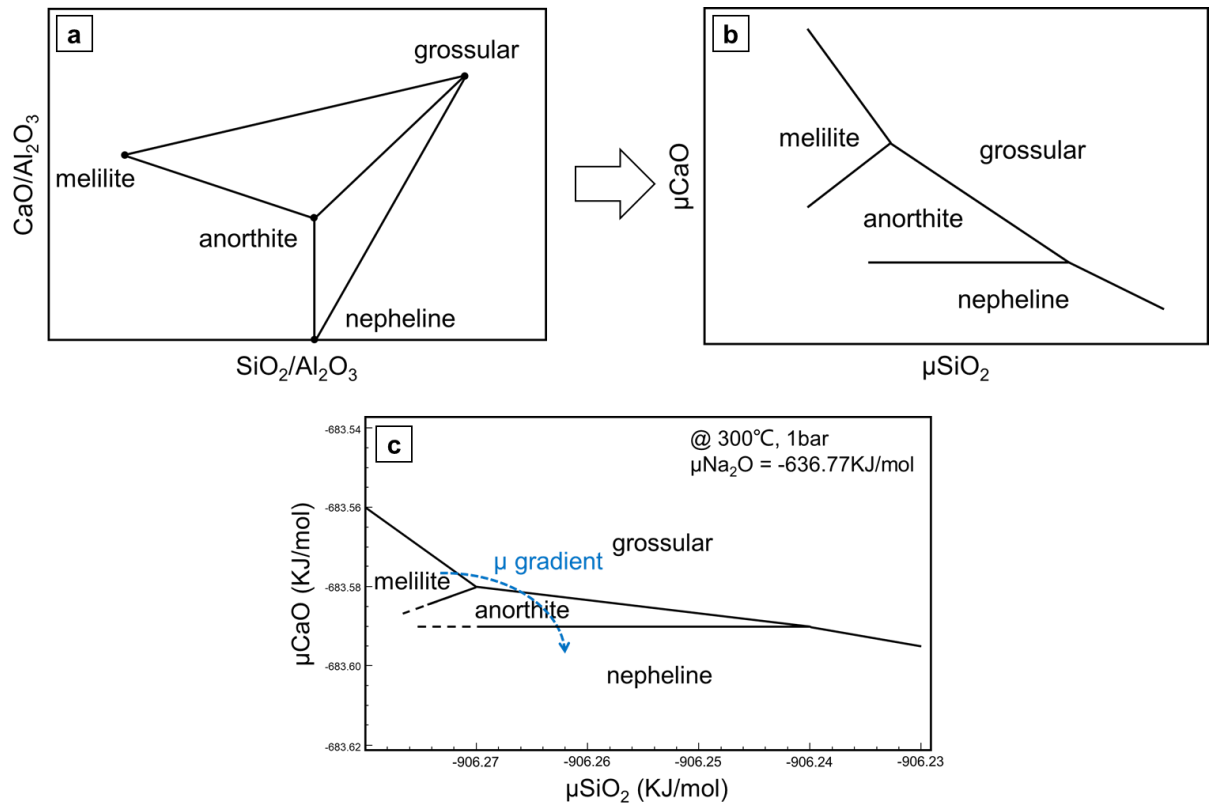


Fig. 9. A chemical potential diagram constructed using the thermodynamic database of Holland and Powell (2011). The conditions are 300°C and 1bar. A qualitative diagram (b) was first constructed based on the tie lines in the compatibility diagram (a). A quantitative diagram (c) was then drawn using the free energy data from the database. The observed alteration sequence in melilite-rich CAIs can be explained as alteration along a μCaO - μSiO_2 gradient, as shown schematically by the blue trend in (c). Since grossular is ubiquitous in the sequence and it often has been partially replaced by Ca-rich feldspar, we only consider the situation where the gradient trend passes the grossular stability field. The extensions of melilite-anorthite and anorthite-nepheline lines are thus drawn as dashed lines.

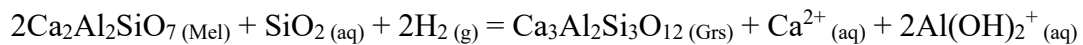
corresponding compatibility diagram (Korzhinskii, 1959; White et al., 2008). Points in the compatibility diagram occur as fields in the μ - μ diagram, tie lines as reaction lines, and triangle fields as intersections. A quantitative μCaO - μSiO_2 diagram (Fig. 9c) was then constructed using the internally consistent thermodynamic dataset of Holland and Powell (2011), and the physical conditions are set at 300°C and 1 bar. All the minerals are considered as pure

endmember phases (e.g., melilite is calculated as gehlenite). The general shape of the diagram would remain the same under a different temperature-pressure condition. The thermodynamic data for dmisteinbergite are not available in the dataset, so we used the data of anorthite to calculate the stability field of Ca-rich feldspar. This does not affect our conclusion, since anorthite and dmisteinbergite have the same chemical formula. With Figure 9c, we can explain the observed melilite-grossular-Ca-rich feldspar-feldspathoids alteration sequence: such a sequence formed on a μCaO - μSiO_2 gradient, as illustrated by the blue arrow in the figure. Decomposition of melilite produced a gradient with the activity of CaO decreasing progressively further away from the alteration front. The establishment of the μSiO_2 gradient is the effect of the equilibration process between aqueous SiO_2 released from melilite dissolution and that originally in the fluid.

4.1.2. Complexities of the alteration sequence

There are some complexities in the alteration sequence. In the alteration sequence of our melilite-rich CAIs, grossular often shows two distinct forms that differ from each other in the grain size and porosity. The relatively coarse-grained, pore-deficient grossular typically grows along the alteration front, while the finer-grained, pore-rich grossular is present further away from the altered melilite, and the pores are usually filled with Ca-rich feldspar. There is a continuous transition between the two forms of grossular. Two occurrences of grossular have been previously reported by several authors (Krot et al., 2007, 2010; Fagan et al., 2007) in Allende Type A, B, and C CAIs. In their work, coarse-grained grossular is closely associated

with other secondary minerals, including monticellite, wollastonite, forsterite, Na-melilite, and wadalite, while fine-grained grossular forms veins. We can gain insights into the formation mechanisms of two occurrences of grossular using the melilite-grossular replacement reaction. Two of the major factors controlling the development of porosity in fluid-induced alteration are the molar volumes and solubility differences of the reactant and product (e.g., Putnis, 2002; Pollok et al., 2011; Ruiz-Agudo et al., 2014). The molar volumes of gehlenite and grossular are 90.32 and 129.84 cm³/mol (WWW-MINCRYST), respectively. A reaction forming grossular from melilite can be written as follows:



where the aqueous aluminum species is considered as Al(OH)₂⁺, one of the dominant species of aluminum in an acidic fluid (e.g., Antonangelo et al., 2017). Aluminum can dissolve into water, forming complex ions and hydroxide ions. The acidic fluid conditions on carbonaceous chondrite parent bodies, as suggested by previous studies (Rosenberg et al., 2001; Zolotov and Mironenko, 2007; Zolotov, 2012), may have enhanced the solubility of Al (e.g., Anderson and Burnham, 1983; Azimov and Bushmin, 2007; Zolotov and Mironenko, 2007). The mobility of Al in melilite-rich CAIs is evidenced by the presence of fine-grained, fibrous Fe-rich spinel. However, the dissolved aluminum does not need to migrate significantly in the fluid, since it should have been used to form other secondary phases in situ, such as Ca-rich feldspar and feldspathoids. The above reaction shows that the formation of one mole of grossular requires

consumption of 2 moles of melilite. Combined with the molar volume values, this reaction implies a decrease in the overall volume. We therefore should expect development of a high porosity along grain boundaries of grossular, which is in contrast to the presence of the pore-deficient grossular layer on the alteration front. One explanation for the formation of such a relatively compact layer is that, as the alteration proceeds, more solid volume was precipitated than dissolved due to the relative solubility difference of melilite and grossular in the altering fluid. The solubility of a solid phase depends on a number of factors, including fluid composition, temperature, pressure, and pH (e.g., Ruiz-Agudo et al., 2013). For our melilite-rich CAIs, the CaO and SiO₂ activities in the fluid may have played an important role. It is likely that the dissolution of melilite produced a thin interfacial fluid layer that is supersaturated with respect to grossular. The presence of such an interfacial fluid layer has been observed in several experimental studies (e.g., Putnis et al., 2005; Putnis and Austrheim, 2013). The supersaturated interfacial layers may have promoted grain growth of grossular by lowering the nucleation energy (e.g., Putnis, 2015), resulting in the formation of a thin, compact and coarse-grained grossular layer on the alteration front.

Another complexity of the alteration sequence is the distribution pattern of feldspathoids. In general, feldspathoids precipitate at locations furthest from the alteration front. This is consistent with our proposed chemical potential gradient model, in which feldspathoids should be stable at relatively low μ_{CaO} and high μ_{SiO_2} . There are, however, often some deviations from the general trend. These Na-rich phases are often filling the interstitial pores between Ca-rich feldspar. This is particularly obvious in CAIs where lath-shaped Ca-rich feldspar crystals

are present. In addition, feldspathoids are sometimes found to form an innermost layer in the alteration sequence. These observations raise an interesting possibility that the formation of some feldspathoids might have been decoupled from the alteration process that has produced the general alteration sequence. We previously reported a Type C CAI that does not contain melilite (Che and Brearley, 2021). Primary anorthite in this CAI has been replaced by nepheline, sodalite, and Fe-rich olivine to various degrees along grain boundaries and veins. No grossular or secondary Ca-rich feldspar was observed. Such a distinct alteration style can be explained by our chemical potential gradient model. The dissolution of primary anorthite is not capable of producing a CaO activity that is high enough to make the fluid become supersaturated with respect to grossular. Instead, nepheline and sodalite, which can stabilize at a relatively low μ_{CaO} , would be the major precipitates in the anorthite alteration process. This mechanism can also explain the alteration style of chondrule mesostasis and plagioclase, which have been mainly replaced by nepheline and sodalite (e.g., Ikeda and Kimura, 1995; Kimura and Ikeda, 1995; Krot et al., 1998; Brearley and Krot, 2013). Dissolution of melilite, as demonstrated by our chemical potential calculations, generates a high μ_{CaO} in the fluid, which would not stabilize feldspathoids; as a consequence, during the fluid-melilite interaction, feldspathoids could only precipitate at the lower end of the chemical potential gradient. The distribution pattern of feldspathoids in the melilite-rich CAIs from Allende thus requires that, at a certain stage of alteration, the fluid composition became suitable for feldspathoids to form anywhere in the alteration region by replacing Ca-rich feldspars. This could be achieved by diffusion of mobile species in the fluid, which could have progressively erased the compositional gradient

and eventually resulted in equilibrium (e.g., Putnis et al., 2005; Ruiz-Agudo et al., 2014). It is likely that some feldspathoids formed when the activity of CaO in the fluid dropped to a threshold level, and they partially replaced early-formed Ca-rich feldspars and filled the void spaces. This may have occurred at the waning stage of the alteration, the release of Ca was dominantly controlled by replacement of Ca-rich feldspars. The relatively fine-grained nature of Ca-rich feldspars, compared with melilite, could have resulted in a fast rate of fluid alteration, facilitating the formation of these late-stage feldspathoids.

4.2. The effects of secondary alteration on WL rims

There are several differences in the alteration behavior of melilite-rich CAIs and their WL rims, which is mainly caused by the difference in their primary mineralogies. For example, the alteration sequence observed in melilite from the host CAIs is almost absent in the WL rims, which is due to the extensive replacement of melilite in the rims by primary anorthite in the solar nebula. We also observe microscale complexities in the altered WL rims, such as the complex alteration texture of diopside by Fe-rich olivine, and the presence of fine-grained ilmenite that is intimately associated with feldspathoids. Below we discuss the possible mechanisms for the formation of these secondary features.

The most interesting aspect of the diopside alteration is that the alteration started from the inner boundary of the diopside layer and proceeded outwards. The diopside layer is usually overgrown by fayalitic olivine, and a replacement relationship is present between them. The response of the diopside layer to alteration is counterintuitive, since it was the outer boundary

of the diopside layer that was first in contact with the fluid. It is thus expected that the fluid should have begun to alter diopside from the outer margin, and progressively consumed it inwards. To explain such an “abnormal” alteration behavior of diopside, we need to take into consideration of the relative resistance of different primary phases to secondary alteration. Based on numerous petrographic observations of altered CAIs and several hydrothermal alteration experiments (e.g., Hashimoto and Grossman, 1987; Tomeoka et al., 1992; Kojima et al., 1995; Krot et al., 1997, 1999, 2001; Nomura and Miyamoto, 1998; Itoh et al., 2004; Rubin, 2012), diopside is one of the most resistant phases to secondary alteration, whereas anorthite and melilite are the first phases to be altered. The formation of Fe-rich olivine between the primary diopside and anorthite layers implies that the alteration of anorthite may have played an important role in producing the observed outward replacement texture of diopside.

Heterogeneous alteration effects have been widely reported in chondrite samples. Such effects can often be seen on a thin section scale; however, evidence for them has also been found on a micrometer scale (e.g., Chen and Brantley, 2000; Brearley and Chizmadia, 2005; Brearley, 2006; Chizmadia et al., 2008; Palmer and Lauretta, 2011). A good example comes from Brearley (2006), where a barred type IIA chondrule from ALH81002 CM2 chondrite shows more extensive replacement of olivine in the interior than the exterior. This observation is contrary to the expectation that the periphery of chondrules, where the alteration initiated, should be more altered than their interior. The key to this problem lies in the heterogeneous nature of the fluid chemistry. Different primary phases respond to alteration differently. In chondrules, for example, glassy mesostasis is among the phases most susceptible to alteration,

and thus it would have been consumed more rapidly than other phases. In addition, the grain size plays an important role in controlling the alteration rate. In general, a finer grain size (a larger surface area) corresponds to a faster alteration rate. All these factors contribute to the chemical heterogeneity of the altering fluid. For the alteration of silicate phases, the hydrolysis reactions increase the local pH condition due to interactions between protons in the fluid and metal-oxygen bonds in silicates (e.g., Drever, 1997; Reed, 1997; Brearley, 2006). Consequently, silicate phases that contain a low cation content and a high number of Si-O-Si bonds would produce a smaller increase in pH. This, combined with the effects of grain size, is capable of producing different microchemical environments on a very local scale. The generation of these microchemical environments can be promoted if the amount of fluid is limited, as is the case for CV3 chondrites (e.g., Clayton and Mayeda, 1999; Krot et al., 1998; Brearley and Krot, 2013). The existence of these microchemical environments implies that dissolution of silicates in chondritic components is kinetically more rapid than diffusion of dissolved species in the fluid.

This microchemical environment mechanism can be applied to the alteration of WL rims on our melilite-rich CAIs. The dissolution rate of diopside is pH-dependent, as demonstrated by previous hydrothermal experiments (e.g., Schott et al., 1981; Knauss et al., 1993; Chen and Brantley, 1998; Bandstra and Brantley, 2008; Brantley, 2008; Gudbrandsson et al., 2011): the dissolution rate decreases with increasing pH. The observed difference in the dissolution rate of the diopside WL rim layer between the inner and outer boundaries probably suggests different local pH conditions. Thermodynamic calculations show that, in the early solar nebula,

HCl gas condenses as solid $\text{HCl}\cdot 3\text{H}_2\text{O}$ on the pre-condensed mineral grains and water ice particles (Zolotov and Mironenko, 2007). These solid HCl hydrates will be gradually melted on the chondrite parent bodies due to the heat release from short-lived radionuclides, and a low pH solution will form when the temperature reaches the H_2O -HCl binary eutectic point (Zolotov and Mironenko, 2007). An early acidic condition is consistent with previous mineralogical and thermodynamic studies of matrices of CM and CI chondrites (e.g., DuFresne and Anders, 1962; Zolensky et al., 1989; Lee, 1993). The precursor matrix materials outside the diopside WL rim layer would have been finer-grained than anorthite in the rim, and therefore they were altered preferentially. In Allende, the matrix was probably modified extensively before significant alteration of the rim occurred. Consequently, the fluid in the matrix may have had a higher pH during the alteration of the WL rim. This resulted in a faster alteration rate of the inner boundary of the diopside layer during the earliest stages of WL rim alteration.

The precipitation of ilmenite in the altered WL rims likely has recorded a late stage of alteration when the fluid became alkaline enough to stabilize ilmenite. Thermodynamic studies of phase stability in the Ti-Fe- H_2O system show that ilmenite tends to dissolve into an acidic fluid, producing pseudorutile ($\text{Fe}_2^{3+}\text{Ti}_3\text{O}_9$) or rutile depending on the redox condition (e.g., McConnel, 1978; Andriamanana et al., 1984; Kelsall and Robbins, 1990; White et al., 1994; Zhang and Nicol, 2009), but is stabilized in more alkaline solutions. The presence of ilmenite in the feldspathoid and olivine layers of the WL rims thus indicates that the pH of the fluid became suitable for ilmenite to precipitate. This further supports our hypothesis that the

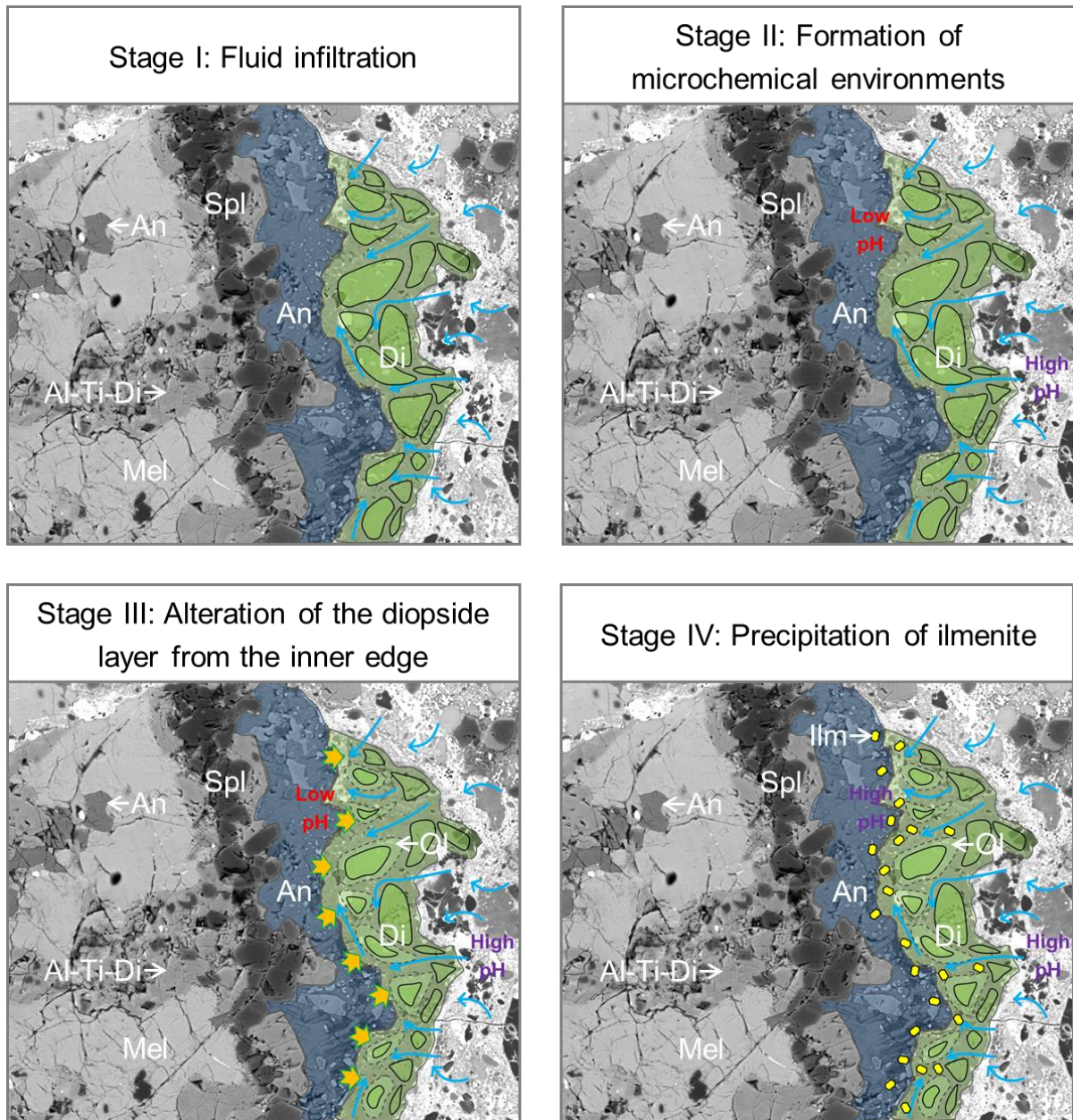


Fig. 10. A schematic diagram illustrating the alteration process of WL rims on Allende melilite-rich CAIs. The CAI on the background is an Efremovka Type B CAI ETS-02 with a relatively pristine WL rim sequence of spinel-anorthite-diopside. Stage I: the fluid was introduced into the WL rim through grain boundaries. Stage II: microchemical environments with different pH conditions were generated in the rim and the matrix. Stage III: diopside grains on the inner edge of the diopside layer experienced more extensive alteration due to the interactions with a more acidic fluid. Stage IV: Ilmenite (yellow, rectangle-shaped crystals) precipitated from the fluid during a late stage of alteration when the fluid pH became more alkaline. Abbreviations: Al-Ti-Di = Al-Ti-rich diopside, An= anorthite, Di = diopside, Ilm = ilmenite, Mel = melilite, Ol = Fe-rich olivine, Spl = spinel.

hydrolysis reactions during the alteration progressively increased the fluid pH. The Ti source for ilmenite may be perovskite in the WL rims, and since perovskite is absent in the unaltered diopside layer, it is possible that many perovskite grains decomposed to aqueous species which diffused outward in the fluid. The precipitation location of ilmenite was likely to be controlled by the least mobile species which, in this case, is the aqueous form of Ti (e.g., TiO^{2+}). Alternatively, since the mobility of Ti has been demonstrated to be very limited in terrestrial metamorphic systems, compared to other elements (e.g., Van Baalen, 1993), the Ti source for ilmenite may be some primary phases in the unaltered diopside layer. It is common for the diopside layer in the WL rims to be compositionally zoned, with decreasing TiO_2 and Al_2O_3 contents towards the matrix (e.g., Han et al., 2019). It is therefore likely that the primary Ti-rich or Ti-bearing diopside grains that have been extensively altered to olivine provided the Ti for the precipitation of ilmenite. The proposed alteration process of the WL rims can be summarized using a schematic diagram (Fig. 10).

5. CONCLUSIONS

Our systematic investigation of melilite-rich CAIs from Allende reveals that the fluid chemistry played an important role in the formation of secondary features in these CAIs. The availability of fluid obviously varied even on the thin section scale, which has resulted in melilite-rich CAIs with different degrees of alteration; however, the same alteration style is observed in these CAIs. The secondary mineralogical zonation in melilite, as well as microscale textural complexities, is the result of the local variations of activities of aqueous

species (e.g., CaO and SiO₂) in the fluid. Such variations were established by the interactions between CAIs and fluid.

The important role of fluid chemistry is further emphasized by the observations of secondary alteration of WL rims on melilite-rich CAIs. The progressive replacement of diopside layers from the inner edge by Fe-rich olivine and the presence of abundant ilmenite grains in the WL rims suggest that localized heterogeneities in pH occurred during the alteration process, which was caused by the difference in the susceptibility to alteration between phases in the matrix and WL rims. Such a pH difference could have been completely erased during more advanced alteration, but some of the resultant secondary features have been preserved in the WL rims, which enables us to gain some insights into the fluid alteration process.

ACKNOWLEDGEMENTS

This work was funded by NASA Cosmochemistry grants NNX15AD28G to A. J. Brearley (PI). We thank Dr. Elena Dobrică and Dr. Ying-Bing Jiang for their help with the TEM operations, and Mike Spilde for his assistance with the electron microprobe analysis. We are grateful to Dr. Aaron Bell and Dr. Steven Simon for helpful discussions and suggestions. Electron microbeam analysis and FIB section preparation were carried out in the Electron Microbeam Analysis Facility, Department of Earth and Planetary Sciences and Institute of Meteoritics, University of New Mexico. The facility is supported by funds from the State of New Mexico, NSF, and NASA.

REFERENCES

- Amelin Y., Krot A. N., Hutcheon I. D. and Ulyanov A. A. (2002) Lead isotopic ages of chondrules and calcium-aluminum-rich inclusions. *Science* **297**, 1678–1683.
- Anderson G. M. and Burnham C. W. (1983) Feldspar solubility and the transport of aluminum under metamorphic conditions. *Am. J. Sci.* **283-A**, 283–297.
- Andriamanana A., Lamache M. and Bauer D. (1984) Etude electrochimique de differentes ilmenites. *Electrochim. Acta* **29**, 1051–1054.
- Antonangelo J. A., Ferrari Neto J., Crusciol C. A. C. and Alleoni L. R. F. (2017) Lime and calcium-magnesium silicate in the ionic speciation of an Oxisol. *Sci. Agric.* **74**, 317–333.
- Ashworth J. R. and Birdi J. J. (1990) Diffusion modelling of coronas around olivine in an open system. *Geochim. Cosmochim. Acta* **54**, 2389–2401.
- Azimov P. Y. and Bushmin S. A. (2007) Solubility of minerals of metamorphic and metasomatic rocks in hydrothermal solutions of varying acidity: Thermodynamic modeling at 400-800°C and 1-5 kbar. *Geochemistry Int.* **45**, 1210–1234.
- Van Baalen M. R. (1993) Titanium mobility in metamorphic systems: A review. *Chem. Geol.* **110**, 233–249.
- Bandstra J. Z. and Brantley S. L. (2008) Surface evolution of dissolving minerals investigated with a kinetic Ising model. *Geochim. Cosmochim. Acta* **72**, 2587–2600.
- Beckett J. R. and Stolper E. (1994) The stability of hibonite, melilite and other aluminous phases in silicate melts: Implications for the origin of hibonite-bearing inclusions from carbonaceous chondrites. *Meteoritics* **29**, 41–65.
- Bischoff A. (1998) Aqueous alteration of carbonaceous chondrites: Evidence for preaccretionary alteration-A review. *Meteorit. Planet. Sci.* **33**, 1113–1122.
- Bodéan J. D., Starkey N. A., Russell S. S., Wright I. P. and Franchi I. A. (2014) An oxygen isotope study of Wark-Lovering rims on type A CAIs in primitive carbonaceous chondrites. *Earth Planet. Sci. Lett.* **401**, 327–336.
- Brantley S. L. (2008) Kinetics of mineral dissolution. In *Kinetics of Water-Rock Interaction* (eds. S. L. Brantley, J. D. Kubicki, and A. F. White). Springer New York, New York, NY.

pp. 151–210.

Brearley A. J. (2006a) The action of water. In *Meteorites and the Early Solar System II* (eds. D. S. Lauretta and H. Y. McSween). University of Arizona Press, Tucson. pp. 587–624.

Brearley A. J. (2006b) The Role of Microchemical Environments in the Alteration of CM Carbonaceous Chondrites. *Lunar Planet. Sci.* **37**, #2074.

Brearley A. J. (2003) Ubiquitous nanophase Fe,Ni carbides in Murchison fine-grained rims: Possible relicts of nebular Fischer-Tropsch reactions. In *Annual Meeting of the Meteoritical Society* p. 5262.

Brearley A. J. and Chizmadia L. J. (2005) On the behavior of phosphorus during the aqueous alteration of CM2 carbonaceous chondrites. *Lunar Planet. Sci.*, 2176.

Brearley A. J. and Jones R. H. (2018) Halogens in chondritic meteorites. In *The Role of Halogens in Terrestrial and Extraterrestrial Geochemical Processes* (eds. D. E. Harlov and L. Aranovich). Springer, Cham. pp. 871–958.

Brearley A. J. and Krot A. N. (2013) Metasomatism in the early solar system: The record from chondritic meteorites. In *Metasomatism and the chemical transformation of rock* (eds. D. E. Harlov and A. Austrheim). Springer, Berlin Heidelberg. pp. 659–789.

Bullock E. S., Macpherson G. J., Nagashima K., Krot A. N., Petaev M. I., Jacobsen S. B. and Ulyanov A. A. (2012) Forsterite-bearing type B refractory inclusions from CV3 chondrites: From aggregates to volatilized melt droplets. *Meteorit. Planet. Sci.* **47**, 2128–2147.

Carlson W. D. (2002) Scales of disequilibrium and rates of equilibration during metamorphism. *Am. Mineral.* **87**, 185–204.

Che S. and Brearley A. J. (2021) The formation and alteration history of a forsterite-bearing Type C CAI from Allende: Evidence for a Type B CAI precursor, and implications for fluid-assisted metasomatism on the CV chondrite parent body. *Geochim. Cosmochim. Acta* **293**, 277–307.

Chen Y. and Brantley S. L. (1998) Diopside and anthophyllite dissolution at 25° and 90°C and acid pH. *Chem. Geol.* **147**, 233–248.

Chizmadia L. J., Xu Y., Schwappach C. and Brearley A. J. (2008) Characterization of micron-sized Fe,Ni metal grains in fine-grained rims in the Y-791198 CM2 carbonaceous

- chondrite: Implications for asteroidal and preaccretionary models for aqueous alteration. *Meteorit. Planet. Sci.* **43**, 1419–1438.
- Ciesla F. J., Lauretta D. S., Cohen B. A. and Hood L. L. (2003) A nebular origin for chondritic fine-grained phyllosilicates. *Science* **299**, 549–552.
- Clayton R. N. and Mayeda T. K. (1999) Oxygen isotope studies of carbonaceous chondrites. *Geochim. Cosmochim. Acta* **63**, 2089–2104.
- Connelly J. N., Bizzarro M., Krot A. N., Nordlund Å., Wielandt D. and Ivanova M. A. (2012) The absolute chronology and thermal processing of solids in the solar protoplanetary disk. *Science* **338**, 651–655.
- Davis A. M., Hashimoto A. and Parsad N. (1999) Trace element fractionation during evaporation in reducing atmospheres. *Lunar Planet. Sci.*, 2023.
- Davis A. M., Macpherson G. J., Clayton R. N., Mayeda T. K., Sylvester P. J., Grossman L., Hinton R. W. and Laughlin J. R. (1991) Melt solidification and late-stage evaporation in the evolution of a FUN inclusion from the Vigarano C3V chondrite. *Geochim. Cosmochim. Acta* **55**, 621–637.
- Drever J. (1997) *The geochemistry of natural waters: Surface and groundwater environments*. Third Edit., Prentice Hall.
- Dufresne E. R. and Anders E. (1962) On the chemical evolution of the carbonaceous chondrites. *Geochim. Cosmochim. Acta* **26**.
- Ebel D. S. (2006) Condensation of rocky material in astrophysical environments. In *Meteorites and the Early Solar System II* (eds. D. S. Lauretta and H. Y. McSween). University of Arizona Press, Tucson. pp. 253–277.
- Fagan T. J., Guan Y. and MacPherson G. J. (2007) Al-Mg isotopic evidence for episodic alteration of Ca-Al-rich inclusions from Allende. *Meteorit. Planet. Sci.* **42**, 1221–1240.
- Fintor K., Park C., Nagy S., Pál-Molnár E. and Krot A. N. (2014) Hydrothermal origin of hexagonal $\text{CaAl}_2\text{Si}_2\text{O}_8$ (dmisteinbergite) in a compact type A CAI from the Northwest Africa 2086 CV3 chondrite. *Meteorit. Planet. Sci.* **49**, 812–823.
- Fisher G. W. (1977) Nonequilibrium thermodynamics in metamorphism. In *Thermodynamics in Geology* (ed. D. G. Fraser). Springer Netherlands, Dordrecht. pp. 381–403.

- Ford R. L. and Brearley A. J. (2010) Discovery of vesuvianite and kaolinite formed during the alteration of melilite in an Allende type A CAI: Characterization by FIB-TEM. *Lunar Planet. Sci.*, 1402.
- Ford R. L. and Brearley A. J. (2008) Element exchange between matrix and CAIs in the Allende meteorite. *Lunar Planet. Sci.* **39**, 2399.
- Gudbrandsson S., Wolff-Boenisch D., Gislason S. R. and Oelkers E. H. (2011) An experimental study of crystalline basalt dissolution from $2 \leq \text{pH} \leq 11$ and temperatures from 5 to 75°C. *Geochim. Cosmochim. Acta* **75**, 5496–5509.
- Guiraud M., Powell R. and Rebay G. (2001) H₂O in metamorphism and unexpected behaviour in the preservation of metamorphic mineral assemblages. *J. Metamorph. Geol.* **19**, 445–454.
- Han J. and Brearley A. J. (2015) Microstructural evidence for complex formation histories of amoeboid olivine aggregates from the ALHA77307 CO3.0 chondrite. *Meteorit. Planet. Sci.* **50**, 904–925.
- Han J., Keller L. P., Liu M. C., Needham A. W., Hertwig A. T., Messenger S. and Simon J. I. (2020) A coordinated microstructural and isotopic study of a Wark-Lovering rim on a Vigarano CAI. *Geochim. Cosmochim. Acta* **269**, 639–660.
- Hashimoto A. and Grossman L. (1987) Alteration of Al-rich inclusions inside amoeboid olivine aggregates in the Allende meteorite. *Geochim. Cosmochim. Acta* **51**, 1685–1704.
- Holland T. J. B. and Powell R. (2011) An improved and extended internally consistent thermodynamic dataset for phases of petrological interest, involving a new equation of state for solids. *J. Metamorph. Geol.* **29**, 333–383.
- Ikeda Y. and Kimura M. (1995) Anhydrous alteration of Allende chondrules in the solar nebula I: Description and alteration of chondrules with known oxygen-isotopic compositions. *Proc. NIPR Symp. Antarct. Meteorites* **8**, 97–122.
- Itoh S., Kojima H. and Yurimoto H. (2004) Petrography and oxygen isotopic compositions in refractory inclusions from CO chondrites. *Geochim. Cosmochim. Acta* **68**, 183–194.
- Keller L. P., Needham A. W. and Messenger S. (2013) A FIB/TEM study of a complex Wark-Lovering rim on a Vigarano CAI. *Annu. Meet. Meteorit. Soc.*, 5300.
- Kelsall G. H. and Robbins D. J. (1990) Thermodynamics of Ti-H₂O-F(-Fe) systems at 298 K.

J. Electroanal. Chem. Interfacial Electrochem. **283**, 135–157.

- Kimura M. and Ikeda Y. (1995) Anhydrous alteration of Allende chondrules in the solar nebula II: Alkali-Ca exchange reactions and formation of nepheline, sodalite and Ca-rich phases in chondrules. *Proc. NIPR Symp. Antarct. Meteorites* **8**, 123–138.
- Knauss K. G., Nguyen S. N. and Weed H. C. (1993) Diopside dissolution kinetics as a function of pH, CO₂, temperature, and time. *Geochim. Cosmochim. Acta* **57**, 285–294.
- Kojima T., Yada S. and Tomeoka K. (1995) Ca-Al-rich inclusions in three Antarctic CO₃ chondrites, Yamato-81020, Yamato-82050 and Yamato-790992: Record of lowtemperature alteration. In *Proceedings of the NIPR Symposium on Antarctic Meteorites* pp. 79–96.
- Krot A. N., Brearley A. J., Ulyanov A. A., Biryukov V. V., Swindle T. D., Keil K., Mittlefehldt D. W., Scott E. R. D., Clayton R. N. and Mayeda T. K. (1999) Mineralogy, petrography, bulk chemical, iodine-xenon, and oxygen-isotopic compositions of dark inclusions in the reduced CV3 chondrite Efremovka. *Meteorit. Planet. Sci.* **34**, 67–89.
- Krot A. N., Nagashima K., Fintor K. and Pál-Molnár E. (2019) Evidence for oxygen-isotope exchange in refractory inclusions from Kaba (CV3.1) carbonaceous chondrite during fluid-rock interaction on the CV parent asteroid. *Geochim. Cosmochim. Acta* **246**, 419–435.
- Krot A. N., Nagashima K., Hutcheon I. D., Ishii H. A., Jacobsen B., Yin Q.-Z., Davis A. M. and Simon S. B. (2010) Mineralogy, petrography, oxygen and magnesium isotopic compositions and formation age of grossular-bearing assemblages in the Allende CAIs. *Lunar Planet. Sci.* **41**, 1406.
- Krot A. N., Nagashima K., van Kooten E. M. M. and Bizzarro M. (2017) High-temperature rims around calcium–aluminum-rich inclusions from the CR, CB and CH carbonaceous chondrites. *Geochim. Cosmochim. Acta* **201**, 155–184.
- Krot A. N., Petaev M. I., Scott E. R. D., Choi B. G., Zolensky M. E. and Keil K. (1998) Progressive alteration in CV3 chondrites: More evidence for asteroidal alteration. *Meteorit. Planet. Sci.* **33**, 1065–1085.
- Krot A. N., Scott E. R. D. and Zolensky M. E. (1995) Mineralogical and chemical modification of components in CV3 chondrites: nebular or asteroidal processing? *Meteoritics* **30**, 748–775.

- Krot A. N., Scott E. R. D. and Zolensky M. E. (1997) Origin of fayalitic olivine rims and lath-shaped matrix olivine in the CV3 chondrite Allende and its dark inclusions. *Meteorit. Planet. Sci.* **32**, 31–49.
- Krot A. N., Ulyanov A. A., Meibom A. and Keil K. (2001) Forsterite-rich accretionary rims around calcium-aluminum-rich inclusions from the reduced CV3 chondrite Efremovka. *Meteorit. Planet. Sci.* **36**, 611–628.
- Krot A. N., Yurimoto H., Hutcheon I. D., Libourel G., Chaussidon M., Tissandier L., Petaev M. I., MacPherson G. J., Paque-Heather J. and Wark D. (2007) Type C Ca, Al-rich inclusions from Allende: Evidence for multistage formation. *Geochim. Cosmochim. Acta* **71**, 4342–4364.
- Lee M. R. (1993) The petrography, mineralogy and origins of calcium sulphate within the Cold Bokkeveld CM carbonaceous chondrite. *Meteoritics* **28**, 53–62.
- McConnel S. R. (1978) Dissolution of ilmenite and related minerals in sulphuric acid. Murdoch University.
- McGuire A. V. and Hashimoto A. (1989) Origin of zoned fine-grained inclusions in the Allende meteorite. *Geochim. Cosmochim. Acta* **53**, 1123–1133.
- Mendybaev R. A., Richter F. M., Georg R. B., Janney P. E., Spicuzza M. J., Davis A. M. and Valley J. W. (2013) Experimental evaporation of Mg- and Si-rich melts: Implications for the origin and evolution of FUN CAIs. *Geochim. Cosmochim. Acta* **123**, 368–384.
- Nomura K. and Miyamoto M. (1998) Hydrothermal experiments on alteration of Ca-Al-rich inclusions (CAIs) in carbonaceous chondrites: Implication for aqueous alteration in parent asteroids. *Geochim. Cosmochim. Acta* **62**, 3575–3588.
- Palmer E. E. and Lauretta D. S. (2011) Aqueous alteration of kamacite in CM chondrites. *Meteorit. Planet. Sci.* **46**, 1587–1607.
- Pollok K., Putnis C. V and Putnis A. (2011) Mineral replacement reactions in solid solution-aqueous solution systems: Volume changes, reactions paths and end-points using the example of model salt systems. *Am. J. Sci.* **311**, 211–236.
- Proyer A. (2003) The preservation of high-pressure rocks during exhumation: metagranites and metapelites. *Lithos* **70**, 183–194.
- Putnis A. (2002) Mineral replacement reactions: from macroscopic observations to

microscopic mechanisms. *Mineral. Mag.* **66**, 689–708.

Putnis A. (2015) Transient porosity resulting from fluid–mineral interaction and its consequences. *Rev. Mineral. Geochemistry* **80**, 1–23.

Putnis A. and Austrheim H. (2013) Mechanisms of metasomatism and metamorphism on the local mineral scale: The role of dissolution-precipitation during mineral re-equilibration. In *Metasomatism and the chemical transformation of rock* pp. 141–170.

Putnis C. V., Tsukamoto K. and Nishimura Y. (2005) Direct observations of pseudomorphism: Compositional and textural evolution at a fluid-solid interface. *Am. Mineral.* **90**, 1909–1912.

Reed H. M. (1997) Hydrothermal alteration and its relationship to ore fluid composition. In *Geochemistry of hydrothermal ore deposits* (ed. H. L. Barnes). John Wiley & Sons. pp. 303–365.

Rosenberg N. D., Browning L. and Bourcier W. L. (2001) Modeling aqueous alteration of CM carbonaceous chondrites. *Meteorit. Planet. Sci.* **36**, 239–244.

Rubin A. E. (2012) Collisional facilitation of aqueous alteration of CM and CV carbonaceous chondrites. *Geochim. Cosmochim. Acta* **90**, 181–194.

Ruiz-Agudo E., Putnis C. V. and Putnis A. (2014) Coupled dissolution and precipitation at mineral-fluid interfaces. *Chem. Geol.* **383**, 132–146.

Ruzicka A. (1997) Mineral layers around coarse-grained, Ca-Al-rich inclusions in CV3 carbonaceous chondrites: Formation by high-temperature metasomatism. *J. Geophys. Res. Planets* **102**, 13387–13402.

Schott J., Berner R. A. and Sjöberg E. L. (1981) Mechanism of pyroxene and amphibole weathering—I. Experimental studies of iron-free minerals. *Geochim. Cosmochim. Acta* **45**, 2123–2135.

Scott E. R. D. and Krot A. N. (2014) Chondrites and their components. In *Treatise on Geochemistry: Second Edition* (eds. H. D. Holland and K. K. Turekian). Elsevier, Oxford. pp. 65–137.

Simon J. I., Hutcheon I. D., Simon S. B., Matzel J. E. P., Ramon E. C., Weber P. K., Grossman L. and DePaolo D. J. (2011) Oxygen isotope variations at the margin of a CAI records circulation within the solar nebula. *Science* **331**, 1175–1178.

- Simon J. I., Young E. D., Russell S. S., Tonui E. K., Dyl K. A. and Manning C. E. (2005) A short timescale for changing oxygen fugacity in the solar nebula revealed by high-resolution ^{26}Al - ^{26}Mg dating of CAI rims. *Earth Planet. Sci. Lett.* **238**, 272–283.
- Simon S. B., Davis A. M. and Grossman L. (1999) Origin of compact type A refractory inclusions from CV3 carbonaceous chondrites. *Geochim. Cosmochim. Acta* **63**, 1233–1248.
- Stolper E. (1982) Crystallization sequences of Ca-Al-rich inclusions from Allende: An experimental study. *Geochim. Cosmochim. Acta* **46**, 2159–2180.
- Tomeoka K., Nomura K. and Takeda H. (1992) Na-bearing Ca-Al-rich inclusions in the Yamato-791717 CO carbonaceous chondrite. *Meteoritics* **27**, 136–143.
- Wark D. A. and Lovering J. F. (1977) Maker events in the early evolution of the solar system: Evidence from rims in Ca-Al-rich inclusions. *Lunar Planet. Sci.* **8**, 95–112.
- Wark D. and Boynton W. V. (2001) The formation of rims on calcium-aluminum-rich inclusions: Step I-fsah heating. *Meteorit. Planet. Sci.* **36**, 1135–1166.
- White A. F., Peterson M. L. and Hochella M. F. (1994) Electrochemistry and dissolution kinetics of magnetite and ilmenite. *Geochim. Cosmochim. Acta* **58**, 1859–1875.
- White R. W. and Powell R. (2011) On the interpretation of retrograde reaction textures in granulite facies rocks. *J. Metamorph. Geol.* **29**, 131–149.
- White R. W., Powell R. and Baldwin J. A. (2008) Calculated phase equilibria involving chemical potentials to investigate the textural evolution of metamorphic rocks. *J. Metamorph. Geol.* **26**, 181–198.
- Yoneda S. and Grossman L. (1995) Condensation of CaO–MgO–Al₂O₃–SiO₂ liquids from cosmic gases. *Geochim. Cosmochim. Acta* **59**, 3413–3444.
- Zhang S. and Nicol M. J. (2009) An electrochemical study of the reduction and dissolution of ilmenite in sulfuric acid solutions. *Hydrometallurgy* **97**, 146–152.
- Zolensky M. E., Bourcier W. L. and Gooding J. L. (1989) Aqueous alteration on the hydrous asteroids: Results of EQ3/6 computer simulations. *Icarus* **78**, 411–425.
- Zolotov M. Y. (2012) Aqueous fluid composition in CI chondritic materials: Chemical equilibrium assessments in closed systems. *Icarus* **220**, 713–729.

Zolotov M. Y. and Mironenko M. V. (2007) Hydrogen chloride as a source of acid fluids in parent bodies of chondrites. *Lunar Planet. Sci.* **38**, 2340.

CHAPTER 6

The formation and alteration history of a forsterite-bearing Type C CAI from Allende: Evidence for a Type B CAI precursor, and implications for fluid-assisted metasomatism on the CV chondrite parent body

Abstract

Type C CAIs are a rare group of refractory inclusions in carbonaceous chondrites that are compositionally and isotopically distinct from the more commonly observed igneous CAIs (i.e., Type As and Type Bs). We have investigated a forsterite-bearing Type C CAI ALNH-04 from the Allende CV3 chondrite. This CAI has both textural and compositional similarities to some of the Type C CAIs previously reported; however, there are notable differences that imply that ALNH-04 may have formed from a different precursor from other Type C inclusions. Based on the bulk composition of ALNH-04 and the minor element contents of forsterite, we suggest that the forsterite grains were inherited from a Forsterite-bearing Type B CAI (FoB) precursor. The presence of augite on the periphery of ALNH-04 implies a re-melting event that probably occurred in a chondrule-forming region.

Another interesting feature of ALNH-04 is the secondary iron-alkali-halogen zoning sequence as manifested by varying proportions of nepheline, sodalite, fayalitic olivine, and sulfides in different regions of the CAI. Nepheline \pm sodalite have replaced anorthite in the outer part of the inclusion, giving way to the presence of ubiquitous sodalite with minor

nepheline, partially replacing anorthite at grain boundaries and fractures in the interior of the inclusion. Sulfides and Fe-bearing olivine form an iron-rich alteration zone. The textural relationships between nepheline and sodalite show no evidence of a direct replacement relationship between the two phases. Combined with the SEM observations, the microstructures are most consistent with a two-stage fluid alteration process: (1) nepheline replaced anorthite in the outer part of the CAI via a fluid with $a_{NaCl(aq)}$ within the stability range of nepheline; (2) a later-stage fluid, with elevated $a_{NaCl(aq)}$ that could preferentially stabilize sodalite, penetrated further into the CAI interior, replacing anorthite with sodalite. The lack of a nepheline-sodalite replacement relationship indicates that the conditions and fluid chemistry were suitable for nepheline and/or sodalite to be stable. Together with other Fe-rich secondary phases, fayalitic olivine may have recorded an increase in pH and $a_{SiO_2(aq)}$ of the fluid. These changes were probably induced by the extensive alteration of the outer part of the CAI to feldspathoids. The observed alteration microstructures are consistent with a coupled dissolution-precipitation alteration mechanism. The fluid alteration was also responsible for the formation of Na- and Ca-rich halos in the matrix surrounding the CAI.

We compared ALNH-04 with other CAIs and chondrules showing alkali-halogen-(iron) zoning sequences in Allende, and found that the observed zoning structures are consistent with the two-stage fluid-assisted metasomatic process mentioned above. The different distribution patterns of nepheline and sodalite in plagioclase-rich CAIs, chondrules, and melilite-rich CAIs may be explained by different chemical potential gradients in SiO_2 in the fluid. Precipitation of nepheline and sodalite may require a higher SiO_2 activity compared to grossular and

dmisteinbergite (\pm secondary anorthite), which controlled the formation location of sodalite during the second fluid alteration event. Fluids with different compositions may be produced by fluid percolation along different directions and pathways, changing convection patterns, or release of water from a differentiated asteroidal interior.

1. INTRODUCTION

Calcium-aluminum-rich inclusions (CAIs) are submillimeter-to-centimeter-sized refractory objects that represent the oldest material formed in the solar nebula (Amelin et al., 2002; Connelly et al., 2012). They have experienced subsequent heating and melting events over a period of at least 0.3 Ma, calculated from their inferred initial $^{26}\text{Al}/^{27}\text{Al}$ ratios (e.g., MacPherson et al., 2010; Kita and Ushikubo, 2012; MacPherson et al., 2012). These refractory inclusions provide important constraints on several aspects of the early evolutionary history of the solar nebula, including the (1) the conditions and sequence of condensation of solid phases from a gas of solar composition (e.g., Grossman, 1972; Yoneda and Grossman, 1995; Petaev and Wood, 1998; Ebel and Grossman, 2000; Petaev et al., 2005; Ebel, 2006); (2) the distribution and evolution of short-lived radionuclides (e.g., ^{26}Al and ^{10}Be) in the protoplanetary disk (e.g., McKeegan, 2000; MacPherson et al., 2003; Larsen et al., 2011; Simon and Young, 2011; Krot et al., 2012; MacPherson et al., 2012; Kita et al., 2013); (3) the early oxygen isotopic evolution and the existence of possible isotopic reservoirs in the solar nebula (e.g., Aléon et al., 2005; Krot et al., 2008, 2010; Yurimoto et al., 2008; Simon et al., 2011; Aléon, 2018); and (4) nucleosynthetic anomalies recorded in FUN (fractionated and

unidentified nuclear effects) CAIs (e.g., Liu et al., 2009; Dauphas and Schauble, 2016; Davis et al., 2018; Kööp et al., 2018).

Despite the significant progress in understanding the origins and implications of CAIs, there still remain many unanswered questions (see review by MacPherson et al. (2005)). Type C CAIs, for example, are rare inclusions, which occur in CV, CR, CO, and several anomalous carbonaceous chondrites (Wark, 1987; Beckett and Grossman, 1988; Lin and Kimura, 1998; Imai and Yurimoto, 2000; Aléon et al., 2002; Itoh et al., 2004; Kita et al., 2004; Krot et al., 2004a, 2005, 2006, 2007a,b, 2008; Kawasaki et al., 2015). They exhibit ophitic textures and mainly consist of spinel + Al-Ti-rich diopside + anorthite \pm melilite. Their bulk compositions deviate significantly from the predicted equilibrium condensation path of a solar gas (MacPherson et al., 2004; MacPherson and Huss, 2005), which may be explained by the pressure-dependent condensation sequence of anorthite and forsterite (MacPherson et al., 2004; Petaev and Wood, 2005). Type C inclusions are different from igneous Type As and Bs in that the former exhibits high Si/Mg ratios and enrichments in light Mg isotopes (Wark, 1987), suggesting that melting may have occurred in a region with high total pressure or dust/gas ratio similar to chondrule-forming regions (Krot et al., 2007a). A similar conclusion has been made, based on the presence of ferromagnesian chondrule materials on the periphery of some Type C CAIs (Krot et al., 2006, 2007a,b). The occurrence of some Type C CAIs with “lacy” textures is difficult to reconcile with the equilibrium crystallization sequence predicted from the CaO-MgO-Al₂O₃-SiO₂ diagram (Krot et al., 2007b), and may require delayed nucleation of anorthite (Wark, 1987), or a high-temperature isothermal interaction of a Type B-like melt with a SiO-

rich gas (Krot et al., 2007b). The high Na₂O contents in melilite from many Allende Type C CAIs (Krot et al., 2007a,b) may be caused by several possible mechanisms, such as melting of a nepheline and/or sodalite-bearing Type B inclusion, addition of Na and Si during gas-melt interaction, and secondary alteration on the parent body. Finally, the precursors to Type C CAIs remain enigmatic, and possible candidates include Type B inclusions (Krot et al., 2007b), fine-grained, spinel-rich inclusions (Lin and Kimura, 1998; Krot et al., 2004b), and FoBs (Che and Brearley, 2017).

Another long-standing problem related to chondrites is the condition and environment of secondary alteration that has modified the primary phase assemblages in different chondrite groups to various degrees (Brearley, 2006a, 2013; Brearley and Krot, 2013; Krot et al., 2015). Refractory inclusions are useful for testing different alteration models due to the susceptibility of their primary phases to secondary alteration, generating a diversity of secondary phases, including, but not limited to, hercynitic spinel, nepheline, sodalite, dmisteinbergite, hedenbergite, wollastonite, andradite, grossular, monticellite, ilmenite, and phyllosilicates (Brearley and Krot, 2013). However, different CAIs show a large range of alteration styles and degrees, and significant heterogeneities may exist even within individual inclusions. This is particularly obvious for CAIs from CV3 chondrites: the dominant alteration process(es) (aqueous alteration and fluid-assisted metamorphism/metasomatism) appear to be distinct among different CV3 subgroups. As a result, an important question is what is the role of fluid in producing the alteration phases and heterogeneities in CV3 CAIs? Previous studies (e.g., Keller and Buseck, 1991; Brearley, 1997; Ford and Brearley, 2010) have discovered minor, but

widespread hydrous minerals in chondrules and CAIs in Allende (e.g., margarite, biopyriboles, kaolinite, and vesuvianite), which demonstrates that water, though limited in amount, was involved in the alteration process. In most cases, the alteration processes did not go to completion, or for coarse-grained inclusions, was minimal, as evidenced by the coexistence of alteration reactants and products (e.g., Brearley and Krot, 2013), which allows for detailed studies of the alteration mechanisms. Many secondary minerals in CV3 CAIs are very fine-grained and challenging to characterize using SEM alone and so their formation reactions remain poorly understood. To date, very few studies of these alteration textures have been performed using transmission electron microscopy (TEM) (e.g., Keller and Buseck, 1991; Ford and Brearley, 2010; Ishii et al., 2010; Fintor et al., 2013, 2014; Brearley et al., 2014). Such microstructural studies are clearly essential to unravel the complex secondary alteration reactions that affected CV3 chondrites.

In this study, we focus on a unique, metasomatized, forsterite-bearing Type C inclusion, ALNH-04 (Fig. 1), from the Allende CV3 chondrite. Two features of this inclusion stand out: the presence of forsterite grains in the central region of the inclusion, and a distinct iron-alkali-halogen zonal sequence. The questions we address in this study are: (1) the nature of the precursor of this CAI and its formation and subsequent thermal processing in the solar nebula and (2) the origin of the secondary zoning, and the possible role of fluid. We will also compare the alteration features of this CAI with previously reported, similar features in other objects from Allende (McGuire and Hashimoto, 1989; Wasserburg et al., 2011; Brearley and Krot, 2013).

2. ANALYTICAL METHODS

The backscattered electron (BSE) images and full spectral X-ray maps of a 1 inch-round polished thin section ALNH prepared from the Allende meteorite were obtained on a FEI Quanta 3D DualBeam[®] field emission gun scanning electron microscope/focused ion beam (FEG-SEM/FIB) instrument fitted with an EDAX Apollo 40 SDD Energy Dispersive Spectroscopy (EDS) system with Genesis software at the University of New Mexico (UNM). Full thin section BSE and X-ray map mosaics were produced using ImageJ software, by combination of multiple image fields. These mosaics were then used to locate refractory inclusions and chondrules on the thin section. The petrology and mineralogy of individual objects were characterized in detail by high resolution BSE imaging and X-ray mapping. The instrument operating conditions for BSE imaging were: accelerating voltages of 30 and 15 kV, and beam currents of 23 and 11 nA, respectively. The X-ray mapping was conducted at 30 kV and 23 nA.

The major and minor element compositions of phases in CAI ALNH-04 were obtained using wavelength dispersive spectrometry (WDS) on a JEOL JXA-8200 electron probe microanalyzer (EPMA) at UNM. All analyses were obtained at an accelerating voltage of 15 kV, a beam current of 20 nA, and a spot size of 1 μm . Taylor Company Microprobe Standards were used for calibration: Na on albite, Mg, Si, and Fe on olivine, Al and K on orthoclase, S on pyrite, Ca on diopside, Ti on titanite, V on V metal, Cr on chromite, Mn on spessartine, Ni on Ni metal. In addition, an almandine oxygen standard and an apatite-F (Wilberforce) standard were also used for Al and P, respectively. The detection limits for Fe and Ni are ~ 0.02 wt%,

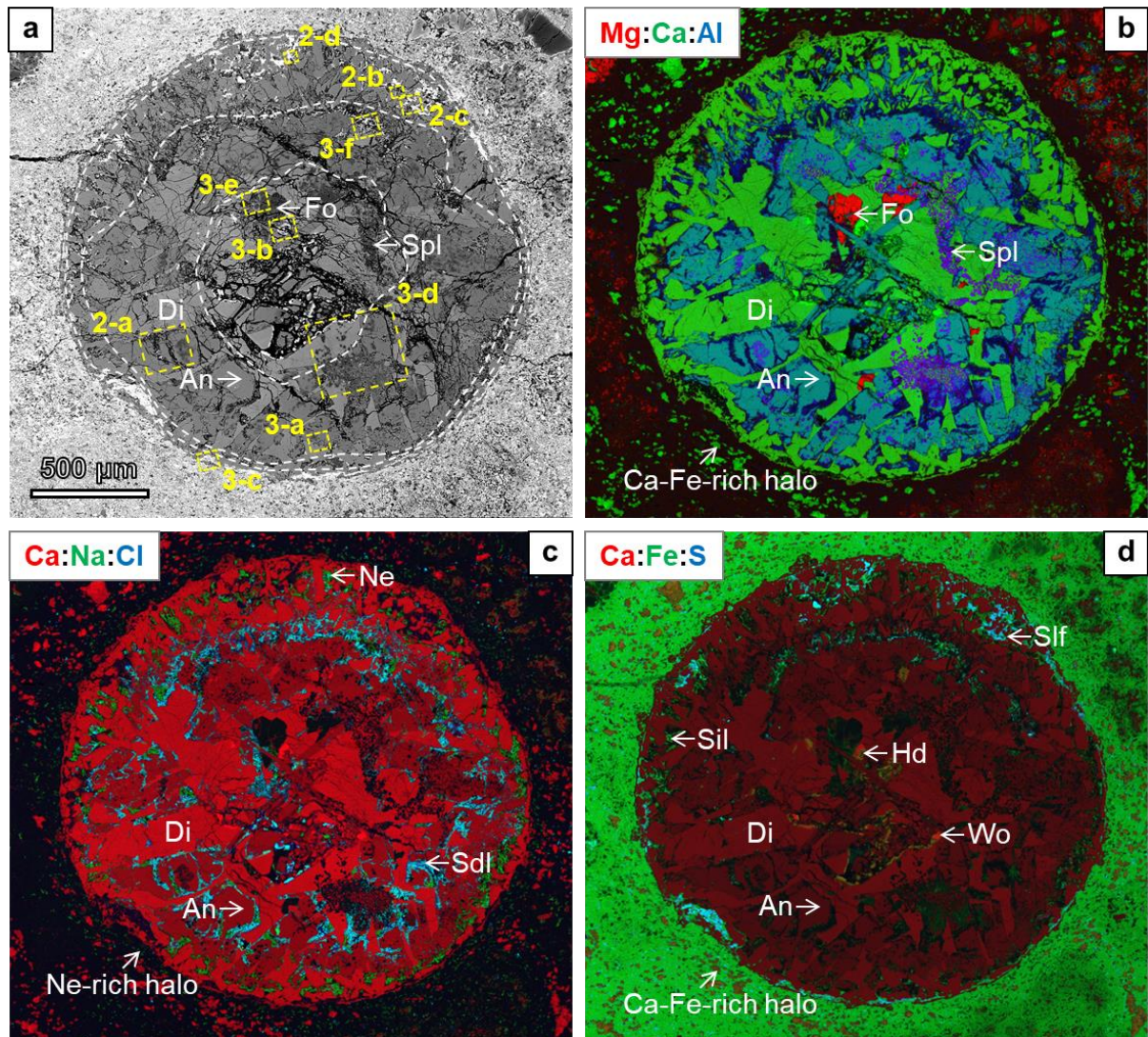


Fig. 1. SEM and X-ray maps of the Type C inclusion ALNH-04 from Allende. The white dashed lines in (a) mark the rough boundaries between the four texturally-distinct regions. Regions outlined by yellow boxes are shown in Fig. 2-3. (a) BSE image of ALNH-04, and combined X-ray elemental maps: (b) in Mg (red), Ca (green), and Al (blue) showing the distribution of anorthite, Al-Ti-bearing diopside, spinel, and forsterite; (c) in Ca (red), Na (green), and Cl (blue), showing a zonal sequence of sodalite and nepheline; (d) in Ca (red), Fe (green), and S (blue), showing the presence of hedenbergite and wollastonite in the core region, as well as the distribution pattern of Fe-rich phases including sulfides and Al-Fe silicate in the outer part of the CAI. Abbreviations: An = anorthite, Di = Al-Ti-bearing diopside, Fo = forsterite, Hd = hedenbergite, Ne = nepheline, Sdl = sodalite, Sil = Al-Fe silicate, Sif = sulfides, Spl = spinel, Wo = wollastonite.

while those for all the other elements are ~ 0.01 wt%. Data were reduced using the modified

ZAF correction procedure in Probe for EPMA.

The modal abundances of major phases in ALNH-04 were determined using the modal recombination analysis method described by Berlin (2010). Several X-ray maps (Mg, Al, S, Ca, and Fe) were used to distinguish between different phases. We assumed that all the secondary phases, except Fe-rich spinel and Fe-bearing diopside, were originally anorthite, and estimated the phase abundances of the pristine CAI (i.e., prior to its secondary alteration on the parent body). Based on this assumption, we obtained a phase image of ALNH-04 (Fig. S1) using Adobe Photoshop[®]. For this process, we used the Magic Wand Tool in Photoshop to select pixels belonging to each phase. Although useful, this tool worked less effectively for finer-grained phases, e.g., spinel and many secondary phases, because they are not clearly resolved from other phases on the X-ray maps. As a consequence, there are uncertainties in the calculated modal abundances. In Fig. S1, white open spaces that are interstitial to the major four mineral phases represent the fine-grained materials or pores that cannot be identified unambiguously by the Magic Wand Tool. These open spaces account for ~0.5% volume percentage of the CAI, with ~0.2% and ~0.3% of the volume represent spinel and altered anorthite, respectively, if we assume the open spaces are pore-free. Four separate layers with different colors for anorthite, diopside, forsterite, and spinel were obtained and then assembled to make the phase image. The area percentages of different phases were acquired using the Threshold tool in ImageJ. With the mineral compositions obtained by EPMA and density data from <http://www.webmineral.com>, we then calculated the bulk composition of ALNH-04. Another error may come from the fact that we are dealing with a 2D cross section of the CAI.

The relative proportions of minor phases, i.e., spinel (2.2 wt%) and forsterite (1.0 wt%), may vary significantly for different cross sections. In particular, the finer-grained forsterite grains with more anhedral shapes may be parts of larger crystals in 3D, resulting in an underestimation of the forsterite abundance.

A total of six FIB sections were prepared from different regions of ALNH-04 using the FEI Quanta 3D FEG-SEM/FIB instrument equipped with an Omniprobe 200 micromanipulator, using the method described by Han and Brearley (2015). The microstructures of the FIB sections were then characterized on a JEOL 2010 transmission electron microscope (TEM) and a JEOL 2010F FASTEM field emission gun scanning TEM (STEM/TEM) at UNM. Both instruments were operated at 200 kV. The techniques we used include bright-field TEM (BF-TEM), dark-field scanning TEM (DF-STEM), and electron diffraction. We also performed quantitative microanalyses using an Oxford Instruments AZtec Energy Dispersive X-ray Spectroscopy system with Oxford Instruments XMax 80N 80mm² SDD detector on the JEOL 2010F FASTEM at UNM. The X-ray elemental mapping was also performed on the JEOL 2010F FASTEM using the AZtec system. The Cliff–Lorimer thin film approximation was used for quantification using theoretical k-factors.

3. RESULTS

3.1. SEM observations

The Allende CAI ALNH-04 has a spherical shape with a diameter of about 2 mm (Fig. 1) and has a dominant ophitic to sub-ophitic texture. This inclusion consists of anorthite (~55

vol%), Al-Ti-bearing diopside (~40 vol%), spinel (~2 vol%), and a minor amount of forsteritic olivine (~1 vol%), as well as some secondary phases (~2 vol%). It can be divided into four texturally-distinct regions, based on the mineral assemblages and grain sizes: (1) a forsterite-bearing core region mainly composed of elongate, prismatic anorthite crystals (~200 μm in the elongation direction), anhedral Al-Ti-bearing diopside (~100 \times 50 μm), and rare, subhedral-to-anhedral forsterite grains (as large as 150 \times 100 μm); (2) a coarse-grained inner mantle composed of lath-shaped anorthite (~500 \times 200 μm on average), euhedral Al-Ti-bearing diopside (as large as 500 \times 250 μm), and spinel (5-15 μm) as palisade, framboids, and separate grains enclosed in anorthite and diopside; (3) a partly preserved outer mantle texturally similar to the inner mantle, but with finer grain sizes, consisting of lath-shaped anorthite and Al-Ti-bearing diopside, minor sub-calcic augite; (4) a 10 μm -thick, discontinuous rim that is composed of diopside with MgO-rich sub-calcic augite and is partly separated from the interior of the CAI by a zone consisting of complex, fine-grained assemblages of sulfides, an unidentified Al-bearing, Fe-rich silicate phase, minor feldspathoids, awaruite, phosphates, and relict diopside grains (Fig. 1d). Based on the TEM observations that will be reported later, the Al-Fe silicate phase is an intergrowth of Fe-bearing olivine and feldspathoids.

This refractory inclusion exhibits significant evidence of development of secondary phases that exemplifies the alteration effects found in Allende CAIs. (1) Anorthite has been partially or completely replaced by different assemblages of secondary phases in different regions along grain boundaries and fractures. Anorthite grains in the fine-grained outer mantle show a higher extent of alteration than those in the inner mantle and core, with the alteration

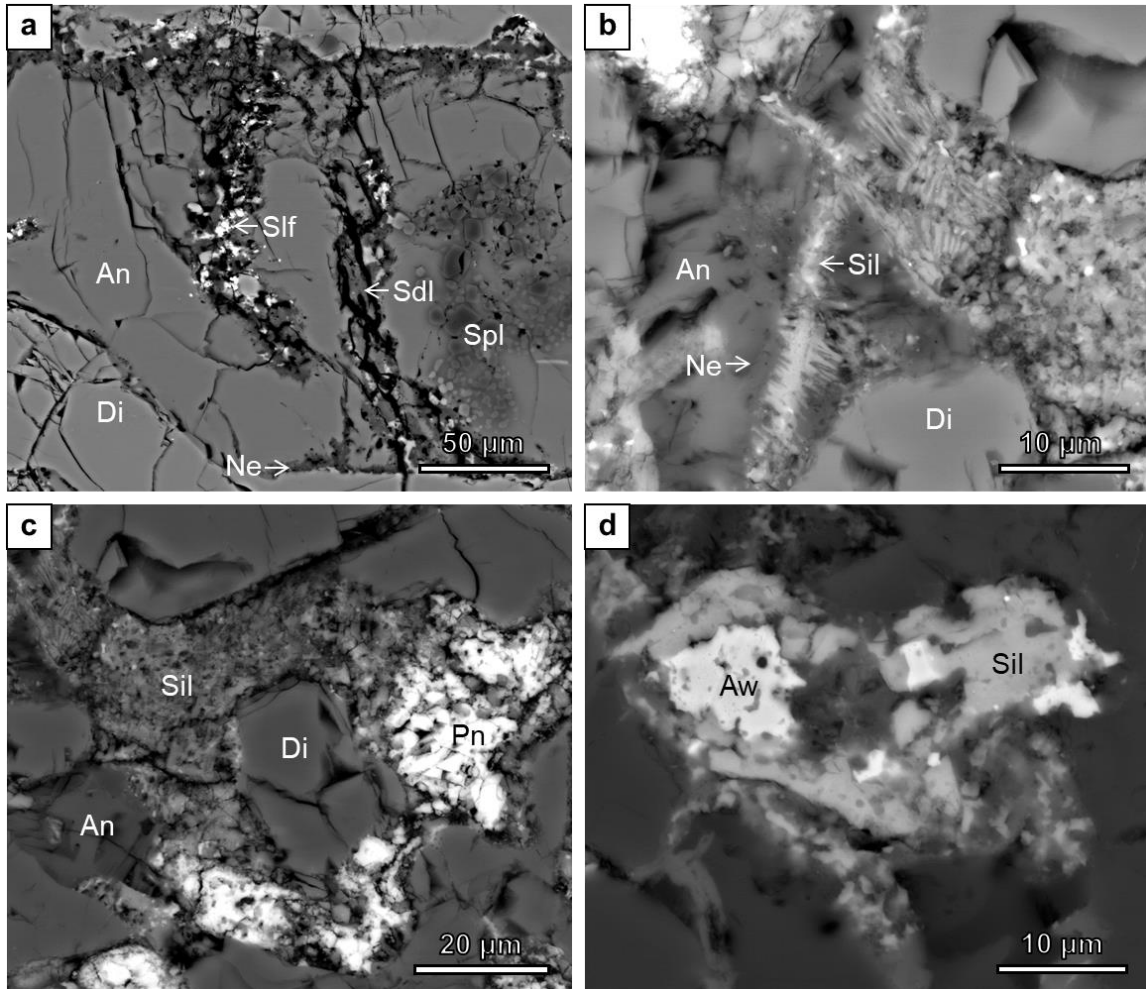


Fig. 2. BSE images showing the alteration features in ALNH-04. (a) Anorthite in the inner mantle region has been replaced by nepheline and sodalite along the interfaces with diopside, as well as along fractures in anorthite. In some regions, alteration along fractures is more extensive than along anorthite-diopside interfaces. Fine-grained sulfides are commonly found to coexist with feldspathoids in the altered regions. (b) In the outer mantle region, the Al-Fe silicate is intimately intergrown with feldspathoids, and forms fine-grained, porous aggregates. Locally, some crystals with an elongate crystal shape occur. (c) Sulfides (pentlandite in this image) that locally form porous aggregates are commonly associated with the Al-Fe silicate in the outer mantle region. (d) Awaruite is also present in the outer mantle region, as a rare phase that is surrounded by Al-Fe silicate. Abbreviations: An = anorthite, Aw = awaruite, Di = Al-Ti-bearing diopside, Ne = nepheline, Pn = pentlandite, Sdl = sodalite, Sil = Al-Fe silicate, Slf = sulfides, Spl = spinel.

scale of anorthite varying significantly from a <5 μm wide layer for coarse grains in the mantle region, to complete replacement of >50 μm for smaller grains on the periphery of the CAI.

Nepheline and sodalite are the dominant alteration minerals (Fig. 2a), and their grain sizes vary from 1 μm to $>10 \mu\text{m}$. On the EDS X-ray mosaic of the inclusion, a zonal sequence of alkali-halogen-rich secondary phases is apparent: nepheline \pm sodalite have replaced anorthite in the outer part of the inclusion, giving way to the presence of ubiquitous sodalite with minor nepheline, partially replacing anorthite at grain boundaries and fractures in the interior of the inclusion (Fig. 1c). Fine-grained sulfides ($<1 \mu\text{m}$) and hercynitic spinel (1-5 μm) are also commonly observed to coexist with feldspathoids. The Al-Fe silicate ($<5 \mu\text{m}$) is a ubiquitous phase replacing anorthite in the outer mantle region of the CAI (Fig. 2b), forming an Fe-rich alteration zone. This phase is highly porous and irregular with abundant submicron inclusions in most cases, but can also be elongate when intergrown with feldspathoids. There seems to be a replacement relationship between nepheline, sodalite, and the Al-Fe silicate; however, the detailed replacement sequence is unclear based just on the BSE images. Sulfides (pentlandite and pyrrhotite) with small diopside grains ($<5 \mu\text{m}$) are intimately associated with this Al-Fe silicate. Sulfides appear to be enclosed in the Al-Fe silicate intergrowth, and in some cases, occur as rims around it (Fig. 2c). Rare awaruite grains are also present in some areas of alteration (Fig. 2d). (2) In many areas, Al-Ti-rich diopside shows Fe-enrichment (compositionally similar to Fe-bearing diopside) on its rim (Fig. 3a). Spinel commonly shows the development of hercynitic rims. In the core region, some Al-Ti diopside grains are locally replaced by fine-grained ($<5 \mu\text{m}$), porous hedenbergite \pm wollastonite (Fig. 3b). Diopside grains in the outer mantle and rim regions of the CAI seem to be replaced by sulfides and Al-Fe silicate (Fig. 3c). (3) Spinel grains enclosed in anorthite and Al-Ti-diopside show Fe-

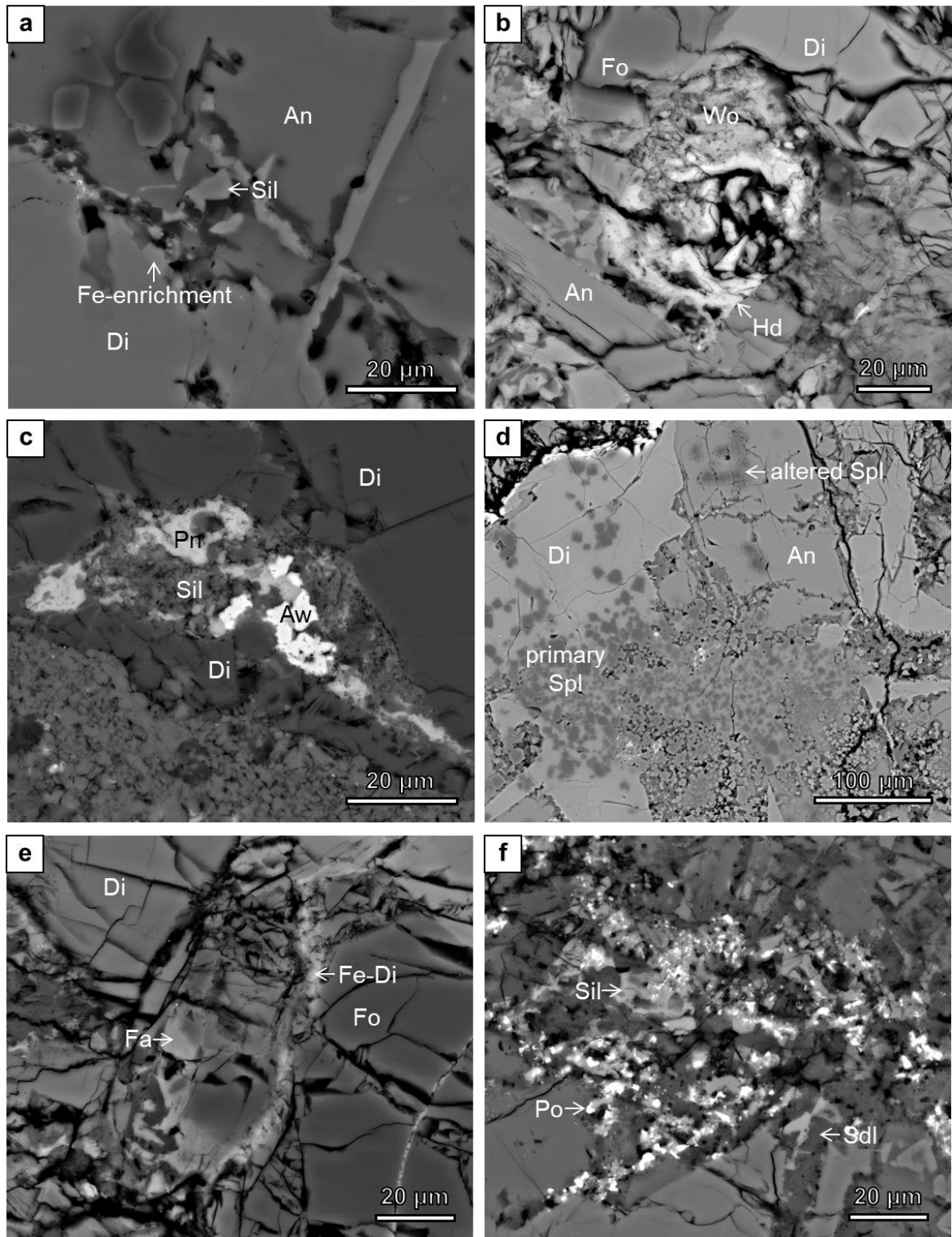


Fig. 3. BSE images showing additional alteration features in ALNH-04. (a) In the mantle region, diopside grains have Fe-enriched rims, with compositions that are similar to Fe-bearing diopside.

Fig. 3. (*continued*) (b) A porous alteration nodule that is composed of wollastonite and hedenbergite, which have replaced diopside in the core region of the CAI. (c) Diopside on the periphery of the CAI showing replacement by sulfides and Al-Fe silicate. (d) Spinel grains show various extents of Fe-enrichment, with higher Fe concentrations in regions of the CAI that show more advanced alteration, such as adjacent to fractures and interfaces between anorthite and diopside. (e) Forsterite in the core region of the CAI has fayalitic olivine rims and Fe-bearing diopside veins. (f) Sulfide-rich zone composed of pentlandite, pyrrhotite, sodalite, Al-Fe-rich silicate, Fe-bearing diopside, and minor nepheline. Abbreviations: An = anorthite, Aw = awaruite, Di = Al-Ti-bearing diopside, Fa = fayalitic olivine, Fo = forsterite, Hd = hedenbergite, Pn = pentlandite, Po = pyrrhotite, Fe-Di = Fe-bearing diopside, Sdl = sodalite, Sil = Al-Fe silicate, Spl = spinel, Wo = wollastonite.

enrichment, with more advanced enrichment adjacent to fractures and grain boundaries between anorthite and Al-Ti-diopside (Fig. 3d). (4) Forsterite in the core region has fayalitic rims and Fe-bearing diopside veins (Fig. 3e). The regions of secondary alteration phases commonly exhibit significant porosity. (5) There is also a sulfide-rich zone that partly separates the outer mantle from the inner mantle, and is composed of pentlandite, pyrrhotite, sodalite, Al-Fe silicate, Fe-bearing diopside, and minor nepheline (Fig. 3f). The sulfides are closely associated with other secondary phases, and often occur along veins and fractures in anorthite. The grain size of anorthite and diopside across this Fe-rich zone changes significantly and abruptly from $\sim 500 \times 200 \mu\text{m}$ to $< 30 \times 100 \mu\text{m}$. (6) In the matrix surrounding the CAI, two halos are present (Fig. 1 c,d): an inner nepheline-rich halo and an outer Ca-Fe-rich halo consisting of hedenbergite (5-8 μm) and Fe-bearing diopside ($\sim 5 \mu\text{m}$) assemblages, and minor sodalite and nepheline grains with typical grain sizes of 5-10 μm .

3.2. Bulk composition and mineral compositions

The estimated phase abundances are shown in Table 1. Endmember I corresponds to the

situation where all the open spaces in Fig. S1 were treated as pores, while in endmember II, the open spaces represent spinel and fine-grained, secondary phases that replace anorthite. The bulk compositions calculated from these two endmember cases are shown in Table 2.

Representative electron microprobe analyses of anorthite, diopside, spinel, forsterite, and Al-bearing, Fe-rich silicate from different regions in ALNH-04 are reported in Table S1-5.

Diopside grains in the core and inner mantle regions have similar compositions, with 11.11-17.87 wt% MgO, 1.04-2.98 wt% TiO₂, 4.86-19.34 wt% Al₂O₃. Compositional zoning was observed in these diopside grains, with decreasing TiO₂ and Al₂O₃ contents from core to rim. Patchy zoning is also present in some of the grains. On the other hand, diopside grains in the outer mantle and rim regions are compositionally homogeneous and contain significantly lower Al₂O₃ (1.37-7.15 wt%), higher MgO contents (16.41-24.54 wt%), and slightly lower TiO₂ contents (0.29-1.56 wt%) (Fig. 4a). In addition, diopside grains in the outer mantle and rim have a slightly higher Cr₂O₃ content than those in the core and inner mantle (Fig. 4b).

Anorthite grains in the core and inner mantle regions are nearly pure endmember (An_{>97.4}); in comparison, the fine-grained anorthite grains in the outer mantle show elevated Na₂O contents, with An contents of 89.9-93.2. Anorthite in the outer mantle also contains a significant amount of MgO (0.22-0.99 wt%) and FeO (0.19-1.13 wt%), much higher than that in the inner mantle and core regions. No compositional zoning was observed in anorthite. Spinels show various degrees of Fe-enrichment, with those enclosed in anorthite appearing to be more Fe-rich, with Fe# (= $\text{Fe} \times 100 / (\text{Fe} + \text{Mg})$) in the range 8.9-21.4. There are also some spinel grains in the core region with a nearly pure endmember composition (FeO < 1 wt%).

Table 1. Data for calculating the bulk composition of ALNH-04.

| Endmember Phase | I | | | | II | | | |
|--------------------|-----------|----------|--------|------------|-----------|----------|--------|------------|
| | Anorthite | Diopside | Spinel | Forsterite | Anorthite | Diopside | Spinel | Forsterite |
| Density | 2.76 | 3.278 | 3.578 | 3.271 | 2.76 | 3.278 | 3.271 | 3.578 |
| Volume | 0.564 | 0.409 | 0.018 | 0.009 | 0.567 | 0.404 | 0.009 | 0.02 |
| Abundance (wt%) | 52.0% | 44.8% | 2.2% | 1.0% | 52.3% | 44.3% | 1.0% | 2.4% |

I: all the open spaces in Fig. S1 were treated as pores.

II: the open spaces represent spinel and fine-grained, secondary phases that replace anorthite.

Table 2. Average compositions of individual minerals and the calculated bulk compositions.

| Con.* | Anorthite | Diopside | Spinel | Forsterite | Bulk I | Bulk II |
|-------|-----------|----------|--------|------------|--------|---------|
| Na | 0.19 | 0.03 | 0.00 | 0.00 | 0.11 | 0.11 |
| Mg | 0.11 | 7.46 | 16.86 | 33.88 | 4.10 | 4.10 |
| Al | 19.60 | 8.16 | 37.57 | 0.05 | 14.67 | 14.77 |
| Si | 20.11 | 21.10 | 0.18 | 19.70 | 20.12 | 20.07 |
| K | 0.00 | 0.00 | 0.00 | 0.00 | 0.00 | 0.00 |
| Ca | 14.32 | 17.56 | 0.17 | 0.74 | 15.33 | 15.28 |
| Ti | 0.02 | 1.15 | 0.15 | 0.02 | 0.53 | 0.53 |
| Cr | 0.00 | 0.18 | 0.38 | 0.10 | 0.09 | 0.09 |
| Mn | 0.01 | 0.03 | 0.05 | 0.08 | 0.02 | 0.02 |
| Fe | 0.19 | 0.17 | 0.94 | 0.88 | 0.21 | 0.21 |
| Ni | 0.00 | 0.00 | 0.00 | 0.00 | 0.00 | 0.00 |
| S | 0.00 | 0.00 | 0.01 | 0.00 | 0.00 | 0.00 |
| P | 0.00 | 0.00 | 0.00 | 0.00 | 0.00 | 0.00 |
| V | 0.01 | 0.04 | 0.35 | 0.02 | 0.03 | 0.03 |
| O | 46.29 | 44.17 | 45.52 | 45.45 | 45.31 | 45.32 |
| Total | 100.86 | 100.06 | 102.19 | 100.95 | 100.52 | 100.53 |

*Con. = concentration; given in wt%.

Bulk I and II represent bulk compositions calculated from endmembers I and II in Table 1, respectively.

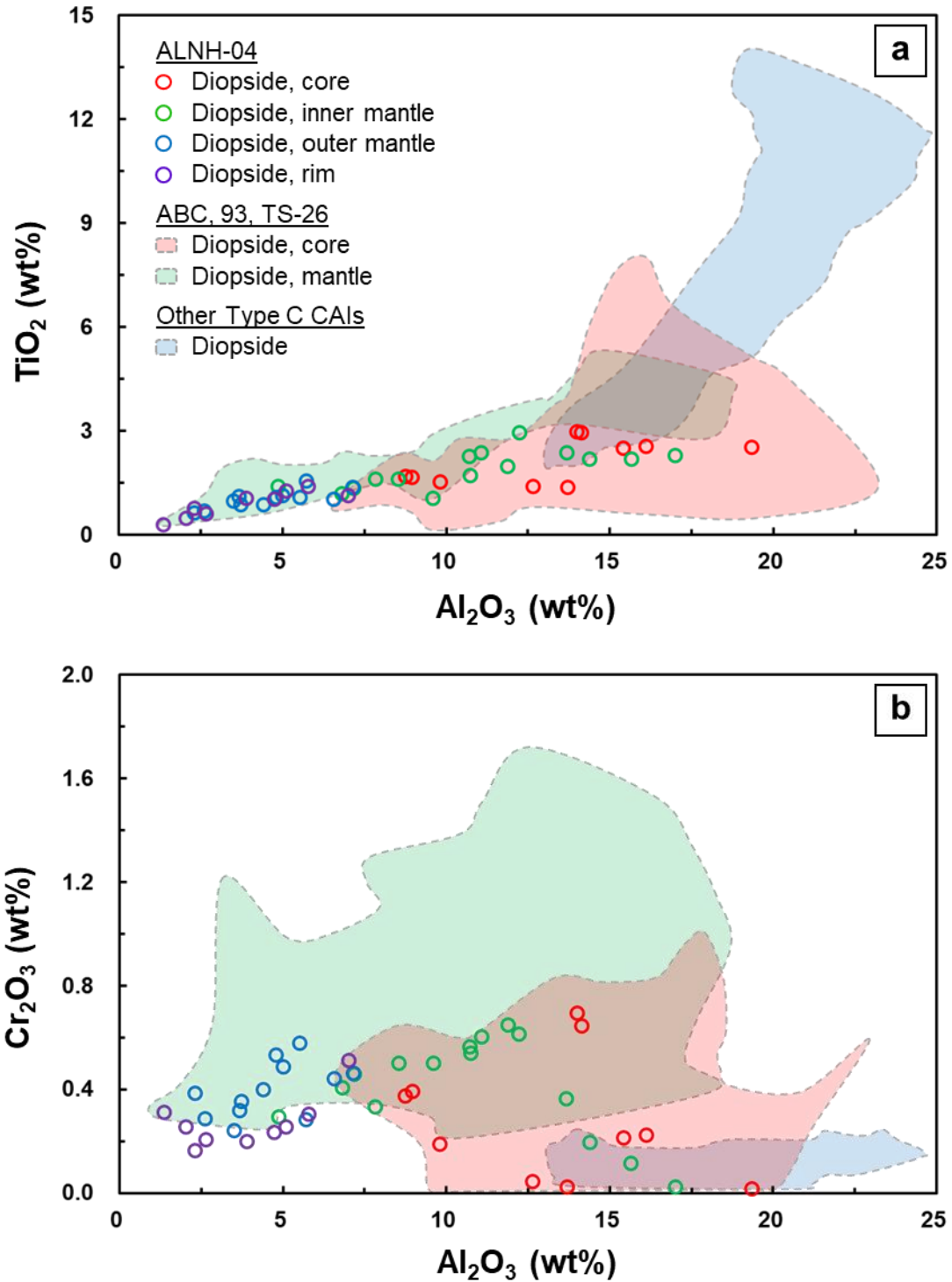


Fig. 4. Plots of diopside compositions in ALNH-04: (a) TiO₂ vs. Al₂O₃ (wt%) and (b) Cr₂O₃ vs. Al₂O₃ (wt%). Also plotted for comparison are diopside grains in Allende Type C CAIs reported by Krot et al. (2007a,b). Diopside in ALNH-04 has a similar TiO₂-Al₂O₃ trend with CAI ABC, 93, and TS-26; however, diopside in the outer part of ALNH-04 contains significantly lower concentrations of Cr₂O₃.

Forsterite contains ~1.04 wt% CaO and ~0.15 wt% Cr₂O₃, and only shows Fe-enrichment on its rim and along the veins. The Wo and Fs contents of sub-calcic augite in the rim region of the CAI are ~34.5 and ~1.1, respectively.

The composition of the Al-Fe silicate phase resembles that of olivine, and thus is calculated based on 4 oxygen anions per formula unit. The Al₂O₃ and FeO contents of this Al-Fe silicate are 0.78-4.17 wt% and 23.52-36.52 wt%. It also contains a minor amount of Na₂O (up to 1.07 wt%).

3.3. Microstructures

Several FIB sections were extracted from the boundaries between anorthite and diopside, in order to investigate the replacement relationships between different phases in the observed zonal sequence. Three FIB sections (FIB-01, -02, and -04) are from the inner mantle region; two sections (FIB-03 and -06) are from the outer mantle region where the Al-bearing, Fe-rich silicates are abundant; FIB-05 is from the core region where sodalite is the dominant secondary phase. The positions of the FIB sections are shown in Fig. 5.

The first FIB section (FIB-01) samples an alteration zone between anorthite and diopside in the inner mantle region of the CAI. Based on X-ray maps, this zone is 0.5-1 μm wide, and dominated by sodalite. The anorthite-sodalite interface has an irregular outline and shows a complex structure (Fig. 6a,b). Although Al-Ti-bearing diopside appears to be unaltered, the surface of the pyroxene is decorated by subhedral, Fe-bearing spinel grains (~100 nm, Fe# = ~20) (Fig. 6c), as well as localized, irregular overgrowths of Ca-Fe pyroxene (~100 nm thick,

$\sim\text{Wo}_{46}\text{Fs}_{13}$). The main part of the alteration zone is composed of sodalite, which contains a few randomly distributed, submicron pores (100-200 nm), as well as anhedral grains of Ca-rich nepheline (Ca/Na ratio up to 0.5) and Mg-spinel (~ 200 nm, $\text{Fe}\# = \sim 12.5$). Electron diffraction patterns combined with EDS analysis confirm the identification of nepheline and sodalite. Nepheline and sodalite are exceptionally beam sensitive and undergo amorphization rapidly under the electron beam. The interfaces between anorthite, nepheline, and sodalite are highly

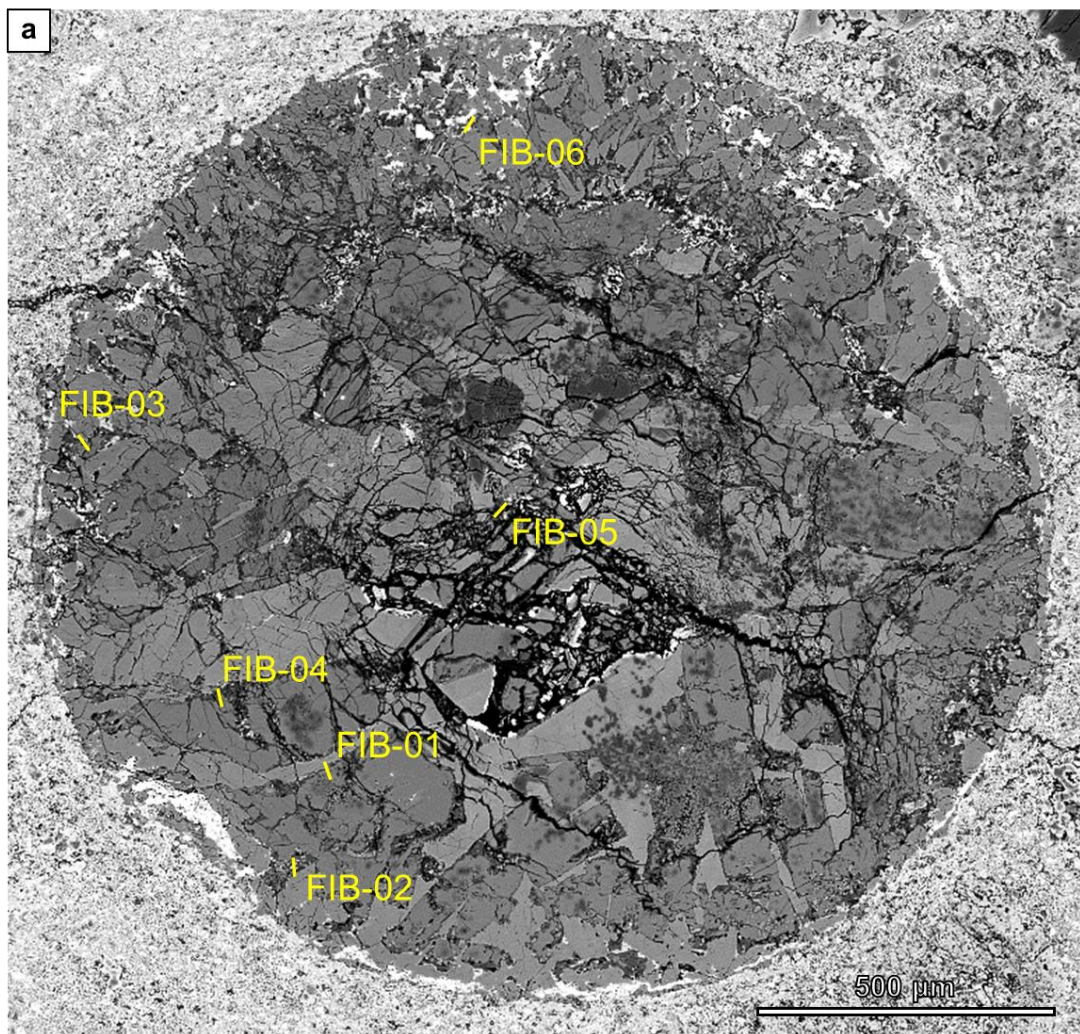


Fig. 5. The locations for the six FIB sections extracted from ALNH-04.

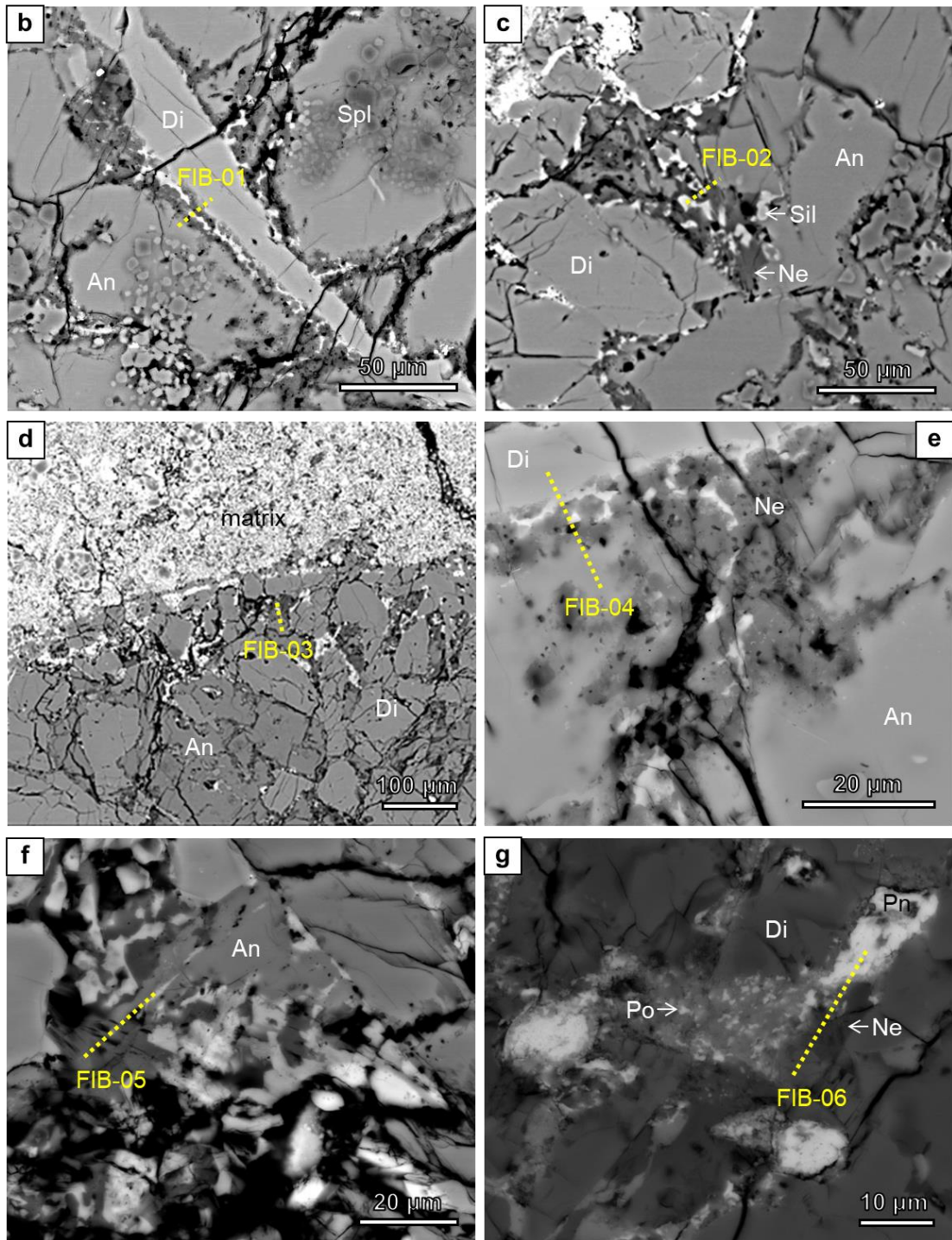


Fig. 5. (*continued*) (a) The relative locations on the combined BSE image of the CAI, and (b-g) shown on higher-magnification BSE images. FIB-01 and -04 are from the inner mantle region; FIB-02, -03, and -06 are from the outer mantle region; and FIB-05 is from the core region. Abbreviations: An = anorthite, Di = Al-Ti-bearing diopside, Ne = nepheline, Pn = pentlandite, Po = pyrrhotite, Sil = Al-Fe silicate, Spl = spinel.

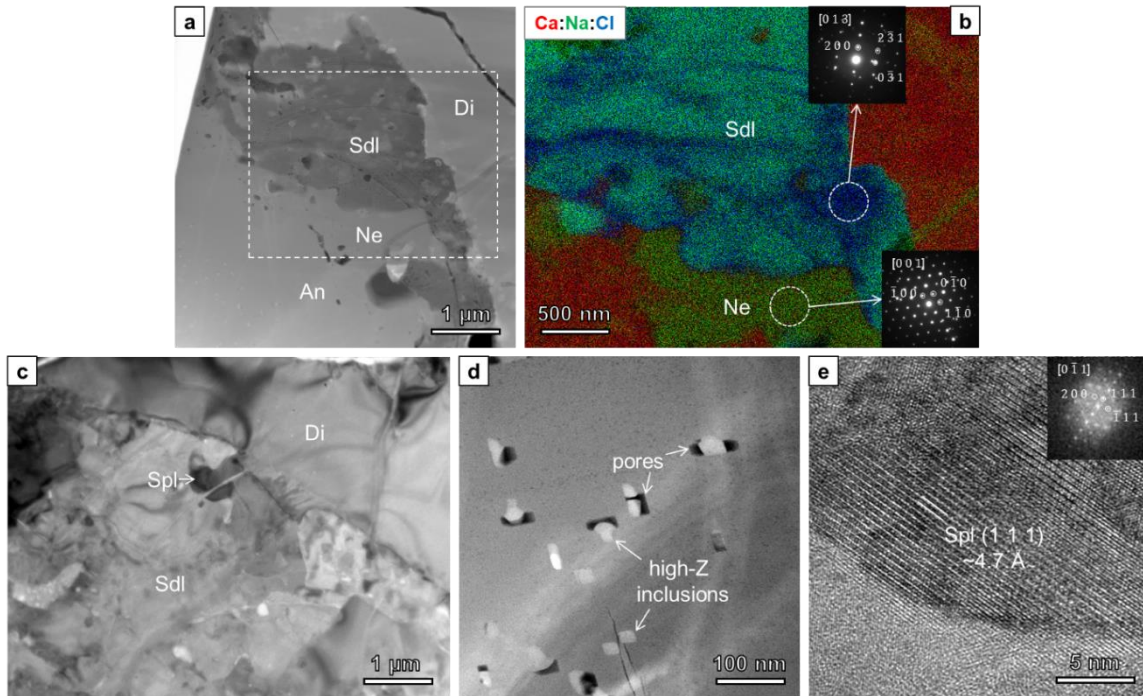


Fig. 6. TEM images of FIB-01 that was extracted from an alteration zone between anorthite and diopside in the inner mantle region of the CAI. (a) DF-STEM image of the alteration interface between anorthite and diopside. (b) Combined EDS X-ray elemental map (Ca (red), Na (green), Cl (blue)) from the region outlined in (a) showing the distribution of sodalite and nepheline. Inserts are electron diffraction patterns of sodalite and nepheline. (c) BF-TEM image shows the presence of Fe-bearing spinel along the interface between anorthite and diopside. (d) DF-STEM image of high-Z inclusions associated with pores in anorthite. (e) A HRTEM image of a high-Z inclusion with inset FFT pattern that is consistent with the $[0\bar{1}1]$ zone axis of spinel. Abbreviations: An = anorthite, Di = Al-Ti-bearing diopside, Ne = nepheline, Sdl = sodalite, Spl = spinel.

curved, and they are decorated by pores. The phase that is most commonly in direct contact with anorthite is nepheline, although sodalite can also be present to a lesser degree. Anorthite close to the interface with the Ca-rich nepheline shows the development of irregularly-shaped pores (~ 150 nm), but the nepheline itself appears to be pore-free. There is no clear replacement relationship between the two types of feldspathoids. Several microns away from the alteration zone, anorthite contains abundant, tiny high-Z phases (~ 40 nm), some of which are associated

with pores (~10 nm) (Fig. 6d). These high-Z phases are enriched in Fe, based on EDS analysis. Fast Fourier Transformation (FFT) analysis of high resolution TEM images of some of the high-Z inclusions, show that the d-spacings and zone axis diffraction patterns are consistent with spinel (Fig. 6e).

We cut another FIB section (FIB-04) from the altered interface between anorthite and diopside in the inner mantle region of the CAI. The major alteration phase in FIB 04 is nepheline, which encloses several randomly distributed fayalitic olivine grains (~60 μm) (Fig. 7a). The most unique feature of this FIB section is the presence of an epoxy vein filled with abundant, elongated, or granular Fe-rich spinel grains (~300 nm, $\text{Fe}\# = \sim 30$) (Fig. 7b). In some regions, these spinel grains are in contact with nepheline and seem to have grown on the latter phase. Similar to the observation in FIB 01, anorthite also contains a zone with abundant Fe-rich phases (30-40 nm). Diopside contains many fractures and several veins, adjacent to which are abundant Fe-rich spinel grains ($\text{Fe}\# = \sim 40$) (Fig. 7c). Diopside shows abundant, thin exsolution lamellae of a low-Ca pyroxene phase (20-40 nm).

A FIB section (FIB-02) was extracted from a fine-grained, extensively altered anorthite grain in the outer mantle region of the CAI to compare the alteration assemblages and textures with alteration in the inner part of ALNH-04 and to investigate the nature of the Al-Fe silicate. The anorthite has been replaced by an assemblage of feldspathoids and Fe-bearing silicate. Under the TEM, the Fe-bearing phase (~5 μm) with a high density of dislocations was found to be in direct contact with nepheline (2-4 μm), and they do not show a complex intergrowth relationship (Fig. 8a). The electron diffraction data and EDS analysis show that this phase is

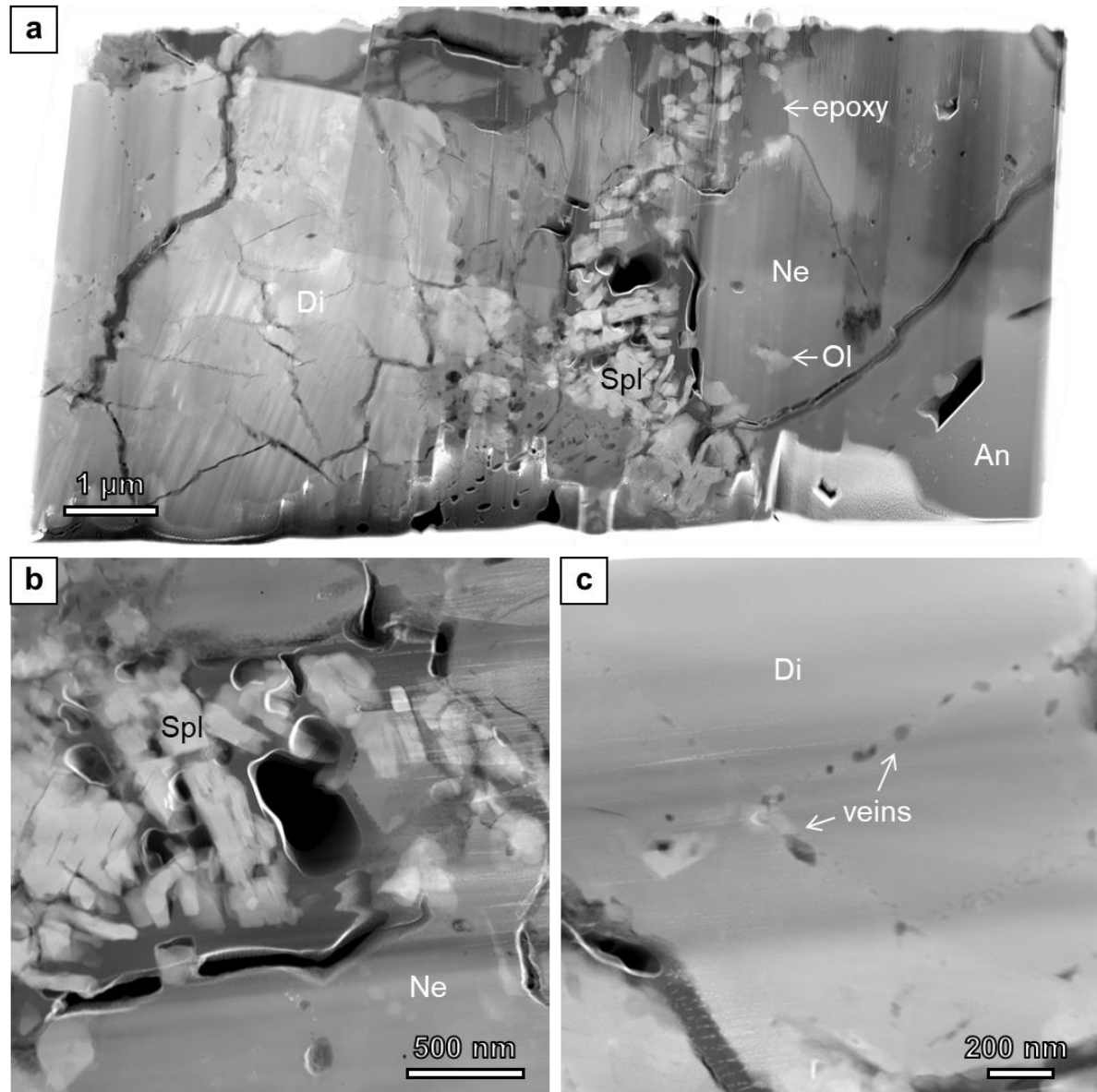


Fig. 7. DF-STEM images of FIB-04 from the altered interface between anorthite and diopside in the inner mantle region of the CAI. (a) Mosaic image of FIB-04, showing the complex structure of the alteration interface between anorthite and diopside. Nepheline contains several fayalitic olivine grains and is in contact with a porous epoxy-filled region that contains abundant Fe-rich spinel grains. Diopside is highly fractured, and contains secondary veins (e.g., the upper left region of the image). A low-Ca pyroxene phase is present as exsolution lamellae in diopside. (b) A higher-magnification image showing abundant elongate, Fe-rich spinel grains adjacent to nepheline. (c) Diopside contains porous, secondary veins that are composed of Fe-bearing diopside. Abbreviations: An = anorthite, Di = Al-Ti-bearing diopside, Ne = nepheline, Ol = olivine, Spl = spinel.

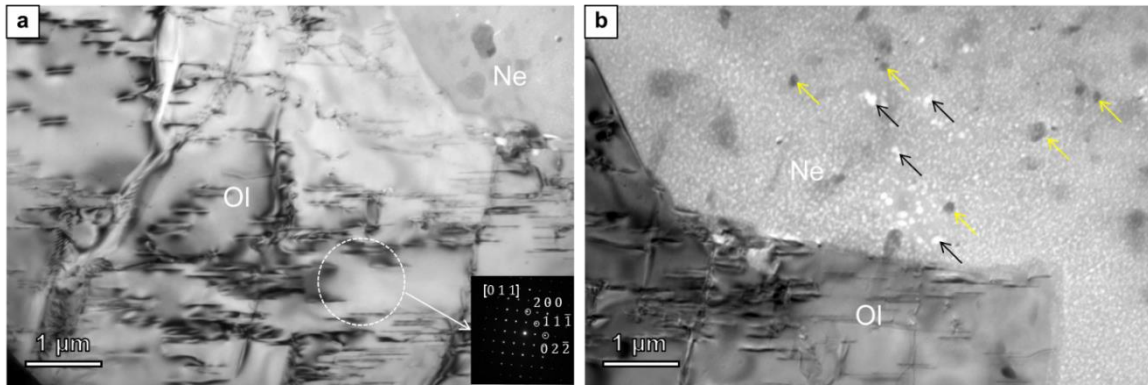


Fig. 8. BF-TEM images of FIB-02 from a fine-grained, extensively altered anorthite grain in the outer mantle region of the CAI. (a) Fe-rich olivine showing a high density of dislocations. The insert shows an [011] zone axis electron diffraction pattern of olivine. (b) The contact between olivine and nepheline is sharp and well-defined with no evidence of a replacement relationship between the two phases. The nepheline has been heavily beam damaged and has been amorphized with the development of numerous nanopores (some of them are indicated by black arrows). Numerous small inclusions (yellow arrows) are apparent within the nepheline. Abbreviations: Ol = olivine, Ne = nepheline.

Fe-bearing olivine (Fa₂₀₋₂₅). The olivine contains no detectable Al₂O₃, it is thus very likely that the Al-bearing, Fe-rich phase detected by SEM EDS analysis is a mixture of Fe-bearing olivine and some Al-rich phases (e.g., feldspathoids). The boundary between this Fe-bearing olivine and nepheline is smooth and shows no clear evidence for a replacement relationship (Fig. 8b).

A second FIB section (FIB-03) was also lifted out from the outer mantle region of the CAI, to study an altered anorthite grain that has been almost completely replaced by feldspathoids and Fe-bearing olivine. In this FIB section, secondary phases penetrate into anorthite, with both nepheline and sodalite occurring as reentrant features with planar, crystallographically-controlled boundaries with the anorthite (Fig. 9). In the STEM images, the high porosity in some feldspathoid grains is attributed to electron beam damage during TEM imaging, since those grains did not have a high abundance of pores at the beginning of

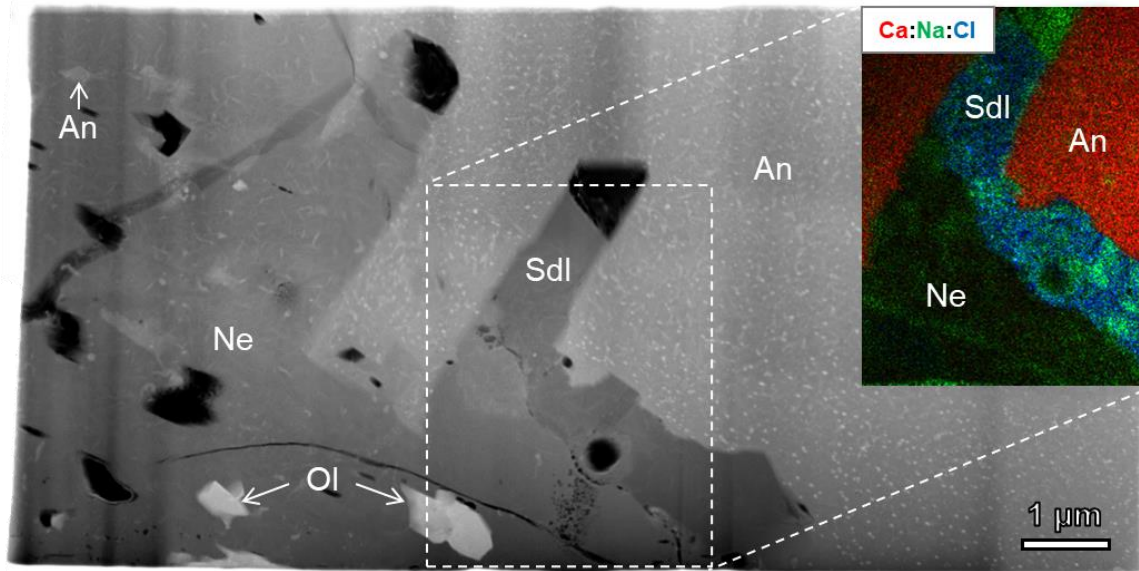


Fig. 9. Mosaic DF-STEM image of FIB-03 that was lifted out from the interface between an anorthite grain and its alteration products (feldspathoids and Fe-bearing olivine) in the outer mantle region of the CAI. Clearly shown in the image are some reentrant features of sodalite and nepheline into anorthite. In the lower left region of the image, several olivine grains with a high Z contrast are enclosed in nepheline. The insert is a combined elemental map (Ca (red), Na (green), Cl (blue)) of the outlined region. The high porosity in some local regions can be attributed to electron beam damage during the TEM imaging process. There are also some relict anorthite grains in nepheline, as shown in the upper left region of the image. Abbreviations: An = anorthite, Ol = olivine, Ne = nepheline, Sdl = sodalite.

TEM imaging. Calcium-potassium-bearing nepheline is the dominant alteration phase, and its contact with sodalite is smooth, with abundant pores (10-20 nm) distributed along their interface. Nepheline contains larger pores (up to 0.8 μm) than sodalite, although the porosity is similar in both phases. In this FIB section, a large pore is present at the end of the two reentrant features. One of them shows a high Na content on the X-ray map, but this is probably caused by the beam damage of nearby nepheline grains. Several fayalitic olivine grains with subhedral shapes and sharp boundaries are enclosed in nepheline. Some relict anorthite grains (~200 nm) are also present within nepheline and contain a small amount of Na₂O. Anorthite

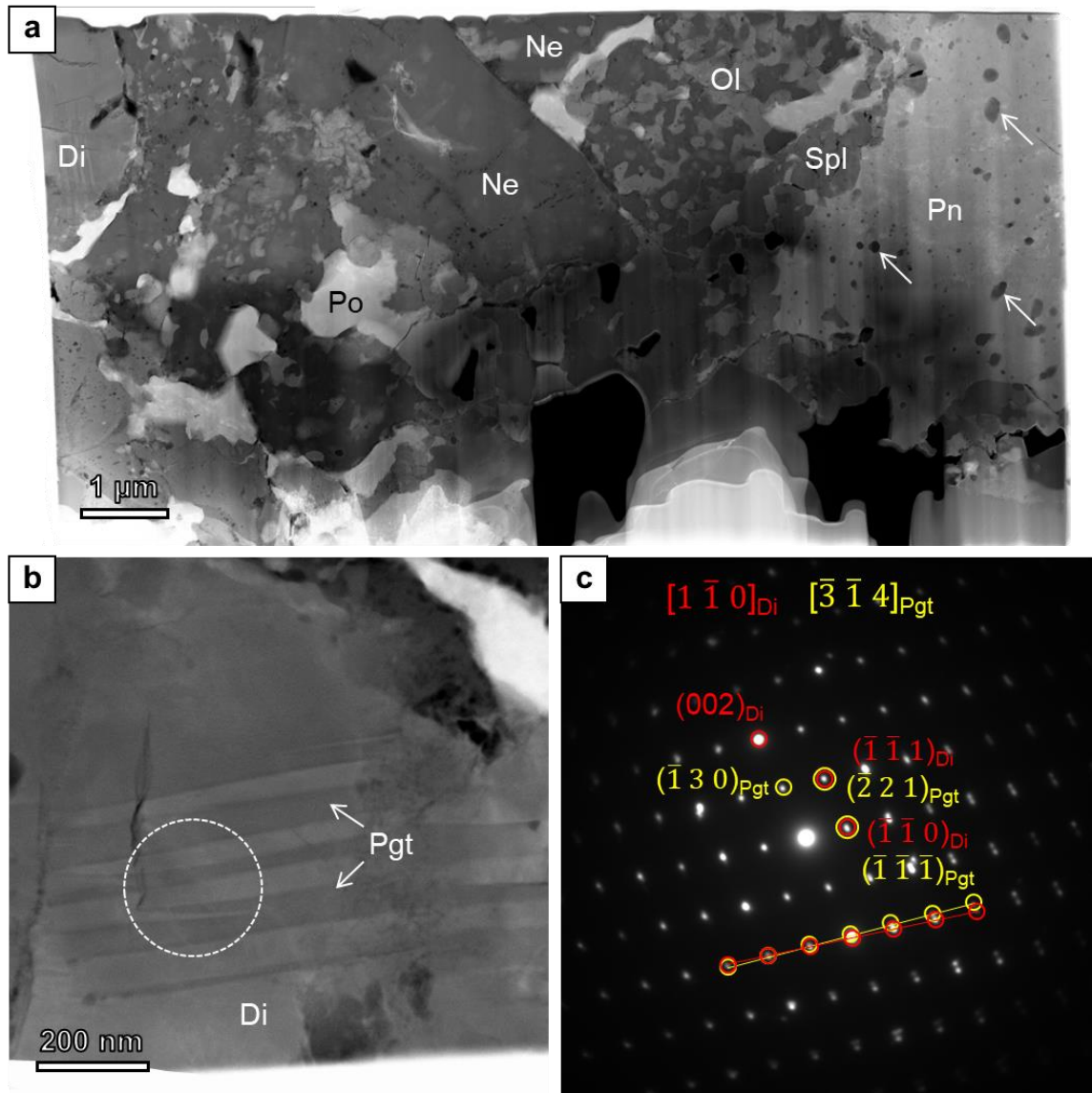


Fig. 10. DF-STEM images (a and b) of FIB-06 that is from an outer mantle region where secondary iron sulfides are abundant. (a) Mosaic of FIB-06 showing the microstructure of the alteration phases. Primary anorthite has been extensively replaced by a complex assemblage of nepheline, ferroan olivine, sulfides (pentlandite and pyrrhotite), and hercynitic spinel. Hercynitic spinel occurs as fine-grained inclusions in nepheline and sulfides. Also enclosed in pentlandite are nanoparticles of ferroan olivine and Ca-rich phosphates (some phosphate grains are indicated by white arrows). (b) Diopside contains exsolution lamellae of pigeonite. Based on the electron diffraction pattern, the pigeonite lamellae are on the (001) plane of diopside, which is a classic orientation relationship in pyroxene exsolution. (c) Electron diffraction pattern of diopside from the region circled in (b). The splitting of the diffraction maxima is caused by the presence of diopside (red circles) and exsolved pigeonite (yellow circles). Abbreviations: Di = diopside, Ol = olivine, Ne = nepheline, Pgt = pigeonite, Pn = pentlandite, Po = pyrrhotite, Sdl = sodalite, Spl = spinel.

contains myriad high-Z inclusions, which appear to be Fe-Mg-rich silicates, based on EDS spectra.

The relationships between feldspathoids, ferroan olivine, and iron sulfides in the outer mantle of the CAI were investigated using FIB section 06 (Fig. 10a). This FIB section was extracted from a region where iron sulfides are abundant. It reveals a complex texture. Anorthite has been almost completely replaced by the secondary phases. Nepheline is the dominant feldspathoid, and it is crosscut by arrays of aligned pores. A minor amount of sodalite is also present. Some of the feldspathoids contain inclusions of hercynitic spinel, ferroan olivine, and pyrrhotite, and others are almost free of such inclusions. The feldspathoids appear to be embayed by ferroan olivine and pyrrhotite along grain boundaries. Adjacent to the feldspathoid-dominant region is a complex intergrowth of ferroan olivine, nepheline, and pyrrhotite. This intergrowth region has a sharp boundary with the feldspathoid-dominant region, suggesting that two separate anorthite grains have been altered. The intergrowth coexists with pentlandite, which contains abundant tiny inclusions (50-100 nm) of hercynitic spinel, ferroan olivine and Ca-rich phosphates. Several diopside grains are found on the periphery of this FIB section, and they show thin exsolution lamellae of a low-Ca pyroxene phase (Fig. 10b). A SAED pattern of the host and exsolved phases can be indexed as diopside and low pigeonite (Fig. 10c).

Anorthite is partially altered to sodalite, nepheline, and ferroan olivine in FIB-05, which was extracted from an altered anorthite grain in the core region of the CAI. The relationship between anorthite and feldspathoids is similar to those found in FIB sections from the mantle

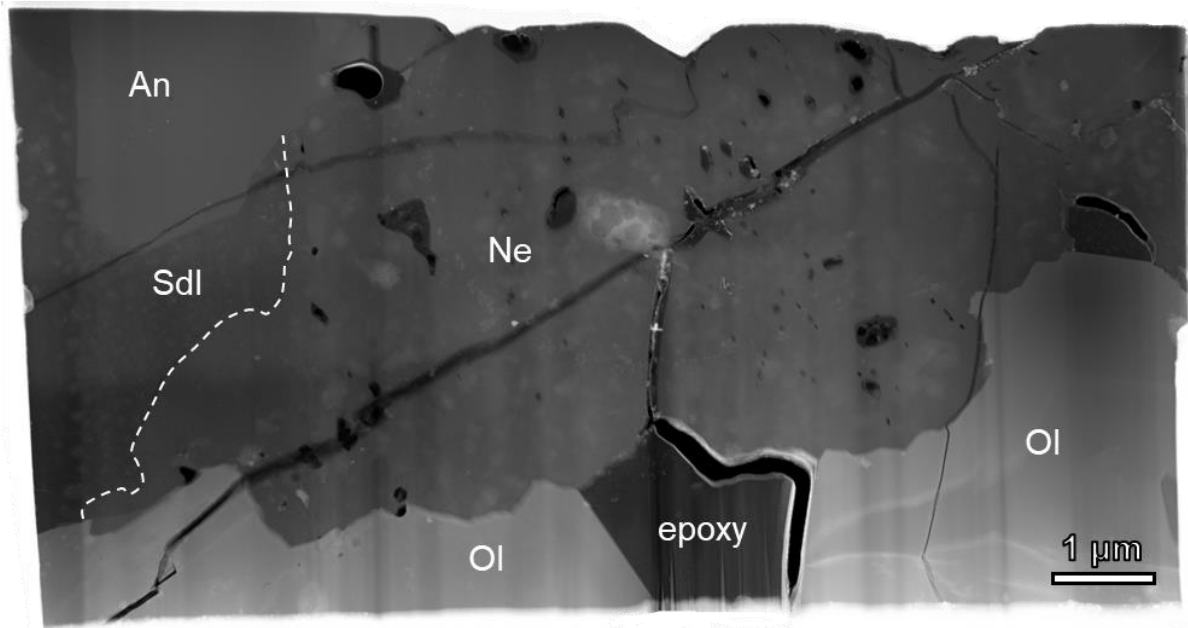


Fig. 11. DF-STEM mosaic image of FIB-05 from an altered anorthite grain in the core region of the CAI. The FIB section consists mostly of porous nepheline, with minor sodalite that has replaced anorthite. Both nepheline and sodalite are in direct contact with anorthite in the upper left of the image, but the replacement relationship between the feldspathoids is ambiguous. The interface between sodalite and nepheline is outlined by the white dashed line. Nepheline has a high porosity, in contrast to sodalite that is free of pores. The lower part of the FIB section consists of ferroan olivine, which is in direct contact with nepheline. This ferroan olivine phase is a secondary product of the alteration of primary forsterite in the core region. Abbreviations: An = anorthite, Ol = olivine, Ne = nepheline, Sdl = sodalite.

region: both nepheline and sodalite are in direct contact with the anorthite (Fig. 11). Nepheline is characterized by a high porosity, with randomly distributed pores ranging from 10 to 500 nm in size, while sodalite is free of pores. Ferroan olivine ($\sim\text{Fa}_{25}$), compositionally similar to olivine grains observed in other FIB sections and represents an alteration product of the primary forsterite, is directly touching nepheline. There is no clear textural evidence for a replacement relation between them.

4. DISCUSSION

Type C CAIs are very rare compared with other CAIs, and are characterized by their anorthite-rich, forsterite-deficient bulk compositions, enrichment in light Mg isotopes and high Si/Mg ratios (Wark, 1987). The presence of spinel, Al-Ti-bearing diopside, and anorthite in ALNH-04 is consistent with the mineralogy of Type C CAIs, and the calculated bulk composition (the averaged value of Bulk I and II in Table 2) of this inclusion plots close to the compositional field of other Type C inclusions on the CMAS (CaO-MgO-Al₂O₃-SiO₂) phase diagram (Fig. 12a). The rounded shape and ophitic to sub-ophitic texture of ALNH-04 indicate an igneous origin. However, this inclusion has some primary features that are distinct from other Type C CAIs reported in CV3 chondrites, which we will discuss in the following section. We will argue that, despite of these differences, ALNH-04 can still be classified as a Type C CAI.

ALNH-04 is unique in several aspects. (1) It has a primary mineralogical zonation that may imply multiple melting events. (2) The presence of forsterite in the core region makes this CAI different from other “typical” Type C CAIs that lack forsterite (e.g., Krot et al., 2007a,b, 2008). (3) It also has a secondary iron-alkali-halogen zoning sequence as manifested by varying proportions of nepheline, sodalite, Fe-bearing olivine, and sulfides in different regions of the CAI. This secondary zonation may indicate changing conditions during the alteration of this inclusion. A good understanding of its formation mechanism would potentially help us interpret other alteration features in CV3 chondrites. (4) A calcium-rich aureole in the matrix surrounding ALNH-04 may be indicative of *in situ* elemental exchange between the CAI and

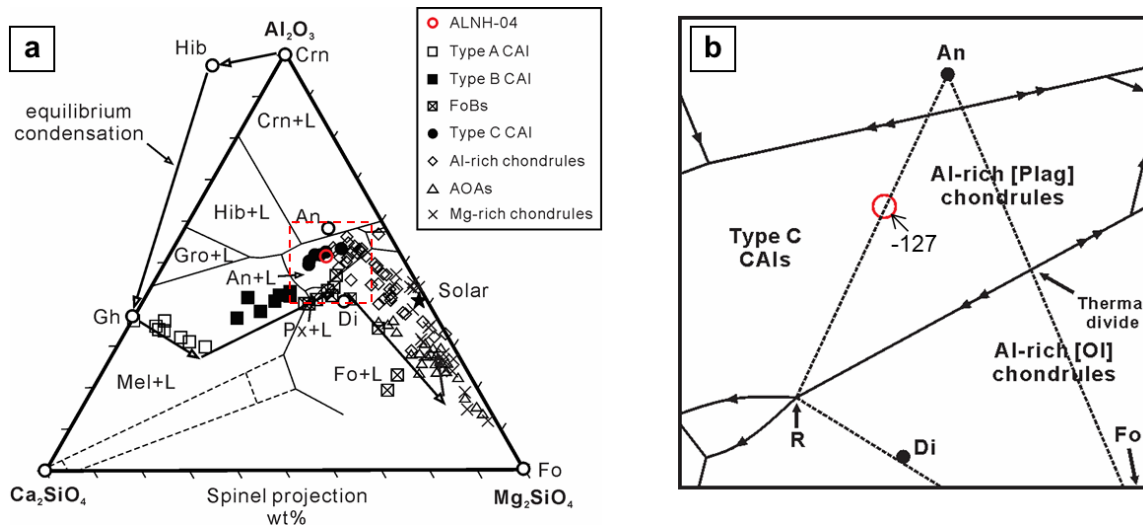


Fig. 12. (a) A CMAS diagram showing the position of the bulk composition of ALNH-04. Other types of refractory inclusions and chondrules are also plotted for comparison. Data from Beckett (1986), Bischoff and Keil (1984), Sheng et al. (1991), Wark (1987), Weisberg (1987), Jones and Scott (1989), Jones (1994), MacPherson and Huss (2005), and Kawasaki et al. (2015). (b) An enlarged plot from the outlined region in (a) showing the position of ALNH-04 relative to the tie line between anorthite and the distributary reaction point “R”. The number “-127” denotes the spinel coordinate of ALNH-04, which is on or slightly below the spinel saturation surface (~ 120). This suggests that anorthite and spinel are the first two crystallizing phases. It is difficult to predict the presence or absence of forsterite in the crystallization sequence based on just the bulk composition. The diagram was modified from Fig. 11 in MacPherson and Huss (2005). Abbreviations: An = anorthite, Crn = corundum, Di = diopside, Fo = forsterite, Hib = hibonite, Gh = gehlenite, Gro = grossite, L = liquid, Mel = melilite solid solution, Ol = olivine, Plag = plagioclase, Px = Ca-pyroxene solid solution.

the matrix, probably facilitated by a fluid.

In following sections, we will first compare ALNH-04 with other Type C CAIs reported in CV3 chondrites and discuss the possible formation mechanisms of its primary features. We will then discuss the origin of the secondary mineralization in this CAI, with a focus on the processes that have produced the observed iron-alkali-halogen zoning sequence and their implications for the alteration conditions. Finally, we will discuss the implications of the alteration features of ALNH-04 for alteration processes in CV3 chondrites, in general.

4.1. The primary features of ALNH-04

4.1.1. Comparison with other Type C CAIs from CV3 chondrites

The petrography, mineral compositions, oxygen isotopes, and ^{26}Al - ^{26}Mg isotope systematics of several coarse-grained igneous Type C CAIs (ABC, 93, TS-26, 100, 160, 6-1-72, 3529-40, and CG5) from the Allende CV3 chondrite have been described in detail by Krot and co-authors (Krot et al., 2007a,b, 2008). These inclusions were divided into three groups (group 1: 100, 160, 6-1-72, and 3529-40; group 2: ABC, 93, and TS-26; group 3: CG5), based on their textures, mineralogy, and possible formation histories (Krot et al., 2007a,b, 2008). They have all experienced melting processes and thus have an igneous origin; however, each inclusion probably had different precursor materials, and interacted with the surrounding nebular gas to different degrees. For example, some Type C CAIs contain relict Type B CAI-like materials, indicative of a Type B CAI precursor, while other inclusions may have been modified from fine-grained, spinel-rich inclusions by exchange with the nebular gas.

Inclusions 100, 160, 6-1-72, and 3529-40 contain coarse-grained Al-Ti-diopside and Na-bearing melilite with a “lacy texture” (diopside and melilite contain abundant rounded and prismatic anorthite inclusions), and fine-grained anorthite as groundmass. Spinel occurs as framboids, aggregates, and isolated grains enclosed in melilite, Al-Ti-diopside, and anorthite. Significant variations in the morphology of melilite and Al-Ti-diopside, and the distribution of spinel grains were reported by Krot et al. (2007a,b) in individual inclusions, and some of these inclusions contain texturally-distinct regions (e.g., anorthite-poor, fine-grained Al-Ti-diopside regions, and a melilite-rich region similar to Type B CAIs in Allende). Melilite grains in these

CAIs are commonly replaced by grossular, monticellite, and forsterite. Nepheline and sodalite are also found to replace anorthite and/or melilite on the periphery of some of the CAIs. The second group including CAI ABC, 93, and TS-26 is characterized by the presence of ferromagnesian chondrule-like materials (forsteritic olivine and low-Ca pyroxene, and coarse-grained igneous rims) in their outer parts. Their cores consist of lath-shaped anorthite, Cr-bearing Al-Ti-diopside (up to 1.6 wt% Cr₂O₃), spinel, and highly åkermanitic and Na-rich melilite. Diopside grains show variable compositions and complex zoning in Al₂O₃ and TiO₂. Grossular, monticellite, wollastonite, nepheline, sodalite, ferroan olivine, titanite, and Fe-Mn-bearing diopside are observed as secondary minerals. The third group includes one single CAI fragment CG5 with an ophitic portion and an anorthite-poor portion. This CAI is composed of lath-shaped anorthite, interstitial Na-bearing melilite, and Al-Ti-diopside, and abundant spinel grains as inclusions in the former three phases.

The CAI ALNH-04 is texturally most similar to Allende Type C inclusions, ABC, 93, and TS-26: they all display an ophitic-to-sub-ophitic texture and contain chondrule-like materials in the rim regions. The sharp change in grain size from the inner to outer regions is similar in TS-26 and ALNH-04, and the two regions are separated by a discontinuous Fe-rich zone in both inclusions. Finally, the anorthite grains in ALNH-04 and 93 show a similar growth style, i.e., radiating away from the periphery of the CAIs. ALNH-04 also has pyroxene compositions that share similarities to ABC, 93 and TS-26 (Fig. 4). The CAIs ABC, 93, and TS-26 experienced re-melting and addition of ferromagnesian chondrule materials in the chondrule-forming region (Krot et al., 2007a,b). The similarity of the TiO₂-Al₂O₃ trend in diopside

between ALNH-04 and these three CAIs (Fig. 4a) indicates a similar re-melting event also affected ALNH-04. Individual diopside grains show core-to-rim zoning in their TiO_2 and Al_2O_3 contents, and diopside grains from different regions have different compositions. There is, however, a notable compositional difference: pyroxene from the rim region of ALNH-04 has lower Cr_2O_3 contents than that from the mantle of CAI ABC, 93, and TS-26 (Fig. 4b), implying precursor materials with different Cr_2O_3 contents. Also, the fine-grained interstitial material consisting of melilite, Cr-free and Ti-poor Al-diopside, grossular, wollastonite, monticellite, and very fine-grained “mesostasis”, and the fine-grained, anhedral Al-Ti-diopside inclusions in anorthite are absent in ALNH-04, but are present in ABC, 93, and TS-26.

ALNH-04 lacks the lacy texture observed in CAI 100, 160, 6-1-72, and 3529-40. The anorthite grains in ALNH-04 are coarse-grained laths, which are distinct from the fine-grained anorthite in those Type C CAIs. ALNH-04 also differs from these other Allende Type C inclusions in lacking melilite, which is a major phase in all four of these inclusions. Spinel is much more abundant in CG5 than ALNH-04, and it does not show a variation in the grain size of anorthite as in ALNH-04, though the two inclusions both have an anorthite-poor region.

Some other Type C CAIs from CV3 chondrites have also been reported in the literature. The Type C inclusion EK1-04-2 (Kawasaki et al., 2015) from Allende displays a zoning texture similar to that of ALNH-04: a spinel-rich core composed of euhedral spinel grains enclosed in euhedral-to-subhedral anorthite and anhedral Al-Ti-diopside, and abundant forsterite crystals; and an anorthite-dominant mantle with a lower amount of spinel and olivine than the core. This CAI is enriched in MgO (core: 15.7 wt%; mantle: 9.0 wt%) and depleted in CaO (core: 12.6

wt%; mantle: 16.8 wt%) compared to typical Type C CAIs (MgO: ~7.7 wt%; CaO: ~21.7 wt%; Wark, 1987), which is consistent with the high abundance of forsterite. Kawasaki et al. (2015) suggested, based on the oxygen and Al-Mg isotopes, that forsterite in EK1-04-2 crystallized from a melted precursor, which also contained forsterite. However, these authors did not further constrain the nature of the precursor.

Other Type C inclusions from Allende (Wark, 1987; Imai and Yurimoto, 2000) and Leoville (Wark, 1987) are texturally and mineralogically similar to those described above, and thus will not be described here.

To summarize, ALNH-04 has textural and compositional similarities to some of the Type C CAIs reported in previous studies. However, there are notable differences between ALNH-04 and these other CAIs, which implies that ALNH-04 may have a different precursor from other Type C CAIs.

4.1.2. Origin of the primary features of ALNH-04

As mentioned previously, the spherical appearance of ALNH-04 and the ophitic texture imply an igneous origin. This is consistent with the conclusions of other workers that all the reported Type C CAIs are crystallization products from once molten objects. The predicted crystallization sequence of major phases based on the texture is spinel, anorthite, and diopside.

Forsterite grains show subhedral shapes, suggesting that they could have crystallized from the melt. Alternatively, forsterite may represent relict grains from the precursor. As shown on the CMAS phase diagram, ALNH-04 plots close to the region occupied by Type C CAIs from

the literature (Fig. 12a), implying that either anorthite or spinel was the liquidus phase. Whether anorthite or spinel was the liquidus phase should not affect the crystallization sequence of other phases, since the calculated spinel coordinate is close to the spinel saturation surface. The bulk composition of ALNH-04 lies near the tie line between anorthite and the distributary reaction point “R” (Fig. 12b). Therefore, whether forsterite appears in the sequence or not is difficult to predict due to the 2D sectioning effect, as described in the Analytical Methods section. If the proportion of forsterite is underestimated due to the 2D sectioning effect, the position of the bulk composition of ALNH-04 on the CMAS ternary may move to the right side of the tie line between anorthite and the distributary reaction point “R”. According to MacPherson and Huss (2005), this tie line provides a meaningful distinction between Type C CAIs and Al-rich, plagioclase-phyrlic chondrules, as indicated on Fig. 12b. However, several rare Type C CAIs, such as EK1-04-2 reported by Kawasaki et al. (2015), plot on the right side of the tie line. The distinction between the two types of objects, therefore, should also consider other aspects, such as textures and phase assemblages. Alternatively, there may not be a clear distinction between Type C CAIs and Al-rich chondrules, as they may just represent objects on a continuous evolutionary trend controlled primarily by vapor-solid processes. This is supported by the presence of spinel palisades and framboids in ALNH-04, which are a common feature in igneous CAIs (e.g., Wark, 1987; Simon and Grossman, 1997). In this case, forsterite could be a crystallization phase after anorthite, if the exact position of the bulk composition of ALNH-04 on the CMAS diagram is the right side of the tie line between anorthite and the distributary reaction point “R”.

In Figure 13, the minor element contents of forsterite in ALNH-04 are compared with those of forsterite in Type C CAIs and AOAs from CV3 chondrites. Forsterite in ALNH-04 has Cr₂O₃ and MnO contents that are within the compositional range of forsterite in AOAs from CV3 chondrites (Efremovka, Vigarano, and Leoville), but are distinct from those of captured chondrule olivine in Type C CAIs ABC, 93, and TS-26 (Fig. 13a,b). The elevated CaO content of forsterite in ALNH-04 sets it apart from forsterite in other refractory inclusions. This high CaO content is, on the other hand, comparable to that of forsterite in FoBs from CV3 chondrites (0.7-1.9 wt%) (Bullock et al., 2012). Calculations on the effects of partial evaporation of FoBs demonstrate the possibility of evolving the melt composition into the spinel+anorthite+liquid field on the CMAS diagram, though the exact evolutionary trend depends on both the relative evaporation effects of Mg and SiO, and the bulk composition (Bullock et al., 2012). Nevertheless, it is likely that the forsterite grains in ALNH-04 crystallized from a melt with a FoB-like composition. Forsterite-bearing Type B CAIs have been proposed to have formed by melting of an AOA-like precursor (Bullock et al., 2012). Accordingly, crystallization of a melted AOA that contained embedded CAI-like materials is also a possible formation mechanism for the forsterite in ALNH-04. In any case, future oxygen isotopic work will help better understand the origin of forsterite in ALNH-04: an ¹⁶O-rich signature points to a relict origin, while an ¹⁶O-poor signature may suggest that forsterite crystallized from a chondrule melt that formed by nearly complete melting of a CAI-like precursor.

If the forsterite has a relict origin, we need to determine its provenance. Several precursor materials have been proposed for Type C CAIs by Krot et al. (2007a,b), including Type Bs,

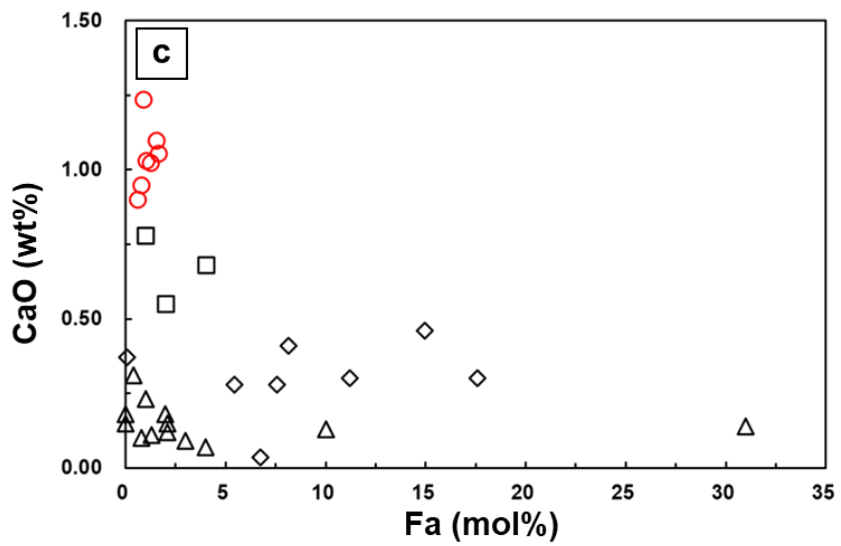
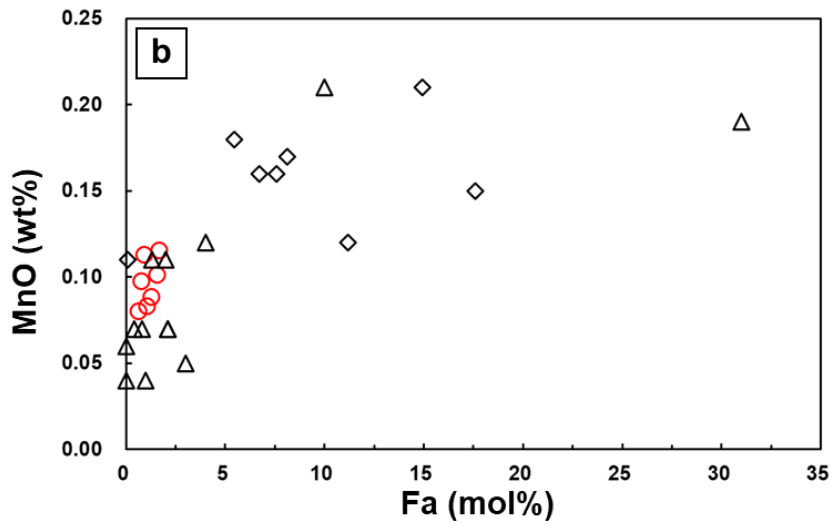
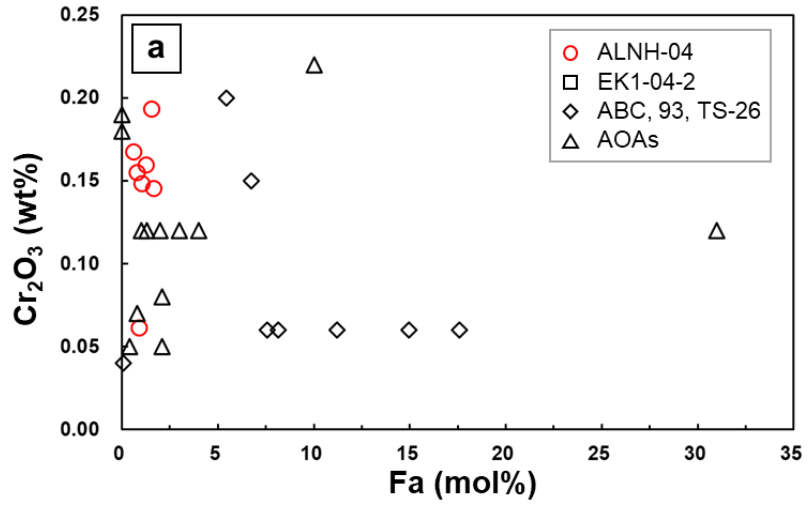


Fig. 13. Minor element plots of (a) Cr₂O₃ (wt%) vs. Fa (mol%), (b) MnO (wt%) vs. Fa (mol%), and (c) CaO (wt%) vs. Fa (mol%) of forsterite in ALNH-04, in comparison with olivine in other Type C CAIs and AOAs from CV3 chondrites. Forsterite in ALNH-04 has Cr₂O₃ and MnO contents that are within the compositional range of forsterite in AOAs. However, the CaO content of forsterite in ALNH-04 is significantly higher than that in other refractory inclusions. Data source: EK1-04-2 from Kawasaki et al. (2015); ABC, 93, and TS-26 from Krot et al. (2007b); AOAs from Komatsu et al. (2001), Fagan et al. (2004), and Krot et al. (2004c).

fine-grained, spinel-rich inclusions and ferromagnesian chondrules. However, as discussed in the previous section, there are notable differences between ALNH-04 and the Type C CAIs described in Krot et al. (2007a,b). In particular, the forsterite grains in the core region of ALNH-04 cannot be explained by any formation mechanisms proposed by Krot et al. (2007a,b): forsterite in those Type C inclusions is formed by incorporation of chondrule materials and is present only in the outer parts of the CAIs. In addition, the incorporated forsterite grains in these Type C inclusions have very different compositions from those in ALNH-04 (Fig. 13). Similarly, forsterite in ALNH-04 cannot be a relict from AOAs from CV3 chondrites due to marked compositional differences. On the other hand, as discussed earlier, FoBs have forsterite that is compositionally comparable to that in ALNH-04. This implies that forsterite in ALNH-04 could possibly be inherited from FoBs.

The primary core-mantle texture in ALNH-04, as indicated by the distinct grain sizes of anorthite and diopside could be attributed to a later, lower-intensity melting event that occurred after the primary igneous crystallization of the CAI. The radiating texture exhibited by the fine-grained anorthite crystals in the outer part of the CAI is similar to that produced experimentally as a result of gas-melt interactions using a Type B CAI-like initial composition (Krot et al.,

2007b). However, compared to the experiment, the texture in ALNH-04 does not require a significant net exchange between the melt and the nebular gas; instead, the radiating growth pattern probably resulted from nucleation from the cooling surface of the molten inclusion. The common association of these finer-grained anorthite grains with augite may indicate capture of ferromagnesian silicates from a chondrule-forming region (Krot et al., 2007a). The ferromagnesian materials were melted during the thermal event that melted the outer mantle of ALNH-04, and then crystallized as augite together with anorthite. Indeed, this textural association is similar to the pigeonite-augite-plagioclase igneous region described in CAI 93 (Krot et al., 2007a). The elevated Na₂O content of anorthite in the outer mantle of the CAI may be attributed to incorporation of a Na-bearing component from the chondrule-forming region.

4.2. Origin of the secondary features of ALNH-04

4.2.1. Nebular vs. parent body alteration

Secondary alteration is complex in CV3 chondrites; in particular, the alteration style and extent vary significantly among different CV subgroups (Brearley and Krot, 2013). Hydrous phases are scarce in reduced CV chondrites, although incipient aqueous alteration features have been previously reported in the matrix of Vigarano (Lee et al., 1996; Abreu and Brearley, 2005, 2011). In contrast, a great variety of phyllosilicates are present in different chondritic components in the Bali-like oxidized subgroup (Cohen et al., 1983; Keller and Buseck, 1990; Tomeoka and Buseck, 1990; Keller et al., 1994; Kimura and Ikeda, 1998). Allende, belonging to the Allende-like oxidized subgroup (CV_{OxA}), contains rare phyllosilicates, talc, amphibole,

and biopyriboles in its CAIs and chondrules (Wark and Lovering, 1977; Tomeoka and Buseck, 1982; Hashimoto and Grossman, 1987; Keller and Buseck, 1991; Brearley, 1999; Ford and Brearley, 2007). Allende-like CV3 chondrites have experienced fluid-assisted metamorphism that has caused a wide range of effects, including metasomatism, oxidation, sulfidization, and carburization, which generated various secondary minerals enriched in mobile elements (Krot et al., 1995; Brearley and Krot, 2013). Both nebular (e.g., Hashimoto and Grossman, 1987; Palme and Fegley, 1990; Weinbruch et al., 1990; Keller and Buseck, 1991; Kimura and Ikeda, 1998; Weisberg and Prinz, 1998) and parent body (e.g., Krot et al., 1995, 1997, 1998a,b, 2000, 2004; Kojima and Tomeoka, 1996; Brearley, 1997; Brearley, 1999; Ford and Brearley, 2008; MacPherson and Krot, 2014) alteration mechanisms have been proposed to explain the secondary features observed in CV3 chondrites.

With respect to the secondary features in ALNH-04, there are several lines of evidence arguing for an asteroidal alteration origin involving a fluid that are consistent with previous observations (e.g., Krot et al., 1995; Brearley and Krot, 2013). First, the pseudomorphic replacement of anorthite along its boundaries with diopside by feldspathoids, coupled with the presence of abundant pores, is consistent with a fluid-induced dissolution-precipitation metasomatic process (e.g., Putnis, 2002, 2009, 2015; Putnis and Putnis, 2007; Putnis and Austrheim, 2010; Ruiz-Agudo et al., 2014). The development of porosity depends on the molar volume of the parent and product phases, as well as their relative solubility in a given solution. For example, pores will be produced, if more solid volume is dissolved than precipitated. The absence of porosity in the sample does not necessarily indicate a lack of fluid-rock interaction,

because the evidence for early-developed pores may have been erased by textural equilibration (e.g., Putnis et al., 2005; Raufaste et al., 2011; Ruiz-Agudo et al., 2014). However, the preservation of nanometer-sized pores, and very fine-grained (submicron) Fe-rich spinel, and sulfides in the FIB sections argues against a significant post-alteration equilibration process. Also, the replacement relationship between anorthite and feldspathoids is well-documented in CAIs from CV_{3OxA} chondrites (e.g., Brearley and Jones, 1998; Lin and Kimura, 1998; Krot et al., 2007a,b, 2008; Brearley and Krot, 2013). This fluid-induced alteration requires introduction of Na and Cl into the CAI, and extensive loss of Ca and Si as primary Ca-rich phases are altered. Although thermodynamic modeling predicts that feldspathoids could condense via interactions between pre-condensed silicates and a nebular gas with a solar composition below ~1000 K (e.g., Grossman and Larimer, 1974; Grossman and Steele, 1976; Wood and Hashimoto, 1988; Petaev and Wood, 1998; Lodders, 2003), this nebular alteration mechanism is inconsistent with the rarity of similar features in CAIs from reduced CV3 chondrites (e.g., Simon et al., 1999; Krot et al., 2004b). In addition, other phases more refractory than feldspathoids, such as enstatite and albitic feldspar, which are predicted to condense prior to feldspathoids in these models, are absent in ALNH-04. ALNH-04 experienced a complex formation history in the solar nebula, therefore feldspathoids, if formed by condensation prior to the later partial melting event, would be destroyed lost rapidly during that process. The feldspathoids must have formed after the solidification of the CAI, and the significant exchange between a nebular gas with a very low partial pressure of, for example, Cl with a solid igneous object to produce sodalite is highly unlikely. In addition, it is difficult

to envision that Ca was extracted into the gas phase during the alteration of anorthite, since Ca should have fully condensed at the temperatures at which feldspaths begin to condense.

Second, the Fe-enrichment in spinel grains enclosed in anorthite and diopside can be readily explained by a Fe-Mg interdiffusion mechanism during metamorphism on chondrite parent bodies (e.g., Brearley and Jones, 1998; Russell et al., 1998; Chizmadia et al., 2002; Itoh et al., 2004; Huss et al., 2006) due to the rapid Fe-Mg interdiffusion rate in spinel (Ando and Oishi, 1974; Freer and O'Reilly, 1980). Spinel grains that are adjacent to alteration regions show more extensive degree of Fe enrichment, which implies that spinel may have undergone equilibration with the Fe-rich fluid as spinel grains were exposed to the altering fluid. Hercynitic spinel is predicted to condense from an oxidized nebular gas, a similar condition where fayalitic olivine can also condense, in some thermodynamic models (e.g., Palme and Fegley, 1990); however, it has been argued that extreme dust/gas enrichments with the addition of water ice are needed to produce such an Fe-enrichment (Fedkin and Grossman, 2006). Similarly, the fayalitic rims on the forsterite grains in the inclusion core region (Fig. 3e), Fe-bearing diopside rims on some diopside grains (Fig. 3a), as well as the Fe-bearing diopside veins crosscutting forsterite (Fig. 3e) can also be explained as products of parent body alteration. In FIB section 04, we observed Fe-rich spinel forming veins near the alteration interface between anorthite and diopside. These Fe-rich spinel grains, thus, are more likely to be precipitates from the fluid.

Another line of evidence for parent body alteration is the presence of halos consisting of mobile-element-rich phases surrounding the CAI. Two halos are present: an inner Na-rich halo

composed of fine-grained anhedral nepheline grains and minor sodalite grains intimately mixed with matrix fayalite, and an outer Ca-Fe-rich halo consisting of hedenbergite + Fe-bearing diopside assemblages. Similar Ca-rich halos around Allende CAIs and dark inclusions have been reported and attributed to element redistribution facilitated by an aqueous fluid, which may be accompanied by high-temperature thermal metamorphism (Krot et al., 2000b; Brenker and Krot, 2004; Ford and Brearley, 2008). In the case of ALNH-04, the alteration of anorthite, and possibly a minor amount of diopside, released Ca, which diffused through an intergranular fluid and precipitated as Ca-rich pyroxene in the surrounding matrix. The Na-rich halo is more complex and cannot be explained by Na migration out of the CAI, because unaltered anorthite grains contain only minor amounts of Na (1.14 wt% Na₂O at maximum). It is more likely that the Na-rich halo stems from Na in the altering fluid that was not completely consumed by its interaction with the CAI. The local Al activity in the fluid may also play an important role. As we will demonstrate in later sections, Al was clearly mobilized during the secondary alteration of ALNH-04. Feldspathoids then formed at the migration front of Al, where the Al activity was high enough.

Finally, the distribution of sulfides and their relationship with other secondary phases favor a parent body alteration scenario. Sulfides, either as aggregates or as discrete grains, commonly form porous assemblages with other secondary phases (Fig. 2c and 3f). Metals are common phases in pristine CAIs (e.g., MacPherson et al., 1988; Weber and Bischoff, 1997; Guan et al., 2000; MacPherson, 2014) and exhibit various compositions. For example, Fremdlinge, complex assemblages of various metals, including refractory metal nuggets,

sulfides, oxides, and phosphates first described in detail by El Goresy et al. (1978) in Allende CAIs, may be products of sulfidation and oxidation processes at higher than solar gas sulfur and oxygen fugacities on the parent body (Blum et al., 1989). The sulfides in ALNH-04 are exclusively found in altered regions, and submicron sulfide grains occur along fractures in anorthite (Fig. 2a), which cannot be produced by any of the primary processes that formed ALNH-04. Sulfides could not be present as primary phases in this CAI, because they condense at much lower temperatures than the refractory phases in CAIs. Additionally, the submicron sulfides would be immiscible and have formed globules in the silicate melt. Sulfides in ALNH-04 show close associations with Fe-bearing olivine and feldspathoids that are replacing anorthite and diopside, and they have a clear pseudomorphic relationship with primary phases in some places, supporting the hypothesis that sulfides in ALNH-04 were produced during the same alteration process that altered the primary minerals in ALNH-04. Since sulfides cannot be among the primary phases of the CAI, their formation requires transportation of Fe and S into the CAI. Possible sources for these species are matrix materials and chondrules.

4.2.2. Origin of the alkali-halogen zonal sequence

The inclusion shows a zonal sequence of alkali-halogen-rich secondary phases, nepheline ± sodalite that have replaced anorthite in the outer part of the inclusion, giving way to the presence of ubiquitous sodalite with minor nepheline, partially replacing anorthite at grain boundaries and fractures in the interior of the inclusion. Similar zoning sequences have been previously reported in several Allende Type B CAIs (Ishii et al., 2010; Brearley and Krot,

2013); however, their detailed formation mechanisms have not been examined. The mineralogical evidence from ALNH-04 demonstrates that significant elemental exchange occurred between the inclusion and the surrounding matrix. Specifically, Fe, Na, Cl, and S were introduced into the CAI, while Ca and Si were lost to form the hedenbergite + diopside assemblages around the periphery of the inclusion. This evidence, combined with the observed porosity along the interface between anorthite and nepheline, indicates that a fluid was present during the alteration process. Below, we evaluate several different formation mechanisms of the alkali-halogen zonal sequence: (1) formation controlled by the primary mineralogical and textural heterogeneity; (2) thermal decomposition of nepheline, sodalite, and related phases due to high-temperature metamorphism; (3) a product of gradual compositional changes of the fluid migration front; (4) a two-stage fluid-assisted alteration event with changing fluid compositions.

Krot et al. (2004b) previously reported several fine-grained, spinel-rich inclusions from Efremovka and Leoville showing zoned textures: Ca-poor, Al-Mg-rich cores and Ca-rich, Al-Mg-poor mantles. These authors explained the zoning texture as a product of evaporation during a reheating process in the solar nebula. The formation of zoning textures with respect to secondary phases has also been described in some Allende CAIs and chondrules (McGuire and Hashimoto, 1989; Wasserburg et al., 2011; Brearley and Krot, 2013), and is partly attributed to the primary mineralogical zoning established in the solar nebula (Brearley and Krot, 2013). There are some differences in mineralogy between the inner and outer regions of ALNH-04, exemplified by the presence of coarse-grained, subhedral-to-anhedral forsterite

grains and abundant spinel grains in the core, and some sub-calcic pyroxene grains in the outer mantle region. However, the major phases being altered, i.e., anorthite and Al-Ti-diopside, are compositionally the same in both regions. Therefore, the similarities in the major mineralogy between the core and mantle regions in ALNH-04 excludes the possibility that primary mineralogy played a significant role in generating the secondary zonal texture. On the other hand, as discussed below, the textural difference, i.e., the grain size, between the two regions could have played a significant role in producing the secondary zonation.

There exists a positive correlation between nepheline abundance in CAIs and chondrules from CO3 carbonaceous chondrites and the degree of thermal metamorphism experienced by their host chondrites (e.g., Kojima et al., 1995; Itoh and Tomeoka, 1998; Russell et al., 1998; Tomeoka and Itoh, 2004), which may imply that nephelinitization was coupled with metamorphism in carbonaceous chondrites (Ichimura et al., 2017). Experimental studies (Nomura and Miyamoto, 1998; Ichimura et al., 2017) successfully produced nepheline via hydrothermal alteration of common silicate phases in CAIs and subsequent heating. Some hydrated transition phases, such as zeolite group minerals, hydroxysodalite and nepheline hydrate, are the products of hydrothermal alteration in these experiments. The temperature ranges (200-700°C) in these experiments are comparable to those estimated for the conditions of secondary alteration on the CV3 parent body (500-700°C) (e.g., Brearley, 1997; Bonal et al., 2006; Huss et al., 2006; Busemann et al., 2007; Krot et al., 2007b; Cody et al., 2008; Brearley and Krot, 2013). The thermal stabilities of nepheline, sodalite, and related hydrated phases in terrestrial environments have been investigated through both thermodynamic modeling and

experiments with and without an aqueous fluid (e.g., Wellman, 1969, 1970; Schipper et al., 1973; Sharp et al., 1989). According to these studies, sodalite can transform to nepheline by heating. For example, Schipper et al. (1973) demonstrated experimentally that carnegieite, which is a high-temperature polymorph of nepheline and is a transitional phase in the Ichimura et al. (2017) experiments, can be produced by thermal decomposition of hydroxysodalite $[\text{Na}_{3+x}\text{Al}_3\text{Si}_3\text{O}_{12}(\text{OH})_x \cdot y\text{H}_2\text{O}]$. Ichimura et al. (2017) also produced nepheline by heating hydroxysodalite above 749 °C. Therefore, it is possible that nepheline in ALNH-04 was also produced by heating of sodalite or hydroxysodalite. However, such a mechanism cannot explain the zoning texture: thermal decomposition would be more consistent with a homogeneous distribution of nepheline and sodalite. Another problem with this mechanism is that the water/rock ratios used in hydrothermal experiments related to carbonaceous chondrites (Nomura and Miyamoto, 1998; Ichimura et al., 2017) are much higher than that estimated for CV chondrites (<0.2 mass ratio) (e.g., Zolensky et al., 1993; Zolotov et al., 2006).

The heterogeneous distribution of secondary phases in carbonaceous chondrites has been attributed to microchemical environments, i.e., variations in fluid chemistry on the millimeter scale (e.g., pH, redox potential, and cation activity), or variations in water/rock ratio (e.g., Chen and Brantley, 2000; Brearley and Chizmadia, 2005; Brearley, 2006b; Chizmadia and Brearley, 2008; Palmer and Lauretta, 2011). Therefore, we also consider the possible role of microchemical environments in producing the observed secondary zoning in ALNH-04. This is particularly important for compositionally heterogeneous systems characterized by water-limited conditions, porosity, and permeability (e.g., Kallemeyn and Wasson, 1981; Burger and

Breareley, 2005; Bland et al., 2006; Breareley, 2006a; Ford and Breareley, 2008; Breareley and Krot, 2013).

The reaction fronts that develop during fluid-induced alteration begin from the outer contact between the solid and fluids, and progress into the solid through pathways formed along grain boundaries, interconnected pores, and fractures (e.g., Putnis et al., 2005; Putnis and Putnis, 2007; Jamtveit et al., 2009; Raufaste et al., 2011; Jonas et al., 2013, 2014). This alteration mechanism, coupled with limited availability of water indicated, for example, by incomplete alteration of primary phases in many chondrites, could result in a progressive change in the fluid composition as alteration proceeded (e.g., Hanowski and Breareley, 2001). For example, as an altering phase is consumed, the concentration of soluble elements from the reactant in solution could increase locally in the rock and conversely soluble elements that form the alteration product will decrease. Whether this occurs or not depends on a number of factors, including, for example, the relative rates of alteration of different phases, the rates of diffusion of ions in solution to and from the fluid-solid reaction interface, and the local permeability and porosity. If this hypothesis is correct, the consequence of a changing fluid composition (i.e., concentration of ions in solution) for the zonal sequence in ALNH-04, as the fluid progressively migrated into the CAI interior, is that the earliest alteration of anorthite was nepheline, because it is concentrated in the outer part of the inclusion. The relative stability of nepheline and sodalite depends mainly on the activity of NaCl ($a_{NaCl(aq)}$) in the fluid. Thermodynamic calculations (Markl, 2001) on the reaction:



show that sodalite becomes more stable than nepheline at higher $a_{\text{NaCl}(\text{aq})}$, and the stability boundary moves to higher $a_{\text{NaCl}(\text{aq})}$ with increasing temperature. Experimental work by Drüppel and Wirth (2018) supports this conclusion, showing that sodalite is the stable product of albite replacement at high salinity (≥ 17 wt % NaCl), while nepheline occurs at lower salinity. In these experiments, nepheline is only stable at temperatures ≥ 700 °C. On the other hand, sodalite is stable over the whole temperature range (200-800 °C) in the experiments. A similar conclusion was reached by Schneider and Jenkins (2020), who showed experimentally that at 750 °C and 0.5-0.6 GPa, sodalite remains stable over a wide range of NaCl activity (> 0.2), while nepheline can also form at a brine activity below 0.02. Applying these results to the migrating reaction front hypothesis mentioned above implies that, in order to form nepheline prior to sodalite, the fluid must have been depleted in NaCl at the beginning, and then became enriched in NaCl to stabilize sodalite. This is difficult to realize for a single fluid alteration event, unless a significant amount of water in the fluid was consumed to reduce the activity of H₂O in the fluid phase and enhance the NaCl activity. Water can be consumed via the formation of hydrous phases or by oxidation reactions. The lack of hydrated phases in Allende and specifically in ALNH-04 clearly indicates that the former process was not important. On the other hand, oxidation of metal affected almost all metal in the matrix and chondrules in Allende (e.g., Brearley and Krot, 2013), which may have consumed some water. Based on Alexander et al. (2010) who studied the responses of hydrogen isotopes to secondary alteration of

chondrites, the fraction of water that was consumed by oxidation of metal prior to and during the thermal metamorphism of CV3 chondrites is much less than in ordinary chondrites. The following Rayleigh fractionation equation was used to estimate the water consumption:

$$\delta D \approx 1000 \left(\left(\frac{\delta D_0}{1000} + 1 \right) f^{\frac{1}{\alpha} - 1} - 1 \right)$$

where δD and δD_0 are H isotopic compositions of the residual and initial water in the leaching experiments, respectively, f is the fraction of water remaining, and α is the equilibrium fractionation factor. Using the measured δD compositions of insoluble organic matter (IOM) acid leaching residues of CV3 chondrites (Alexander et al., 2010), and the temperatures during the thermal metamorphism of CV3 chondrites (e.g., Brearley, 1997; Krot et al., 2007b; Cody et al., 2008), up to about 55% water may have been consumed for a water/rock ratio that is relevant to CV3 chondrites (0.8-1.1; Zolensky et al., 1993). Although this consumption of water is significant, it is insufficient to increase the NaCl activity by one order of magnitude, and therefore oxidation itself cannot consume enough water to stabilize sodalite. However, we cannot completely rule out the role of oxidation in contributing to increasing the salinity of the aqueous fluid to promote stabilization of sodalite. It may still have some contributions, at least locally. Shock metamorphism on the Allende parent body may also have contributed to the loss of water (e.g., MacPherson and Krot, 2014), which could have helped stabilize sodalite.

An alternative to the mechanism above is that, despite the low permeability of the original

CAI, some fluid could have penetrated into the interior of the inclusion, resulting in simultaneous alteration in both the outer and inner parts (though more limited in the interior). The consequence of this behavior is: (1) a fluid initially enriched in NaCl reacted with primary anorthite in both the inner and outer regions of the CAI, causing the anorthite to dissolve and precipitating sodalite; (2) the fluid became progressively depleted in NaCl due to precipitation of sodalite causing the NaCl activity to eventually reach the threshold below which nepheline is more stable than sodalite; (3) because the outer part of the CAI is where the alteration initiated, and was more connected to the fluid reservoir in the matrix, the outer part of the inclusion should have been more extensively altered. This mechanism requires a clear replacement relationship, i.e., nepheline replaces sodalite. Using molar volume data (data source: WWW-MINCRYST) for sodalite ($420.35 \text{ cm}^3/\text{mol}$) and nepheline ($192.81 \text{ cm}^3/\text{mol}$), the reaction of nepheline replacing sodalite would result in an increase in volume. The common presence of pores in nepheline is, however, inconsistent with such a reaction. One explanation is that much more sodalite was dissolved than the amount of nepheline that precipitated. A similar explanation can also account for the pores in sodalite that replaces anorthite (molar volume: $105.05 \text{ cm}^3/\text{mol}$). Three moles of anorthite are required to produce one mole of sodalite, based on the mass balance. Therefore, more anorthite should have been dissolved than the amount of sodalite that formed. One problem with such an alteration mechanism is that, in the FIB sections, we did not observe any unambiguous replacement relationship between nepheline and sodalite, though they show embayed interfaces.

A more likely mechanism involves two stages of fluid infiltration. In the first stage, a fluid

with $a_{NaCl(aq)}$ within the stability range of nepheline was introduced into the rock, replacing anorthite with nepheline. In this stage, the pathways of fluid infiltrations were limited, and the water-rock interactions started first at locations on the exterior of the CAI, which enhanced reaction rates as pores gradually developed and more surface area became available for reaction (and more pathways for fluid infiltration). The initial fluid may also have a high Na/Cl ratio, based on the bulk composition of the reduced CV chondrite Vigarano (Na/Cl weight ratio ~12.2-19.4; Wasson and Kallemeyn, 1988; Lodders and Fegley, 1998). A second fluid with an elevated NaCl activity later penetrated into the rock, producing sodalite in the inner region of the CAI. In this case, since the fine-grained anorthite in the outer mantle region had already been extensively replaced by nepheline, there was a very limited amount of anorthite left for sodalite to replace. This mechanism requires that nepheline produced in the earlier alteration stage was not extensively replaced by sodalite, preserving the nepheline-rich zone in the outer mantle region. Based on experimental data, nepheline and sodalite could coexist over a limited salinity and temperature range (Drüppel and Wirth, 2018). In addition, the preservation of nepheline also depends on the relative stability of nepheline and anorthite in the NaCl-rich fluid. It is likely that anorthite is more susceptible to alteration by the NaCl-rich fluid, and was thus preferentially altered, leaving nepheline unaffected. This is supported by albitization of anorthite in terrestrial metamorphic rocks (e.g., Morad et al., 1990; Ramseyer et al., 1992; Perez and Boles, 2005; Engvik et al., 2008), and experimental work (e.g., Moody et al., 1985; Hövelmann et al., 2010), in which sodic feldspar is more stable than anorthite during the secondary alteration, and the alteration rates increase with an increasing anorthite content in

plagioclase. Anorthite shows a replacement relationship with sodalite in many regions. On the other hand, the TEM observations from the FIB sections demonstrate that there is no clear evidence of a replacement relationship between the two feldspathoids, which supports our hypothesis that nepheline was not significantly affected by the sodalite formation process.

To summarize, a two-stage fluid-assisted metasomatic process is the most likely mechanism for producing the alkali-halogen zonal sequence in ALNH-04. We suggest that hydrolysis and oxidation reactions on the Allende parent body themselves are not capable of producing a significant increase in $a_{NaCl(aq)}$ that is required for stabilizing sodalite, though they may have contributed to the increase in $a_{NaCl(aq)}$ locally. This, combined with the observation that an unambiguous replacement relationship between nepheline and sodalite (or the reverse) is absent, argues against a single-stage fluid alteration process. The development of porosity in the sample requires that the volume of solid that was dissolved into the fluid is more than was precipitated.

4.2.3. Relationship of the Fe-rich secondary phases with the alkali-halogen zoning sequence

In addition to nepheline and sodalite, ALNH-04 also contains abundant Fe-rich secondary phases, e.g., Fe-bearing olivine, pentlandite, and pyrrhotite. They have two major occurrences: (1) those in the outer mantle region that show an intimate association with feldspathoids (Fig. 2b), and (2) those separating the sub-calcic augite rim from the CAI interior and are associated with relict diopside and some phosphate grains (Fig. 3f). The preferential distribution of these Fe-rich phases in the outer mantle and the rim region of the CAI indicates that they are

secondary phases. Some rare awaruite grains could be products of thermal metamorphism (McSween, 1977; Kallemeyn et al., 1991; Rubin, 1991; Krot et al., 1998). In some local regions, secondary sulfides are rimmed by Fe-bearing olivine (Fig. 2c), indicating that the latter are replacing the former.

As mentioned in the preceding section, microchemical environments can be an important factor in controlling the distribution of secondary phases (e.g., Chen and Brantley, 2000; Brearley and Chizmadia, 2005; Brearley, 2006b; Chizmadia and Brearley, 2008; Palmer and Lauretta, 2011). Microchemical environments can also be used to explain the preferential distribution of sulfides. Sulfides are concentrated in the outer part of the CAI where the alteration is the most extensive. Fluid-induced alteration can be interpreted as a coupled dissolution and precipitation process (e.g., Putnis, 2002, 2009; Putnis and Putnis, 2007; Putnis and Austrheim, 2010; Ruiz-Agudo et al., 2014), and for alteration of silicate minerals, the hydrolysis reactions during the dissolution stage produce alkaline fluids due to the interaction between protons and metal-oxygen bonds in silicates (Drever and Stillings, 1997; Reed, 1997; Brearley, 2006b). Reed and Palandri (2006) investigated the effect of pH on the solubility of sulfide minerals and demonstrated that for a simple sulfide-solution system, sulfide solubility decreases with increasing pH. This process can be illustrated by a simple dissolution-precipitation reaction involving galena: $\text{PbS}_{(\text{galena})} + \text{H}^+_{(\text{aq})} = \text{Pb}^{2+}_{(\text{aq})} + \text{HS}^-_{(\text{aq})}$; lower H^+ activity (higher pH condition) drives the reaction towards the left side, stabilizing the solid sulfide phase. Other studies on pentlandite and pyrrhotite dissolution in terrestrial settings obtain similar conclusions (e.g., Warner et al., 1996). Nickel solubility also tends to decrease with

increasing pH (Anderson and Christensen, 1988; Åström, 1998; Bullock et al., 2005). Therefore, the spatial distribution of sulfides in ALNH-04 can be attributed to different pH conditions in the outer and inner parts of the CAI, which could be caused by the differential alteration extents in these two regions. Sulfides precipitated preferentially in the outer part of the CAI where conditions were more alkaline due to more extensive hydrolysis reactions that consumed protons. The difference in pH between the two regions does not have to be large, because only a small increment in pH is capable of precipitating sulfides from an Fe-bearing solution (e.g., Singerling and Brearley, 2020). In summary, sulfide precipitation in ALNH-04 is induced by the replacement reactions of anorthite by feldspathoids, and thus is coupled to the development of alkali-halogen zoning. It should be noted that some sulfides could have formed by alteration of primary Fe,Ni metal that may have been added during the remelting event of this CAI.

A similar situation applies to ferroan olivine. An elevated $a_{SiO_2(aq)}$ in the fluid in the outer part of the CAI due to extensive alteration would increase the stability field of fayalitic olivine (Zolotov et al., 2006). An increase in $a_{Fe^{2+}(aq)}$ in the fluid, as evidenced by the presence of sulfides and Fe-rich spinel, would also promote the precipitation of ferroan olivine from the fluid.

Such an alteration hypothesis is supported by the TEM observations of FIB-06. The presence of nepheline grains free of Fe-rich phases, together with the observation that pentlandite contains abundant feldspathoid inclusions, demonstrates that formation of feldspathoids started prior to that of the Fe-rich phases. The sharp boundary between the

inclusion-free nepheline grains and the adjacent intergrowth of nepheline and Fe-rich phases suggests that rather than a replacement relationship between the two, the Fe-rich phases formed coevally with some feldspathoids, and represent a later stage of the more alkaline alteration event.

4.3. The role of fluid in altering ALNH-04

In this section, we discuss the evidence for the presence of fluid during the alteration of ALNH-04 and the role of fluid in producing the secondary features in ALNH-04. As argued in Section 4.3.1., there are several observations that are consistent with a coupled dissolution-precipitation alteration mechanism (e.g., Putnis, 2002, 2009, 2015; Putnis and Putnis, 2007; Putnis and Austrheim, 2010; Ruiz-Agudo et al., 2014). The sharp compositional boundaries, even at the TEM scale, between the host anorthite and the alteration products are strong evidence against a solid-state diffusion mechanism. In addition, fluids can move preferentially along grain boundaries, fractures, and defects that may form as the alteration interface develops. This is consistent with the reentrant features observed in FIB-03 (Fig. 9).

The presence of Na-rich and Ca-rich halos in the matrix surrounding ALNH-04 also attests to a fluid-assisted process. Similar halos around CAIs, chondrules, and dark inclusions have been described in several papers (e.g., Krot et al., 1998, 2000b; Ford and Brearley, 2008). The implication of these halos and other alteration features is that there was elemental exchange between the objects and the surrounding matrix. For ALNH-04, Fe, Na, Cl, and S were introduced into the CAI, and Ca and Si from anorthite and diopside were lost. All of these

elements are highly mobile in solution, which strongly supports the role of fluid in altering ALNH-04. The precipitation of hedenbergite-diopside assemblages was probably controlled by the local fluid chemistry and redox conditions, e.g., the local $\text{Fe}^{2+}/\text{Ca}^{2+}$ ratio was in the stability field of hedenbergite, and the conditions were not oxidized enough to stabilize andradite (Krot et al., 1998; Fig. 15 in their paper). Nepheline and sodalite in the Na-rich halo commonly contain elongated fayalitic olivine crystals from the matrix. While feldspathoids replacing anorthite in ALNH-04 do contain some ferroan olivine grains, these olivine crystals are not elongated and have much finer grain sizes. Therefore, physical fragmentation and redistribution of feldspathoids, as proposed for the matrix of the anomalous CV3 chondrite Ningqiang (Matsumoto et al., 2014, 2017) was not likely for Allende. Instead, we propose that the Na-rich halo was formed by direct precipitation of feldspathoids from the fluid that altered ALNH-04. The source of elements required for production of this halo may be the residual aqueous species in the fluid, which could either be the earlier NaCl-poor fluid, or the later one that had become depleted in NaCl due to production of sodalite, or both.

Aluminum was certainly mobilized during the alteration process, because there is only a very limited aluminum reservoir in the matrix, as evidenced by the matrix mineralogy of reduced CV3 chondrites (e.g., Krot et al., 2000a). The mobilization of aluminum is consistent with a coupled dissolution-precipitation mechanism and represents an unusual situation for the alteration of chondritic components. Aluminum usually shows minimum mobility compared with other elements during alteration of chondrites (e.g., Larimer and Wasson, 1988; Burger and Brearley, 2004; Hezel and Palme, 2008; Palme et al., 2015) and is thus commonly used as

a reference element for mass balance calculations; however, studies on white matrix in, for example, the ordinary chondrite, Tieschitz (e.g., Hutchison et al., 1998; Dobrică and Brearley, 2014; Martínez-Jiménez et al., 2016) and bleached chondrules in several ordinary chondrites (e.g., Grossman et al., 2000) show that mass transport of aluminum can occur during alteration by fluids. However, it is likely that the mobility of aluminum depends strongly on the local geochemical conditions and fluid chemistry. There is a positive correlation between Al solubility and temperature (Beitter et al., 2008), and the high metamorphic temperature for ALNH-04 (500-700 °C; e.g., Brearley, 1997; Krot et al., 2007b; Cody et al., 2008) can therefore enhance solubility of Al. The mobility of Al may also indicate acidic pH conditions of the initial solutions (e.g., Anderson, 1983; Azimov and Bushmin, 2007; Zolotov and Mironenko, 2007), which is consistent with previous models for aqueous alteration on carbonaceous chondrite parent bodies that argued for the presence of an early acidic fluid (Rosenberg et al., 2001; Zolotov and Mironenko, 2007; Zolotov, 2012). An initially acidic fluid is also consistent with the alteration veins in diopside in FIB-04 (Fig. 7c), since the solubility of Fe–Mg minerals and the mobility of base cations (Mg and Fe) are enhanced in acidic solutions (Dymkin et al., 1984; Azimov and Bushmin, 2007).

4.4. Implications on the alteration processes on the CV3 parent body

We found several other CAIs and chondrules from the same Allende thin section that display similar alteration zoning sequences. These objects can be classified into two categories, based on their zoning patterns: category I (such as ALNH-14, and -ch-04; Fig. 14a-d) show the

same distribution of feldspathoids as in ALNH-04, i.e., nepheline and sodalite are concentrated in the outer and inner parts, respectively; category II (such as ALNH-06 and -08; Fig. 14e-h) show an inverse pattern, with sodalite dominating the outer parts of the inclusions. One of the CAIs (ALNH-14) also contains ferroan olivine that is intergrown with nepheline on the

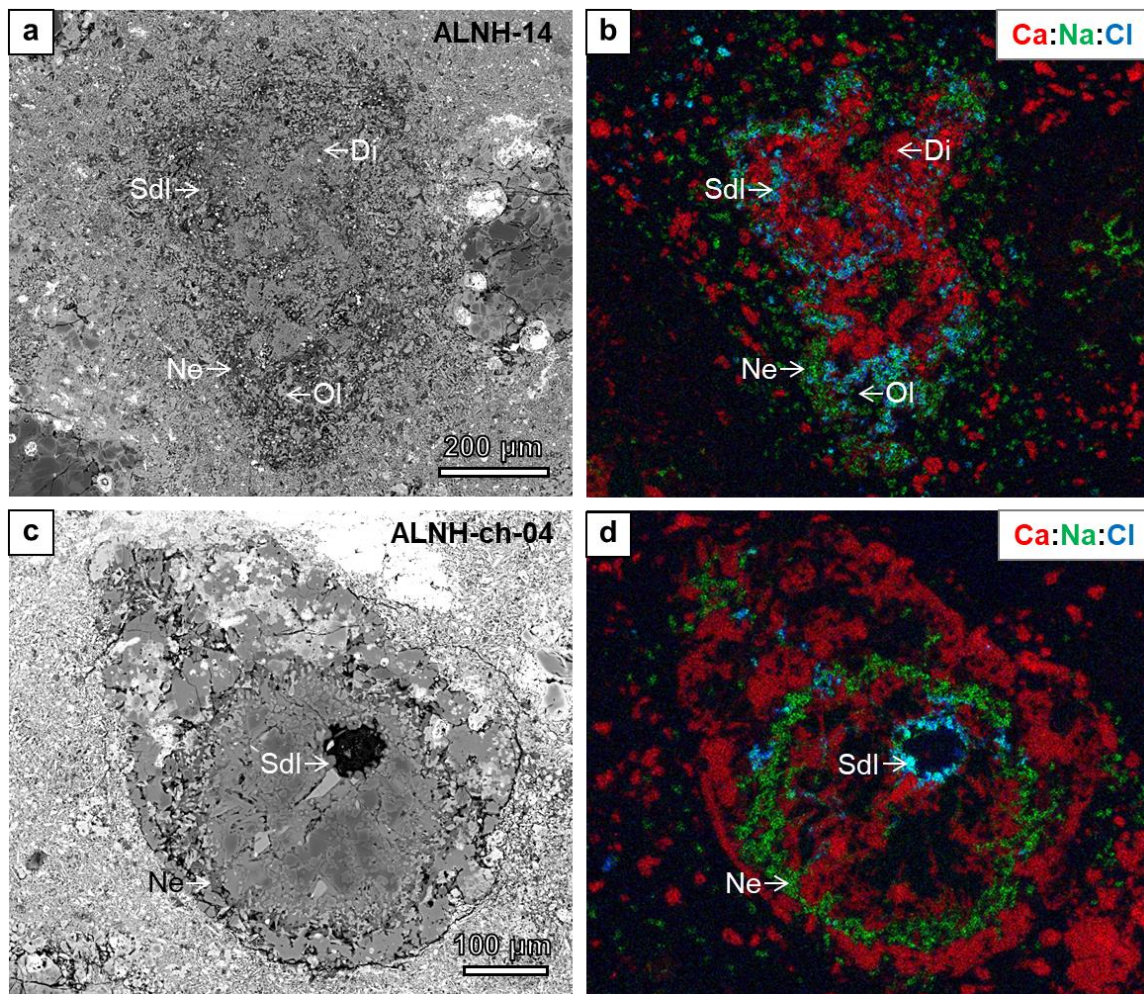


Fig. 14. BSE images (a, c, e, g) and combined elemental maps (Ca (red), Na (green), and Cl (blue)) (b, d, f, h) of CAIs and chondrules in the ALNH thin section from Allende, which also show iron-alkali-halogen zonal sequences. ALNH-14 is a fine-grained, spinel-rich inclusion, ALNH-ch-04 is a chondrule, and ALNH-06 and -08 are melilite-rich inclusions. ALNH-14 and ALNH-ch-04 have a zoning sequence, which is the same as that observed in ALNH-04.

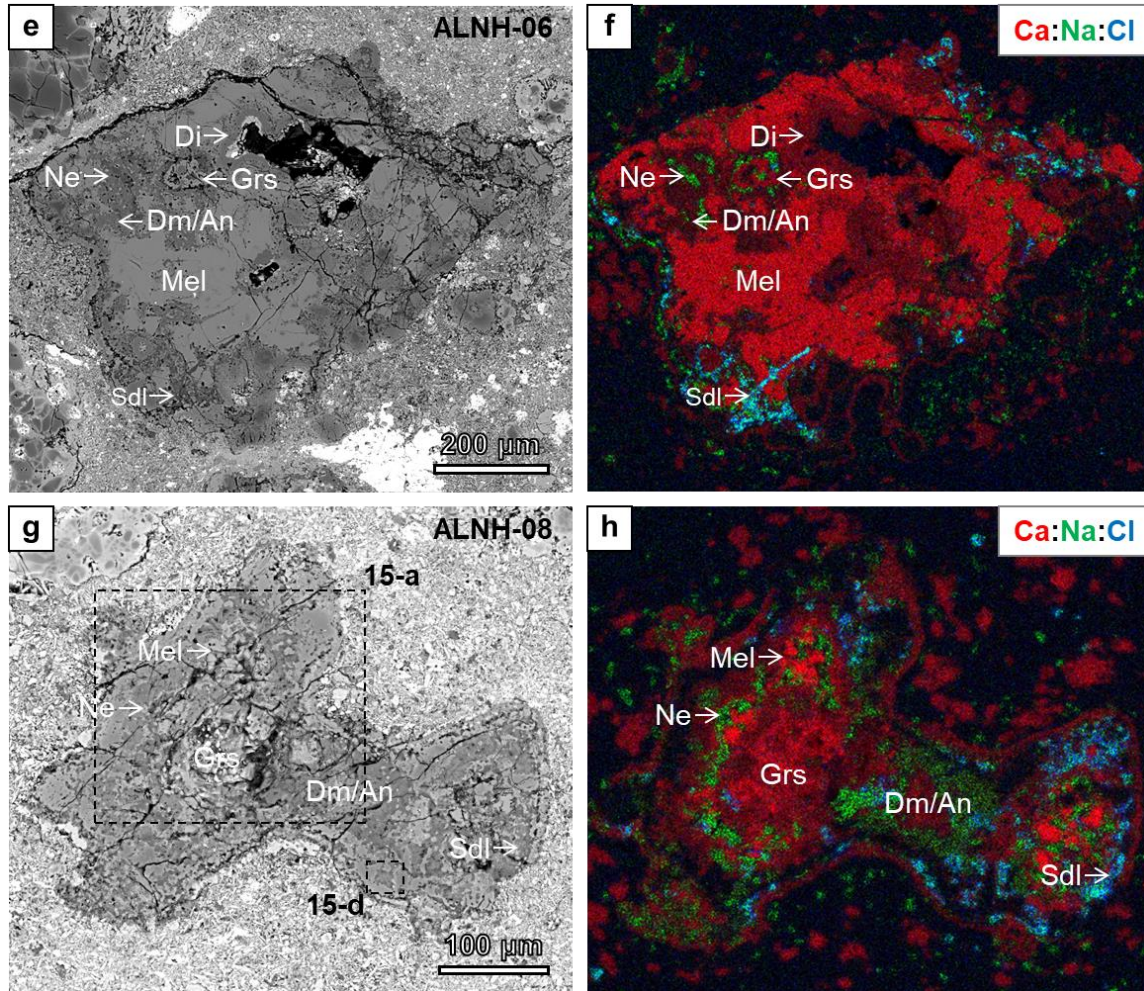


Fig. 14. (*continued*) On the other hand, ALNH-06 and -08 show a reversed alteration zoning, with nepheline and sodalite concentrated in the inner and outer regions of the CAIs, respectively. Melilite has been replaced extensively by grossular, dmisteinbergite and/or secondary anorthite, nepheline, and sodalite. Abbreviations: An = anorthite, Di = diopside, Dm = dmisteinbergite, Grs = grossular, Mel = melilite, Ne = nepheline, Ol = ferroan olivine, Sdl = sodalite.

periphery (Fig. 14a). The secondary zoning patterns in category I can be readily explained by the two-stage alteration model proposed in Section 4.3. In ALNH-ch-04, for example, nepheline was produced in the earlier fluid alteration event, replacing the partly recrystallized mesostasis, and a later NaCl-rich fluid penetrated into the deeper interior of the chondrule, replacing mesostasis by sodalite. The mesostasis in this chondrule has been partly leached away,

also testifying to the mobility of aluminum during alteration.

Category II objects, on the other hand, seem to conflict with the proposed model. However, a careful examination of the replacement textures of these objects reveals that the alteration style is the same, though the alteration process is more complex than that for category I objects. Inclusion ALNH-08 is a melilite-rich CAI that is enclosed by a Wark-Lovering (WL) rim (Fig. 14g-h). This inclusion shows a progressive alteration sequence from the inner to the exterior of grossular, dmisteinbergite and/or secondary anorthite, nepheline, and sodalite (Fig. 15a). The sequence of melilite being replaced by grossular, dmisteinbergite (\pm secondary anorthite), and feldspathoids (mainly nepheline) represents a gradual decrease in the chemical potential of CaO outward. Nepheline is in contact with dmisteinbergite (\pm secondary anorthite) in many regions (Fig. 15b), and also has a direct contact with melilite locally (Fig. 15c). Compared to nepheline, sodalite is concentrated in the outer region of the CAI, commonly displaying a replacement relationship with dmisteinbergite (\pm secondary anorthite) (Fig. 15d). Sodalite also shows an intergrowth relationship with nepheline on the peripheries of the CAIs, but no replacement relationship is observed between them. In addition to the two categories of CAIs and chondrules described above, there are some melilite-rich CAIs in which melilite has been replaced by a grossular-dmisteinbergite (\pm secondary anorthite)-nepheline alteration sequence, and almost no sodalite is present. These CAIs are mineralogically similar to CAIs in category II, in that the dominant primary phase that has been affected by secondary alteration is melilite. It is therefore likely that these melilite-rich CAIs respond to the secondary alteration in a similar way.

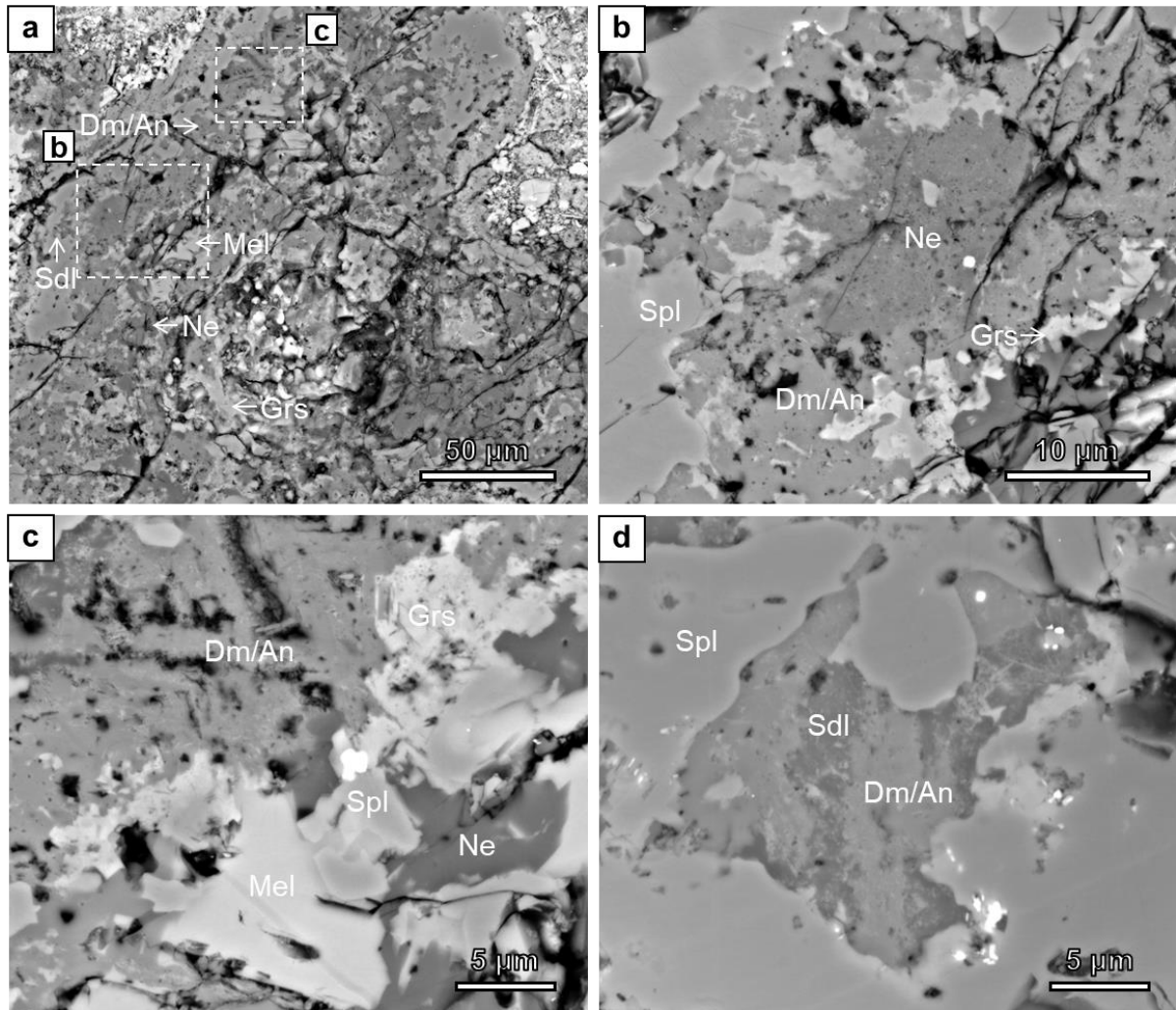
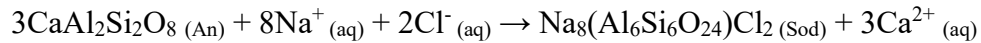
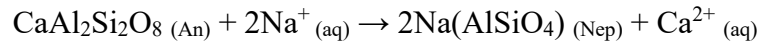
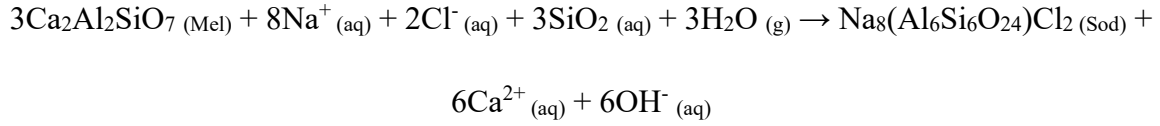
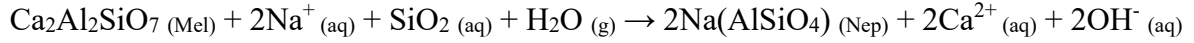
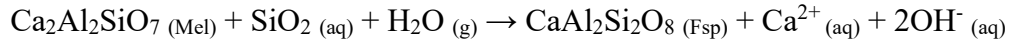
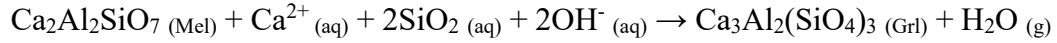


Fig. 15. BSE images of the alteration features in ALNH-08. (a) Melilite has been extensively replaced by a zonal alteration sequence progressing outwards: grossular, dmisteinbergite and/or secondary anorthite, nepheline, and sodalite. (b) Nepheline shows a clear replacement relationship with dmisteinbergite. (c) Nepheline also appears to have replaced melilite locally. (d) Sodalite has replaced dmisteinbergite and/or secondary anorthite in the outer part of the CAI. Abbreviations: An = anorthite, Di = diopside, Dm = dmisteinbergite, Grs = grossular, Mel = melilite, Ne = nepheline, Sdl = sodalite, Spl = spinel.

Empirical reactions for melilite and anorthite replacement reactions based on the textural observations can be written as the following:



It should be noted that, the use of OH⁻ in the reactions does not necessarily imply an alkaline condition. It was just used to balance the charge. In the real alteration system, the reactions should have involved more phases, such Fe²⁺, hercynite, aqueous Al species, etc. The reactions suggest that alteration of melilite requires a net influx of SiO₂, which is different from the anorthite alteration that results in loss of SiO₂, as discussed previously. As a consequence, the alteration processes of melilite and anorthite should have produced opposite chemical potential gradients in SiO₂ (μSiO₂) in the fluid, i.e., μSiO₂ increases away from the melilite-fluid interface, while the opposite occurs for anorthite. The chemical potential gradient of SiO₂ may have a controlling effect on the formation locations of nepheline and sodalite relative to the alteration front. Precipitation of nepheline and sodalite during the alteration of melilite-rich CAIs should require a higher SiO₂ activity compared to grossular and dmisteinbergite (±secondary anorthite). A single fluid alteration event cannot account for the different zonal distribution patterns of nepheline and sodalite in categories I and II. This is because μSiO₂ does

not affect the relative locations of nepheline and sodalite on a μSiO_2 gradient, based on the fact that these two phases have the same $\text{SiO}_2/\text{Al}_2\text{O}_3$ ratio. The single fluid alteration mechanism is also inconsistent with the absence of sodalite in some of the melilite-rich CAIs. A two-stage fluid alteration event, on the other hand, is a more likely mechanism. The first fluid alteration event produced nepheline in CAIs and chondrules in both categories. In the second stage of alteration, a fluid with a higher $a_{\text{NaCl}(aq)}$ was introduced into the rock. In category I objects, sodalite tends to form close to the anorthite-fluid interface, where μSiO_2 is the highest. In contrast, sodalite formed preferentially on the exterior of the CAIs in category II, i.e., where μSiO_2 is higher. Some melilite-rich CAIs that do not contain sodalite may have escaped the second fluid alteration event, which may be caused by a heterogeneous distribution of the fluid in the rock.

Consequently, the two-stage fluid alteration mechanism that we propose to explain the iron-alkali-halogen zonal sequence in ALNH-04 can be applied to other CAIs and chondrules showing secondary zoning sequences. It should be noted that such a two-stage alteration mechanism only represents a part of the complex alteration histories of Allende CAIs, and other types of metasomatism clearly have occurred, producing various alteration features (e.g., Brearley and Krot, 2013). Fluids on carbonaceous chondrite parent bodies may be generated by melting of water ice particles that accreted with other solid phases (e.g., silicates and oxides) (e.g., Grimm and McSween, 1989; McSween et al., 2002; Zolotov and Mironenko, 2007). There are several ways to generate fluids with different compositions in an asteroid. Heterogeneities may be generated by percolation of fluids in different directions (Ganino and

Libourel, 2017), or by progressively more vigorous fluid convection in the asteroid (e.g., Grimm, 2007; Palguta et al., 2010). Chondrite parent asteroids could also have released fluids from the parent body interior, if internal differentiation occurred due to progressive radiogenic heating (e.g., Corporzen et al., 2011; Elkins-Tanton et al., 2011; Sahijpal et al., 2011; Cournede et al., 2015; Gattacceca et al., 2016; Aléon et al., 2020). Because of the distinct mineralogy and textures of different chondritic components in Allende, the responses of these components to secondary alteration should vary significantly. At a more local scale, components that are more susceptible to alteration must have played a more significant role in controlling the fluid chemistry. This is supported by studies of, for example, CM chondrites, in which chondrule mesostases are among the most easily altered components in chondrules. Their high Si contents result in a smaller increase in local pH in the chondrule interior than the exterior (Brearley, 2006b). In addition, a limited amount of fluid in Allende means that chemical potential gradients can be easily sustained during the alteration. This should have facilitated the formation of local heterogeneities in fluid chemistry. The implication is that when studying the fluid-assisted metasomatic process on the CV3 chondrite parent body, we should consider the microenvironment as an important factor in controlling the formation of secondary phases.

5. CONCLUSIONS

The forsterite-bearing Type C CAI ALNH-04 from Allende shows unique features, both primary and secondary, that offer an opportunity to better understand the formational and evolutionary histories of CAIs from CV3 chondrites in the solar nebula and on the parent body.

Our textural observations of the primary phases in ALNH-04, together with compositional analyses, suggest that this CAI is different from other Type C CAIs reported in CV3 chondrites, and may have originated from a FoB precursor. The outer part of ALNH-04 contains augite, and shows a radiating texture, which implies a later re-melting event that possibly occurred in a chondrule-forming region.

The secondary alkali-halogen zoning sequence in ALNH-04, as manifested by different proportions of nepheline and sodalite in inner and outer regions of the CAI, can be best explained by a two-stage fluid alteration process: (1) nepheline replaced anorthite in the outer part of the CAI via a fluid with $a_{NaCl(aq)}$ within the stability range of nepheline; (2) a later-stage fluid, with elevated $a_{NaCl(aq)}$ that could preferentially stabilize sodalite, which penetrated further into the CAI interior, replacing anorthite with sodalite. The precipitation of secondary Fe-rich phases may have recorded an increase in pH and $a_{SiO_2(aq)}$ of the fluid, which was caused by the extensive alteration of the outer part of the CAI by feldspathoids.

A comparison with other CAIs and chondrules from Allende shows that similar alkali-halogen-(iron) zoning sequences are commonly observed, and the proposed two-stage alteration mechanism can be applied to all these objects. The SiO_2 chemical potential gradient in the fluid, which was generated by alteration of anorthite, mesostasis, and melilite, played an important role in producing different distribution patterns of nepheline and sodalite in CAIs and chondrules. Several mechanisms can produce compositionally different fluids that are responsible for the two-stage alteration process, such as fluid percolation along different directions, changing convection patterns, or release of water from a differentiated interior.

ACKNOWLEDGEMENTS

We thank Dr. Noriyuki Kawasaki, two anonymous reviewers, and Associate Editor Dr. Alexander Krot for their thoughtful and constructive comments that helped improve the manuscript significantly. The editorial handling by Dr. Alexander Krot is gratefully acknowledged. This work was funded by NASA Cosmochemistry grants NNX15AD28G to A. J. Brearley (PI). We thank Dr. Elena Dobrică and Dr. Ying-Bing Jiang for their help with the TEM operations, and Mike Spilde for his assistance with the electron microprobe analysis. Electron microbeam analysis and FIB section preparation were carried out in the Electron Microbeam Analysis Facility, Department of Earth and Planetary Sciences and Institute of Meteoritics, University of New Mexico. The facility is supported by funds from the State of New Mexico, NSF, and NASA.

REFERENCES

- Abreu N. M. and Brearley A. J. (2005) Carbonates in Vigarano: Terrestrial, preterrestrial, or both? *Meteorit. Planet. Sci.* **40**, 609–625.
- Abreu N. M. and Brearley A. J. (2011) Deciphering the nebular and asteroidal record of silicates and organic material in the matrix of the reduced CV3 chondrite Vigarano. *Meteorit. Planet. Sci.* **46**, 252–274.
- Aléon J. (2018) Closed system oxygen isotope redistribution in igneous CAIs upon spinel dissolution. *Earth Planet. Sci. Lett.* **482**, 324–333.
- Aléon J., Aléon-Toppani A., Platevoet B., Bardintzeff J.-M., McKeegan K. D. and Brisset F. (2020) Alkali magmatism on a carbonaceous chondrite planetesimal. *Proc. Natl. Acad. Sci.* **117**, 8353–8359.

- Aléon J., Krot A. N. and McKeegan K. D. (2002) Calcium-aluminum-rich inclusions and amoeboid olivine aggregates from the CR carbonaceous chondrites. *Meteorit. Planet. Sci.* **37**, 1729–1755.
- Aléon J., Krot A. N., McKeegan K. D., MacPherson G. J. and Ulyanov A. A. (2005) Fine-grained, spinel-rich inclusions from the reduced CV chondrite Efremovka: II. Oxygen isotopic compositions. *Meteorit. Planet. Sci.* **40**, 1043–1058.
- Alexander C. M. O. D., Newsome S. D., Fogel M. L., Nittler L. R., Busemann H. and Cody G. D. (2010) Deuterium enrichments in chondritic macromolecular material—Implications for the origin and evolution of organics, water and asteroids. *Geochim. Cosmochim. Acta* **74**, 4417–4437.
- Amelin Y., Krot A. N., Hutcheon I. D. and Ulyanov A. A. (2002) Lead isotopic ages of chondrules and Calcium-aluminum-rich inclusions. *Science* **297**, 1678–1683.
- Anderson M. G. (1983) Feldspar solubility and the transport of aluminum under metamorphic conditions. *Am. J. Sci.* **283**, 283–297.
- Anderson P. R. and Christensen T. H. (1988) Distribution coefficients of Cd, Co, Ni, and Zn in soils. *J. Soil Sci.* **39**, 15–22.
- Ando K. and Oishi Y. (1974) Self-diffusion coefficients of oxygen ion in single crystals of MgO·n Al₂O₃ spinels. *J. Chem. Phys.* **61**, 625–629.
- Åström M. (1998) Mobility of Al, Co, Cr, Cu, Fe, Mn, Ni and V in sulphide-bearing fine-grained sediments exposed to atmospheric O₂: An experimental study. *Environ. Geol.* **36**, 219–226.
- Azimov P. Y. and Bushmin S. A. (2007) Solubility of minerals of metamorphic and metasomatic rocks in hydrothermal solutions of varying acidity: Thermodynamic modeling at 400–800°C and 1–5 kbar. *Geochemistry Int.* **45**, 1210–1234.
- Beckett J. R. (1986) The origin of calcium-aluminum-rich inclusions from carbonaceous chondrites: An experimental study. Ph.D. Thesis. University of Chicago. 373 pp.
- Beckett J. R. and Grossman L. (1988) The origin of Type C inclusions from carbonaceous chondrites. *Earth Planet. Sci. Lett.* **89**, 1–14.
- Beitter T., Wagner T. and Markl G. (2008) Formation of kyanite–quartz veins of the Alpe Sponda, Central Alps, Switzerland: Implications for Al transport during regional

metamorphism. *Contrib. to Mineral. Petrol.* **156**, 689–707.

Berlin J. (2010) *Mineralogy and bulk chemistry of chondrules and matrix in petrologic type 3 chondrites: Implications for early solar system processes* (Ph.D. thesis). University of New Mexico, Albuquerque, NM, USA.

Bischoff A. and Keil K. (1984) Al-rich objects in ordinary chondrites: Related origin of carbonaceous and ordinary chondrites and their constituents. *Geochim. Cosmochim. Acta* **48**, 693–709.

Bland P. A., Zolensky M. E., Benedix G. K. and Sephton M. A. (2006) Weathering of chondritic meteorites. *Meteorites Early Sol. Syst. II*, 853–867.

Blum J. D., Wasserburg G. J., Hutcheon I. D., Beckett J. R. and Stolper E. M. (1989) Origin of opaque assemblages in C3V meteorites: Implications for nebular and planetary processes. *Geochim. Cosmochim. Acta* **53**, 543–556.

Bonal L., Quirico E., Bourot-Denise M. and Montagnac G. (2006) Determination of the petrologic type of CV3 chondrites by Raman spectroscopy of included organic matter. *Geochim. Cosmochim. Acta* **70**, 1849–1863.

Brearley A. J. (1997) Disordered biopyriboles, amphibole, and talc in the Allende meteorite: Products of nebular or parent body aqueous alteration? *Science* **276**, 1103–1105.

Brearley A. J. (2014) Nebular versus parent body processing. In *Meteorites and Cosmochemical Processes, Treatise on Geochemistry* (ed. A. M. Davis), second ed. Elsevier-Pergamon, Oxford, pp. 309–334.

Brearley A. J. (1999) Origin of graphitic carbon and pentlandite in matrix olivines in the allende meteorite. *Science* **285**, 1380–1382.

Brearley A. J. (2006a) The action of water. In *Meteorites and the Early Solar System II* (eds. D. S. Lauretta and H. Y. McSween). University of Arizona Press, Tucson, pp. 584–624.

Brearley A. J. (2006b) The role of microchemical environments in the alteration of CM carbonaceous chondrites. *Lunar Planet. Sci.* **27**, 2074 (abstract).

Brearley A. J. and Chizmadia L. J. (2005) On the behavior of phosphorus during the aqueous alteration of CM2 carbonaceous chondrites. *Lunar Planet. Sci.* **36**, 2176 (abstract).

Brearley A. J., Fagan T. J., Washio M. and MacPherson G. J. (2014) FIB-TEM characterization

of dmisteinbergite with intergrown biopyriboles in Allende Ca-Al-Rich inclusions: Evidence for alteration in the presence of aqueous fluid. *Lunar Planet. Sci.* **45**, 2287 (abstract).

Brearley A. J. and Jones R. H. (1998) Chondritic meteorites. In *Planetary Materials, Reviews in Mineralogy*, vol. 36 (ed. J. J. Papike). Mineralogical Society of America, p. 398.

Brearley A. J. and Krot A. N. (2012) Metasomatism in the early solar system: the record from chondritic meteorites. In *Metasomatism and the Chemical Transformation of Rock – Lecture Notes in Earth System Sciences*, pp. 659–789.

Brenker F. E. and Krot A. N. (2004) Late-stage, high-temperature processing in the Allende meteorite: Record from Ca,Fe-rich silicate rims around dark inclusions. *Am. Mineral.* **89**, 1280–1289.

Bullock E. S., Gounelle M., Lauretta D. S., Grady M. M. and Russell S. S. (2005) Mineralogy and texture of Fe-Ni sulfides in CI1 chondrites: Clues to the extent of aqueous alteration on the CI1 parent body. *Geochim. Cosmochim. Acta* **69**, 2687–2700.

Bullock E. S., Macpherson G. J., Nagashima K., Krot A. N., Petaev M. I., Jacobsen S. B. and Ulyanov A. A. (2012) Forsterite-bearing Type B refractory inclusions from CV3 chondrites: From aggregates to volatilized melt droplets. *Meteorit. Planet. Sci.* **47**, 2128–2147.

Burger P. V. and Brearley A. J. (2004) Chondrule glass alteration in type IIA chondrules in the CR2 chondrites EET 87770 and EET 92105: Insights into elemental exchange between chondrules and matrices. *Lunar Planet. Sci.* **35**, 1966 (abstract).

Burger P. V. and Brearley A. J. (2005) Localized chemical redistribution during aqueous alteration in CR2 carbonaceous chondrites EET 87770 and EET 92105. *Lunar Planet. Sci.* **36**, 2288 (abstract).

Busemann H., Alexander C. M. O. D. and Nittler L. R. (2007) Characterization of insoluble organic matter in primitive meteorites by microRaman spectroscopy. *Meteorit. Planet. Sci.* **42**, 1387–1416.

Carporzen L., Weiss B. P., Elkins-Tanton L. T., Shuster D. L., Ebel D. and Gattacceca J. (2011) Magnetic evidence for a partially differentiated carbonaceous chondrite parent body. *Proc. Natl. Acad. Sci.* **108**, 6386–6389.

Che S. and Brearley A. J. (2017) Textural evidence for a FoB-like precursor and a multiple

evolution history of an Allende forsterite-bearing Type C CAI. *Lunar Planet. Sci.* **48**, 2414 (abstract).

Chen Y. and Brantley S. L. (2000) Dissolution of forsteritic olivine at 65°C and 2 < pH < 5. *Chem. Geol.* **165**, 267–281.

Chizmadia L. J. and Brearley A. J. (2008) Mineralogy, aqueous alteration, and primitive textural characteristics of fine-grained rims in the Y-791198 CM2 carbonaceous chondrite: TEM observations and comparison to ALHA81002. *Geochim. Cosmochim. Acta* **72**, 602–625.

Chizmadia L. J., Rubin A. E. and Wasson J. T. (2002) Mineralogy and petrology of amoeboid olivine inclusions in CO3 chondrites: Relationship to parent-body aqueous alteration. *Meteorit. Planet. Sci.* **37**, 1781–1796.

Cody G. D., Alexander C. M. O. D., Yabuta H., Kilcoyne A. L. D., Araki T., Ade H., Dera P., Fogel M., Militzer B. and Mysen B. O. (2008) Organic thermometry for chondritic parent bodies. *Earth Planet. Sci. Lett.* **272**, 446–455.

Cohen R. E., Kornacki A. S. and Wood J. A. (1983) Mineralogy and petrology of chondrules and inclusions in the Mokoia CV3 chondrite. *Geochim. Cosmochim. Acta* **47**, 1739–1757.

Connelly J. N., Bizzarro M., Krot A. N., Nordlund Å., Wielandt D. and Ivanova M. A. (2012) The absolute chronology and thermal processing of solids in the solar protoplanetary disk. *Science* **338**, 651–655.

Cournede C., Gattacceca J., Gounelle M., Rochette P., Weiss B. P. and Zanda B. (2015) An early solar system magnetic field recorded in CM chondrites. *Earth Planet. Sci. Lett.* **410**, 62–74.

Dauphas N. and Schauble E. A. (2016) Mass fractionation laws, mass-independent effects, and isotopic anomalies. *Annu. Rev. Earth Planet. Sci.* **44**, 709–783.

Davis A. M., Zhang J., Greber N. D., Hu J., Tissot F. L. H. and Dauphas N. (2018) Titanium isotopes and rare earth patterns in CAIs: Evidence for thermal processing and gas-dust decoupling in the protoplanetary disk. *Geochim. Cosmochim. Acta* **221**, 275–295.

Dobrică E. and Brearley A. J. (2014) Widespread hydrothermal alteration minerals in the fine-grained matrices of the Tieschitz unequilibrated ordinary chondrite. *Meteorit. Planet. Sci.* **49**, 1323–1349.

- Drever J. I. and Stillings L. L. (1997) The role of organic acids in mineral weathering. *Colloids Surfaces A Physicochem. Eng. Asp.* **120**, 167–181.
- Drüppel K. and Wirth R. (2018) Metasomatic replacement of albite in nature and experiments. *Minerals*. **8**, 214.
- Dymkin A. M., Purtov V. K. and Yatluk G. M. (1984) Transport of iron in high-temperature hydrothermal solutions. *Int. Geol. Rev.* **26**, 1180–1184.
- Ebel D. S. (2006) Condensation of rocky material in astrophysical environments. In *Meteorites and the Early Solar System II* (eds. D. S. Lauretta and H. McSween). University of Arizona, Tucson, pp. 253–277.
- Ebel D. S. and Grossman L. (2000) Condensation in dust-enriched systems. *Geochim. Cosmochim. Acta* **64**, 339–366.
- El Goresy A., Nagel K. and Ramdohr P. (1978) Fremdlinge and their noble relatives. *Lunar Planet. Sci. Conf. Proc.* **9**, 1279–1303.
- Elkins-Tanton L. T., Weiss B. P. and Zuber M. T. (2011) Chondrites as samples of differentiated planetesimals. *Earth Planet. Sci. Lett.* **305**, 1–10.
- Engvik A. K., Putnis A., Fitz Gerald J. D. and Austrheim H. (2008) Albitization of granitic rocks: The mechanism of replacement of oligoclase by albite. *Can. Mineral.* **46**, 1401–1415.
- Fagan T. J., Krot A. N., Keil K. and Yurimoto H. (2004) Oxygen isotopic evolution of amoeboid olivine aggregates in the reduced CV3 chondrites Efremovka, Vigarano, and Leoville. *Geochim. Cosmochim. Acta* **68**, 2591–2611.
- Fedkin A. V. and Grossman L. (2006) The fayalite content of chondritic olivine: obstacle to understanding the condensation of rocky material. In *Meteorites and the Early Solar System II* (eds. D. S. Lauretta and H. Y. McSween Jr.). University of Arizona Press, Tucson, pp. 279–294.
- Fintor K., Park C., Nagy S., Pál-Molnár E. and Krot A. N. (2014) Hydrothermal origin of hexagonal $\text{CaAl}_2\text{Si}_2\text{O}_8$ (dmisteinbergite) in a compact Type A CAI from the Northwest Africa 2086 CV3 chondrite. *Meteorit. Planet. Sci.* **49**, 812–823.
- Fintor, Walter and Nagy (2013) Petrographic and micro-Raman analysis of chondrules and Ca, Al-rich inclusions of NWA 2086 CV3 type carbonaceous chondrite. *Lunar Planet. Sci.*

48, 1719 (abstract).

Ford and Brearley (2007) Phyllosilicates in two coarse-grained Allende CAIs: Evidence for advanced hydration. *Lunar Planet. Sci.* **38**, 2411 (abstract).

Ford R. L. and Brearley A. J. (2008) Element exchange between matrix and CAIs in the Allende meteorite. *Lunar Planet. Sci.* **39**, #2399 (abstract).

Ford R. L. and Brearley A. J. (2010) Discovery of vesuvianite and kaolinite formed during the alteration of melilite in an Allende Type A CAI: Characterization by FIB/TEM. *Lunar Planet. Sci.* **41**, 1533 (abstract).

Freer W. and O'Reilly R. (1980) The diffusion of Fe²⁺ ions in spinels with relevance to the process of maghemitization. *Mineral. Mag.* **43**, 889–899.

Ganino C. and Libourel G. (2017) Reduced and unstratified crust in CV chondrite parent body. *Nat. Commun.* **8**, 261.

Gattacceca J., Weiss B. P. and Gounelle M. (2016) New constraints on the magnetic history of the CV parent body and the solar nebula from the Kaba meteorite. *Earth Planet. Sci. Lett.* **455**, 166–175.

Grimm R. (2007) Fluid flow on carbonaceous chondrite parent bodies. *Lunar Planet. Sci.* **38**, 1327 (abstract).

Grimm R. E. and Mccsween H. Y. (1989) Water and the thermal evolution of carbonaceous chondrite parent bodies. *Icarus* **82**, 244–280.

Grossman J. N., Alexander C. M. O. D., Wang J. and Brearley A. J. (2000) Bleached chondrules: Evidence for widespread aqueous processes on the parent asteroids of ordinary chondrites. *Meteorit. Planet. Sci.* **35**, 467–486.

Grossman L. (1972) Condensation in the primitive solar nebula. *Geochim. Cosmochim. Acta* **36**, 597–619.

Grossman L. and Larimer J. W. (1974) Early chemical history of the solar system. *Rev. Geophys.* **12**, 71–101.

Grossman L. and Steele I. M. (1976) Amoeboid olivine aggregates in the Allende meteorite. *Geochim. Cosmochim. Acta* **40**, 149–155.

- Guan Y., Huss G. R., MacPherson G. J. and Wasserburg G. J. (2000) Calcium-aluminum-rich inclusions from enstatite chondrites: Indigenous or foreign? *Science* **289**, 1330–1333.
- Han J. and Brearley A. J. (2015) Microstructural evidence for complex formation histories of amoeboid olivine aggregates from the ALHA77307 CO3.0 chondrite. *Meteorit. Planet. Sci.* **50**, 904–925.
- Hanowski N. P. and Brearley A. J. (2001) Aqueous alteration of the chondrules in the CM carbonaceous chondrite, Alla Hills 81002: Implications for parent body alteration. *Geochim. Cosmochim. Acta* **65**, 495–518.
- Hashimoto A. and Grossman L. (1987) Alteration of Al-rich inclusions inside amoeboid olivine aggregates in the Allende meteorite. *Geochim. Cosmochim. Acta* **51**, 1685–1704.
- Hezel D. C. and Palme H. (2008) Constraints for chondrule formation from Ca-Al distribution in carbonaceous chondrites. *Earth Planet. Sci. Lett.* **265**, 716–725.
- Hövelmann J., Putnis A., Geisler T., Schmidt B. C. and Golla-Schindler U. (2010) The replacement of plagioclase feldspars by albite: observations from hydrothermal experiments. *Contrib. to Mineral. Petrol.* **159**, 43–59.
- Huss G. R., Rubin A. E. and Grossman J. N. (2006) Thermal Metamorphism in Chondrites. In *Meteorites and the Early Solar System II* (eds. D. S. Lauretta and , Jr.H. Y. McSween). University of Arizona Press, Tucson, 943 pp., pp. 567–586.
- Hutchison R., Alexander C. M. O. and Bridges J. C. (1998) Elemental redistribution in Tieschitz and the origin of white matrix. *Meteorit. Planet. Sci.* **33**, 1169–1179.
- Ichimura S., Seto Y. and Tomeoka K. (2017) Nepheline formation in chondrite parent bodies: Verification through experiments. *Geochim. Cosmochim. Acta* **210**, 114–131.
- Imai H. and Yurimoto H. (2000) Oxygen and magnesium isotopic distributions in a Type C CAI from the Allende meteorite. *Lunar Planet. Sci.* 28, 1510 (abstract).
- Ishii H. A., Krot A. N., Bradley J. P., Keil K., Nagashima K., Teslich N., Jacobsen B. and Yin Q. Z. (2010) Discovery, mineral paragenesis, and origin of wadalite in a meteorite. *Am. Mineral.* **95**, 440–448.
- Itoh D. and Tomeoka K. (1998) Na-bearing Ca-Al-rich inclusions in four CO3 chondrites, Kainsaz, Ornans, Lance, and Warrenton. In *Antarctic Meteorites XXIII* pp. 42–44.

- Itoh S., Kojima H. and Yurimoto H. (2004) Petrography and oxygen isotopic compositions in refractory inclusions from CO chondrites. *Geochim. Cosmochim. Acta* **68**, 183–194.
- Jamtveit B., Putnis C. V and Malthe-Sørenssen A. (2009) Reaction induced fracturing during replacement processes. *Contrib. to Mineral. Petrol.* **157**, 127–133.
- Jonas L., John T., King H. E., Geisler T. and Putnis A. (2014) The role of grain boundaries and transient porosity in rocks as fluid pathways for reaction front propagation. *Earth Planet. Sci. Lett.* **386**, 64–74.
- Jonas L., John T. and Putnis A. (2013) Influence of temperature and Cl on the hydrothermal replacement of calcite by apatite and the development of porous microstructures. *Am. Mineral.* **98**, 1516–1525.
- Jones R. H. (1994) Petrology of FeO-poor, porphyritic pyroxene chondrules in the Semarkona chondrite. *Geochim. Cosmochim. Acta* **58**, 5325–5340.
- Jones R. H. and Scott E. R. D. (1989) Petrology and thermal history of type IA chondrules in the Semarkona (LL3.0) chondrite. *Lunar Planet. Sci.* **19**, 523–536 (abstract).
- Kallemeyn G. W., Rubin A. E. and Wasson J. T. (1991) The compositional classification of chondrites: V. The Karoonda (CK) group of carbonaceous chondrites. *Geochim. Cosmochim. Acta* **55**, 881–892.
- Kallemeyn G. W. and Wasson J. T. (1981) The compositional classification of chondrites-I. The carbonaceous chondrite groups. *Geochim. Cosmochim. Acta* **45**, 1217–1230.
- Kawasaki N., Kato C., Itoh S., Wakaki S., Ito M. and Yurimoto H. (2015) ^{26}Al - ^{26}Mg chronology and oxygen isotope distributions of multiple melting for a Type C CAI from Allende. *Geochim. Cosmochim. Acta* **169**, 99–114.
- Keller L. P. and Buseck P. R. (1990) Aqueous alteration in the Kaba CV3 carbonaceous chondrite. *Geochim. Cosmochim. Acta* **54**, 2113–2120.
- Keller L. P. and Buseck P. R. (1991) Calcic micas in the Allende meteorite: Evidence for hydration reactions in the early solar nebula. *Science* **252**, 946–949.
- Keller L. P., Thomas K. L., Clayton R. N., Mayeda T. K., DeHart J. M. and McKay D. S. (1994) Aqueous alteration of the Bali CV3 chondrite: Evidence from mineralogy, mineral chemistry, and oxygen isotopic compositions. *Geochim. Cosmochim. Acta* **58**, 5589–5598.

- Kimura M. and Ikeda Y. (1998) Hydrous and anhydrous alterations of chondrules in Kaba and Mokoia CV chondrites. *Meteorit. Planet. Sci.* **33**, 1139–1146.
- Kita N. T., Lin Y., Kimura M. and Morishita Y. (2004) The ^{26}Al - ^{26}Mg chronology of a Type C CAI and POIs in Ningqiang carbonaceous chondrite. *Lunar Planet. Sci.* **35**, 1471 (abstract).
- Kita N. T. and Ushikubo T. (2012) Evolution of protoplanetary disk inferred from ^{26}Al chronology of individual chondrules. *Meteorit. Planet. Sci.* **47**, 1108–1119.
- Kita N. T., Yin Q. Z., Macpherson G. J., Ushikubo T., Jacobsen B., Nagashima K., Kurahashi E., Krot A. N. and Jacobsen S. B. (2013) ^{26}Al - ^{26}Mg isotope systematics of the first solids in the early solar system. *Meteorit. Planet. Sci.* **48**, 1383–1400.
- Kojima T. and Tomeoka K. (1996) Indicators of aqueous alteration and thermal metamorphism on the CV parent body: Microtextures of a dark inclusion from Allende. *Geochim. Cosmochim. Acta* **60**, 2651–2666.
- Kojima T., Yada S. and Tomeoka K. (1995) Ca-Al-rich inclusions in three Antarctic CO3 chondrites, Yamato-81020, Yamato-82050 and Yamato-790992: Record of lowtemperature alteration. In *Proceedings of the NIPR Symposium on Antarctic Meteorites* pp. 79–96.
- Komatsu M., Krot A. N., Petaev M. I., Ulyanov A. A., Keil K. and Miyamoto M. (2001) Mineralogy and petrography of amoeboid olivine aggregates from the reduced CV3 chondrites Efremovka, Leoville and Vigarano: Products of nebular condensation, accretion and annealing. *Meteorit. Planet. Sci.* **36**, 629–641.
- Kööp L., Nakashima D., Heck P. R., Kita N. T., Tenner T. J., Krot A. N., Nagashima K., Park C. and Davis A. M. (2018) A multielement isotopic study of refractory FUN and F CAIs: Mass-dependent and mass-independent isotope effects. *Geochim. Cosmochim. Acta* **221**, 296–317.
- Krot A. N., Brearley A. J., Petaev M. I., Kallemeyn G. W., Sears D. W. G., Benoit P. H., Hutcheon I. D., Zolensky M. E. and Keil K. (2000) Evidence for low-temperature growth of fayalite and hedenbergite in MacAlpine Hills 88107, an ungrouped carbonaceous chondrite related to the CM-CO clan. *Meteorit. Planet. Sci.* **35**, 1365–1386.
- Krot A. N., Chaussidon M., Yurimoto H., Sakamoto N., Nagashima K., Hutcheon I. D. and MacPherson G. J. (2008) Oxygen isotopic compositions of Allende Type C CAIs: Evidence for isotopic exchange during nebular melting and asteroidal metamorphism.

Geochim. Cosmochim. Acta **72**, 2534–2555.

Krot A.N., MacPherson G. J., Ulyanov A. A. and Petaev M. I. (2004b) Fine-grained, spinel-rich inclusions from the reduced CV chondrites Efremovka and Leoville: I. Mineralogy, petrology, and bulk chemistry. *Meteorit. Planet. Sci.* **39**, 1517–1553.

Krot A. N., Makide K., Nagashima K., Huss G. R., Ogliore R. C., Ciesla F. J., Yang L., Hellebrand E. and Gaidos E. (2012) Heterogeneous distribution of ^{26}Al at the birth of the solar system: Evidence from refractory grains and inclusions. *Meteorit. Planet. Sci.* **47**, 1948–1979.

Krot A. N., Meibom A. and Keil K. (2000a) A clast of Bali-like oxidized CV material in the reduced CV chondrite breccia Vigarano. *Meteorit. Planet. Sci.* **35**, 817–825.

Krot A. N., Nagashima K., Alexander C. M. O. D., Ciesla F. J., Fujiya W. and Bonal L. (2015) Sources of water and aqueous activity on the chondrite parent asteroids. In *Asteroids IV* University of Arizona Press. pp. 635–660.

Krot A. N., Nagashima K., Ciesla F. J., Meyer B. S., Hutcheon I. D., Davis A. M., Huss G. R. and Scott E. R. D. (2010) Oxygen isotopic composition of the sun and mean oxygen isotopic composition of the protosolar silicate dust: Evidence from refractory inclusions. *Astrophys. J.* **713**, 1159–1166.

Krot A. N., Petaev M. I. and Bland P. A. (2004) Multiple formation mechanisms of ferrous olivine in CV carbonaceous chondrites during fluid-assisted metamorphism. *Antarct. Meteor. Res.* **17**, 153.

Krot A. N., Petaev M. I. and Keil K. (2006) Mineralogy and petrology of Al-rich objects and amoeboid olivine aggregates in the CH carbonaceous chondrite North West Africa 739. *Chemie der Erde* **66**, 57–76.

Krot A. N., Petaev M. I., Meibom A. and Keil K. (2000b) In situ growth of Ca-rich rims around Allende dark inclusions. *Geochemistry Int.* **38**, S351–S368.

Krot A. N., Petaev M. I., Russell S. S., Itoh S., Fagan T. J., Yurimoto H., Chizmadia L., Weisberg M. K., Komatsu M., Ulyanov A. A. and Keil K. (2004c) Amoeboid olivine aggregates and related objects in carbonaceous chondrites: Records of nebular and asteroid processes. *Chemie der Erde* **64**, 185–239.

Krot A. N., Petaev M. I., Scott E. R. D., Choi B. G., Zolensky M. E. and Keil K. (1998) Progressive alteration in CV3 chondrites: More evidence for asteroidal alteration.

Meteorit. Planet. Sci. **33**, 1065–1085.

Krot A. N., Petaev M. I., Zolensky M. E., Keil K., Scott E. R. D. and Nakamura K. (1998) Secondary calcium-iron-rich minerals in the Bali-like and Allende-like oxidized CV3 chondrites and Allende dark inclusions. *Meteorit. Planet. Sci.* **33**, 623–645.

Krot A. N., Scott E. R. D. and Zolensky M. E. (1995) Mineralogical and chemical modification of components in CV3 chondrites: nebular or asteroidal processing? *Meteoritics* **30**, 748–775.

Krot A. N., Scott E. R. D. and Zolensky M. E. (1997) Origin of fayalitic olivine rims and lath-shaped matrix olivine in the CV3 chondrite Allende and its dark inclusions. *Meteorit. Planet. Sci.* **32**, 31–49.

Krot A. N., Yurimoto H., Hutcheon I. D., Chaussidon M., MacPherson G. J. and Paque J. (2007a) Remelting of refractory inclusions in the chondrule-forming regions: Evidence from chondrule-bearing Type C calcium-aluminum-rich inclusions from Allende. *Meteorit. Planet. Sci.* **42**, 1197–1219.

Krot A. N., Yurimoto H., Hutcheon I. D., Libourel G., Chaussidon M., Tissandier L., Petaev M. I., MacPherson G. J., Paque-Heather J. and Wark D. (2007b) Type C Ca, Al-rich inclusions from Allende: Evidence for multistage formation. *Geochim. Cosmochim. Acta* **71**, 4342–4364.

Krot A. N., Yurimoto H., Hutcheon I. D. and Macpher-Son G. J. (2005) Relative chronology of CAI and chondrule formation: Evidence from chondrule-bearing igneous CAIs. *Lunar Planet. Sci.* **36**, 1482 (abstract).

Krot A. N., Yurimoto H., Petaev M. I., Hutcheon I. D. and Wark D. (2004a) Type C CAIs: New insights into early solar system processes. *Annu. Meet. Meteorit. Soc.* **67**, 5042.

Larimer J. W. and Wasson J. T. (1988) Refractory lithophile elements. In *Meteorites and the Early Solar System* (eds. J. F. Kerridge and M. S. Matthews). University of Arizona, Tucson, pp. 394–415.

Larsen K. K., Trinquier A., Paton C., Schiller M., Wielandt D., Ivanova M. A., Connelly J. N., Nordlund Å., Krot A. N. and Bizzarro M. (2011) Evidence for magnesium isotope heterogeneity in the solar protoplanetary disk. *Astrophys. J. Lett.* **735**.

Lee M. R., Hutchison R. and Graham A. L. (1996) Aqueous alteration in the matrix of the Vigarano (CV3) carbonaceous chondrite. *Meteorit. Planet. Sci.* **31**, 477–483.

- Lin Y. and Kimura M. (1998) Anorthite-spinel-rich inclusions in the Ningqiang carbonaceous chondrite: genetic links with Type A and C inclusions. *Meteorit. Planet. Sci.* **33**, 435–446.
- Liu M.-C., McKeegan K. D., Goswami J. N., Marhas K. K., Sahijpal S., Ireland T. R. and Davis A. M. (2009) Isotopic records in CM hibonites: Implications for timescales of mixing of isotope reservoirs in the solar nebula. *Geochim. Cosmochim. Acta* **73**, 5051–5079.
- Lodders K. (2003) Solar system abundances and condensation temperatures of the elements. *Astrophys. J.* **591**, 1220–1247.
- Lodders K. and Fegley B. J. (1998) *The planetary scientist's companion*. Oxford University Press, Oxford, UK.
- MacPherson G. J. (2014) Calcium-aluminum-rich inclusions in chondritic meteorites. In *Meteorites and Cosmochemical Processes, Treatise on Geochemistry* (ed. A. M. Davis), second ed. Elsevier-Pergamon, Oxford, pp. 309–334.
- MacPherson G. J., Bullock E. S., Janney P. E., Kita N. T., Ushikubo T., Davis A. M., Wadhwa M. and Krot A. N. (2010) Early solar nebula condensates with canonical, not supracanonical, initial $^{26}\text{Al}/^{27}\text{Al}$ ratios. *Astrophys. J. Lett.* **711**, 117–121.
- MacPherson G. J., Fahey A. J., Lundberg L. L. and Zinner E. (1988) Al-Mg isotopic systematics and metamorphism in five coarse-grained Allendale CAIs. *Meteoritics* **23**, 286.
- MacPherson G. J. and Huss G. R. (2005) Petrogenesis of Al-rich chondrules: Evidence from bulk compositions and phase equilibria. *Geochim. Cosmochim. Acta* **69**, 3099–3127.
- MacPherson G. J., Huss G. R. and Davis A. M. (2003) Extinct ^{10}Be in Type A calcium-aluminum-rich inclusions from CV chondrites. *Geochim. Cosmochim. Acta* **67**, 3165–3179.
- MacPherson G. J., Kita N. T., Ushikubo T., Bullock E. S. and Davis A. M. (2012) Well-resolved variations in the formation ages for Ca-Al-rich inclusions in the early Solar System. *Earth Planet. Sci. Lett.* **331–332**, 43–54.
- MacPherson G. J. and Krot A. N. (2014) The formation of Ca-, Fe-rich silicates in reduced and oxidized CV chondrites: The roles of impact-modified porosity and permeability, and heterogeneous distribution of water ices. *Meteorit. Planet. Sci.* **49**, 1250–1270.

- MacPherson G. J., Simon S. B., Davis A. M., Grossman L. and Krot A. N. (2005) Calcium-aluminum-rich inclusions: Major unanswered questions. *Chondrites Protoplanetary Disk. Vol. 341* **341**, 225–251.
- MacPherson G. J., Petaev M. and Krot A. N. (2004) Bulk compositions of CAIs and Al-rich chondrules: Implications of the reversal of the anorthite-forsterite condensation sequence at low nebular pressures. *Lunar Planet. Sci.* **35**, 1838 (abstract).
- Markl G. (2001) A new type of silicate liquid immiscibility in peralkaline nepheline syenites (lujavrites) of the Ilimaussaq complex, South Greenland. *Contrib. to Mineral. Petrol.* **141**, 458–472.
- Martínez-Jiménez M., Trigo-Rodríguez J. M., Brearley A. J., Llorca J. and Mestres N. (2016) Aqueous Alteration in the Unequilibrated H/L Ordinary Chondrite Tieschitz. *Lunar Planet. Sci.* **47**, 1903 (abstract).
- Matsumoto M., Tomeoka K. and Seto Y. (2017) Nepheline and sodalite in chondrules of the Ningqiang carbonaceous chondrite: Implications for a genetic relationship with those in the matrix. *Geochim. Cosmochim. Acta* **208**, 220–233.
- Matsumoto M., Tomeoka K., Seto Y., Miyake A. and Sugita M. (2014) Nepheline and sodalite in the matrix of the Ningqiang carbonaceous chondrite: Implications for formation through parent-body processes. *Geochim. Cosmochim. Acta* **126**, 441–454.
- McGuire A. V. and Hashimoto A. (1989) Origin of zoned fine-grained inclusions in the Allende meteorite. *Geochim. Cosmochim. Acta* **53**, 1123–1133.
- McKeegan K. D. (2000) Incorporation of short-lived ^{10}Be in a calcium-aluminum-rich inclusion from the Allende meteorite. *Science* **289**, 1334–1337.
- McSween H. Y., Ghosh A., Grimm R. E., Wilson L. and Young E. D. (2002) Thermal evolution models of asteroids. In *Asteroids III* pp. 559–571.
- McSween H. Y. (1977) Chemical and petrographic constraints on the origin of chondrules and inclusions in carbonaceous chondrites. *Geochim. Cosmochim. Acta* **41**.
- Moody J. B., Jenkins J. E. and Meyer D. (1985) An experimental investigation of the albitization of plagioclase. *Can. Mineral.* **23**, 583–596.
- Morad S., Bergan M., Knarud R. and Nystuen J. P. (1990) Albitization of detrital plagioclase in Triassic reservoir sandstones from the Snorre Field, Norwegian North Sea. *J. Sediment.*

Res. **60**, 411–425.

- Nomura K. and Miyamoto M. (1998) Hydrothermal experiments on alteration of Ca-Al-rich inclusions (CAIs) in carbonaceous chondrites: Implication for aqueous alteration in parent asteroids. *Geochim. Cosmochim. Acta* **62**, 3575–3588.
- Palguta J., Schubert G. and Travis B. J. (2010) Fluid flow and chemical alteration in carbonaceous chondrite parent bodies. *Earth Planet. Sci. Lett.* **296**, 235–243.
- Palme H. and Fegley B. (1990) High-temperature condensation of iron-rich olivine in the solar nebula. *Earth Planet. Sci. Lett.* **101**, 180–195.
- Palme H., Hezel D. C. and Ebel D. S. (2015) The origin of chondrules: Constraints from matrix composition and matrix-chondrule complementarity. *Earth Planet. Sci. Lett.* **411**, 11–19.
- Palmer E. E. and Lauretta D. S. (2011) Aqueous alteration of kamacite in CM chondrites. *Meteorit. Planet. Sci.* **46**, 1587–1607.
- Perez R. J. and Boles J. R. (2005) An empirically derived kinetic model for albitization of detrital plagioclase. *Am. J. Sci.* **305**, 312–343.
- Petaev, Krot and Wood (2005) Nebular condensation under incomplete equilibrium: Implications for the fine-grained spinel-rich CAIs. In *Lpsc*
- Petaev M. I. and Wood J. A. (2005) Meteoritic constraints on temperatures, pressures, cooling rates, chemical compositions and modes of condensation in the solar nebula. In *Chondrites and the Protoplanetary Disk* (eds. A. N. Krot, E. R. D. Scott and B. Reipurth). ASP Conference Series, pp. 373–406.
- Petaev M. I. and Wood J. A. (1998) The condensation with partial isolation (CWPI) model of condensation in the solar nebula. *Meteorit. Planet. Sci.* **33**, 1123–1137.
- Putnis A. (2002) Mineral replacement reactions: from macroscopic observations to microscopic mechanisms. *Mineral. Mag.* **66**, 689–708.
- Putnis A. (2009) Mineral replacement reactions. *Rev. Mineral. Geochemistry* **70**, 87–124.
- Putnis A. (2015) Transient porosity resulting from fluid-mineral interaction and its consequences. *Rev. Mineral. Geochemistry* **80**, 1–23.
- Putnis A. and Austrheim H. (2010) Fluid-induced processes: metasomatism and

metamorphism. *Geofluids* **10**, 254–269.

Putnis A. and Putnis C. V. (2007) The mechanism of reequilibration of solids in the presence of a fluid phase. *J. Solid State Chem.* **180**, 1783–1786.

Putnis C. V., Tsukamoto K. and Nishimura Y. (2005) Direct observations of pseudomorphism: Compositional and textural evolution at a fluid-solid interface. *Am. Mineral.* **90**, 1909–1912.

Ramseyer K., Boles J. R. and Lichtner P. C. (1992) Mechanism of plagioclase albitization. *J. Sediment. Res.* **62**, 349–356.

Raufaste C., Jamtveit B., John T., Meakin P. and Dysthe D. K. (2011) The mechanism of porosity formation during solvent-mediated phase transformations. *Proc. R. Soc. A Math. Phys. Eng. Sci.* **467**, 1408–1426.

Reed H. M. (1997) Hydrothermal alteration and its relationship to ore fluid composition. *Geochemistry hydrothermal ore Depos.*, 303–365.

Reed M. H. and Palandri J. (2006) Sulfide mineral precipitation from hydrothermal fluids. *Rev. Mineral. Geochemistry* **61**, 609–631.

Rosenberg N. D., Browning L. and Bourcier W. L. (2001) Modeling aqueous alteration of CM carbonaceous chondrites. *Meteorit. Planet. Sci.* **36**, 239–244.

Rubin A. E. (1991) Euhedral awaruite in the Allende Meteorite: Implications for the origin of awaruite- and magnetite-bearing nodules in CV3 chondrites. *Am. Mineral.* **76**, 1356–1362.

Ruiz-Agudo E., Putnis C. V. and Putnis A. (2014) Coupled dissolution and precipitation at mineral-fluid interfaces. *Chem. Geol.* **383**, 132–146.

Russell S. S., Huss G. R., Fahey A. J., Greenwood R. C., Hutchison R. and Wasserburg G. J. (1998) An isotopic and petrologic study of calcium-aluminum-rich inclusions from CO3 meteorites. *Geochim. Cosmochim. Acta* **62**, 689–714.

Sahijpal S. and Gupta G. (2011) Did the carbonaceous chondrites evolve in the crustal regions of partially differentiated asteroids? *J. Geophys. Res. Planets* **116**, 1–10.

Schipper D. J., Lathouwers T. W. and van Doorn C. Z. (1973) Thermal decomposition of sodalites. *J. Am. Ceram. Soc.* **56**, 523–525.

- Schneider J. B. and Jenkins D. M. (2020) Stability of sodalite relative to nepheline in NaCl–H₂O brines at 750 °C: Implications for hydrothermal formation of sodalite. *Can. Mineral.* **58**, 3–18.
- Sharp Z. D., Helffrich G. R., Bohlen S. R. and Essene E. J. (1989) The stability of sodalite in the system NaAlSiO₄-NaCl. *Geochim. Cosmochim. Acta* **53**, 1943–1954.
- Sheng Y. J., Hutcheon I. D. and Wasserburg G. J. (1991) Origin of plagioclase-olivine inclusions in carbonaceous chondrites. *Geochim. Cosmochim. Acta* **55**, 581–599.
- Simon J. I., Hutcheon I. D., Simon S. B., Matzel J. E. P., Ramon E. C., Weber P. K., Grossman L. and DePaolo D. J. (2011) Oxygen isotope variations at the margin of a CAI records circulation within the solar nebula. *Science* **331**, 1175–1178.
- Simon J. I. and Young E. D. (2011) Resetting, errorchrons and the meaning of canonical CAI initial ²⁶Al/²⁶Al values. *Earth Planet. Sci. Lett.* **304**, 468–482.
- Simon S. B., Davis A. M. and Grossman L. (1999) Origin of compact Type A refractory inclusions from CV3 carbonaceous chondrites. *Geochim. Cosmochim. Acta* **63**, 1233–1248.
- Simon S. B. and Grossman L. (1997) In situ formation of palisade bodies in calcium, aluminum-rich refractory inclusions. *Meteorit. Planet. Sci.* **32**, 61–70.
- Singerling S. A. and Brearley A. J. (2020) Altered primary iron sulfides in CM2 and CR2 carbonaceous chondrites: Insights into parent body processes. *Meteorit. Planet. Sci.* **28**, maps.13450.
- Tomeoka, K., Buseck, P.R., 1982. Intergrown mica and montmorillonite in the Allende carbonaceous chondrite. *Nature* **299**, 326–327.
- Tomeoka K. and Buseck P. R. (1990) Phyllosilicates in the Mokoia CV carbonaceous chondrite: Evidence for aqueous alteration in an oxidizing environment. *Geochim. Cosmochim. Acta* **54**, 1745–1754.
- Tomeoka K. and Itoh D. (2004) Sodium-metasomatism in chondrules in CO3 chondrites: Relationship to parent body thermal metamorphism. *Meteorit. Planet. Sci.* **39**, 1359–1373.
- Wark D. A. (1987) Plagioclase-rich inclusions in carbonaceous chondrite meteorites: Liquid condensates? *Geochim. Cosmochim. Acta* **51**, 221–242.

- Wark D. A. and Lovering J. F. (1977) Marker events in the early evolution of the solar system: Evidence from rims on Ca-Al-rich inclusions in carbonaceous chondrites. *Proc. Lunar Sci. Conf.* **8**, 95–112.
- Warner T. E., Rice N. M. and Taylor N. (1996) Thermodynamic stability of pentlandite and violarite and new EH-pH diagrams for the iron-nickel sulphur aqueous system. *Hydrometallurgy* **41**, 107–118.
- Wasserburg G. J., Hutcheon I. D., Aléon J., Ramon E. C., Krot A. N., Nagashima K. and Brearley A. J. (2011) Extremely Na- and Cl-rich chondrule from the CV3 carbonaceous chondrite Allende. *Geochim. Cosmochim. Acta* **75**, 4752–4770.
- Wasson J. T. and Kallemeyn G. W. (1988) Compositions of chondrites. *Philos. Trans. R. Soc. London. Ser. A, Math. Phys. Sci.* **325**, 535–544.
- Weber D. and Bischoff A. (1997) Refractory inclusions in the CR chondrite acfer 059-El djouf 001: Petrology, chemical composition, and relationship to inclusion populations in other types of carbonaceous chondrites. *Chemie der Erde* **57**, 1–24.
- Weinbruch S., Palme H., Müller W. F. and El Goresy A. (1990) FeO-rich rims and veins in Allende forsterite: Evidence for high temperature condensation at oxidizing conditions. *Meteoritics* **25**, 115–125.
- Weisberg M. K. (1987) Barred olivine chondrules in ordinary chondrites. *J. Geophys. Res. Solid Earth* **92**, E663–E678.
- Weisberg M. K. and Prinz M. (1998) Fayalitic olivine in CV3 chondrite matrix and dark inclusions: A nebular origin. *Meteorit. Planet. Sci.* **33**, 1087–1099.
- Wellman T. R. (1970) The stability of sodalite in a synthetic syenite plus aqueous chloride fluid system. *J. Petrol.* **11**, 49–72.
- Wellman T. R. (1969) The vapor pressure of NaCl over decomposing sodalite. *Geochim. Cosmochim. Acta* **33**, 1302–1303.
- Wood J. A. and Hashimoto A. (1988) The condensation sequence under non-classic conditions ($P < 10^{-3}$ atm, non-cosmic compositions). *Proc. Lunar Planet. Sci. Conf.* **19**, 1291–1292.
- Yoneda S. and Grossman L. (1995) Condensation of CaO–MgO–Al₂O₃–SiO₂ liquids from cosmic gases. *Geochim. Cosmochim. Acta* **59**, 3413–3444.

- Yurimoto H., Krot A. N., Choi B.-G., Aléon J., Kunihiro T. and Brearley A. J. (2008) Oxygen Isotopes of Chondritic Components. *Rev. Mineral. Geochemistry* **68**, 141–186.
- Zolensky M., Barrett R. and Browning L. (1993) Mineralogy and composition of matrix and chondrule rims in carbonaceous chondrites. *Geochim. Cosmochim. Acta* **57**, 3123–3148.
- Zolotov M. Y. (2012) Aqueous fluid composition in CI chondritic materials: Chemical equilibrium assessments in closed systems. *Icarus* **220**, 713–729.
- Zolotov M. Y. and Mironenko M. V. (2007) Hydrogen chloride as a source of acid fluids in parent bodies of chondrites. *Lunar Planet. Sci. Conf.* **38**, 2340 (abstract).
- Zolotov M. Y., Mironenko M. V. and Shock E. L. (2006) Thermodynamic constraints on fayalite formation on parent bodies of chondrites. *Meteorit. Planet. Sci.* **41**, 1775–1796.

SUPPLEMENTARY DATA

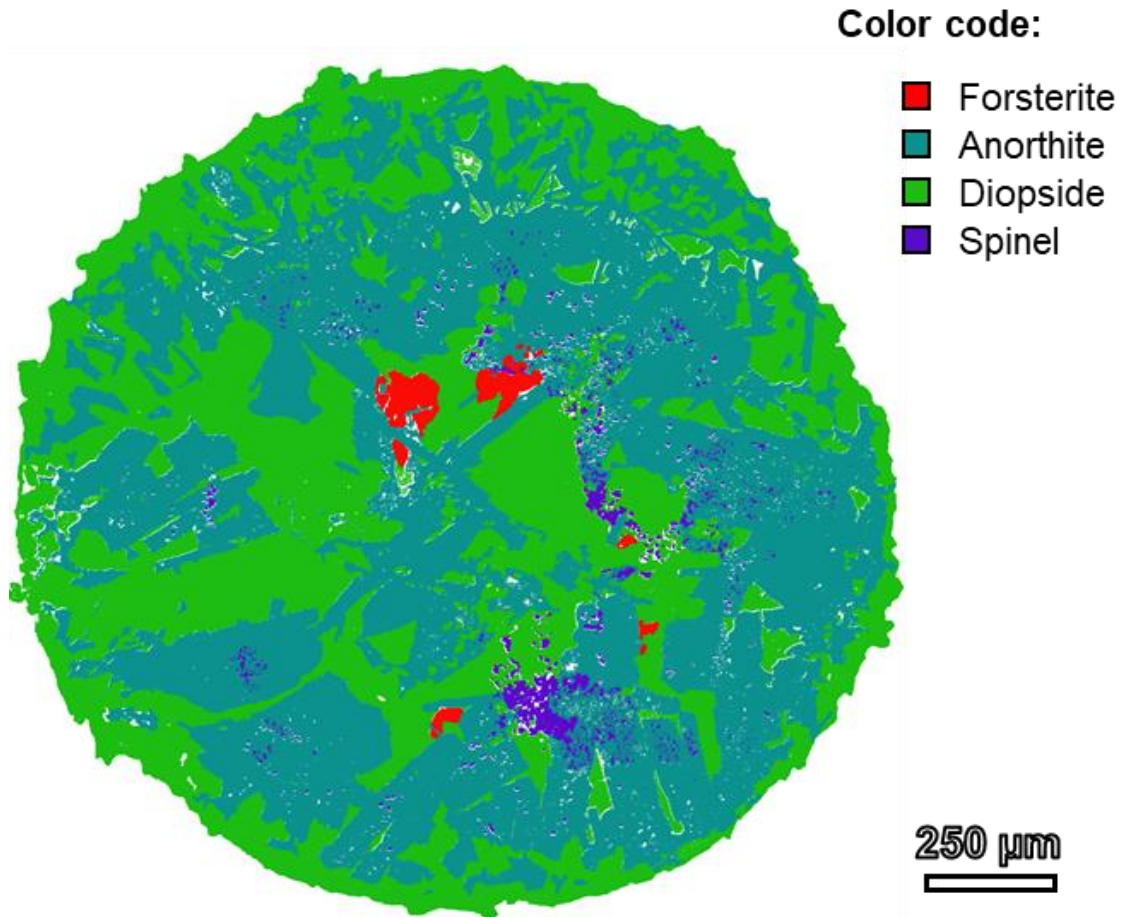


Fig. S1. The phase image of ALNH-04 produced using the modal recombination analysis method by Berlin (2012). Detail methodology is described in the text.

Table S1. Representative electron microprobe analyses of anorthite in ALNH-04.

| Region | Core | | Inner mantle | | Outer mantle | |
|--------------------------------|------------------|--------|--------------|-------|--------------|--------|
| | SiO ₂ | 42.98 | 42.95 | 42.52 | 42.13 | 43.86 |
| TiO ₂ | 0.04 | 0.05 | 0.04 | 0.03 | 0.01 | 0.04 |
| Al ₂ O ₃ | 36.82 | 37.02 | 35.89 | 36.29 | 33.12 | 34.17 |
| V ₂ O ₃ | 0.02 | 0.01 | 0.02 | bd | bd | 0.02 |
| Cr ₂ O ₃ | bd | bd | bd | bd | bd | bd |
| FeO | 0.14 | 0.10 | 0.13 | 0.04 | 1.13 | 0.86 |
| MnO | 0.01 | bd | bd | bd | bd | 0.01 |
| MgO | 0.26 | 0.24 | 0.29 | 0.13 | 0.42 | 0.54 |
| CaO | 20.06 | 20.12 | 20.11 | 20.20 | 18.41 | 18.67 |
| Na ₂ O | 0.27 | 0.23 | 0.27 | 0.14 | 1.13 | 1.09 |
| K ₂ O | bd | bd | bd | bd | 0.02 | 0.01 |
| Total | 100.59 | 100.74 | 99.27 | 98.96 | 98.09 | 100.07 |
| Cations per 8 oxygen anions | | | | | | |
| Si | 1.983 | 1.978 | 1.989 | 1.976 | 2.079 | 2.072 |
| Ti | 0.001 | 0.002 | 0.001 | 0.001 | 0.000 | 0.001 |
| Al | 2.002 | 2.010 | 1.979 | 2.006 | 1.850 | 1.868 |
| V | 0.001 | 0.000 | 0.001 | - | - | 0.001 |
| Cr | - | - | - | - | - | - |
| Fe | 0.005 | 0.004 | 0.005 | 0.002 | 0.045 | 0.034 |
| Mn | 0.000 | - | - | - | - | 0.000 |
| Mg | 0.018 | 0.017 | 0.020 | 0.009 | 0.029 | 0.037 |
| Ca | 0.992 | 0.993 | 1.008 | 1.015 | 0.935 | 0.928 |
| Na | 0.024 | 0.020 | 0.024 | 0.012 | 0.103 | 0.098 |
| K | - | - | - | - | 0.001 | 0.001 |
| Total | 5.026 | 5.025 | 5.029 | 5.020 | 5.044 | 5.039 |

Note: bd = below detection limits.

Table S2. Representative electron microprobe analyses of pyroxene in ALNH-04.

| Region | Core | | Inner mantle | | Outer mantle | | Rim | |
|--------------------------------|--------|--------|--------------|--------|--------------|--------|--------|--------|
| SiO ₂ | 41.49 | 43.51 | 50.27 | 49.49 | 53.38 | 51.39 | 56.45 | 51.07 |
| TiO ₂ | 2.54 | 2.56 | 1.19 | 1.33 | 0.69 | 1.07 | 0.29 | 1.14 |
| Al ₂ O ₃ | 19.34 | 16.11 | 6.81 | 7.17 | 2.62 | 5.52 | 1.37 | 7.02 |
| V ₂ O ₃ | 0.02 | 0.04 | 0.04 | 0.14 | 0.13 | 0.02 | 0.03 | 0.07 |
| Cr ₂ O ₃ | 0.02 | 0.22 | 0.40 | 0.46 | 0.29 | 0.58 | 0.31 | 0.51 |
| FeO | 0.30 | 0.18 | 0.13 | 0.13 | 0.36 | 0.28 | 0.72 | 0.58 |
| MnO | 0.05 | 0.04 | 0.04 | 0.01 | 0.05 | 0.11 | 0.07 | 0.06 |
| MgO | 11.11 | 12.44 | 16.88 | 16.95 | 18.78 | 16.65 | 24.54 | 16.59 |
| CaO | 25.34 | 25.16 | 24.46 | 24.30 | 23.76 | 24.46 | 18.27 | 24.56 |
| Na ₂ O | 0.02 | 0.01 | 0.01 | 0.01 | bd | 0.01 | bd | 0.01 |
| K ₂ O | bd | bd | 0.01 | 0.01 | bd | 0.01 | bd | bd |
| Total | 100.20 | 100.27 | 100.23 | 100.01 | 100.07 | 100.11 | 102.05 | 101.59 |
| Cations per 6 oxygen anions | | | | | | | | |
| Si | 1.508 | 1.579 | 1.812 | 1.790 | 1.920 | 1.854 | 1.957 | 1.818 |
| Ti | 0.069 | 0.070 | 0.032 | 0.036 | 0.019 | 0.029 | 0.008 | 0.030 |
| Al | 0.829 | 0.689 | 0.289 | 0.306 | 0.111 | 0.235 | 0.056 | 0.294 |
| V | 0.000 | 0.001 | 0.001 | 0.004 | 0.004 | 0.001 | 0.001 | 0.002 |
| Cr | 0.000 | 0.006 | 0.012 | 0.013 | 0.008 | 0.016 | 0.009 | 0.014 |
| Fe | 0.009 | 0.005 | 0.004 | 0.004 | 0.011 | 0.009 | 0.021 | 0.017 |
| Mn | 0.001 | 0.001 | 0.001 | 0.000 | 0.001 | 0.003 | 0.002 | 0.002 |
| Mg | 0.602 | 0.673 | 0.907 | 0.914 | 1.007 | 0.896 | 1.269 | 0.880 |
| Ca | 0.987 | 0.978 | 0.944 | 0.942 | 0.916 | 0.946 | 0.679 | 0.937 |
| Na | 0.001 | 0.001 | 0.001 | 0.001 | - | 0.001 | - | 0.001 |
| K | - | - | 0.000 | 0.000 | - | 0.001 | - | - |
| Total | 4.007 | 4.003 | 4.004 | 4.010 | 3.997 | 3.990 | 4.001 | 3.996 |

Note: bd = below detection limits.

Table S3. Representative electron microprobe analyses of spinel in ALNH-04.

| Region | Core | | | Inner mantle | | |
|--------------------------------|------------------|--------|--------|--------------|--------|--------|
| | SiO ₂ | 0.07 | 0.09 | 0.08 | 0.06 | 0.15 |
| TiO ₂ | 0.26 | 0.26 | 0.24 | 0.23 | 0.25 | 0.23 |
| Al ₂ O ₃ | 71.98 | 70.74 | 71.22 | 68.35 | 68.78 | 67.64 |
| V ₂ O ₃ | 0.60 | 0.66 | 0.52 | 0.57 | 0.47 | 0.60 |
| Cr ₂ O ₃ | 0.39 | 0.41 | 0.33 | 0.48 | 0.34 | 0.33 |
| FeO | 0.85 | 2.77 | 1.74 | 6.05 | 4.46 | 9.15 |
| MnO | 0.06 | 0.10 | 0.05 | 0.06 | 0.10 | 0.06 |
| MgO | 28.26 | 26.35 | 27.70 | 24.38 | 25.70 | 22.14 |
| CaO | 0.14 | 0.13 | 0.11 | 0.05 | 0.14 | 0.10 |
| Na ₂ O | bd | bd | 0.01 | 0.01 | 0.01 | 0.02 |
| K ₂ O | 0.01 | bd | bd | bd | 0.01 | 0.01 |
| Total | 102.61 | 101.50 | 101.99 | 100.23 | 100.39 | 100.34 |
| Cations per 4 oxygen anions | | | | | | |
| Si | 0.002 | 0.002 | 0.002 | 0.001 | 0.004 | 0.002 |
| Ti | 0.005 | 0.005 | 0.004 | 0.004 | 0.004 | 0.004 |
| Al | 1.972 | 1.977 | 1.970 | 1.963 | 1.958 | 1.968 |
| V | 0.011 | 0.013 | 0.010 | 0.011 | 0.009 | 0.012 |
| Cr | 0.007 | 0.008 | 0.006 | 0.009 | 0.006 | 0.006 |
| Fe | 0.017 | 0.055 | 0.034 | 0.123 | 0.090 | 0.189 |
| Mn | 0.001 | 0.002 | 0.001 | 0.001 | 0.002 | 0.001 |
| Mg | 0.979 | 0.931 | 0.969 | 0.886 | 0.926 | 0.815 |
| Ca | 0.003 | 0.003 | 0.003 | 0.001 | 0.004 | 0.003 |
| Na | - | - | 0.000 | 0.000 | 0.000 | 0.001 |
| K | 0.000 | - | - | - | 0.000 | 0.000 |
| Total | 2.998 | 2.995 | 3.000 | 3.001 | 3.004 | 3.001 |
| Fe# | 1.662 | 5.565 | 3.405 | 12.230 | 8.862 | 18.819 |

Note: bd = below detection limits.

Table S4. Representative electron microprobe analyses of forsterite in ALNH-04.

| Spot# | 1 | 2 | 3 | 4 | 5 | 6 |
|--------------------------------|--------|--------|--------|--------|--------|--------|
| SiO ₂ | 42.16 | 42.15 | 42.21 | 42.16 | 42.14 | 42.01 |
| TiO ₂ | 0.05 | 0.04 | 0.05 | 0.04 | 0.03 | 0.02 |
| Al ₂ O ₃ | 0.15 | 0.12 | 0.10 | 0.09 | 0.09 | 0.07 |
| V ₂ O ₃ | 0.04 | 0.01 | 0.03 | 0.04 | 0.06 | 0.03 |
| Cr ₂ O ₃ | 0.19 | 0.06 | 0.16 | 0.15 | 0.16 | 0.15 |
| FeO | 1.57 | 0.91 | 1.28 | 1.06 | 0.80 | 1.68 |
| MnO | 0.10 | 0.11 | 0.09 | 0.08 | 0.10 | 0.12 |
| MgO | 55.75 | 56.29 | 55.85 | 56.23 | 56.51 | 55.79 |
| CaO | 1.10 | 1.24 | 1.02 | 1.03 | 0.95 | 1.05 |
| Na ₂ O | 0.01 | bd | 0.01 | 0.01 | 0.01 | bd |
| K ₂ O | bd | 0.01 | 0.01 | bd | bd | bd |
| Total | 101.12 | 100.94 | 100.81 | 100.89 | 100.84 | 100.92 |
| Cations per 4 oxygen anions | | | | | | |
| Si | 0.988 | 0.987 | 0.991 | 0.988 | 0.987 | 0.987 |
| Ti | 0.001 | 0.001 | 0.001 | 0.001 | 0.000 | 0.000 |
| Al | 0.004 | 0.003 | 0.003 | 0.003 | 0.002 | 0.002 |
| V | 0.001 | 0.000 | 0.001 | 0.001 | 0.001 | 0.001 |
| Cr | 0.004 | 0.001 | 0.003 | 0.003 | 0.003 | 0.003 |
| Fe | 0.031 | 0.018 | 0.025 | 0.021 | 0.016 | 0.033 |
| Mn | 0.002 | 0.002 | 0.002 | 0.002 | 0.002 | 0.002 |
| Mg | 1.948 | 1.965 | 1.954 | 1.964 | 1.972 | 1.955 |
| Ca | 0.028 | 0.031 | 0.026 | 0.026 | 0.024 | 0.027 |
| Na | 0.000 | - | 0.001 | 0.000 | 0.000 | - |
| K | - | 0.000 | 0.000 | - | - | - |
| Total | 3.006 | 3.009 | 3.006 | 3.007 | 3.008 | 3.010 |
| Fa | 1.55 | 0.90 | 1.27 | 1.04 | 0.78 | 1.66 |

Note: bd = below detection limits.

Table S5. Representative electron microprobe analyses of Al-Fe silicate in ALNH-04.

| Spot# | 1 | 2 | 3 | 4 | 5 |
|--------------------------------|-------|-------|-------|--------|--------|
| SiO ₂ | 34.51 | 34.86 | 36.24 | 37.72 | 38.69 |
| TiO ₂ | 0.02 | 0.06 | 0.03 | 0.03 | 0.10 |
| Al ₂ O ₃ | 0.78 | 1.82 | 3.73 | 4.17 | 4.08 |
| V ₂ O ₃ | 0.01 | 0.03 | 0.01 | 0.02 | 0.02 |
| Cr ₂ O ₃ | 0.04 | 0.05 | bd | 0.01 | 0.02 |
| FeO | 36.52 | 35.96 | 26.61 | 26.64 | 23.52 |
| MnO | 0.24 | 0.21 | 0.15 | 0.16 | 0.14 |
| MgO | 25.81 | 26.12 | 31.29 | 30.52 | 31.72 |
| CaO | 0.27 | 0.39 | 0.26 | 0.56 | 2.48 |
| Na ₂ O | 0.07 | 0.10 | 1.07 | 0.96 | 0.35 |
| K ₂ O | bd | bd | 0.01 | 0.19 | 0.15 |
| Total | 98.26 | 99.59 | 99.40 | 100.99 | 101.28 |
| Cations per 4 oxygen anions | | | | | |
| Si | 0.982 | 0.965 | 0.968 | 0.986 | 0.994 |
| Ti | 0.000 | 0.001 | 0.001 | 0.001 | 0.002 |
| Al | 0.026 | 0.059 | 0.117 | 0.128 | 0.124 |
| V | 0.000 | 0.001 | 0.000 | 0.000 | 0.000 |
| Cr | 0.001 | 0.001 | - | 0.000 | 0.000 |
| Fe | 0.869 | 0.833 | 0.594 | 0.583 | 0.506 |
| Mn | 0.006 | 0.005 | 0.003 | 0.004 | 0.003 |
| Mg | 1.095 | 1.078 | 1.246 | 1.190 | 1.215 |
| Ca | 0.008 | 0.012 | 0.007 | 0.016 | 0.068 |
| Na | 0.004 | 0.005 | 0.055 | 0.049 | 0.018 |
| K | - | - | 0.000 | 0.006 | 0.005 |
| Total | 2.991 | 2.960 | 2.993 | 2.963 | 2.935 |

Note: bd = below detection limits.